



UNIVERSITAT POLITÈCNICA
DE CATALUNYA
BARCELONATECH

PhD program in civil engineering

Multiscale subsurface characterization for geo-energy applications

Author's name

Dario Sciandra

Supervised by

Dr. Víctor Vilarrasa Riaño

Dr. Iman Rahimzadeh Kivi

Tutored by

Dr. Sebastià Olivella Pastalle

Department of Civil and Environmental Engineering (DECA), Universitat
Politécnica de Catalunya (UPC), Barcelona

Ph.D. Thesis

Multiscale subsurface characterization for geo-energy applications

BY

Dario Sciandra

AT

Universitat Politècnica de Catalunya

Supervised by

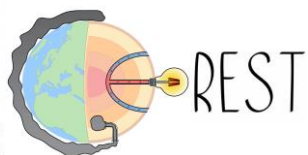
Dr. Víctor Vilarrasa Riaño

Dr. Iman Rahimzadeh Kivi

Tutored by

Dr. Sebastià Olivella Pastalle

This thesis was funded by the European Research Council (ERC) under the European Union's Horizon 2020 Research and Innovation Program through the Starting Grant GGeoREST (www.georest.eu) under Grant agreement No. 801809.



ABSTRACT

Geological Carbon Storage (GCS) is considered a promising technology to lower atmospheric emissions of CO₂. Guaranteeing the sealing capacity of caprocks in this case becomes paramount as CO₂ storage scales up to the gigaton scale. Many laboratory experiments have been performed with samples of intact rock, showing that low-permeability and high-entry pressure caprocks have excellent sealing capacities to contain CO₂ deep underground. However, discontinuities, such as bedding planes, fractures, and faults, affect the rock properties at the field scale, being at the same time challenging to monitor in industrial-scale applications. The main objective of the thesis is to develop a methodology to characterize potential sites for low-carbon geo-energy applications at multiple scales in space and time, taking into account coupled processes. To achieve this objective, it is necessary to understand the complexity of the problem at multiple scales, starting from large-scale investigations, passing through in-situ underground rock laboratories, to laboratory investigations. This is why this thesis approaches characterizations that span a wide range of spatiotemporal scales from the order of millimeters and nanoseconds to the order of kilometers and decades.

To achieve this general objective, the first part of the thesis explores four analytical solutions of pore pressure diffusion with periodic sources under relevant model geometries and boundary conditions to enable real-time interpretation of in-situ data. We compare the results with numerical solutions, assuming the same conditions as the analytical cases and incorporating reservoir deformation due to pressure waves. Encompassing three different cases to span a wide array of scenarios, we evaluate the attenuation of the signal at varying distances from the source. Numerical and analytical solutions fit when identical assumptions are upheld. Furthermore, the influence of effective mean stress variations yields errors of less than 3% across all the considered cases. Our findings reveal distinct wave propagation depending on the application. For energy storage in highly porous and permeable rocks, the wave propagation extends over kilometer scales. In the case of liquid injection into tight shale, the wave propagation is confined to tens of centimeters. Meanwhile, for enhanced geothermal systems stimulation in crystalline rock, the wave propagation occurs in the order of tens of meters. While numerical solutions can consider multidimensional hydro-mechanical rock response to periodic signals, analytical solutions provide an immediate initial approximation of the problem, enabling rapid reactions to unexpected events.

Next, we perform plane-strain coupled hydro-mechanical simulations using a linear transversely isotropic poroelastic model of periodic CO₂ injection for 20 years to simulate the planned CO₂LPIE experiment at Mont Terri Underground Rock Laboratory, in Switzerland. Simulation results show that pore pressure changes and the resulting stress variations are controlled by the anisotropic behavior of the material, producing a preferential advance along the bedding planes. CO₂ cannot penetrate Opalinus Clay due to the strong capillary effects in the nanoscale pores, but advances dissolved into the resident brine. We find that the pore pressure oscillations imposed at the injection well are attenuated within tens of cm, requiring a close location of the monitoring boreholes for the injection interval to observe the periodic signal.

Finally, we develop a 3D numerical model of water injection into the fractured specimen to replicate steady-state flow experiments on a naturally fractured Opalinus Clay specimen. This model explicitly accounts for fracture geometry with stress-dependent aperture changes. Simulation results reveal that fracture permeability spans up to nine orders of magnitude. This significant change in permeability has profound implications for the fluid flow within the rock specimen. Our numerical model achieves the best fit with the experimental results by incorporating a natural fracture normal stiffness from 18.7 MPa/mm at effective mean stresses

below 12 MPa to 187.2 MPa/mm at higher confinements. This outcome highlights the critical importance of defining the hydro-mechanical parameters of fractures under realistic effective stress conditions with far-reaching implications for secure underground storage.

RESUMEN

El almacenamiento geológico de carbono se considera una tecnología prometedora para reducir las emisiones atmosféricas de CO₂. Garantizar la capacidad de sellado de las rocas sello resulta importante a medida que el almacenamiento de CO₂ alcanza la escala de gigatoneladas. Se han realizado muchos experimentos de laboratorio con muestras de roca intacta, que demuestran que las rocas de baja permeabilidad y alta presión de entrada tienen una excelente capacidad de sellado para contener CO₂ en el subsuelo. Sin embargo, las discontinuidades, como los planos de estratificación, las fracturas y las fallas, afectan a las propiedades de la roca a escala de campo, siendo al mismo tiempo difíciles de controlar en aplicaciones a escala industrial. El objetivo principal de la tesis es desarrollar una metodología para caracterizar emplazamientos potenciales para aplicaciones geo-energéticas con bajas emisiones de carbono a múltiples escalas en el espacio y el tiempo, teniendo en cuenta los procesos acoplados. Para alcanzar este objetivo, es necesario comprender la complejidad del problema a múltiples escalas, empezando por las investigaciones a gran escala, pasando por los laboratorios in situ de rocas subterráneas, hasta las investigaciones de laboratorio. Por ello, esta tesis aborda caracterizaciones que abarcan un amplio abanico de escalas espaciotemporales del orden de los milímetros y nanosegundos hasta el orden de los kilómetros y décadas.

Para alcanzar este objetivo general, la primera parte de la tesis explora cuatro soluciones analíticas de la difusión de la presión de poro con fuentes periódicas bajo geometrías y condiciones de contorno del modelo relevantes para permitir la interpretación en tiempo real de los datos in situ. Comparamos los resultados con las soluciones numéricas, asumiendo las mismas condiciones que en los casos analíticos e incorporando la deformación del yacimiento debida a las ondas de presión. Evaluamos la atenuación de la señal a distintas distancias de la fuente en tres casos diferentes para abarcar una amplia gama de escenarios. Las soluciones numéricas y analíticas se ajustan cuando se mantienen supuestos idénticos. Además, la influencia de las variaciones de la tensión media efectiva arroja errores inferiores al 3% en todos los casos considerados. Nuestros resultados revelan una propagación de ondas distinta en función de la aplicación. En el caso del almacenamiento de energía en rocas muy porosas y permeables, la propagación de las ondas se extiende a escala kilométrica. En el caso de la inyección de fluidos en lutitas compactas, la propagación de las ondas se limita a decenas de centímetros. Mientras que, en el caso de la estimulación de sistemas geotérmicos mejorados, la propagación de las ondas se produce en el orden de decenas de metros. Mientras que las soluciones numéricas pueden considerar la respuesta hidromecánica multidimensional de la roca a señales periódicas, las soluciones analíticas proporcionan una aproximación inicial inmediata del problema, lo que permite reaccionar con rapidez ante acontecimientos inesperados.

A continuación, realizamos simulaciones hidromecánicas acopladas por deformación plana utilizando un modelo poro-elástico lineal transversalmente isótropo de inyección periódica de CO₂ durante 20 años para simular el experimento CO₂LPIE previsto en el laboratorio subterráneo de roca de Mont Terri, en Suiza. Los resultados de la simulación muestran que los cambios de presión de poro y las variaciones de tensión resultantes están controlados por el comportamiento anisótropo del material, produciendo un avance preferencial a lo largo de los planos de estratificación. El CO₂ no puede penetrar en la arcilla Opalinus debido a los fuertes efectos capilares en los poros a nano-escala, pero avanza disuelto en la salmuera residente. Encontramos que las oscilaciones de la presión de poro impuestas en el pozo de inyección se atenúan en decenas de cm, lo que requiere una localización cercana de los sondeos de monitorización del intervalo de inyección para observar la señal periódica.

Por último, desarrollamos un modelo numérico en 3D de la inyección de agua en la muestra fracturada para reproducir los experimentos de flujo en estado estacionario en una muestra de arcilla Opalinus fracturada de forma natural. Este modelo tiene en cuenta explícitamente la geometría de la fractura con cambios de apertura dependientes de la tensión. Los resultados de la simulación revelan que la permeabilidad de la fractura se extiende hasta nueve órdenes de magnitud. Este cambio significativo en la permeabilidad tiene profundas implicaciones para el flujo de fluidos dentro del espécimen de roca. Nuestro modelo numérico logró el mejor ajuste con los resultados experimentales incorporando una rigidez normal natural de la fractura de 18.7 MPa/mm a tensiones medias efectivas inferiores a 12 MPa hasta 187.2 MPa/mm a confinamientos superiores. Este resultado pone de relieve la importancia crítica de definir los parámetros hidromecánicos de las fracturas en condiciones de tensión efectiva realistas, con implicaciones de gran alcance para el almacenamiento subterráneo seguro.

List of Contents

CHAPTER 1	1
INTRODUCTION.....	1
1.1. Background and motivation	1
1.2. Objectives and methodology.....	4
1.3. Thesis layout	5
CHAPTER 2	7
REVIEW OF MULTISCALE CLAY-RICH CAPROCK CHARACTERIZATION FOR GEOLOGIC CARBON STORAGE.....	7
2.1. Introduction	7
2.2. Laboratory characterization	9
2.2.1. Diffusive leakage	9
2.2.2. Capillary leakage.....	12
2.2.3. Permeability of the shale matrix and fractures	16
2.3. Underground Rock Laboratory characterization	18
2.3.1. Hydraulic properties of the matrix	18
2.3.2. Transport properties of the matrix.....	18
2.3.3. Fault testing.....	19
2.4. In situ monitoring and characterization.....	20
2.5. Future work	21
CHAPTER 3	25
CHARACTERIZATION OF HYDRAULIC ROCK DIFFUSIVITY USING OSCILLATORY PORE PRESSURE	25
3.1. Introduction	25
3.2. Theory	27
3.2.1. The diffusion equation for poroelastic materials.....	27
3.2.2. Uncoupled 1D diffusion for incompressible solid matrix	28
3.2.3. Uncoupled 1D diffusion of oscillatory input.....	28
3.2.4. 1D diffusion of oscillatory input at constant lateral stress	29
3.2.5. Uncoupled cylindrical two-dimensional diffusion of periodic pressure.....	30
3.3. Test cases and numerical models	30
3.3.1. Geometry definition	32
3.3.2. Hydraulic model.....	32
3.3.3. Hydro-mechanical model	33
3.4. Results	34
3.4.1. Comparison between analytical and numerical solutions	34

3.4.2.	Attenuation ratios for various analytical solutions	36
3.5.	Discussion	38
3.5.1.	Pore pressure response affected by rock properties	38
3.5.2.	Pore pressure response affected by fluid properties	39
3.5.3.	Pore pressure response affected by the period	40
3.5.4.	Accuracy of analytical models and contribution of the reservoir deformation	41
3.5.5.	Applications of the methods to support design and monitoring stages	41
3.6.	Conclusions	43
 CHAPTER 4		 45
 HYDRO-MECHANICAL RESPONSE OF OPALINUS CLAY IN THE CO₂ LONG-TERM PERIODIC INJECTION EXPERIMENT (CO₂LPIE) AT THE MONT TERRI ROCK LABORATORY		 45
4.1.	Introduction	45
4.2.	Overview of the Mont Terri rock laboratory and the CO₂LPIE experiment	47
4.3.	Methodology	49
4.3.1.	Description of the Hydro-Mechanical model	49
4.3.2.	Geometry and model setup	51
4.3.3.	Model parameters	52
4.4.	Results	54
4.4.1.	Reference case with amplitude $A_I = 0.5$ MPa	54
4.4.2.	Long-term rock stability and deformation	59
4.4.3.	Sensitivity analysis of the amplitude of the periodic injection	60
4.4.4.	Sensitivity analysis of hydraulic properties at the site scale	63
4.5.	Discussion	63
4.6.	Conclusions	65
 CHAPTER 5		 67
 REVEALING HYDRO-MECHANICAL PROPERTIES OF FRACTURES IN SHALE		 67
5.1.	Introduction	67
5.2.	Methodology	68
5.2.1.	Governing equations	68
5.2.2.	Specimen description	69
5.2.3.	Experimental procedure	71
5.2.4.	Numerical model geometry, initial and boundary conditions	72
5.3.	Results	74
5.3.1.	Hydro-mechanical properties	74
5.3.2.	Stress-dependent normal stiffness of the fracture	76
5.3.3.	Fracture deformation	77
5.3.4.	Permeability changes and flow along the fractured specimen	79
5.4.	Discussion	81

5.5. Conclusions	83
CHAPTER 6	85
CONCLUSIONS.....	85
APPENDIX A	87
VALIDATION OF ADACHI AND DETOURNAY (1997) SOLUTION AT THE CORE SCALE.....	87
APPENDIX B.....	91
3D HYDRO-MECHANICAL MODELING OF SHALY CAPROCK RESPONSE TO CO₂ LONG-TERM PERIODIC INJECTION EXPERIMENT (CO₂LPIE).....	91
APPENDIX C	103
SOLUTION OF THE HYDRAULIC PROBLEM AND CALIBRATION OF NATURAL FRACTURE INITIAL APERTURE	103
REFERENCES	107

Chapter 1

INTRODUCTION

1.1. Background and motivation

The lack of a clearly defined methodological characterization protocols in geo-energy projects has led to undesirable consequences and failures. Examples of such consequences are induced earthquakes that, in a few occasions, have ended up with the cancellation of projects, such as occurred at the underground gas storage project of Castor, Spain (Cesca et al., 2014; Vilarrasa et al., 2021) and the Enhanced Geothermal Systems (EGS) of Basel, Switzerland (Häring et al., 2008), and Pohang, South Korea (Ellsworth et al., 2019; Kim et al., 2018; Lee et al., 2019). To approach similar challenges, it is imperative to conduct thorough characterization before, during and after the project. The overall cost of precise subsurface characterization is relatively inconsequential when weighed against the potential benefits. Indeed, the mitigation of uncertainties in design and the ability to adapt during operations can be achieved through meticulous investigation, ongoing characterization, and refine modeling. Insufficient and/or incorrect design hypotheses often lead to unexpected expenses.

This general discussion applies at every low-carbon geo-energy application, i.e., geothermal energy production, Geological Carbon Storage (GCS) and subsurface hydrogen storage. Subsurface characterization requires determining hydraulic, thermal, geomechanical, seismic and geochemical properties of the zone of interest, which in the case of geo-energy applications usually refers to the reservoir and its surrounding confining rock and faults. In more practical terms, we could say that the characterization has the purpose of providing the information needed for defining predictive numerical models and the input parameters to be used for the area of interest, taking into account both spatial and time changes. Nonetheless, the characterization that should be performed in every site before the start of the project is not enough because the characterized volume of rock is small during the initial characterization tests. Given that pore pressure diffusion advances with the square root of time, the region affected by geo-energy projects will be of tens to hundreds of kilometers after several decades of injection. Thus, the operation of projects can be used as a long-term characterization test by itself, providing information of a continuously increasing rock volume. Furthermore, since rock properties may evolve during and after the injection, the characterization must continue during operation and models and parameters need to be regularly updated in order to reduce subsurface uncertainty and obtain more reliable predictive simulations.

Hydraulic characterization focuses on determining the capacity of the reservoir, generally a confined aquifer, to store and/or transfer mass and/or heat and the sealing capacity of the confinement layers. For this reason, the permeability of both units (aquifer and confinement layers) is a key parameter, together with porosity, transmissivity and capillary properties (Ferris et al., 1962; Bear, 2013). Several methods and theories are used to evaluate those parameters, for example pumping tests. The idea is to pump or inject water in the formation of interest while measuring the water level changes in the observation points. To have more information, monitoring usually continues after the injecting phase until the pressure returns to the initial state. This latter test is known as “recovery test” and is classified as passive. However, these characterization approaches should be applied to fractured media with caution or after appropriate modifications of their implementation or interpretation. This is due to irreversible or partially reversible changes in rock imposed by pressure-induced fracture opening and/or

shear slip on their surfaces. Cyclic and step rate testing have been proposed to deal with these challenges (Hofmann et al., 2019). They provide useful information on when new fractures occur or pre-existing fractures open/propagate and how they affect rock properties, mainly hydraulic conductivity.

To characterize transport properties in the field, tracer tests are usually performed (Mazurek et al. 2011). With tracer testing, we identify the injection into the hydrogeological system of one or more substances called tracers. Tracer methods are used to study flow and transport properties and also reactions of fluids and components. Therefore, in addition to hydraulic tests, chemical and thermal tests can be performed depending on the tracer. Another advantage that makes this technique particularly suitable in applications like GCS is the possibility to access a wide range of space and time scales, since they can be used both before and after injection of CO₂.

Rock strength and geomechanical response of the rock (represented by Young's modulus and Poisson's ratio while rock behaves elastically) control the maximum sustainable injection pressure and associated deformation. These geomechanical properties are usually evaluated by comparing in-situ field observations with laboratory test results. Despite its elevated cost, intact rock is sometimes recovered from boreholes to provide samples for laboratory testing. In this way, it is possible to determine, in a small scale but with high precision, the properties of the sample, generally indicated as intact rock properties. With in-situ observations, it is then possible to extend the core-scale laboratory information to the geotechnical unit, generally indicated as rock mass (e.g., Vilarrasa et al., 2013).

In common practice, the hydraulic, thermal, geomechanical, seismic and geochemical behaviors are analyzed from independent tests in distinct moments of the designing and monitoring process. However, it is well known that those aspects influence each other. For example, when a fluid is injected into a fracture, the fracture opens in response to pore pressure increase, enhancing its permeability, which in turn lowers pore pressure buildup. Furthermore, if the increased pore pressure is high enough to induce shear slip on rough fracture surfaces, the fracture will permanently open because of the shear-induced dilation, causing permeability enhancement and changes in the flow field. The shear slip also leads to stress relaxation and variations in the initial state of stress (Ye and Ghassemi, 2018). Besides, the temperature can also change during the lifespan of geo-energy projects and affect the reservoir and confining rocks in different spatial scales. The cooling- and heating-induced stresses in the target formation may contribute to the shear-slip of fractures and related changes in productivity or injectivity (Min et al., 2013). These thermal stresses are also likely to take place in the caprock during CO₂ injection and can affect the caprock sealing capacity (Vilarrasa et al., 2015). Thus, this process must not be considered just as purely hydraulic. This and other coupled processes control the response of rock mass to fluid injection and/or extraction. Appropriate conceptual, analytical and numerical modeling approaches should be employed to deal with the complex interplay between these mechanisms.

The interpretation of coupled processes is usually neglected but valuable information can be extracted from them, depending on the specific site characteristics. This thesis aims at contributing to the reduction of this knowledge gap, as well as extending the characterization to a continuous one during the whole lifetime of projects.

In the case of geo-energy, a fluid injection and/or extraction is always involved. For clarity, let us take the typical example of gas injection into a saturated formation to explain coupled processes. If the injection pressure overcomes the capillary entry pressure, gas bubbles displace the liquid in place and enter the reservoir as a free phase. This process is governed by the retention properties. The van Genuchten model is generally used for this purpose (van Genuchten, 1980). Besides, the gas may also partially dissolve into the reservoir fluid. The spatial difference in the dissolved gas concentration leads to another flow mechanism, called

molecular diffusion. In cases where the dissolved gas (for example CO_2) changes the fluid pH and hence the acidity, geochemical reactions within the rock will occur in terms of mineral dissolution/precipitation. These reactions induce irreversible changes in mechanical, capillary and flow properties of the rock. The increase in fluid pressure, caused by injection, changes the initial effective stress distribution which governs the mechanical behavior of the rock. The injection can influence pre-existing fractures and faults or create new ones. This is a delicate aspect, due to the possibility of inducing seismicity. In addition, the injected fluid has generally a lower temperature than the reservoir, causing cooling-induced changes both in fluid flow behavior (due to viscosity changes) and stress variations (due to thermal-stress reduction). In some EGS sites, this behavior is provoked on purpose, because cooling generates contraction of the rock skeleton and opening of fractures, increasing the permeability of the reservoir. All these processes evolve and influence each other dynamically for all the duration of the project, which can last for tens of years, and even after the end of operation, the processes continue evolving, producing Thermo-Hydro-Mechanical-Chemical (THMC) and even seismic coupled effects (Figure 1.1).

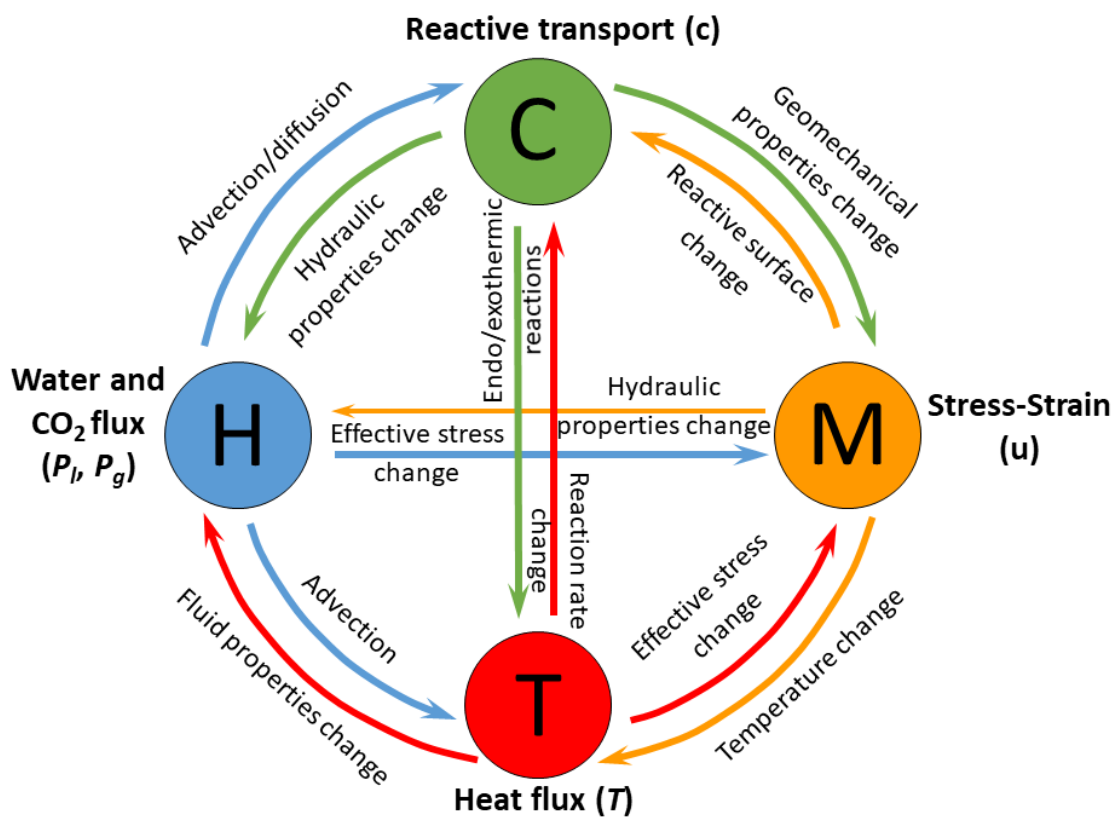


Figure 1.1. THMC coupled processes in geo-energy applications.

Given the complexity of the problem, some simplifying approaches can be used to improve our process understanding of the problem, like considering all the processes separately and then, superpose their effects to analyze the relative weight of each of them (De Simone et al., 2017). In general, to model this complex behavior, a series of parameters, determined with specific investigations, are needed. The details of how to obtain them are beyond the objective of this thesis. For the purposes of this thesis, Hydro-Mechanical (HM) coupled characterization is addressed, as synthetically reported in Figure 1.2.

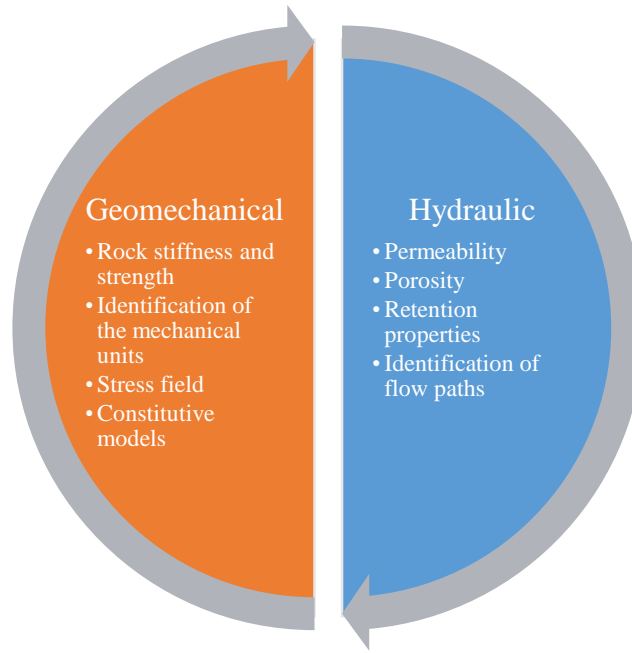


Figure 1.2. Hydro-Mechanical (HM) characterization process.

1.2. Objectives and methodology

The methodology followed in this thesis covers multiple scales, from the sub-millimeter to kilometer scale (Figure 1.3).

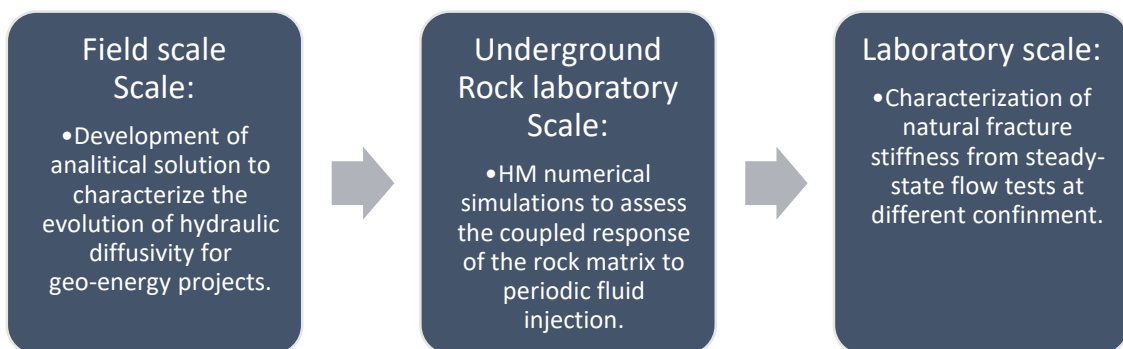


Figure 1.3. Description of the objectives of this thesis at each scale proposed.

At the field scale, a continuous characterization methodology for geo-energy projects is proposed, taking advantage of the cyclic nature that some of these application have. The first considered analytical solution, which is purely hydraulic, was carried out by Ferris (1952). He proposed to use the cyclic fluctuation of the water level to determine the transmissivity of aquifers. The advantages of this formulation are that: (1) it is relatively simple to apply, (2) it has a physical base (Jacob, 1950), and (3) it has been defined and tested at field scale (Ferris et al., 1962). However, the deformation of the solid phase is neglected and one phase flow is considered. A second analytical solution, this one taking into account rock deformation (Adachi

and Detournay, 1997), i.e., a poroelastic model, is also used in this study. This poromechanical solution was built on a former model proposed by Kranz et al. (1990), who hypothesized a Skempton B coefficient equal to zero, i.e., the mechanical effect is neglected. The limitation of Adachi and Detournay (1997) solution is that it was derived for slender specimens under boundary conditions typical of laboratory experiments. The last analytical solution is based on the analogy with the thermal diffusion equation for an infinite cylinder (Carslaw and Jaeger, 1959). The analysis is carried out by plotting the attenuation of the amplitude as a function of the distance from the source and the HM properties of the rock, synthesized by the hydraulic diffusivity.

At the Underground Rock Laboratory (URL) scale, the problem is addressed numerically to describe the anisotropic behavior of Opalinus Clay during the injection planned for the CO₂ Long-term Periodic Injection Experiment (CO₂LPIE), a test that will be performed at the Mont Terri Rock Laboratory, in Switzerland (Rebscher et al., 2020). The objective is to assist in the design of the experiment. Numerical simulations with both 2D and 3D geometries are defined to better understand the HM coupled processes occurring in the CO₂LPIE experiment. The simulations are performed with the fully-coupled finite-element code CODE_BRIGHT (Olivella et al., 1996). Its adaptability allows to analyze the contribution of each single process and their combined effect, as it is well known that all the processes interact and influence each other (Figure 1.1).

Finally, at the laboratory scale, flow into two Opalinus Clay specimens is analyzed, an intact one and one containing a natural fracture. The different permeability of the specimens is to be attributed to the presence of a natural fracture that intersect the whole length of one of the two specimens. Given the lack of instrumentation on the fracture, the first objective was to characterize its HM behavior of the fracture

1.3. Thesis layout

This thesis is organized into 6 chapters, starting with a general review of the problem (Chapter 2) to then address specific objective at the different scales, from the larger in situ scale (Chapter 3), to URL scale (Chapter 4), and finally the laboratory scale (Chapter 5). At the end, the main conclusions of the thesis are summarized (Chapter 6). Each chapter is then contributing to the multiscale characterization process, but it can also be taken as an independent research:

- Chapter 2 gives a general review of the problem, focusing on the clay-rich caprock characterization for geologic carbon storage, considering laboratory, underground rock laboratory, and in situ scales. The contents of this Chapter will be submitted to a scientific journal.
- Chapter 3 explores four analytical solutions of pore pressure diffusion with periodic sources under relevant model geometries and boundary conditions to enable real-time interpretation of in-situ data. We compare the results with numerical solutions, assuming the same conditions as the analytical cases and incorporating reservoir deformation due to pressure waves. The contents of this Chapter have been submitted to a scientific journal and are currently under review.
- Chapter 4 explores HM simulations using a linear transversely isotropic poroelastic model of periodic CO₂ injection for 20 years to simulate the planned CO₂LPIE experiment at Mont Terri underground rock laboratories, in Switzerland. Simulation results show that pore pressure changes and the resulting stress variations are controlled by the anisotropic behavior of the material, producing a preferential advance along the

bedding planes. The contents of this Chapter have been presented in several conferences (e.g., Sciandra et al., 2022a) and published in *Geomechanics and Geophysics for Geo-Energy and Geo-Resources* (Sciandra et al., 2022b).

- Chapter 5 shows the 3D numerical model of water injection into the fractured specimen to replicate steady-state flow experiments on a naturally fractured Opalinus Clay specimen. This model explicitly accounts for fracture geometry with stress-dependent aperture changes. Our numerical model achieved the best fit with the experimental results by incorporating a stress-dependent natural fracture normal stiffness. The contents of this Chapter have been submitted to a scientific journal and are currently under review.

Appendixes and references are reported at the end of the thesis, in this order.

Chapter 2

Review of multiscale clay-rich caprock characterization for geologic carbon storage

2.1. Introduction

Geological Carbon Storage (GCS) is considered one of the most promising technologies available to lower atmospheric emissions of CO₂ from large industrial emitters (Bennaceur et al., 2008; IPCC, 2022). The targets for GCS are commonly deep saline aquifers (Niemi et al., 2017; Vilarrasa et al., 2010b), oil and gas fields depleted or requiring enhanced recovery (Li et al., 2006; Whittaker et al., 2011), and unminable coal seams (Reeves, 2001; Oudinot et al., 2011).

To enhance the efficiency of GCS in sedimentary basins, it is advantageous to inject the CO₂ in a supercritical state (scCO₂) due to its higher density compared to gaseous CO₂ at ambient conditions. Achieving temperatures and pressures beyond the critical point necessitates injection at depths over 800 meters (Shukla et al., 2010; Song and Zhang, 2013; Vilarrasa et al., 2014; Ajayi et al., 2019; Kalam et al., 2021). ScCO₂ exhibits gas-like viscosity while maintaining a liquid-like density ranging from approximately 640 to 800 kg/m³ (Span and Wagner, 1996; Vilarrasa et al., 2010a). Owing to its lower density compared to the in situ brine, scCO₂ tends to migrate upward by buoyancy. Consequently, secure subsurface disposal mandates the presence of an adequately impermeable sealing rock layer (caprock) above the underground storage zone to prevent the upward migration of the injected fluid (Figure 2.1). Indeed, the surface release of CO₂ poses environmental risks and potential impacts on biodiversity (Benson and Myer, 2002; Pruess, 2008). The effectiveness of GCS is contingent on maintaining leakage rates below 0.001% per year over 10⁴ years (IPCC, 2022; Alcalde et al., 2018).

Commercial GCS sites typically involve the injection of megatonnes of CO₂ into the subsurface over several decades, resulting in the formation of a CO₂-caprock interface with a substantial area, often spanning several tens of square kilometers. In these extensive areas, the caprock may include heterogeneities at varying scales, ranging from micrometer pore space heterogeneities to submillimeter-scale fissures to meter- and kilometer-long fractures and faults (Figure 2.1). The assessment of caprock performance in GCS projects should consider the effect of these pore structural complexities and discontinuity structures.

Multiple concurrent processes, including but not limited to multi-phase flow and mechanical deformation, could be operative in CO₂ migration out of the storage aquifer. The effective stress change of rocks and associated deformation play a key role, as injecting CO₂ primarily increases pore pressure, propagating proportionally to the square root of time, and alters the stress distribution in the reservoir and overlaying layers. The change in the stress field can impact the performance of the GCS site in several ways. Firstly, the induced stresses, if large enough, may cause failure in the caprock, potentially generating new high-permeability fractures that could enhance leakage. Secondly, the induced stresses may influence pre-existing faults and fractures, causing either opening or shear displacement and, possibly, increase in their permeability. Thirdly, the injection of supercritical CO₂ can lead to observable surface uplift due to a reduction in effective stress in the aquifer and the lower part of the caprock (Figure 2.1) (Rutqvist and Tsang, 2002; Vasco et al., 2008; Rutqvist et al., 2010; Vilarrasa et al., 2011; Rutqvist 2012; 2015; Vilarrasa et al., 2019).

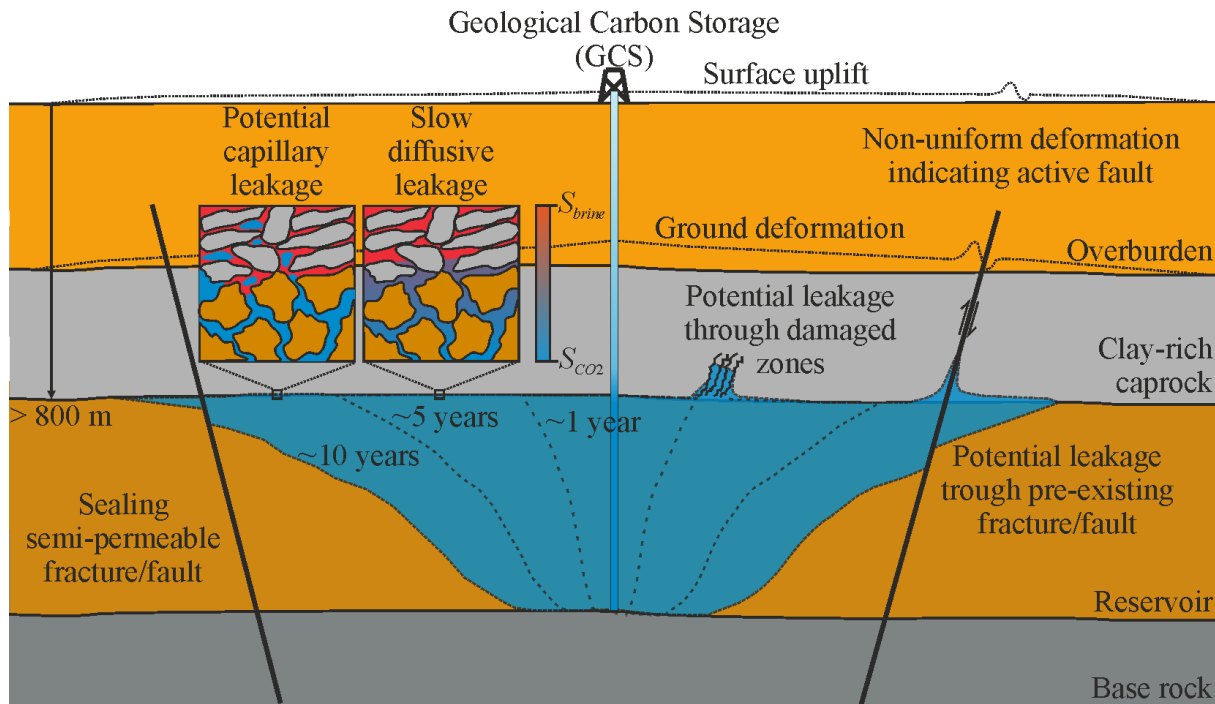


Figure 2.1. Potential leakage mechanisms during the spread of CO₂ plumes in Geologic Carbon Storage (GCS) sites include diffusion and capillary leakage. Surface uplift results from the injection-induced expansion of the aquifer, possibly leading to relative movements in superficial faults. Shearing may enhance fracture permeability and the possibility of leakage.

Significant Hydro-Mechanical (HM) alterations in a caprock have the potential to compromise its sealing efficacy for the secure and sustained containment of CO₂ in the subsurface. In GCS projects, when considering leakage through the caprock, three critical hydraulic processes must be characterized: molecular diffusion of CO₂ through the brine-saturated caprock, surpassing the capillary entry pressure leading to CO₂ leakage via interconnected flow paths in the caprock's pore system, and localized flow through permeable fractures (refer to Figure 2.1) (Vavra et al., 1992; Al-Bazali et al., 2005; Edlmann et al., 2013; Song and Zhang, 2013; Kivi et al., 2022a). However, due to financial and technological constraints, the collection of subsurface data is typically confined to specific intervals, resulting in sparse temporal and spatial characterization of caprock properties (Iding and Ringrose, 2009; Niemi et al., 2017). Potential caprocks considered for GCS typically exhibit permeabilities below 10⁻¹⁸ m² and elevated CO₂ entry pressures, ranging from approximately 1 to more than 10 MPa (IPCC, 2005; Makhnenko et al., 2017). Clay-rich sedimentary formations are characterized by low mass-transfer properties, significant heterogeneity, and effective sealing attributes due to high capillary entry pressure, low permeability, and swelling characteristics (Neuzil, 1986; 2019). Given these favorable properties, clay-rich caprocks, including shales and mudstones, emerge as prevalent choices for GCS applications (Orr, 2009; Espinoza and Santamarina, 2017). Moreover, in the case of over 70 naturally occurring CO₂ storage sites, 70% of the caprocks consist of mudstones, shales, and interlayered carbonate, mudstones, and shales (Niemi et al., 2017). The assurance of secure storage is often associated with caprock thicknesses of approximately 300 meters (Miocic et al., 2017).

Interacting with the geomechanical response induced by overpressure, the injected CO₂ initiates cooling in the surrounding rock, resulting in reservoir contraction and the subsequent development of thermal stresses, potentially impacting caprock integrity (Vilarrasa and

Rutqvist, 2017). Moreover, chemical reactions may introduce alterations in the hydro-mechanical properties of rocks and faults (Rohmer et al., 2016). A comprehensive characterization of these coupled processes at various scales, including core samples tested in the laboratory, underground rock laboratory testing, and in situ scale, is imperative for minimizing uncertainties associated with caprock behavior during CO₂ injection.

In this review, we gather insights gained from the characterization of shales as caprocks for GCS projects at varying scales from laboratory experiments on cm-long sample to decameter-size underground rock laboratories to field-wide injections. These laboratory experiments are primarily focused on characterizing the diffusive and capillary properties, as well as the permeability-porosity relationships of materials resembling caprock. A comprehensive understanding of the fracture network is crucial, particularly for clay-rich rocks associated with low-permeable caprock structures. In such cases, permeability is commonly perceived to be governed by discontinuities across various scales, encompassing fractures and faults. Nevertheless, considering the spatial and temporal scales typically involved, reaching up to centimeters and months, there arises a need to verify the representativeness of the measured properties for in situ caprocks.

In light of the excavation and establishment of several Underground Rock Laboratories (URLs) within shale formations, originally designed for assessing the viability of nuclear waste disposal and now recognized as formations conducive to studying caprock behavior in GCS, the second section of this review is dedicated to initial findings relevant to GCS. Given the broader spatial and temporal scales inherent in GCS projects, the testing conducted in URLs offers insights for upscaling laboratory-derived properties, providing a more representative characterization at the in situ scale. The third section elucidates how innovative monitoring techniques, coupled with model validation, were employed to assess the sealing properties of diverse GCS sites. At each scale, we highlight contributions that enhance our comprehension of the hydro-mechanical behavior of clay-rich caprocks, compare various characterization methods, and delineate the respective advantages and limitations of each approach.

2.2. Laboratory characterization

The initial step in obtaining high-quality laboratory results from shale samples involves preserving them effectively following recovery. While some loss of pore fluid is inevitable during the depressurization of cores from their original in situ conditions, it should be minimized, as excessive liquid loss can alter the hydraulic and mechanical properties of shales (Einstein, 1989; Schmitt et al., 1994). Once proper sample preservation is ensured, the laboratory-scale characterization of the rock matrix is essential, focusing on its ability to act as a seal, considering both diffusive and capillary properties, as well as assessing its seal integrity concerning mechanical properties.

2.2.1. Diffusive leakage

In the context of Geological Carbon Storage (GCS), the molecular diffusion process within the caprock refers to the movement of aqueous CO₂ species through the brine-saturated pore spaces (Figure 2.1a). Diffusion experiments are conducted by establishing varying CO₂ concentration gradients across a brine-saturated sample while maintaining the brine pressure constant across the rock. In those conditions, the amount of CO₂ that can pass through the intact caprock is determined by the effective diffusion coefficient (D_{eff}). D_{eff} is influenced by the pore structure complexities, as outlined by previous studies

$$D_{eff} = D \cdot \tau ; \quad (2.1)$$

where D represents the molecular diffusivity of CO₂ within the bulk water medium and typically falls within the range of 1 to 3×10⁻⁹ m²/s (Gertz and Loeschke, 1956; Tewes and Boury, 2005), while τ denotes tortuosity, a measure of the convoluted pathways within the caprock and assumes values from 0 to 1 (Bear, 2013). Some authors define tortuosity as $\tau' = \tau^{-1}$ (Krooss et al., 1992; Busch et al., 2008; Song and Zhang, 2013).

The diffusion of CO₂ through a saturated caprock is significantly affected by the inherent pore structures of the caprock. An increase in effective stress results in decreased porosity and increased τ , which, in turn, diminishes the D_{eff} (Krooss and Leythaeuser, 1988). Existing data from diffusion experiments suggests that D_{eff} for CO₂ within shales can be as small as 10⁻¹¹ m²/s (Krooss et al., 2005; Busch et al., 2008; Wollenweber et al., 2009; 2010, as reported in Table 1). Diffusion measurements involving heavy water (D₂O) provide an upper bound for D_{eff} . In the case of two samples obtained from the upper portion of the Dogger formation in France, this upper limit is determined to be 1.5·10⁻¹⁰ m²/s (Fleury et al., 2009). Considering various low-permeability sedimentary formations, the D_{eff} ranges from 10⁻¹¹ to 10⁻⁹ m²/s (Hildenbrand and Krooss, 2003).

Sorption processes influence the D_{eff} of CO₂ within shales, potentially slowing the diffusion front and strengthening CO₂ trapping in the subsurface (Angeli et al., 2009; Busch et al., 2010). The potential for CO₂ sorption is closely linked to the Total Organic Carbon (TOC) content of the shale and the water content of the rock matrix. Furthermore, the isothermal sorption behavior changes upon reaching the critical pressure of CO₂ (Busch et al., 2008). Over the past two decades, there has been a growing understanding of these processes at the laboratory scale, primarily due to their significance in the field of enhancing gas recovery from shales, as discussed by Klewiah et al. (2020). In terms of the hydromechanical behavior of the caprock within GCS, sorption-induced swelling has the effect of reducing permeability, driven by changes in effective stress and alterations in the pore structure. However, this may also result in the formation of microcracks within the caprock, thereby increasing the risk of leakage (Busch et al., 2010).

Conducting diffusion experiments at elevated pressures offers valuable insights for predicting and modeling processes during GCS across various scales (Kivi et al., 2022b). It is generally observed that diffusive losses through the caprock matrix are usually negligible compared to pressure-driven bulk CO₂ flow (Hildenbrand and Krooss, 2003; Krooss et al., 2004; Angeli et al., 2009; Wollenweber et al., 2009; Busch et al., 2010; Wollenweber et al., 2010).

Table 2.1. Effective diffusion coefficients for different shales from the literature.

Material	Working fluids	Effective diffusion ($\cdot 10^{-10} \text{ m}^2/\text{s}$)	Porosity (-)	Pressures (MPa)	Effective mean stress (MPa)	Temperature s (oC)	Sample dimensions (mm)	Reference
Samples from: Boom Clay, Belgium; Opalinus Clay, Switzerland; silt-stone from the Vorderhön, Germany; calcareous rocks from Montmiral, France; and pelitic rock from Florina, Greece.	Water, CO ₂ (gas), Nitrogen (gas)	from 0.1 to 10	-	< 20	< 10	50	10.0 to 30.0x28.5 (cylinder)	Hildenbrand and Krooss 2003
2 samples of Muderong Shale	Water (permeability) and scCO ₂	0.308 - 0.481	~0.2	6.0-7.0	23.0-24.0	50	28.5 (diameter)	Krooss et al. 2005; Busch et al. 2008
2 samples from Bathonian and Callovian units	Water and heavy water (D ₂ O)	2.4 - 1.5	0.1	~0.1 (atm pressure)	-	30	10.3x10.4x10.9 (cube) 10.5x10.5 (cylinder)	Fleury et al. 2009
Clay-rich Emscher Marl sample	Water, He, scCO ₂	0.78 - 1.19	0.2	3.0-6.0	-	21 - 45	10.0x28.5 (cylinder)	Wollenweber et al. 2009; 2010
Sultani shale sample, Jordan	Water, CO ₂ (gas), Hydrogen (gas)	8.4	-	5.0 - 10.0	-	-	8.3 (sphere diameter)	Samara et al. 2024

2.2.2. Capillary leakage

The injection of CO₂ increases the pore pressure within the subsurface. The capillary pressure is defined as the difference between the pressure of the injected CO₂ (generally representing the non-wetting phase) and that of the in situ brine (typically representing the wetting phase). The capillary pressure could build up at the interface with the caprock until infiltrating the caprock's pore network. The minimum threshold capillary pressure required for free-phase CO₂ to enter into the caprock is referred to as the breakthrough pressure. In laboratory settings, this parameter is directly evaluated by incrementally elevating the upstream pressure of the non-wetting phase until a continuous flow forms across the rock sample (Thomas et al. 1968). The precision of the approach is thus affected by the pressure increments at each step (Al-Bazali et al., 2005; Angeli et al., 2009; Makhnenko et al., 2017).

Given the extended duration required for direct breakthrough pressure measurements, ranging from days to months (refer to Table 2), indirect measurements are applied. In such approaches, inspired by the pressure-pulse decay method (Brace et al. 1968; Hsieh et al. 1981), an instantaneous high CO₂ pressure is applied at the inlet, creating a differential pressure between CO₂ and water across the specimen large enough to surpass the CO₂ breakthrough pressure and initiate flow (Hildenbrand et al., 2002; Hildenbrand and Krooss, 2003; Egermann et al., 2006). In this configuration, the drainage and imbibition processes of the test are sequentially measured. Researchers have examined a capillary threshold pressure, often termed the snap-off pressure, defined as the pressure at which CO₂ ceases to flow through the specimen following the cessation of injection (Wollenweber et al., 2010; Amann-Hildenbrand et al., 2012, 2013). However, inconsistencies have been observed between indirect and direct breakthrough pressure measurements with the direct method being more representative of in situ conditions (Boulin et al., 2013).

The breakthrough pressure can alternatively be estimated from the mercury intrusion capillary pressure experiments. This approach relies on the application of the theoretical Young-Laplace equation, assuming that the pores exhibit ideal cylindrical characteristics (Washburn, 1921)

$$p_c = \frac{4\gamma \cos(\theta)}{d} \quad (2.2)$$

This expression is an intrinsic property of the shale pore throat with diameter d , in the order of tens of nm (Table 2), the interfacial tension γ between CO₂ and water (brine), and the contact angle θ . The interfacial tension and contact angle are highly pressure-dependent. Under experimental conditions representing in situ pressures, the contact angle for the CO₂-water-caprock system is approximately 30 to 40 degrees (Espinoza and Santamarina, 2010) while interfacial tension ranges between 20 to 50 mN/m (Chalbaud et al., 2009; Samara et al., 2024). Recent laboratory investigations conducted on an outcrop shale sample from the Sultani shale in Jordan reveal a notable decrease in interfacial tension at elevated pressures. This phenomenon results in a reduction in capillary pressure (Samara et al., 2024). This finding highlights the critical importance of accurately assessing in situ pressure conditions. Furthermore, it is observed that the interfacial tension between CO₂ and water is comparatively lower than that of nitrogen-, oil-, and methane-water systems. This characteristic lowers the capillary sealing capacity of a given caprock for CO₂ when contrasted with other hydrocarbons (Li et al., 2006; Rezaeyan et al., 2015). Consequently, geological formations that effectively sealed natural gases over geological time scales still need to be investigated concerning their sealing capacity for CO₂ storage purposes.

In Table 2, the recorded breakthrough pressure values for various shale samples are presented. Generally, the breakthrough pressure would be lower for supercritical CO₂ due to its lower interfacial surface tension in comparison to liquid CO₂. Makhnenko et al. (2017) conducted

measurements on remolded shale, representative of the fault core in a shale formation, and observed that the breakthrough pressure for supercritical CO₂ is approximately two times lower than that for liquid CO₂, ranging from 2.8 MPa to 5.0 MPa, respectively. Their findings led to the conclusion that correlating breakthrough pressure with the intrinsic permeability of the caprock, as suggested for gases like nitrogen (Thomas et al., 1968; Boulin et al., 2013), may not be applicable in the case of CO₂.

The laboratory results imply that as long as the capillary pressure resulting from injection remain below the capillary entry threshold, the potential for capillary flow leakage through the caprock pore network in the context of CO₂ storage conditions should be minimal. A study by Busch et al. (2010) provides insight into this phenomenon, demonstrating that under an overpressure of 2 MPa beyond the capillary entry pressure for CO₂, the breakthrough of the caprock occurs over an extended period, ranging from hundreds to thousands of years. This observation holds for caprocks characterized by medium to low permeability and with a realistic thickness of 100 meters. In another study, Kivi et al. (2022a) show that in a multi-layered geological setting, comprising a high-frequency sequence of caprocks and aquifer, even if the caprocks are pervasively fractured and have large intrinsic permeability and small capillary entry pressure, the CO₂ leakage is still very unlikely. These investigations suggest that the assessment of CO₂ leakage potential needs to be viewed in the context of subsurface structural and physical complexities rather than single hydraulic properties of the caprocks.

Table 2.2. Breakthrough pressures in different shales from the literature. In parenthesis, we identify the method used to calculate the breakthrough pressure: “direct” refers to the step-by-step pressure method, “indirect” refers to the instantaneous high-pressure method, and “estimated” refers to the use of Youg-Laplace equation (Equation (2.2)).

Pore diameter (nm)	Interfacial tension (mN/m)	Pressure (MPa)	Effective mean stress	Temperature (°C)	Sample dimensions (mm)	duration	Reference
~ 86 (breakthrough) - ~ 40 (MIP)	50 (assumed)	< 17	< 13	-	28.5x30 (cylinder)	from 18 to 1300 h	Hildenbrand et al. 2002
-	-	< 20	< 10	50	28.5x10.0 to 30.0 (cylinder)	up to 3 mouths	Hildenbrand and Krooss 2003
63.6 for Pierre - 51.6 for C1 - 40.2 for Arco-China (estimated)	from 5.8 of the mud to 72 of the Nitrogen (measured)	< 7	-	70	6.35 (thickness)	from 40 to 110 h (direct)	Al-Bazali 2005
7 (MIP)	20 - 40 (assumed)	7.5 - 13.5	1.5 - 5.5	35	40x38 (cylinder)	~ 60 days (direct)	Angeli et al. 2009
-	-	3.0 - 6.0	-	21 - 45	28.5x10.0 (cylinder)	up to 150 h (indirect)	Wollenweber et al. 2009; 2010
10	73 (assumed)	3.0 - 5.0	up to 26	~25	41x29.5 (cylinder)	48 days (direct)	Boulin et al. 2013
2	-	0.7 - 5.5	up to 30	35, 90	38x29 (cylinder)	~ 50 h (direct)	Rezaeyan et al. 2015
-	-	8.0 - 20.0	~ 9 - 10	24 - 40	12.5x35 (cylinder)	-	Makhnenko et al. 2017
570 for sandy clayey (MIP)	-	-	1.0 - 20.0	~22-25 (room temperature)	50.8x70-68 (Eau Claire) 25x25x30 (Maquoketa)	from 1.3 to 9 d	Kim and Makhnenko 2023a, b

Material	Working fluids	Breakthrough pressure (MPa)
7 samples: 2 from Tertiary mudstone, Norwegian Shelf, Norway; 1 from Opalinus Clay, Mont Terri, Switzerland; 3 from Boom Clay, Molenbeersel, Belgium; 1 from Boom Clay, Mol, Belgium	Water, brine, CO ₂ (gas)	No breakthrough was observed in Opalinus Clay
Samples from: Boom Clay, Belgium; Opalinus Clay, Switzerland; siltstone from the Vorderhön, Germany; calcareous rocks from Montmiral, France; and pelitic rock from Florina, Greece.	Water, CO ₂ gas, Nitrogen Gas	0.06 - 6.7 (indirect)
3 samples: 1 from Pierre shale; 1 from C1-shale; and 1 from Arco-China shale	Water, Oil-Based Mud, from Decane, Crude Oil, Nitrogen Gas	1.0 to 4.3 for Pierre - from 1.7 to 4.8 for C1 - from 2.1 to 5.5 for Arco-China (direct)
3 samples from Draupne formation, Troll East field, Norway	Water, scCO ₂	3.6 to 4.0 (direct) - 2.2 to 5.3 (estimated)
1 Clay-rich Emscher Marl sample	Water, He, scCO ₂	0.43-0.64 (indirect)
1 sample from Weser formation, Ketzin CCs, Germany	Water, nitrogen	12 (direct)
1 sample of shale from Gachsaran formation, Iran	Brine, CO ₂ , Nitrogen, and Methane gases	2.76 for CO ₂ - 4.96 for Nitrogen - 5.52 for Methane (direct)
2 samples: 1 from Opalinus Clay, Mont Terri; and 1 of remolded Opalinus Clay	In situ brine, CO ₂ (liquid and supercritical)	0.9 to 1.6 MPa for OPA - 2.8 to 5.0 MPa for remolded (direct)
2 shale samples of Eau Claire formation, Illinois Basin, US, divided in sandy; and clayey; and 1 sample for Maquoketa formation, Illinois Basin, US	Pure water; and CO ₂ dissolved in water	0.10 for sandy - 0.40 for clayey - 13.8 for Maquoketa (direct)

2.2.3. Permeability of the shale matrix and fractures

If the CO₂ capillary pressure exceeds the breakthrough threshold within the caprock, the fluid initiates the displacement of in situ brine, initiating flow through the formation. The rate of flow is contingent upon the intrinsic permeability, which, in the case of shales and mudstones, ranges from approximately 10⁻²³ to 10⁻¹⁶ m² (Neuzil, 1994; 2019). The low permeability of these formations renders them favorable candidates for caprock functionality. For instance, measurements of permeabilities in various lithologies from Wabamun and Zama in Canada indicate that shales from the Colorado Group and Calmar Formation exhibit intrinsic permeabilities over five orders of magnitude smaller than sandstone and carbonate formations in the same region (Bachu and Bennion, 2008; Bennion and Bachu, 2008). Laboratory-derived results on relative permeability for distinct supercritical CO₂ saturation stages are commonly fitted with the Brooks-Corey model (Brooks, 1965),

$$\begin{cases} k_b(S_e) = k_{bs} S_e^\lambda \\ k_{CO_2}(S_e) = k_{bs} (1 - S_e)^\lambda \end{cases}; \quad (2.3)$$

where k_{bs} is the saturated brine permeability; k_b is the brine permeability at the effective brine saturation S_e ; k_{CO_2} is the CO₂ permeability at the effective brine saturation S_e ; and λ is the Corey, approximately 6 for tight rocks during CO₂ drainage (Bachu and Bennion, 2008; Bennion and Bachu, 2008). This value doubles that of reservoir rocks, indicating a more pronounced effect of multiphase interference in tight rocks (Bachu and Bennion, 2008; Bennion and Bachu, 2008). Conventional steady-state flow tests can be adopted for permeability measurements in shales (Schlömer and Krooss, 1997; Kim and Makhnenko, 2020). However, due to the extended time required to reach steady-state conditions, transient methods, such as the pressure-pulse decay method, have been widely employed to characterize the permeability of shales (Brace et al., 1968; Hsieh et al., 1981).

The permeability in shales is commonly linked to their porosity and pore structure (Dewhurst et al., 1999). Given the substantial variability and the inherent difficulties associated with measuring the low permeability of clay-rich rocks, relationships between permeability, porosity, and clay content can be highly advantageous. However, these models rely on empirical approaches, leveraging insights gained from laboratory measurements (Dewhurst et al., 1999; Revil and Cathles, 1999; Yang and Aplin, 2010; Zhang et al., 2015; Neuzil, 2019; Kim and Makhnenko, 2020).

The theoretical model for predicting the permeability of porous rock is the Kozeny-Carman equation, which results in a cubic exponential relationship between permeability and porosity (Kozeny, 1927; Carman, 1938, 1956). However, the assumption of parallel and uniformly distributed pipe conduits with spherical particles has been demonstrated to be adequately accurate for sandstones but lacks reliability for clay-rich, low-permeable formations (Neuzil, 1994; Dewhurst et al., 1999; Bustin et al., 2008; Ross and Bustin, 2009; Kim and Makhnenko, 2020). In line with the principles of this theoretical model, various authors have attempted to come up with a more generic exponential empirical relationship (Dewhurst et al., 1999; Kim and Makhnenko, 2020)

$$k = k_0 \left(\frac{\phi}{\phi_0} \right)^n; \quad (2.4)$$

where k is the matrix permeability at the porosity ϕ , while k_0 is a reference measured permeability at the initial porosity ϕ_0 , and n is a constant fitted on experimental data.

Empirical observations in the Sichuan Basin, China, for shale with an initial permeability around 10⁻¹⁹ m² and porosity of 0.03, report n values ranging from 2 to 5 (Zhang et al., 2015). Revil and Cathles (1999) indicate that shales and shaly sands exhibit a higher exponent

compared to clean sand, indicating that shale permeability is more significantly influenced by changes in porosity than sandstone. They introduce three distinct exponents based on the clay mineral forming the shale, resulting in n values of approximately 8.2, 9.8, and 12.5 for kaolinite, illite, and smectite, respectively. Applying Equation (3), Kim and Makhnenko (2020) determined an exponent of 16 for Opalinus Clay. Those laboratory results show that the permeability of shales is more susceptible to porosity changes than high-permeability sedimentary rocks. To fit a large amount of data, some authors propose a log-linear correlation between porosity and permeability (Neuzil, 1994; Yang and Aplin, 2010; Neuzil, 2019). Neuzil (2019) demonstrates that the permeability of shales and mudstones is also influenced by clay content. Dewhurst et al. (1998), in a comparative study of two London Clay samples with different clay content, illustrated the impact of both porosity and clay fraction on the samples' permeability. It was suggested that permeability losses due to compaction are minimized at low clay fractions through the mechanical support of non-clay grains that may come into contact (Schneider et al., 2011). Yang and Aplin (2010) proposed a logarithmic permeability–porosity relationship, considering clay content, and fitted a dataset of clay-rich material with permeabilities ranging from 1.6×10^{-16} to 2.5×10^{-22} m², porosities from 0.04 to 0.78, and clay content from 12 to 97%.

Beyond the permeability of the rock matrix, the primary concern regarding the sealing integrity of the caprock is associated with the presence of discontinuities, particularly fractures. Natural fractures can serve as preferential flow paths through the caprock. Additionally, the rise in formation pressure has the potential to reactivate pre-existing faults or fractures, induce hydrofracturing, and trigger shear fracturing in the overlying caprock. These fractures may act as conduits for CO₂ leakage (Rutqvist, 2012). Consequently, laboratory efforts have been dedicated to characterizing the hydro-mechanical properties of fractures.

Laboratory testing of single fractures has been a practice for over five decades. However, existing experimental data dominantly focuses on hard rocks as conduits for fluid flow (Bandis et al., 1983; Barton et al., 1985; Pyrak-Nolte and Morris, 2000). Conversely, limited data is available for softer, naturally fractured shaly materials regarding fracture hydraulic properties in response to changes in normal and shear stresses across the fracture. The pioneering experimental work by Capuano (1993) was the first to report laboratory testing with evidence of fracture flow in a shale matrix. Capuano tested naturally fractured shale specimens obtained from depths between 3 and 5 km in the Frio Formation, Texas. Utilizing the parallel plate model (Snow, 1969; Witherspoon et al., 1980), the estimated permeability of the fracture was in the order of 10^{-13} m², matching that of the reservoir rock (Capuano, 1993). Gutierrez et al. (2000) investigated four naturally fractured Kimmeridge shale samples from the North Sea. The radial flow test revealed an initial permeability of the fracture approximately nine orders of magnitude higher than that of the rock matrix. Empirically, permeability exhibited an exponential reduction with increasing normal stress. The effect of shear was observed to be dependent on normal stress, with shear-induced dilation causing permeability enhancement at stresses akin to in situ conditions. However, at higher stresses, shear-induced compaction resulted in a six-order-of-magnitude reduction in fracture permeability, likely due to cementation (Gutierrez et al., 2000). Edlmann et al. (2013) conducted tests on two naturally fractured caprock samples from the East Brae field, North Sea, at a depth of around 4 km. Injecting CO₂ at different states revealed that aperture size is the primary factor controlling CO₂ flow. However, distinct phases appeared to have different threshold apertures for flow initiation. Further laboratory tests are essential to elucidate capillary characteristics and multiphase CO₂-brine flow in shales, encompassing both the rock matrix and fractures.

2.3. Underground Rock Laboratory characterization

The feasibility of conducting tests on clay-rich rocks at a scale spanning tens of meters has been primarily demonstrated in the context of geological radioactive waste disposal (Neuzil, 2013). Underground Rock Laboratories (URLs) exemplifying this approach include the Hades laboratory in Mol, Belgium, excavated in Boom clay (Yu et al., 2011; 2013); the Meuse/Haute Marne laboratory in Eastern France, excavated in Callovo-Oxfordian claystone (Zhang and Rothfuchs, 2004); and the Mont Terri laboratory in northern Switzerland, excavated in Opalinus clay (Thury and Bossart, 1999; Bossart et al., 2018). These URLs, through the implementation of in situ tests, provide a platform for the analysis of shale sealing and integrity behavior under subsurface conditions representative of Geological Carbon Storage (GCS) sites.

2.3.1. Hydraulic properties of the matrix

In the context of GCS and geological repositories for radioactive waste, the paramount objective is the characterization of the hydraulic properties of rock, encompassing key factors such as porosity and permeability, and discerning their response under varying effective stresses. Within URLs, the evaluation of rock behavior is conducted through borehole testing, aiming to delineate the intricate features of rock mechanics and subsequently align these observations with outcomes derived from laboratory experiments for the sake of developing upscaling approaches.

In the Hades laboratory, established within Boom Clay at an approximate depth of 200 m in 1980, under in situ stresses, both laboratory investigations and field studies consistently reveal permeabilities in the order of 10^{-19} m² (Wemaere et al., 2008; Deng et al., 2011; Yu et al., 2013). This can be attributed in part to the homogeneous mineralogical composition of Boom Clay (Zeelmaekers, 2011). The anisotropy ratio between horizontal and vertical permeabilities is approximately 2.5, representing an average value for consolidated clays (Clennell et al., 1999; Yu et al., 2013). The observed variations in permeability at a regional scale are associated with distinct burial depths of the rock, influencing the porosity of Boom Clay. Meanwhile, local variabilities are elucidated by grain size heterogeneities (Yu et al., 2013).

Opalinus Clay is generally considered to have lower permeability compared to Boom Clay (Hildebrand et al., 2002). Yu et al. (2019) conducted a comparative analysis of two methods for estimating the permeability of Opalinus Clay. The first method involves the application of a Poiseuille-type law, incorporating petrophysical laboratory measurements, and is juxtaposed with in situ hydraulic pumping and pulse tests. The permeability range in Opalinus Clay, as determined by the first method, spans from $2 \cdot 10^{-21}$ to $6.9 \cdot 10^{-19}$ m², while in situ tests suggest slightly higher values, around $7.9 \cdot 10^{-19}$ m². The same range of permeabilities has been found in borehole testing for Callovo-Oxfordian claystone (Vinsot et al., 2001). While core analysis provides an economical estimation of the hydraulic properties of a homogeneous shale matrix, in situ tests deal with larger-scale heterogeneities, including potential conductive fractures.

2.3.2. Transport properties of the matrix

In the Callovo-Oxfordian claystone formation, the PGZ1 experiment was conducted to investigate gas flow and transport properties through injection. The permeability value fitted for the undisturbed zone aligns with radial permeability values obtained through laboratory testing. The nitrogen entry pressure is estimated at approximately 2 MPa, corresponding to an average pore radius of 70 μ m (Harrington et al., 2012). Laboratory experiments on Callovo-

Oxfordian claystone revealed weak adsorption of nitrogen and strong adsorption of CO₂ (Yuan et al., 2017). Consequently, the effective permeability of CO₂ is an order of magnitude lower, ranging from 10⁻¹⁹ to 10⁻²⁰ m², compared to helium and nitrogen. This phenomenon is attributed to the swelling induced by gas adsorption, narrowing the pore channel and causing a reduction in gas permeability (Yuan et al., 2017). The PGZ1 experiment further confirmed that gas injection is associated with dilation of the clay fabric, as evidenced by laboratory results (Angeli et al., 2009).

Transport properties in Boom Clay were investigated using tracers, as detailed in the work by Mazurek et al. (2011). The study employed helium profile modeling to examine molecular diffusion transport in Boom Clay. Under a low-pressure gradient (approximately 0.2 to 0.4 kPa/m), the formation's low permeability results in negligible water flow, making molecular diffusion the dominant transport mechanism. Similar findings were observed in laboratory testing of Opalinus Clay (Hildebrand et al., 2002; Kivi et al., 2022b), and initial simulation results from the Long-Term Periodic Injection Experiment (CO₂LPIE) support this trend under a mean overpressure injection of 1 MPa (Sciandra et al., 2022).

2.3.3. Fault testing

Apart from the characterization of the rock matrix, URLs containing meter-scale natural faults providing a unique opportunity to test the hydromechanical properties of these discontinuities. The key idea is to pressurize a sealed section of a borehole intersecting a fault zone by injecting a fluid (water, brine or CO₂-in-brine solution), lowering the effective normal stress acting on the fault to induce millimeter-scale slips of the fault. This is the case of the Mont Terri, where the main fault crosses a gallery of the URL, and has been extensively characterized (Jaeggi et al., 2018). The in situ measurements show that the Main Fault has similar Hydro-Mechanical properties to the host rock in undisturbed conditions (Gautschi, 2001; Wenning et al., 2021).

Two complementary injection experiments were conducted in proximity to the main fault, namely the CS-D (Zappone et al., 2018; 2020) and the FS-B (Guglielmi et al., 2020a; 2020b). The primary objective of both experiments is to characterize the hydro-mechanical behavior of the fault and its affection by potential chemical reactions during long-term CO₂ injections. While both projects involved the injection of CO₂ saturated in brine, the CS-D project focused on the response to a small injection rate, approximately 0.05 ml/min, below the fault activation pressure. In contrast, the FS-B project aimed to activate the main fault by injecting at rates exceeding 5 L/min. Measurements useful for characterization were also taken during the latest extension of the URL (Hopp et al., 2022).

The main fault and its surrounding area were extensively instrumented with 23 boreholes containing various monitoring tools. These tools were designed to detect pressure and flow rate into multiple injection intervals, measure geomechanical strain, monitor both active and passive seismicity, employ electrical resistivity sensors, and analyze fluid and gas chemistry (Hopp et al., 2022). Specifically, high-resolution monitoring devices were utilized to record the activation of the natural fault during the injection of CO₂ dissolved in brine. This allowed for the detailed tracking of fault slip and induced seismicity near the nucleation zone. While a comprehensive understanding of the two experiments is still lacking, preliminary results indicate the potential of Distributed Strain Sensing (DSS) fiber optics in monitoring the slow shear of faulted zones in shales (Hopp et al., 2022). This application aims to enhance our knowledge of leakage and induced seismicity in these zones.

2.4. In situ monitoring and characterization

The injection of CO₂ induces an increase in pore pressure, leading to various geomechanical effects such as reservoir expansion, caprock deformation, potential fault reactivation, and ground uplift (Rutqvist et al., 2010; 2016). Hydro-mechanical investigations have primarily focused on determining the maximum sustainable injection pressure (Streit and Hillis, 2004; Rutqvist et al., 2007) and assessing fault reactivation resulting from CO₂ injection (Ferronato et al., 2010; Cappa and Rutqvist, 2011). Fault opens up when effective normal stress approaches its tensile strength or reactivates in shear mode when shear stresses overcome its frictional strength. If the slip relaxes the stored elastic energy in a seismic way, it can be tracked through in situ microseismic monitoring. Reactivation leads to small changes in the fracture aperture, in the micron scale (Guglielmi et al., 2008), yet imposing significant alteration of fracture permeability according to the cubic law (Snow, 1965). This alteration can create potential pathways for fluid migration through the caprocks (Oldenburg et al., 2009; Rutqvist, 2012; Rutqvist et al., 2016; Song and Zhang, 2013). The deformation of the caprock is controlled by the initial stress regime: the entire thickness of the caprock undergoes deformation in a normal faulting stress regime (when horizontal stress is lower than vertical stress), whereas the caprock deformation is limited to the vicinity of the aquifer-caprock interface within a strike-slip stress regime (when horizontal stress exceeds vertical stress) (Vilarrasa et al., 2011). Therefore, precise estimation of the three-dimensional in situ stress field is essential for supporting the characterization of GCS sites (Rutqvist et al., 2008).

Diverse methodologies were employed to measure these perturbations of the initial state during CO₂ injection in GCS sites, with monitoring tools categorized based on whether they investigate surface or subsurface phenomena. A comprehensive review of GCS monitoring, including both surface and subsurface measurements, is provided by Jenkins et al. (2015) and Jenkins (2020). Superficial deformation measurements, utilizing Interferometric Synthetic Aperture Radar (InSAR), leverage radar imaging to capture phase differences at defined reflection points, enabling precise characterization of ground movements at the millimeter scale (Vasco et al., 2010). For instance, InSAR applied at the In Salah CO₂ storage site in Algeria detected GCS-induced ground motion resulting in approximately 5 mm/year uplift, with cumulative deformations reaching centimeter-scale magnitudes (Onuma and Ohkawa, 2009; Tamburini et al., 2010). The rate and pattern of surface displacement were evaluated to understand the reservoir-caprock-overburden system, facilitating the reproduction of surface deformations (Rutqvist et al., 2010). In addition to regional scale uplift, local deformations were observed, displaying a double-lobe pattern interpreted as a consequence of fracture activation in the reservoir (Vasco et al., 2010). A similar pattern was identified using InSAR during the 2019 Rongxian-Weiyuan earthquake and utilized to define the rupture dimensions of the Molin fault during the main shock (Yang et al., 2020).

The In Salah project stands as a significant case study for GCS initiatives, illustrating the efficacy of InSAR surface monitoring (Ringrose et al., 2013). InSAR, characterized by its cost-effectiveness, offers valuable insights into the hydro-mechanical stability of the reservoir-caprock-overburden system. However, the application of this monitoring technique is limited to onshore storage sites and factors such as elevated atmospheric humidity, dense vegetation, and noise originating from pressure fluctuations in zones above the reservoir can further diminish measurement precision when compared to the conditions at In Salah (Jenkins et al., 2015). Other tools for surface monitoring encompass displacement extensometers and seismic geophones strategically placed on the ground within the storage sites (Seto and McRae, 2011). Geophysical measurements serve as a robust monitoring tool for characterizing the evolution of the CO₂ plume and detecting potential leakage. Originating from technologies employed in the petroleum industry, this knowledge has been effectively adapted for GCS applications.

Notable instances include the utilization of this approach in projects such as Sleipner (Arts et al., 2004), Snøhvit (Hansen et al., 2013), and Weyburn (Verdon et al., 2010). Time-lapse variations in seismic amplitude and time shifts can be systematically observed and correlated with subsurface measurements and multi-physical simulations, enabling the identification of distinct layers (White, 2013), discontinuities (Iding and Ringrose, 2009; Duxbury et al., 2012), CO₂ saturation (Arts et al., 2004), and pressure changes (Hansen et al., 2013).

Permanently deployed fiber optic sensors present a non-intrusive methodology for monitoring the movement of near-wellbore CO₂ plumes by capturing deformation-thermal variations (Vilarrasa and Rutqvist, 2017). This approach eliminates the necessity of installing multiple tools in the wellbore, thereby mitigating potential disturbances to readings (Reinsch et al., 2013). Despite common limitations such as low accuracy and resolution in traditional methods (Lu et al., 2019), these technologies can harness consolidated geophysical acquisition and analysis to visualize the behavior of the formation throughout the stages of CO₂ injection (Sun et al., 2018). Fiber-optic sensing technology emerges as a promising supplement and alternative for characterizing Geological Carbon Storage (GCS) sites, demonstrating adaptability and potential for continuous in-situ monitoring in GCS applications (Sun et al., 2018; 2021). This adaptability is particularly crucial for gaining comprehensive insights into CO₂ plume fronts, thermodynamic evolutions within and adjacent to injection formations, and even observable surface uplift. The field of downhole fiber-optic sensing is rapidly advancing and is anticipated to be extensively deployed in future sites. Key technologies include Distributed Temperature Sensing (DTS), Distributed Acoustic Sensing (DAS) for active seismic imaging and recording seismic events, and Distributed Strain Sensing (DSS) for directly measuring rock strain (Lu et al., 2019; Sun et al., 2021).

2.5. Future work

In clay-rock caprocks for Geological Carbon Storage (GCS), it is imperative to address four distinct phenomena to prevent the vertical flow of CO₂: (1) molecular diffusion of CO₂ within the in situ brine driven by concentration gradients; (2) capillary intrusion and two-phase flow of CO₂, initiated when capillary pressures overcome the local caprock entry pressure; (3) CO₂ flow along localized dilatant pathways and newly created microfractures, resulting from low effective stresses induced during injection; and (4) CO₂ flow on semipermeable and permeable faults (Figure 2.1).

The parameters governing these phenomena are typically determined in the laboratory, where well-defined boundary conditions are maintained on specimens of dimensions not exceeding tens of centimeters in size and a few months in time (Figure 2.2). In certain instances, field-scale permeabilities of clay-rich rock appear to surpass those measured on laboratory core plugs. Bredehoeft et al. (1983) documented a regional absolute permeability of 10^{-16} m² in the Pierre Shale, whereas at the laboratory scale, the matrix permeability was 10^{-20} m² (Neuzil, 1993). The apparent scale dependence of permeability is indicative of the heterogeneous structure of shales, influenced by fractures and faults, which can significantly increase effective permeability by orders of magnitude (van der Kamp, 2001), although their detection or prediction remains challenging (Bredehoeft et al. 1983; Neuzil, 2019; Kim and Makhnenko, 2020). An integrated approach addressing the upscaling of the measurements of hydro-mechanical properties from laboratory to larger regional scales is currently lacking. A comprehensive understanding of these scale issues is imperative for robustly characterizing caprock behavior at CO₂ storage sites. This characterization is essential for advancing our understanding and prediction capabilities of processes occurring in caprocks during CO₂ injection at the in situ scale.

Laboratory-scale tests conducted at dimensions up to a few centimeters hardly capture the intricacies of an extensive caprock-CO₂ interface spanning several kilometers. Pilot- and industrial-scale sites offer some insights but operate under constraints that inherently limit control over boundary conditions. To bridge the gap between these scales, experiments in Underground Rock Laboratories (URLs) at spatial scales of tens-of-meters and durations approaching several years enable a more controlled and monitored environment. These underground laboratories address specific issues, ranging from validating the representativeness of small-scale hydro-mechanical (HM) measurements for large-scale assessments to assessing anisotropy in HM properties across shale formations, and provide an opportunity to evaluate new monitoring technologies before the in situ implementation (Figure 2.2). The challenge lies in achieving a comprehensive understanding of the generalized behavior of these clays when exposed to a more complex environment compared to laboratory testing. The interpretation of results is generally aided by numerical analyses.

In modeling the behavior of in situ caprocks, the scarcity of data poses a significant challenge in accurately predicting fluid flow, overpressure, and stress developments. For instance, the permeability of shale in large-scale numerical simulations is commonly expressed as a function of porosity, but the appropriate porosity-permeability relationship remains unclear. Default relationships used for shales in different simulators have led to predicted permeabilities varying by several orders of magnitude at low porosities (Dewhurst, 1999). Neuzil (2019) suggests that in such cases, the clay content plays a crucial role, but incorporating this influence into in situ scale modeling is still unclear.

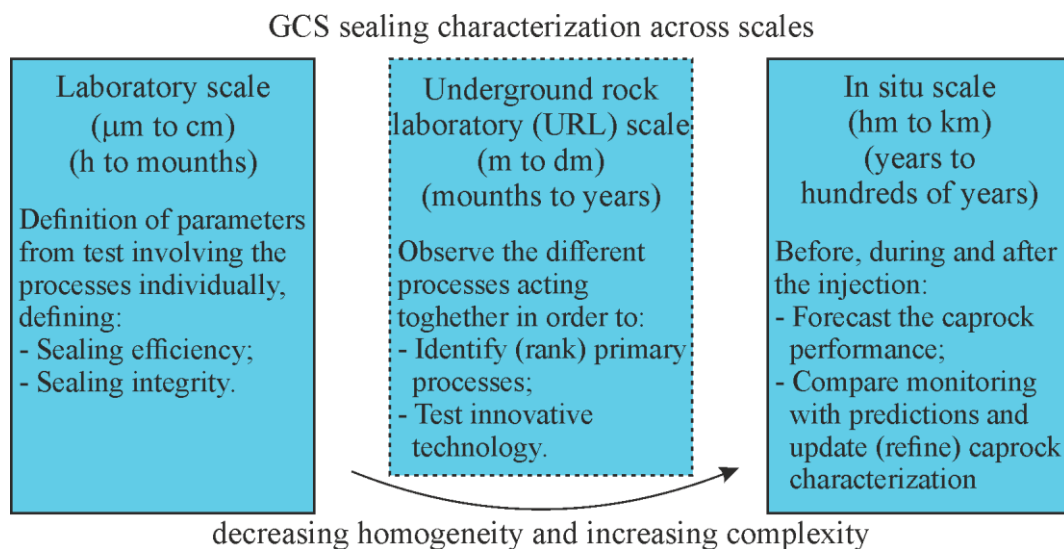


Figure 2.2. The upscaling problem for shale caprocks for Geological Carbon Storage (GCS). The problem is addressed by adding Underground Rock Laboratory (URL) testing to bridge the large gap in spatiotemporal scales involved.

Uncertainties also exist regarding the influence of faults and fractures during injection. Hydraulic fractures are either activated or formed when the pore pressure surpasses the tensile or shear strength of the sediment. The reduction in pore pressure during fluid expulsion may facilitate mineral precipitation along the fracture, potentially leading to its sealing. This sealing process can trigger a subsequent episode of overpressuring and fluid leakage during continuous compaction and pressure buildup in the sediment. Another significant concern is the alteration in fracture flow properties due to changes in pore pressure. Most of the basin scale models assume constant permeability of the fractured seal due to the lack of data on stress-dependent

fracture permeability. While there have been extensive studies on the alteration of intact sediment permeability with stress changes (or indirectly via porosity changes), there appears to be a lack of data on the pressure-dependent behavior of fractured sediments. The model proposed by Olivella and Alonso (2008) incorporates changes in fracture permeability by adjusting the fracture opening linearly with volumetric deformation. However, the long-term behavior of fractures at the in situ scale remains inadequately understood, posing challenges in realistically modeling them.

The exhibition of effective monitoring and characterization techniques, mitigating the risk of leakage in the context of GCS holds significance not only for ensuring the project's success but also for bolstering public and regulatory confidence in validating the safety of subsurface CO₂ storage.

Chapter 3

Characterization of hydraulic rock diffusivity using oscillatory pore pressure

3.1. Introduction

Several geo-energy technologies, such as subsurface energy storage, geological carbon storage, and geothermal energy, have become increasingly attractive in recent years owing to their key role in the green energy transition for mitigating climate change (IPCC, 2022). These activities entail fluid injection into (or extraction from) the subsurface, which, in turn, perturb the initial equilibrium state of pore pressure and stress underground, giving rise to coupled hydro-mechanical (HM) effects. These include induced seismicity (Ge and Saar, 2022), ground surface deformation (Rutqvist et al., 2010) and compromising the caprock integrity (Vilarrasa, 2014). In particular, concerns around CO₂ leakage through fine-grained caprocks (e.g., shales) should be addressed before the widespread deployment of geologic carbon storage (Kivi et al., 2022). The growing number of perceivable and damaging earthquakes induced by subsurface energy utilization and changes to the hydraulic system has negatively impacted the public perception of these resources (Ellsworth, 2013; Foulger et al., 2018). It is conceived that proper HM characterization of the subsurface is essential to minimize the risks posed by these unsolicited side-effects of geo-energy developments (Vilarrasa et al., 2013; Verdon, 2014). However, the lack of clearly defined site characterization protocols, particularly in low-permeability rocks considering coupled HM effects, warrants revisiting existing characterization techniques.

The spatial and temporal evolution of pore pressure and fluid flow in the subsurface as a result of fluid injection or extraction is governed by hydraulic diffusivity $D = \kappa/S_s$, where $\kappa = k\rho g/\mu$ is the hydraulic conductivity, k is the intrinsic permeability, ρ is fluid density, g is gravity acceleration, μ is fluid viscosity, and S_s is the specific storage coefficient. The higher the diffusivity, the faster the propagation of pressure perturbation through the rock (Ferris et al., 1962; Hantush, 1964; Shih, 2018). However, fluid flow in porous media is acknowledged as a coupled HM problem (Biot, 1941; Cryer, 1963; Cheng, 2016). Pore pressure fluctuations give rise to changes in stresses, which, in turn, cause the rock to deform and induce undrained pressure alterations through the storage of the rock. Indeed, laboratory and field observations of instantaneous and reverse pressure changes, e.g., injection-induced pressure decline in the adjacent low-permeability layers or water level rise in wells (Hsieh, 1996; Blöcher et al., 2008; Slack et al., 2013) can be reproduced only by considering coupled HM effects (Hsieh, 1996; Wang, 2000; Blöcher et al., 2008; Slack et al., 2013).

It is common practice in hydrogeology to derive diffusivity at the field scale from pumping tests (Ferris et al., 1962; Kruseman et al., 1970; Lohman, 1972; Maliva, 2016; Walton, 2020). This technique is suitable for high-permeability aquifers, but unfeasible in low-permeability rock because fluid diffusion in tight rock takes place at slow rates and is highly affected by their storage capacity. By drilling a well that fully penetrates an aquifer and pumping fluid at a constant rate, the hydraulic properties can be derived from the pressure evolution at an observation well located at a certain distance from the source, e.g., using the solutions for steady-state flow Thiem (1906) or transient flow (Theis, 1935; Cooper Jr and Jacob, 1946). These solutions assume uniaxial strain in the vertical direction, i.e., neglecting deformations in horizontal directions.

Pressure fluctuations of groundwater of natural origin are ubiquitous, offering an opportunity to characterize rock, particularly if situated in the proximity of the surface water bodies (i.e., a river, a lake, or an ocean). Ferris (1952) provided an analytical solution of the diffusion-type equation of tidal effects and applied it at the Ashland well station near Plate River, Nebraska, to determine the hydraulic properties of the rock. Bredehoeft (1967) developed a theory to estimate the specific storage coefficient of laterally extensive aquifers (exclusively vertical deformation), knowing their tidal response and Poisson's ratio. Those theories assume that the solid grains of the rock are incompressible and can be inferred from the general three-dimensional theory of poroelasticity (Biot, 1941). Hsieh et al. (1987; 1988) revised the theory and used it to calculate the transmissivity of the formation from the phase difference between tidal disturbances and water level fluctuations in observation wells. Jiao and Tang (1999) modified Ferris's traditional hydraulic solution, adding a term to account for potential leakage through confining layers, and applied the solution at the coastal aquifer in Chek Lap Kok Airport, Hong Kong.

The possibility of interpreting the oscillating pore pressure signal(s) to estimate the hydraulic properties of rock has been scrutinized in the laboratory (Kranz et al., 1990; Faulkner and Rutter, 2000; Takahashi, 2003; Bernabé et al., 2004; Candela et al., 2015; Hasanov et al., 2019). The experiments comprise imposing at one end face of the specimen a harmonic pore pressure excitation while recording the fluctuating pressure response on the other side. Kranz et al. (1990) developed a hydraulic solution to the problem (assuming constant external stresses) and applied it to estimate the hydraulic diffusivity of Tennessee and Berea sandstones. Adachi and Detournay (1997) introduced a simplified HM coupling to Kranz's solution to deal with the effect of varying axial stress in response to the oscillating pore pressure. Applying the solutions to oscillating pore pressure experiments at varying frequencies, Hasanov et al. (2020) highlighted a consistent discrepancy between model predictions and measurements at relatively high frequencies (> 0.3 Hz). Although considering the coupled HM effects qualitatively helped to capture the observed trends rendering their significant contribution to the pore pressure response, the accuracy of the proposed solution remains arguable.

This study aims at providing an improved understanding of injection-induced pore pressure oscillations in confined formations and a description on the use of periodic signals (of either natural or anthropogenic origin) for characterizing hydraulic diffusivity. We revisit the existing analytical solutions to the problem of cyclic fluid injection into geologic formations of one-dimensional or axisymmetric geometries and compare their performance against numerical simulations, including uncoupled purely hydraulic (H) and fully coupled HM solutions. We investigate the solutions in three main applications: a) energy storage in porous rock, b) CO₂ leakage through a caprock in an underground rock laboratory experiment, and c) stimulation of an enhanced geothermal system in crystalline rock (Figure 3.1). We choose representative formations, including Berea sandstone, Opalinus Clay (shale), and Westerly granite, respectively, and assign a periodicity for each application.

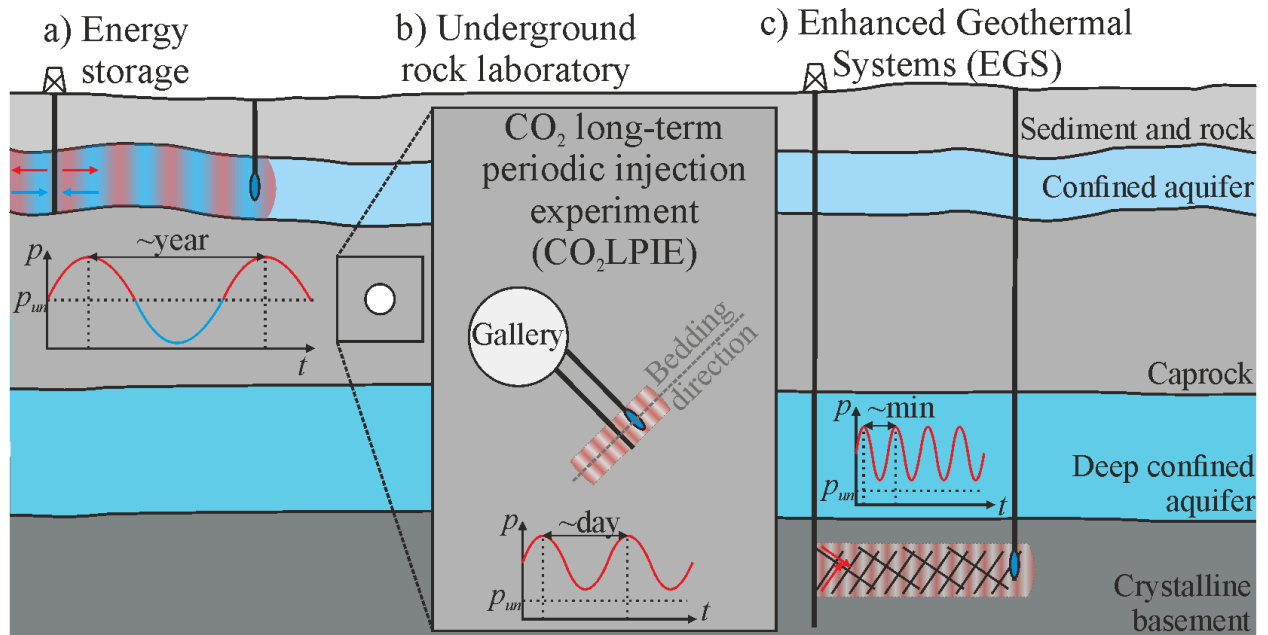


Figure 3.1. Three geo-energy applications considered: a) energy storage in shallow confined aquifers, b) CO₂ Long-term Periodic Injection Experiment (CO₂LPIE) at Mont Terri underground rock laboratory, and c) Enhanced Geothermal Systems (EGS) stimulation. The target rock formations are becoming deeper from left to right, while injection periodicity (or frequency) is lowering from left to right.

3.2. Theory

3.2.1. The diffusion equation for poroelastic materials

Combining Darcy's law with the fluid mass conservation equation leads to the pore pressure diffusion equation for a poroelastic material (Cheng, 2016). Assuming an isotropic, homogeneous rock and constant fluid viscosity, the diffusion equation in terms of the pore pressure p and the mean stress $\sigma_m = \sigma_{kk}/3$ writes (Biot, 1941; 1956; Cheng 2016)

$$A = \pi r^2$$

$$\frac{\partial p}{\partial t} - D \nabla^2 p = \frac{B}{3} \frac{\partial \sigma_{kk}}{\partial t}, \quad (3.1)$$

Here the diffusion coefficient $D = \kappa/S_s$, in which the specific storage can be expressed as $S_s = [\phi/K_f + 1/K - (1+\phi)/K_s]\rho g$. ϕ , K_f , K , and K_s denote, respectively, the effective rock porosity and bulk moduli of pore fluid, the rock skeleton under drained conditions, and the solid phase including isolated pores. The first invariant of the stress tensor $\sigma_{kk} = \sigma_{xx} + \sigma_{yy} + \sigma_{zz}$ is taken positive under compression. B is the Skempton coefficient and defines the pore pressure change as a result of changes in the mean stress under undrained conditions, i.e., $B = \Delta p/\sigma_m|_{un}$. The stress term on the right-hand side of Equation (3.1) accounts for mechanical coupling in the pore pressure diffusion model, because the dynamic parameter σ_{kk} can be related to the rock deformation using the poroelastic relationship (Cheng, 2016).

We analyze four analytical solutions for the diffusion equation with oscillating input pore pressure, under simplified flow and stress conditions. In particular, we consider 1D flow under constant stress assuming incompressible solid matrix, 1D and cylindrical infinite flow under

constant stress where the problem reduces to the traditional hydraulic diffusivity problem (stress and strain variations are neglected), and 1D flow under constant lateral stresses that accounts for a simplified HM coupling (Chapter 4). For convenience, we report the results normalized by the characteristic length λ , which is a function of both the material properties (through the diffusivity D) and the imposed pore pressure wave (through the frequency ω), $\lambda = (D/\omega)^{1/2}$.

3.2.2. Uncoupled 1D diffusion for incompressible solid matrix

This analytical solution considers a steady-periodic propagation of the pore pressure wave on an infinite-extent domain in the x direction, i.e., $\partial^2 p/\partial y^2 = 0$ and $\partial^2 p/\partial z^2 = 0$. The rock is subject to constant stress in all directions resulting in $\partial \sigma_{kk}/\partial t = 0$. Following Ferris (1952), if the solid phase is assumed incompressible, i.e., $1/K_f$ and $1/K \gg 1/K_s$, which is a common assumption in the context of soil mechanics, the hydraulic diffusivity D reduces to D_s and Equation (3.1) to

$$\begin{cases} \frac{\partial p}{\partial t} - D_s \frac{\partial^2 p}{\partial x^2} = 0 \\ D_s = \kappa \left(\frac{\phi}{K_f} + \frac{1}{K} \right)^{-1} \end{cases} \quad (3.2)$$

At the source ($x = 0$), we consider a sinusoidal pressure oscillation of constant amplitude p_0 and frequency $\omega = 2\pi/T$, where T is the period of the pressure wave, i.e., $p(0,t) = p_0 \sin(\omega t)$. Under these conditions, Jacob (1950) and Ferris (1952) derived an analytical solution for pore pressure amplitude as

$$A_F(x) = \frac{p(x)}{p_0} = e^{-x\sqrt{\frac{\omega}{2D_s}}} = e^{-\frac{x}{\lambda}\sqrt{\frac{D}{2D_s}}} \quad (3.3)$$

where the pore pressure amplitude ratio A_F decreases exponentially with distance from the source and the square root of the frequency of the signal.

3.2.3. Uncoupled 1D diffusion of oscillatory input

In contrast to the assumption made by Jacob (1950) and Ferris (1952), the compressibility of the solid phase is non-negligible in rocks, oftentimes being on the same order of magnitude as its bulk compressibility (Cheng, 2016). For this reason, we release here the incompressibility hypothesis, meaning that the hydraulic diffusivity depends also on the compressibility of the solid phase and isolated pores ($1/K_s$), while fluid flow and normal stress in the x -direction remain constant. Using these assumptions for a finite domain of length L , Kranz et al. (1990) developed an analytical solution by decomposing the pore pressure oscillation into amplitude $p(x)$ and harmonic components, i.e., $p(x,t) = p(x) \cdot e^{i\omega t}$ with $p(x)$ being a decreasing monotonic function of x . Imposing a constant amplitude and frequency at the source, the pore pressure amplitude as a function of distance is calculated as

$$\frac{p(x)}{p_0} = \frac{[i\omega - S_D(1+i)N]e^{(1+i)N(x-L)} - [i\omega + S_D(1+i)N]e^{-(1+i)N(x-L)}}{[i\omega - S_D(1+i)N]e^{-(1+i)NL} - [i\omega + S_D(1+i)N]e^{(1+i)NL}}; \quad (3.4)$$

where $N = (\omega/2D)^{1/2}$, and $S_D = \kappa\pi RK_f/V_D$ is a storativity term introduced by the laboratory setup, where R denotes the radius of the specimen cross-section and V_D is the volume of the downstream compartment.

Considering an infinite domain ($L \rightarrow \infty$) yields an expression for pore pressure diffusion at the field scale

$$A_K(x) = \left| \frac{p(x)}{p_0} \right| = \left| e^{-x(1+i)\sqrt{\frac{\omega}{2D}}} \right| = \left| e^{-(1+i)\frac{x}{\sqrt{2\lambda}}} \right| \quad (3.5)$$

where $|p(x)/p_0| = \{[\text{Re}(p(x)/p_0)]^2 + [\text{Im}(p(x)/p_0)]^2\}^{1/2}$ indicates the absolute value of the complex number in between. Equations (3.3) and (3.5) share similar exponential forms but with different hydraulic diffusivities. In particular, we notice that D as defined in Equation (3.1) is larger than D_s , and consequently $A_K(x) \geq A_F(x)$, i.e., the amplitude diffuses further through materials with compressible solid constituents, and $A_K(x)$ solution coincides with $A_F(x)$ under the assumption of an incompressible solid matrix.

3.2.4. 1D diffusion of oscillatory input at constant lateral stress

Previous simplified solutions consider constant stress (Sections 3.2.2 and 3.2.3), uncoupling the pore pressure diffusion with stress and strain of the material, i.e., considering only the left-hand side of Equation (3.1). Assuming constant lateral stress, i.e., $\partial\sigma_{kk}/\partial t = \partial\sigma_{xx}/\partial t$, the 1D diffusion equation becomes

$$\frac{\partial p}{\partial t} - D \frac{\partial^2 p}{\partial x^2} = \frac{B}{3} \frac{\partial \sigma_{xx}}{\partial t} \quad (3.6)$$

Adachi and Detournay (1997) solved this equation for a homogeneous elastic rock sample of length L and radius R under the same pore pressure oscillation of the previous case, i.e., $p(0,t) = p_0 \cdot e^{i\omega t}$. They assumed 1D flow in the x -direction and negligible shear stresses, acceptable for slender specimens of $R \ll L$. The solution is the superposition of the hydraulic and mechanical effects, with the former corresponding to Kranz's solution as in Equation (3.4) and the latter being

$$\left(\frac{p(x)}{p_0} \right)_m = \frac{B}{3} \frac{(1 - e^{(1+i)Nx}) \left[\frac{S_D}{D} (1 - e^{(1+i)N(x-2L)}) - (1+i)N (e^{-(1+i)NL} - e^{(1+i)N(x-2L)} - 1 + e^{(1+i)N(x-L)}) \right]}{S_D + (1+i)N + e^{-(1+i)N2L} \left[\frac{S_D}{D} - (1+i)N \right]} \quad (3.7)$$

For an infinite domain where $L \rightarrow \infty$, the diffusivity equation becomes

$$\begin{aligned} A_{AD}(x) = A_K(x) + A_m(x) &= \left| e^{-x(1+i)\sqrt{\frac{\omega}{2D}}} \right| + \left| \frac{B}{3} \left(1 - e^{-x(1+i)\sqrt{\frac{\omega}{2D}}} \right) \right| = \\ &= \left| e^{-(1+i)\frac{x}{\sqrt{2\lambda}}} \right| + \left| \frac{B}{3} \left(1 - e^{-(1+i)\frac{x}{\sqrt{2\lambda}}} \right) \right| \end{aligned} \quad (3.8)$$

Where $A_K(x)$ accounts for the pore pressure amplitude ratio under constant stresses (see Equation (3.5)) and $A_m(x)$ represents the mechanical effect due to stress variation along the diffusion direction.

Comparing Equations (3.8) and (3.5), we notice that $A_{AD}(x) \geq A_K(x)$, since $A_m(x) \geq 0$. $A_m(x)$ is an increasing monotonic function of x , contrary to $A_K(x)$, meaning that the mechanical effect becomes more important at large distances, depending on the frequency of the signal.

3.2.5. Uncoupled cylindrical two-dimensional diffusion of periodic pressure

All the previous solutions assume 1D diffusion of pore pressure; however, for a vertical injection well (Figure 3.1), cylindrical two-dimensional diffusion should be considered. Assuming constant stress, resulting in $\partial\sigma_{kk}/\partial t = 0$, the pore pressure diffusion equation (Equation (3.1)) can be expressed in the cylindrical coordinates as

$$\frac{\partial p}{\partial t} - \frac{D}{r} \left[\frac{\partial}{\partial r} \left(r \frac{\partial p}{\partial r} \right) + \frac{\partial}{\partial \theta} \left(\frac{1}{r} \frac{\partial p}{\partial \theta} \right) + \frac{\partial}{\partial z} \left(r \frac{\partial p}{\partial z} \right) \right] = 0 \quad (3.9)$$

where r is the radial distance from the source, z is the location along the axis of symmetry (vertical), and θ is the angular coordinate. Considering a homogeneous isotropic material, i.e., $\partial p/\partial z; \partial p/\partial \theta = 0$, and a stationarity pressure fluctuation $p(r,t) = p(r) \cdot e^{i\omega t}$, we obtain

$$Dr \frac{d^2 p(r)}{dr^2} + D \frac{dp(r)}{dr} - i\omega r \cdot p(r) = 0 \quad (3.10)$$

For an infinite domain, the solution of Equation (3.10) is a linear combination of two Bessel functions of zero order (Olver and Maximon, 2010)

$$p(r) = a \cdot I_0(\sqrt{ir}\lambda^{-1}) + b \cdot K_0(\sqrt{ir}\lambda^{-1}), \quad (3.11)$$

where I_0 is a hyperbolic Bessel function of the first kind of order zero, and K_0 is a hyperbolic Bessel function of the second kind of order zero calculated for the complex number $(i)^{1/2}r/\lambda$, and a and b are constant values to be defined from boundary conditions. The same theory was employed by Carslaw and Jaeger (1959) to address the heat conduction problem.

We consider an injection well of radius r_0 and no far-field pressure variation as r approaches infinity, i.e., $p(r_0) = p_0$ and $p(r \rightarrow \infty) = 0$, respectively. Under these conditions, the first term in Equation (3.11) can be neglected as $a = 0$ and b corresponds to $p_0/K_0((i)^{1/2}r_0/\lambda)$. The amplitude attenuation with distance is thus governed by

$$A_R = \frac{p(r)}{p_0} = \frac{K_0(\sqrt{ir}\lambda^{-1})}{K_0(\sqrt{ir_0}\lambda^{-1})} \quad (3.12)$$

3.3. Test cases and numerical models

We apply the analytical solutions of pore pressure diffusion to three geo-energy applications that involve oscillating pore pressure with different periods: a) energy storage in porous rock, b) caprock integrity during periodic CO₂ injection (the CO₂LPIE experiment) (Rebscher et al., 2020; and Chapter 4), and c) enhanced geothermal system stimulation (Figure 3.1).

For the energy storage, we assign a period of one year, following the annual fluctuations in energy demand and production, as happens in natural gas storage and is expected to happen in hydrogen storage (Lysy et al., 2021). In the CO₂LPIE experiment, we assign a period of one week, which permits observation of periodic pore pressure variation at distances in the order of tens of centimeters. Considering the stimulation of an enhanced geothermal system, we assign a short period, in the order of hours – typical of the so-called cyclic or soft stimulation (Hofmann et al., 2018; 2019). In this way, we cover a wide range of both rock diffusivity and the period of the signal.

We select three well-characterized rocks as representative hosts for these applications: Berea sandstone for energy storage (Makhnenko and Labuz, 2016), Opalinus Clay (shale) from Mont Terri Lab as a representative caprock for CO₂ storage (Makhnenko et al., 2017; Makhnenko and Podladchikov, 2018), and Westerly granite for enhanced geothermal system stimulation (Nur and Byerlee, 1971). The properties controlling the hydraulic conductivity and storage

coefficient are representative of stresses associated with ~200 m for Berea sandstone, ~300 m for Opalinus Clay, and ~1000 m for Westerly granite, their properties are listed in Table 3.1.

Table 3.1. Hydro-mechanical properties of the rock types considered in this study.

Property	Berea sandstone ¹ ($T=365$ d)	Opalinus Clay ^{2,3} ($T=7$ d)	Westerly granite ⁴ ($T=0.5$ d)
K (GPa)	6.7	1.9	25.0
K_s (GPa)	30.0	8.1	45.4
K_f (GPa)	2.25	2.25	2.25
ϕ (-)	0.23	0.12	0.01
k (m ²)	$1.9 \cdot 10^{-13}$	$2.0 \cdot 10^{-20}$	$4.0 \cdot 10^{-19}$
B (-)	0.80	0.90	0.81
D_s (m ² /s)	0.76	$3.45 \cdot 10^{-8}$	$9.00 \cdot 10^{-6}$
D (m ² /s)	0.90	$4.53 \cdot 10^{-8}$	$1.80 \cdot 10^{-5}$
λ (m)	$2.28 \cdot 10^3$	$6.60 \cdot 10^{-2}$	$4.98 \cdot 10^{-1}$

¹Makhnenko and Labuz (2016); ²Makhnenko et al. (2017); ³Makhnenko and Podladchikov (2018); ⁴Nur and Byerlee (1971).

We assume that the injected fluid for storage and stimulation purposes can be represented by water, which has a compressibility $1/K_f$ around 0.44 GPa^{-1} and a viscosity of $\mu = 0.001 \text{ Pa}\cdot\text{s}$ at room temperature (Cheng, 2016). The host rock for CO₂LPIE is Opalinus Clay, a shale characterized by a low diffusivity and considered as a representative caprock for CO₂ storage. The experiment aims at injecting gaseous CO₂ at a mean overpressure of 1 MPa, with an amplitude in the order of 0.1 MPa. Preliminary simulation results show that the high capillary entry pressure of Opalinus Clay prevents free-phase CO₂ intrusion into the pore network, while the periodic pore pressure signal propagates much ahead of the diffusive aqueous CO₂ front (Chapter 4). Therefore, we also assume water flow for this case. Given the reported hydro-mechanical properties, we derive the hydraulic diffusivities D and D_s (Table 3.1). The diffusivities vary by several orders of magnitude among the three materials. The effect of solid phase compressibility on diffusion coefficient, i.e., the difference between D and D_s , is the most pronounced for Westerly granite (a factor of two), since the rock has a large bulk modulus K and small porosity ϕ , decreasing the contribution of rock and fluid on the storage coefficient. Finally, combining the representative material and signal properties, we derive the characteristic length λ (Table 3.1).

3.3.1. Geometry definition

We assess the applicability and accuracy of the analytical solutions presented through comparison with numerical simulations. We solve the problem for two different geometries using the fully-coupled finite-element code CODE_BRIGHT (Olivella et al. 1994; 1996). The linear flow model is compared with the uncoupled 1D diffusion of oscillatory pressure, both for the case of compressible and incompressible solid matrices A_K and A_F (Sections 3.2.3 and 3.2.2, respectively) and the 1D diffusion under constant lateral stress A_{AD} (Section 3.2.4). The axisymmetric solution is compared with the uncoupled radial diffusion of periodic pressure perturbation A_R (Section 3.2.5).

In all simulations, the hydraulic diffusion coefficient D is employed as given in Table 3.1. Indeed, in addition to considering the compressibility of the solid matrix, D is used for almost all the analytical solutions reported here, leaving D_s to Ferris' formulation alone (Section 3.2.2) that has been previously validated for in-situ conditions (Ferris, 1952). We define two different areas: one from the injection source on the left boundary to x_1 (and r_1), on which the results are presented, hereinafter also referred to as the monitoring region. The other are include an extension of the model geometry to a distance of x_2 (and r_2), to avoid boundary effects (Figures 3.2 and 3.3). To evaluate these distances, we rearrange Equation (3.5) into

$$x_j = -\sqrt{\frac{2D}{\omega}} \cdot \ln(A_j) = -\sqrt{2}\lambda \cdot \ln(A_j) \quad \text{with } j = 1, 2 \quad (3.13)$$

We define x_1 (and r_1) and x_2 (and r_2), as distances at which amplitude ratios attenuate to $A_1=10^{-3}$ and $A_2=10^{-9}$, respectively. This implies that for an initial amplitude p_0 in the order of MPa, the minimum amplitude recorded across the monitoring region will be on the order of kPa. The criterion for the definition of A_2 takes into account the precision limits of the numerical simulations. We adopt the same distances for the cylindrical geometry for the sake of comparison with the 1D geometry. The calculated values of the boundary locations for the three geo-energy applications subject to representative pressure fluctuation periods are listed in Table 3.2.

Table 3.2. Length of the domain, evaluated with Equation (3.13) for amplitude attenuations of 10^{-3} and 10^{-9} , respectively.

Distances	Berea sandstone ($T=365$ d)	Opalinus Clay ($T=7$ d)	Westerly granite ($T=0.5$ d)
$x_1; r_1$ (m)	$2.27 \cdot 10^4$	0.65	3.4
$x_2; r_2$ (m)	$6.80 \cdot 10^4$	1.92	10.3

3.3.2. Hydraulic model

For both 1D and axisymmetric geometries, we assume horizontal flow, neglecting the effect of gravity forces. In addition, we impose no flow on the top and bottom boundaries and constant pressure on the right boundary. At the left boundary, we impose a sinusoidal variation of the pore pressure with constant amplitude p_0 and frequency ω (Figure 3.2). Finally, we solve numerically Equation (3.1) with the diffusivity coefficient D and the right-hand side dealing

with stress changes set to zero. Throughout this paper, we refer to this model as hydraulic and accordingly, the obtained pressure amplitude as A_H , since mechanical constraints on pressure diffusion are not considered, although we partly take into account the effect of the reservoir stiffness through the storage term S_s introduced into the diffusivity equation.

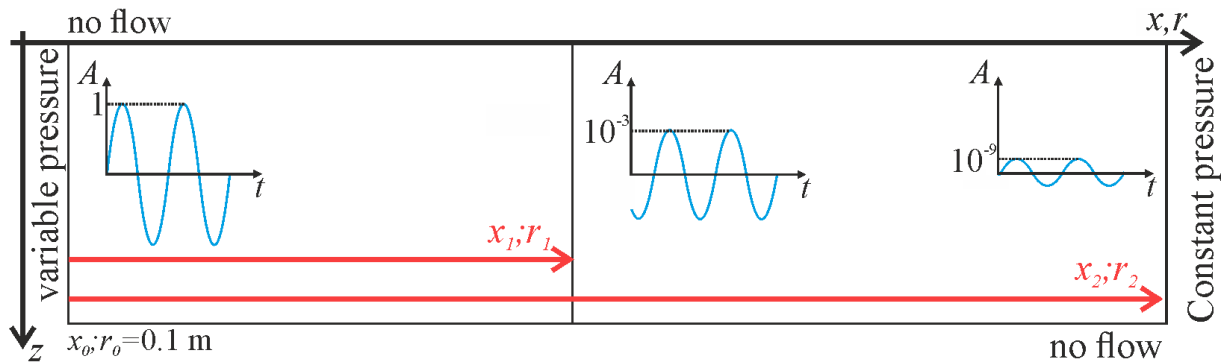


Figure 3.2. Geometry and boundary conditions of the hydraulic model. The sketch represents both the 1D and the radial case. The only difference is that for the radial case, we assume symmetry around $r = 0$.

3.3.3. Hydro-mechanical model

We assume a homogeneous isotropic proelastic material fully saturated with water. We solve the mass conservation of water and Darcy's law together with linear momentum balance and poroelastic constitutive equations of the porous medium in a fully-coupled manner. The mechanical boundary conditions include zero displacements perpendicular to lateral and bottom boundaries and a uniformly distributed stress on the upper one (Figure 3.3). Note that these boundary conditions, which are representative of the HM problem at the field scale, are not the same as those considered by Adachi and Detournay (1997). They assumed no displacement in the upper and lower boundaries and constant stress at the right boundary (Section 3.2.4) being representative of laboratory experiments in a core holder. In the following results (Section 3.4), we refer to this model as hydro-mechanical and the obtained pressure amplitude as A_{HM} .

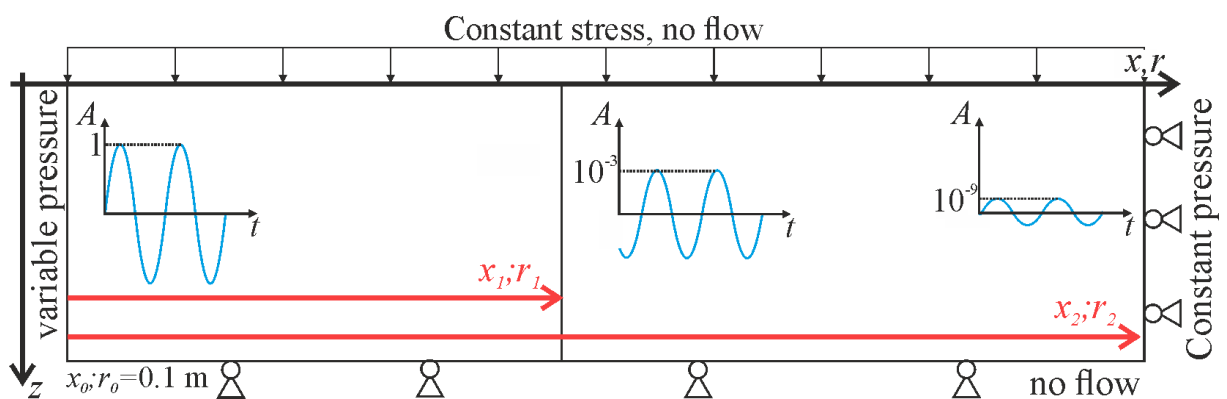


Figure 3.3. Geometry and boundary conditions of the coupled hydro-mechanical model. The sketch represents both the 1D and the radial case. The only difference is that for the radial case, we assume symmetry around $z = 0$.

3.4. Results

3.4.1. Comparison between analytical and numerical solutions

Figures 3.4 and 3.5 illustrate pressure propagation in confined geological layers of infinite extent, two flow geometries (linear and cylindrical) are considered. We show the results in terms of dimensionless attenuation of the injection/extraction wave amplitude obtained for different theories and case studies (described in Section 3.3). For the sake of comparison between different scenarios, we normalize the distance from the source using the characteristic length λ (Table 3.1), allowing us to present them all in one unified plot.

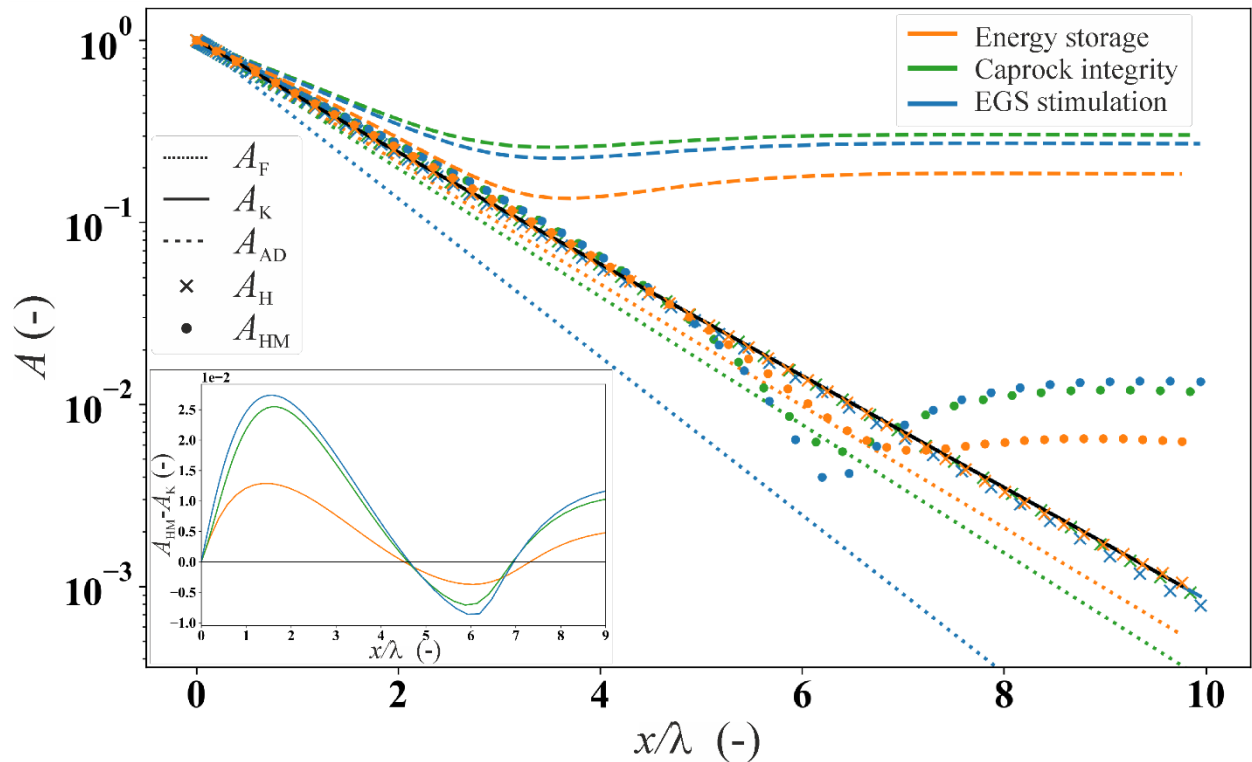


Figure 3.4. Amplitude ratio A as a function of linear distance from the well, normalized by the characteristic length λ , for the three examined case studies (Figure 3.1). The lines represent the analytical solutions while the symbols represent the numerical solutions. In the inset, we plot the difference between the HM and Kranz's (H) solutions, $A_{HM} - A_K$, for all three case studies.

The analytical solutions A_F , A_K , and the numerical solution A_H for the one-dimensional diffusion assumption, exhibit linear trends in the semi-logarithmic plot (Figure 3.4). This linear behavior arises due to the constant value of the specific storage S_s in the three solutions, wave propagation-induced deformations are neglected. Specifically, for a fixed characteristic length λ , the solutions A_K and A_H (represented by the black line and cross, respectively, in Figure 3.4) coincide with each other for all three scenarios, representing a good match between the analytical and numerical solutions for the purely hydraulic problem.

A_F curves (dotted lines in Figure 3.4) exhibit for all scenarios a steeper slope compared to A_K (and A_H), indicating a greater attenuation of the wave. This increased attenuation is attributed to the absence of compression/expansion of the solid constituents caused by the injection/extraction in the A_F model. While such an assumption may be acceptable for shallow

or unconsolidated sediments where the bulk modulus of the soil can be much smaller than that of solid constituents, it appears inadequate for consolidated rock (Cheng, 2016). This behavior is more evident for enhanced geothermal systems stimulation than for both the CO₂LPIE and energy storage cases because of the lower Biot coefficient α (higher K/K_s ratio) of the stiff Westerly granite, approximately equal to 0.44, compared to the 0.76 and 0.78 for Opalinus Clay and Berea sandstone, respectively (Table 3.1).

The analytical solution A_{AD} (dashed lines in Figure 3.4) and the numerical solution A_{HM} (dots in Figure 3.4) include the instantaneous deformation of the rock induced by pore pressure wave propagation. In all scenarios, both solutions indicate a non-linear behavior of the amplitude ratio that approaches a constant value at some distance from the source. The A_{HM} considers vertical deformation, while the simplified analytical solution A_{AD} accounts solely for the lateral deformation. Considering A_{HM} with boundary conditions being more representative of underground conditions as the reference scenario, we find that A_{AD} yields a significant overestimation of the amplitude ratio (Figure 3.4). Yet, the accuracy of the A_{AD} solution for its simplifying assumptions is verified through comparison with numerical solutions with the identical boundary conditions (see Appendix A).

A comparison between hydraulic solutions A_H and A_K and the mechanical solution A_{HM} (see inset in Figure 3.4) shows that the difference between the two couplings initially increases with distance from the source until it reaches a peak (around $x/\lambda = 2$), followed by a decrease and becoming negative after x/λ approximating 4.5, and then increasing to converge towards a positive value. Additionally, we note that the magnitude of $A_{HM} - A_K$ remains limited to 10^{-2} , i.e., 1%. This difference is less pronounced in the energy storage scenario compared to the CO₂LPIE and enhanced geothermal systems stimulation cases.

In the context of cylindrical pore pressure diffusion (Figure 3.5), determining the dimensionless distance requires subtracting the radius of the cylindrical source r_0 , before dividing by the characteristic length λ . Similar to the linear geometry, the analytical solution A_R is in good agreement with the numerical solution A_H for the cylindrical geometry. The amplitude attenuation is higher compared with the linear geometry (Figure 3.4), when all other conditions remain constant, as the cylindrical flow provides more space for the pressure to diffuse. Specifically, the analytical solution A_R exhibits a non-linear attenuation trend for values of the radial dimensionless distance smaller than 2 (Figure 3.5). This decrease is more pronounced in energy storage application, moderately visible in enhanced geothermal systems stimulation, and almost negligible for CO₂LPIE, exhibiting an inverse proportionality to the rock's diffusivity D (Table 3.1). Notably, the periodicity does not impact this behavior, which is solely governed by the rock properties. Conversely, for values of the dimensionless distance larger than 2, the curves exhibit a linear decrease in a semi-logarithmic plot (Figure 3.5).

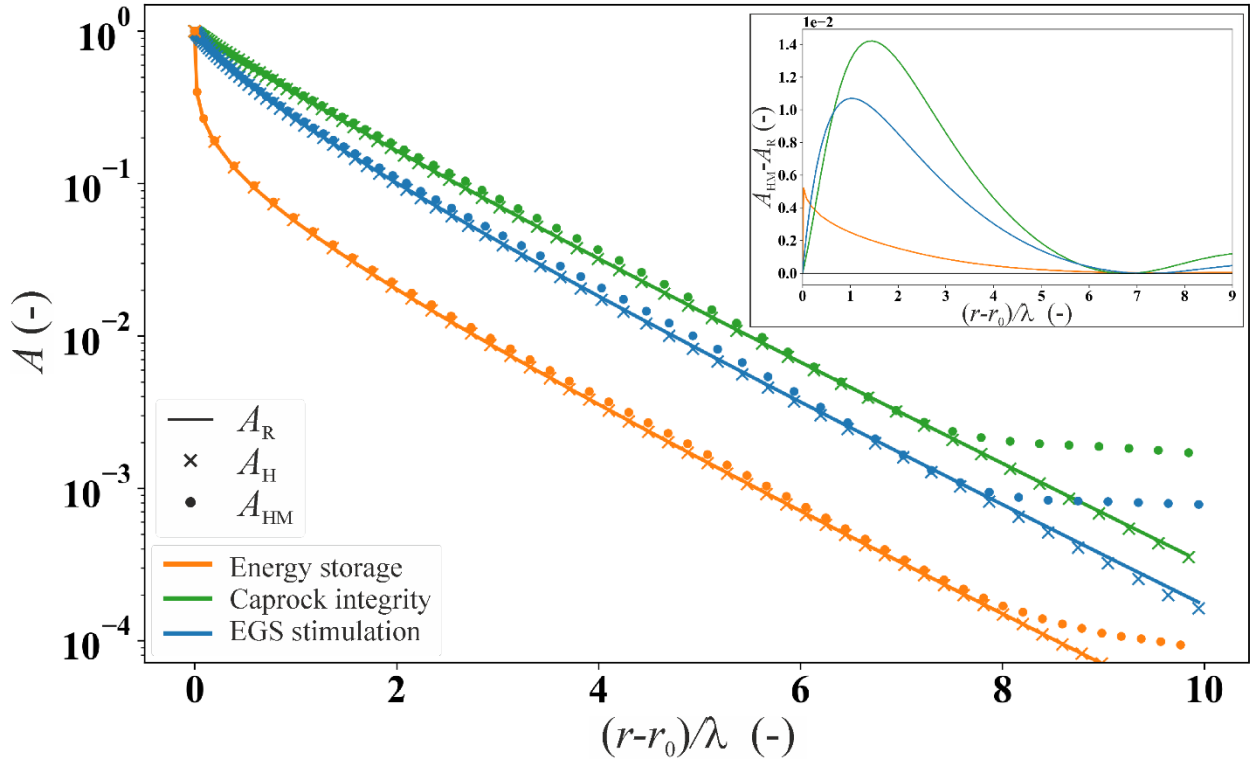


Figure 3.5. Amplitude ratio A as a function of the dimensionless radial distance from the well, normalized by the characteristic length λ , for the three examined case studies (Figure 3.1). The lines represent the analytical solutions while the symbols represent the numerical solutions. In the inset, we plot the difference between $A_{HM} - A_R$, for all three case studies.

A comparison between the hydro-mechanical solution A_{HM} , achieved numerically, and hydraulic solutions A_H and A_R for the cylindrical geometry shows that the deformation of the reservoir affects the results for values of $(r-r_0)/\lambda > 7$, leading to a significant divergence between the two couplings (Figure 3.5). However, when observing the difference $A_{HM} - A_R$ (inset in Figure 3.5), we note that the disparity is confined to 10^{-2} , i.e., 1%. This follows a similar behavior as analyzed for the one-dimensional case (inset in Figure 3.4), albeit with lower absolute values for each case.

3.4.2. Attenuation ratios for various analytical solutions

Following the comparison of the analytical solutions (A_K and A_R) with the numerical solution (A_{HM} , provided for both geometries), we observe that the difference of amplitude ratio remains limited to around 1% for both linear and cylindrical flow cases (insets in Figure 3.4 and Figure 3.5, respectively). Consequently, we deem it reasonable to establish a threshold for the amplitude ratio at 10%, one order of magnitude higher (Figure 3.6), to compare the extent to which pore pressure oscillations penetrate into the rock under different conditions. We exclude the analytical solution A_{AD} in further analysis because it was developed to represent laboratory conditions, but not field cases. We include the typical range of properties of sandstones, granites, and shales based on typical ranges of hydraulic properties indicated for these rock types (Brace, 1980).

The attenuation curves exhibit an increasing linear trend for both geometries (red dashes – for 1-D and black – for radial lines in Figure 3.6), indicating that higher diffusivity leads to enhanced wave propagation. Similarly, an increase in the wave period T (or a decrease in

frequency) shifts the curves towards greater distances for both geometries without altering their slopes, implying that the slope of amplitude attenuation depends on the flow geometry rather than the wave's nature, i.e., the period T . Comparing A_K (Equation (3.5), red dashed line in Figure 3.6) with A_R (Equation (3.12), black dashed line), we observe a more pronounced attenuation in the propagation of the pressure wave for the case of cylindrical flow A_R , as anticipated by the previous results. This is evident through the curves' shift towards higher values and a steeper slope for the cylindrical geometry. For instance, considering $T = 1$ day, A_K reaches approximately 400 m, 0.08 m, and 2 m for Berea sandstone, Opalinus Clay, and Westerly granite, respectively, while A_R is limited to 90 m, 0.05 m, and 0.6 m for the same rocks. This results in a ratio of about 4 for the first case, 1.6 for the second, and 3.33 for the third. In other words, the influence of the geometry becomes more pronounced with higher diffusivity of the material D .

Figure 3.7 illustrates the contour plot of $A_R(r)$, representing the cylindrical diffusion of periodic pressure perturbation under constant stress for one week, and a threshold of 0.1, alongside the line $A_K(x) = 0.1$ to visualize the difference between the two solutions. In the contour plot, it becomes evident that isolines with high A_R values (> 0.4) exhibit an exponential trend for the aquifer diffusivity when presented in a bi-logarithmic diagram, while for lower values, they tend towards a linear trend. Conversely, the iso- A_K curves remain straight, as they follow a negative exponential function of x and the square root of $1/D$ (Equation (3.5)). This further accentuates the disparities between the two geometries and emphasizes the significance of selecting right solutions according to the physics of the problem.

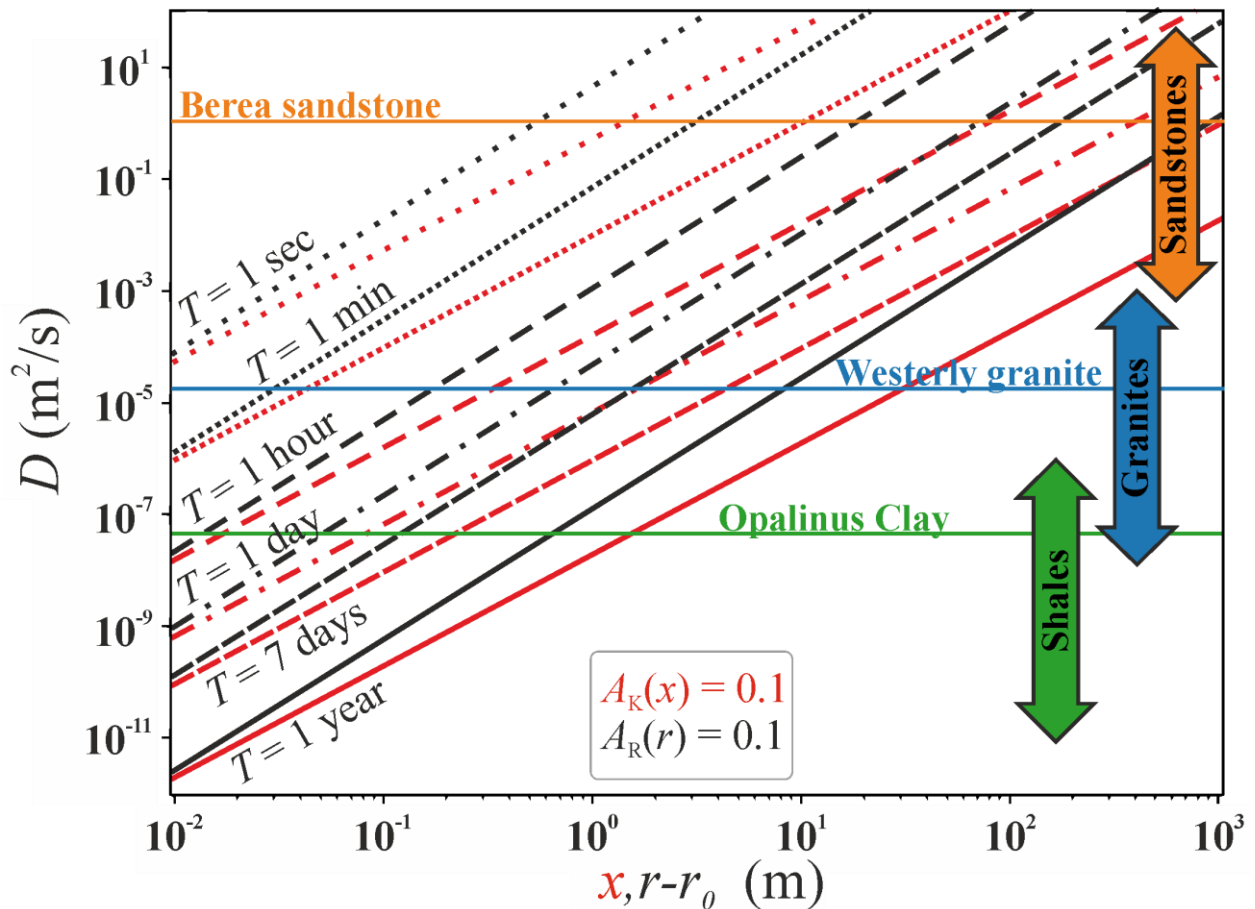


Figure 3.6. Variation of threshold values for the attenuation ratio $A_K = 0.1$ (red lines) and $A_R = 0.1$ (black lines), as a function of the hydraulic diffusivity D for different periods T . The orange, blue, and green lines refer to D values for the considered geo-energy applications

(Section 3.3), while the ranges of D for different rock types (sandstone, granites, and shales) are based on hydraulic data from Brace (1980).

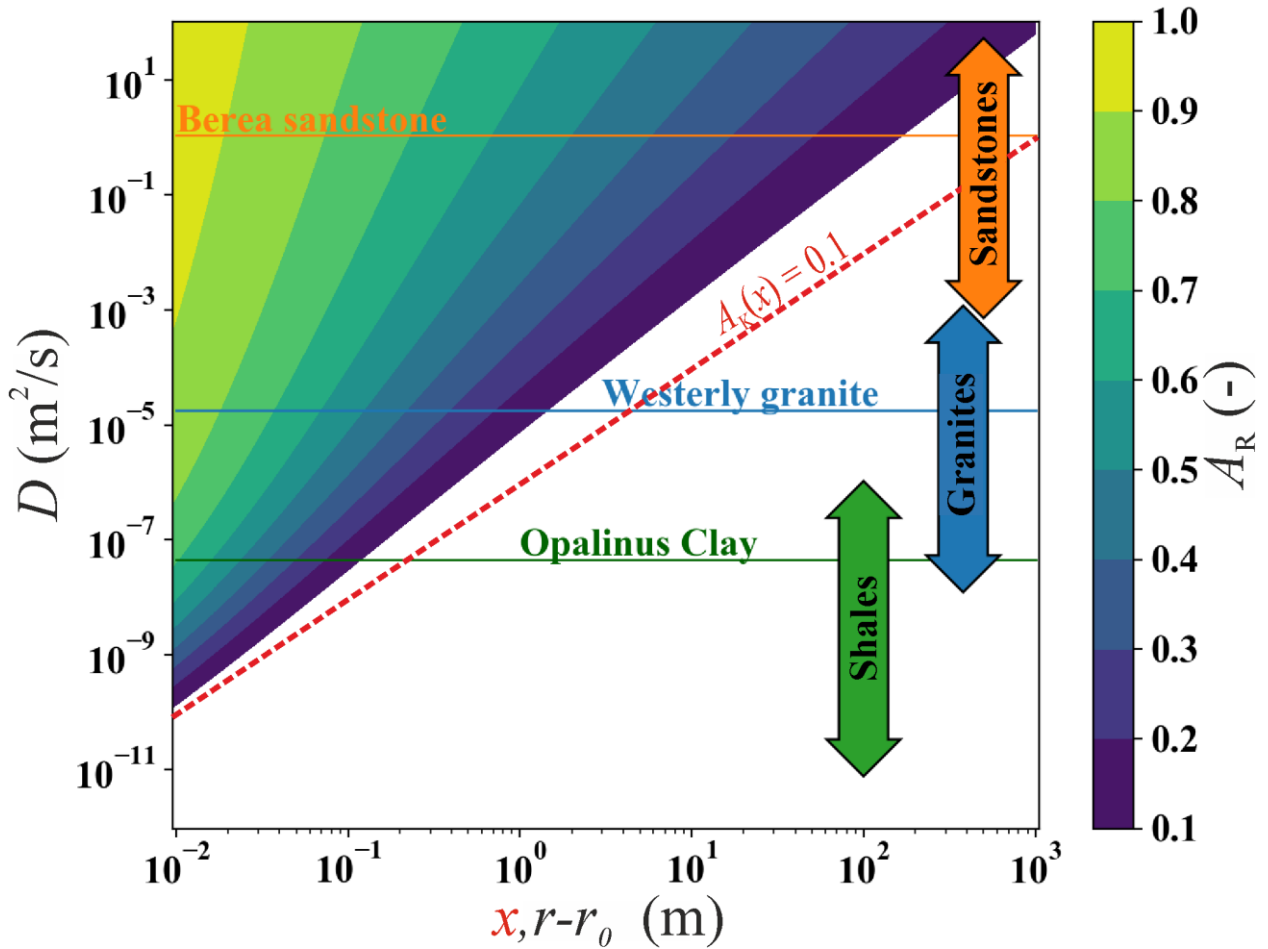


Figure 3.7. Contour plot of the amplitude ratio A_R as a function of radial distance from the source ($r-r_0$) with a fixed period ($T = 7$ days). Additionally, we have overlaid the line representing $A_K = 0.1$ for the one-dimensional distance from the source (x) with the same period (T) depicted as a red dashed line. The horizontal orange, blue, and green lines correspond to the diffusivity (D) values used in our case studies (Section 3.3), while the diffusivity ranges for different rock types, namely sandstones, granites, and shales, are based on the data from Brace (1980).

3.5. Discussion

3.5.1. Pore pressure response affected by rock properties

The diffusivity D , defined as the ratio of hydraulic conductivity κ to specific storage S_s , controls the amplitude attenuation and shift in the period of periodic signals in porous rock. High diffusivity is obtained by a combination of high stiffness (or low specific storage) and high permeability (and transmissivity). Notably, the significant difference in diffusivity between shales ($D \sim 10^{-11}$ to 10^{-6} m²/s) and sandstones ($D \sim 10^{-3}$ to 10^2 m²/s) is mainly caused by their permeability contrast (Brace, 1980). Additionally, the variation in diffusivity between shales

and granites ($D \sim 10^{-8}$ to 10^{-3} m²/s) is a consequence of the higher stiffness exhibited by the latter material, as indicated in Table 3.1. It should be noted that the values we have assigned to the rock formations correspond to the intact material, rather than the entire rock mass. In the case of low-permeability rocks like shales and granites, the hydraulic properties of the formation are significantly affected by the presence of fractures (Brace, 1980; van der Kamp, 2001), which can result in a permeability enhancement of two to three orders of magnitude (Neuzil, 1986).

We report analytical solutions for specific geometries: A_K for one-dimensional flow (Equation 3.5) and A_R for radial flow (Equation 3.12). Comparing these with the more comprehensive numerical solution A_{HM} (Section 3.3.3), we find discrepancy across three geo-energy applications with highly diverse periodic signals and hosting rock characteristics (insets in Figure 3.4 and Figure 3.5). This disparity is principally attributed to neglecting mechanical controls on pressure diffusion by hydraulic solutions. While A_K and A_R assume uncoupled conditions, the coupled A_{HM} accounts for the instantaneous deformations of the rock caused by the oscillatory pore pressure perturbation and changes in the effective stresses. Besides, fluid accommodation and expulsion by porous rock involve various mechanisms, including the expansion/compaction of the solid frame, solid constituent, and the pore fluid characterized by their compressibilities and weighted by the rock porosity. In unconsolidated aquifers where the rock body is highly compliant, it is common to neglect the compressibility of solid constituents when interpreting in-situ tests (Jacob, 1950; Ferris, 1952). However, in stiff aquifers, the compressibility of solid constituent is not negligible for the diffusion of periodic pore pressure, consistent with observations on tidal fluctuation by van der Kamp and Gale (1983).

The nearly constant amplitude attenuation that is observed away from a certain distance from the injection well is relevant when considering the hydro-mechanical coupling. In particular, for the design of the periodic CO₂-rich water injection in caprock (CO₂LPIE experiment), it is crucial to define the best location of the monitoring wells with respect to the injection well (Chapter 4). Results show that the amplitude rapidly attenuates within a few tens of centimeters, suggesting that monitoring wells should be placed as close as possible to the injection well. However, some limitations exist related to the minimum distance between boreholes to avoid interferences and affections between the drillings and stability of the boreholes. Thus, the minimum required distance may be farther away from the injection well than the distance at which the amplitude attenuation becomes constant. Being aware of this hydro-mechanical response of the rock is essential when interpreting monitoring data to avoid misinterpretations of diffusivity estimates.

3.5.2. Pore pressure response affected by fluid properties

The diffusivity parameter D is inversely proportional to fluid viscosity μ while decreasing with the increase in fluid compressibility β , which results in higher storativity. In this study, we consistently assumed water at 20 °C as the injected fluid in all test cases (Section 3.3) to put our emphasis on the role of injection parameters and rock characteristics. However, μ varies with temperature (e.g., decreases by a factor of 2 for water at 50 °C) and is relatively insensitive to pressure gradients. This dependence of viscosity on temperature is especially relevant in enhanced geothermal systems, which seek temperatures around 180 °C, representing a viscosity reduction of around one order of magnitude. Additionally, β can change with pressure, temperature, and salinity, but generally remains within the same order of magnitude (Osif, 1988). While these observations apply to water, they may not be applicable when considering other fluids at different physical states.

In the context of energy storage and for CO₂ Long-term Periodic Injection Experiment (CO₂LPIE) scenarios (a and b in Figure 3.1, respectively), the injected fluid could be H₂, CH₄, or CO₂, in either liquid, gas or supercritical phases. For instance, in the case of underground storage of H₂ with an approximate compressibility of 3 GPa⁻¹ and a viscosity of around 8.9·10⁻⁶ Pa·s (Zivar et al., 2001), the resulting diffusivity in Berea Sandstone is approximately 32 m²/s, representing an increase by one order of magnitude compared to the one of water (Table 3.1). Consequently, at a radial distance of 2 km and an annual period, the amplitude attenuation A_R (Equation 3.12) increases from around 12% to about 23%.

Similarly, considering gaseous CO₂ injection in CO₂LPIE experiment, the compressibility becomes approximately 5 GPa⁻¹, with a viscosity of around 3.6·10⁻⁵ Pa·s (Span and Wagner, 1996), leading to a diffusivity of approximately 5.6·10⁻⁷ m²/s, one order of magnitude higher than the one considering water (Table 3.1). Consequently, at a radial distance of 0.1 m and a period of a week, the amplitude ratio A_R would increase from about 25% to approximately 56%. Nonetheless, CO₂ cannot easily penetrate into shale like Opalinus Clay because of its high entry pressure, which prevents CO₂ to enter into the small pore throats of the rock. Therefore, the periodic signal of the injected gaseous CO₂ is transmitted to the resident pore water, which is in essence the fluid that controls the amplitude attenuation and the shift in the periodic signal. CO₂ will dissolve into the water and will advance by advection and diffusion, but not in free phase (Chapter 4).

A more complex scenario involves the examination of the interplay between two distinct fluids and their impact on the exposed rock. Two-phase flow in porous media is controlled by capillary pressure and relative permeability (Blunt et al., 1992). Laboratory investigations, when capillary displacements assume dominance in the flow regime, are often conducted to determine these parameters (Bennion and Bachu, 2008; Makhnenko et al., 2017). However, on a reservoir scale, the dynamics are predominantly governed by the interplay of viscous and buoyancy forces (Blunt et al., 1992). For analytical solutions, the gap between macroscopic flow and pore-scale displacements can be bridged through the utilization of the multiphase Darcy's law, as implemented in numerical simulations (Vilarrasa and Makhnenko, 2017; Kivi et al., 2022a; b).

3.5.3. Pore pressure response affected by the period

Our results exhibit an exponential decay of the amplitude ratio A on the characteristic length λ . Specifically, this characteristic length corresponds to the distance at which a one-dimensional amplitude attenuation of approximately 37% in the pressure wave is achieved, as described in Section 2.3. By defining the characteristic distance in terms of the period, we derive the expression $\lambda = (TD/2\pi)^{1/2}$ (Section 3.2.1). Consequently, an increase in the period T causes the increase in λ , thereby amplifying the diffusion of the pressure wave's amplitude. Therefore, when comparing different applications, short-period (or high-frequency) waves have a similar effect to fast pumping tests affecting a small portion of the aquifer, while long-period (or low-frequency) waves allow to characterize larger areas of the aquifer (Alcaraz et al., 2021). Accordingly, adopting a seasonal period, as in the case of energy storage (Lysyy et al. 2021) facilitates the diffusion of the pressure wave over kilometer-scale distances. Concerning the CO₂ Long-term Periodic Injection Experiment (CO₂LPIE), the optimal period remains a subject of ongoing discussion, spanning from daily to weekly scales, also being mindful of the relevant periods of the earth tides. For example, focusing on the representative radial diffusion A_R (Section 3.2.5), this translates to an attenuation ranging from 0.008% for $T = 1$ day to 1.65% for $T = 1$ week at a distance of 0.3 m. This phenomenon has motivated the increase in period, rather than elevation of the initial amplitude, particularly in laboratory settings where downstream wave pressure measurements may fall below the transducer resolution (Faulkner

and Rutter, 2000). Nonetheless, it is crucial to carry out an adequate number of cycles in order to accurately distinguish the influence of periodic injections at the measurement locations and allow for stacking analysis of small response signals. For instance, in the CO₂CRC Otway field test, only three temporal cycles of pore pressure change were introduced, which proved to be insufficient to isolate their effects from other contributing factors (Ennis-King et al., 2017).

In the context of enhanced geothermal systems stimulation, the implementation of cyclic stimulation has emerged as a potential strategy to mitigate the risks associated with induced seismicity (Zang et al. 2013; 2019). For this reason, Hofmann et al. (2018) introduced an injection protocol comprising distinct cycles characterized by varying time scales: short-term cycles with periods on the order of minutes or less, medium-term cycles lasting for hours, and long-term cycles spanning a few days or weeks. The ultimate signal becomes a combination of these distinct time-scale cycles. By considering representative periods of 6 minutes, 1 hour, and 1 day — similar to the Pohang enhanced geothermal system site in South Korea (Hofmann et al., 2019), the attenuation A_R obtained at a distance of 1 m equals to $6 \cdot 10^{-9}\%$, 0.02%, and 7%, respectively. This outcome underscores the effectiveness of cyclic or soft stimulation to reduce the risk of induced seismicity because the amplitude vanishes within a few centimeters for periods in the order of minutes (as done in Pohang). This rapid attenuation of the periodic signal impedes the progressive degradation of fracture strength that is sought with this stimulation to reduce induced seismicity. Thus, the pressure perturbation in tight, stiff crystalline rock is very similar to constant pressure or periodic pressure injection with periods on the order of minutes.

3.5.4. Accuracy of analytical models and contribution of the reservoir deformation

The expansion (or compaction) of a rock caused by fluid injection/extraction can induce notable alterations in its storage behavior. As the rock undergoes expansion, there is a potential for pore spaces to open up, leading to increased effective porosity. This, in turn, can improve fluid flow pathways, ultimately enhancing the effective permeability and thus the rock transmissivity. Additionally, expansion increases the storativity by providing additional storage volume as the pore space expands. These effects are contingent on multiple factors, including the geological attributes of the rock, the characteristics of the fluids being injected or extracted, the rate of deformation, and the boundary conditions (Bear, 2013). In particular, hydro-mechanical coupling becomes critically important in low-permeability rocks, like shales and crystalline basements, through changing their storage behavior (De Simone and Carrera, 2017). This statement is in line with the results obtained in this study, showing that the coupled hydro-mechanical effects on pressure amplitude attenuation, i.e., $A_{HM} - A_H$, during CO₂ injection in underground rock laboratory and enhanced geothermal systems stimulation are twice as large as that calculated for energy storage applications in permeable rock (insets in Figure 3.4 and Figure 3.5).

3.5.5. Applications of the methods to support design and monitoring stages

We consider the application of the methodologies presented in this study in two ways: "direct" and "indirect" (Figure 3.8). The direct utilization of the equations is principally subject to an initial estimation of material properties to calculate the diffusivity D and design the input signal characteristics, including the period T . After selecting a suitable solution for the specific application, it is possible to project the signal attenuation at varying distances from the source. In the context of the indirect application of the equations, the focus shifts to employing monitoring data, including the amplitude at distance ($p(x)$ or $p(r)$), to infer the properties of the

rock mass between the source and the monitoring devices, which can be the injection/production well and the monitoring well, respectively (Figure 3.8). If the theories are employed to interpret signals originating from passive sources, as in the case of natural Earth tides, or those generated in laboratory setups featuring finite specimen lengths, additional parameters may be needed to interpret the propagating pressure waves. The former requires knowledge of the source amplitude, phase, loading efficiency, and location (Merritt, 2004; Alcaraz et al., 2021). For the latter, solutions rely on the storage behavior of the injection setups (Hsieh et al., 1981). As the need to know such parameters in purposefully-designed injections at field scales is eliminated, the focus can be directed toward in-situ characterization of the rock layers.

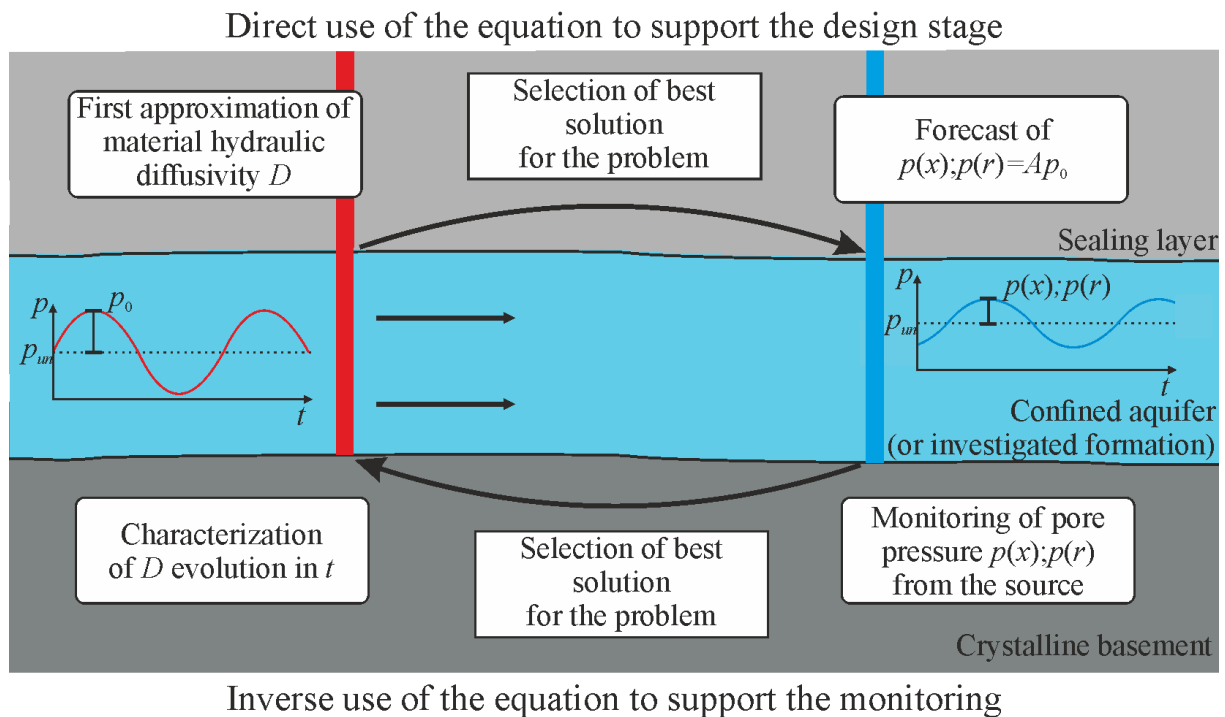


Figure 3.8. Description of “direct” and “indirect” use of the methods described in this article.

The obtained results show that the proper selection of a suitable and physically grounded model, within realistic boundary conditions, is of paramount importance for both direct and indirect applications (Figure 3.8). Generally, during the design phase, numerical models hold greater relevance due to their capacity to replicate system deformations without temporal constraints for solution attainment. In contrast, the adoption of analytical solutions finds greater utility in aiding the monitoring stage for continuous characterization purposes. For example, in the case of CO₂LPIE, in which CO₂ dissolves into the water, reducing its pH and, as a result, causing mineral dissolution that enhances porosity and permeability and lowers stiffness, diffusivity continuously evolves and the monitoring of the periodic signal can provide valuable information on how CO₂ injection affects rock properties with time. These solutions provide a rapid understanding, albeit approximate, of reservoir behavior evolution, facilitating quick insights into system dynamics, particularly when computational speed is a crucial factor.

3.6. Conclusions

In this study, we have investigated the feasibility of rock characterization through diverse analytical and numerical solutions for the interpretation of periodic pressure signals, employing both one-dimensional and cylindrical two-dimensional geometries. This investigation covers substantial rock dimensions, ranging from kilometers for energy storage scenarios to approximately half a meter for CO₂ Long-term Injection Experiment (CO₂LPIE), and a few meters for enhanced geothermal systems stimulation.

For any application, it is crucial to acknowledge that assuming the uncoupling of pore pressures and stress variations in the rock introduces an element of error that warrants analysis. Our findings reveal that the relative error between the uncoupled problem and a simplified geometry is less than 3% for one-dimensional diffusion and less than 1.4% for radial diffusion. However, it is essential to recognize that more complex in-situ scenarios, including geological inhomogeneity, hydraulic barriers, and potential leakage sources, may introduce even more substantial errors that require careful examination for each specific case.

While hydro-mechanical numerical solutions account for multidimensional aquifer deformations, analytical solutions provide an immediate initial approximation of the problem, facilitating a better understanding of reservoir behavior evolution. This enables time prompt reaction to potentially unexpected events, safeguarding the integrity of the project.

Chapter 4

Hydro-Mechanical response of Opalinus Clay in the CO₂ long-term periodic injection experiment (CO₂LPIE) at the Mont Terri rock laboratory

4.1. Introduction

Effective scenarios to mitigate climate change should target rapid global decarbonization and net withdrawal of CO₂ from the atmosphere (IPCC, 2014; Warszawski et al., 2021). A feasible and credible solution to substantially reducing anthropogenic CO₂ emissions and achieving carbon neutrality is Carbon Capture and Storage (CCS) in geological formations at the gigaton scale (Bui et al., 2018; Ringrose et al., 2021). The best-practice guidelines suggest injecting CO₂ at depths greater than 800 m to ensure that it stays in the supercritical state (IEA GHG, 2009; Miocic et al., 2016). Relatively high density of supercritical CO₂ increases the subsurface storage capacity and alleviates buoyancy forces driving upward migration of CO₂ (Bachu, 2003). However, CO₂ is still buoyant at temperature (> 31 °C) and pressure (> 7.38 MPa) conditions of sedimentary basins considered for CCS, raising concerns about potential leakage to shallow groundwater aquifers or even back to the surface and into the atmosphere. As a result, large-scale deployment of CCS and long-term CO₂ containment in the subsurface relies primarily on competent caprock formations hindering upward CO₂ migration out of the reservoir complex.

Over three decades of research and practice in geologic carbon storage provide invaluable insights into the Hydro-Mechanical (HM) behavior of the caprock controlling the long-term fate of injected CO₂. Much can be learned from laboratory experiments, numerical simulations, and monitoring of CO₂ storage sites or naturally occurring reservoirs. Breakthrough experiments have provided a reliable measure of capillary properties for intact caprock samples under representative subsurface conditions (Hildenbrand et al., 2002; Boulin et al., 2013; Makhnenko et al., 2017; Minardi et al., 2021). These experiments render high capillary entry pressures in the order of several MPa for shaly caprocks, making these formations appropriate to act as a seal for CO₂ storage. However, injection-induced overpressure and potential CO₂ intrusion into the caprock may lead to pore system expansion and caprock damage that could potentially deteriorate the caprock sealing capacity (Rutqvist, 2012; Vilarrasa et al., 2015). In particular, the pressure-induced expansion of the lowermost portion of the caprock at the In Salah storage site had a significant contribution to the measured surface uplift (Rutqvist et al., 2010). More importantly, expansion causes an increase in porosity, which may significantly enhance permeability even for small porosity increments because the permeability-porosity relationship for caprock can take a power-law form with exponents in the range of 15 to 17 (Kim and Makhnenko, 2020). At the same time, simulation results of lab- and field-scale CO₂ injections indicate that CO₂ may penetrate into the caprock in the range from a few centimeters to meters (Rutqvist et al., 2008; Vilarrasa et al., 2010b; Kivi et al., 2022).

Laboratory experiments on centimeter-scale caprock specimens provide key insights into relevant HM processes and are necessary for initializing numerical simulations, but can hardly deal with field-scale complexities. Heterogeneities on varying scales, starting from pores and microfractures to bedding planes and fault zones that are several meters thick, can be present in the caprock and may provide preferential flow paths as well as localized deformations

(Rutqvist and Tsang, 2002; Rutqvist et al., 2016). For example, the fast vertical migration of the CO₂ plume across the thin mudstone layers in the Sleipner storage site is analyzed to be indicative of pervasive fracturing with effective capillary entry pressures 35 times smaller than those measured in the laboratory on intact shale specimens (Cavanagh and Haszeldine 2014). Plausible alterations of the rock microstructure and water content over the course of coring and sample preservations, as well as the inability to reproduce the subsurface temperature and stresses in the laboratory, raise questions about the full representativeness of the laboratory experiments and inferred conclusions (Vilarrasa et al., 2017). Therefore, growing efforts are devoted to developing and exploiting precise techniques of monitoring CO₂ injection projects. Previous monitoring efforts primarily targeted the CO₂ plume migration (Arts et al., 2004), pressure changes in the overlying aquifers (Kim and Hosseini, 2014), induced seismicity (Verdon et al., 2011) and surface uplift (Ringrose et al., 2013) to demonstrate secure storage of CO₂ with minimum detrimental environmental impacts.

Field-scale CO₂ injection poses challenges in monitoring at increasing depths, as well as in the interpretation of the ongoing processes. To address these challenges, controlled underground rock-laboratory experiments at meter to decameter scale have drawn special attention to fill the gap between the core scale (cm) and industrial-scale (km) observations (Bossart et al., 2018). These experiments take advantage of realistic conditions of the subsurface, thoroughly characterized geological settings, controlled injection conditions, and detailed and comprehensive monitoring in the proximity of the injection zone. The meso-scale experiments can be useful to bring the knowledge of CO₂ leakage mechanisms into maturity, improve simulation models, develop and examine innovative monitoring approaches, and establish strategies and protocols to ensure long-term caprock integrity.

The CO₂ Long-term Periodic Injection Experiment (CO₂LPIE) aims at investigating the sealing capacity of a caprock in response to direct CO₂ injection at the decameter scale (Rebscher et al., 2020). CO₂LPIE will be carried out in a highly monitored environment in the Mont Terri Underground rock laboratory, Switzerland (Figure 4.1). The host rock for CO₂LPIE is Opalinus Clay, a claystone with high capillary entry pressure and low permeability, considered to be a good representative caprock for CO₂ storage (Bossart et al., 2018; Vilarrasa and Makhnenko, 2017; Minardi et al., 2021; Zappone et al., 2021). At an appropriate distance from the injection point, observation boreholes will be drilled and instrumented with high-resolution pressure transducers and deformation sensors. This setting allows continuous monitoring of pressure changes and rock deformation, as well as geochemical sampling while recording the injection flow rate and fluid pressure. Given the low intrinsic permeability of the shale, optimizing the injection scheme and accurately locating the monitoring boreholes become a priority. An effective recording of the rock response should be guaranteed, while obeying the constraints given by (a) the extension of the zone disturbed by the drilling process and (b) the need to prevent a hydraulic connection between boreholes.

The main objective of this study is to assist in designing CO₂LPIE in the light of preliminary numerical modeling of the involved HM processes. We first present a brief description of the Mont Terri rock laboratory, the geological structures, and the CO₂LPIE experimental setting. We then focus on 2D fully coupled HM numerical simulations. In addition, we describe the relevant governing equations, the model geometry, initial and boundary conditions, and material properties. Next, we describe the performed sensitivity analyses, including variations of the amplitude of the periodic injection and rock properties. Here, results on the pore pressure development and stress perturbations due to CO₂ injection in different scenarios are of special interest. Finally, we discuss the inferred HM behavior and how it helps with the design of the CO₂ injection scheme and the monitoring program.

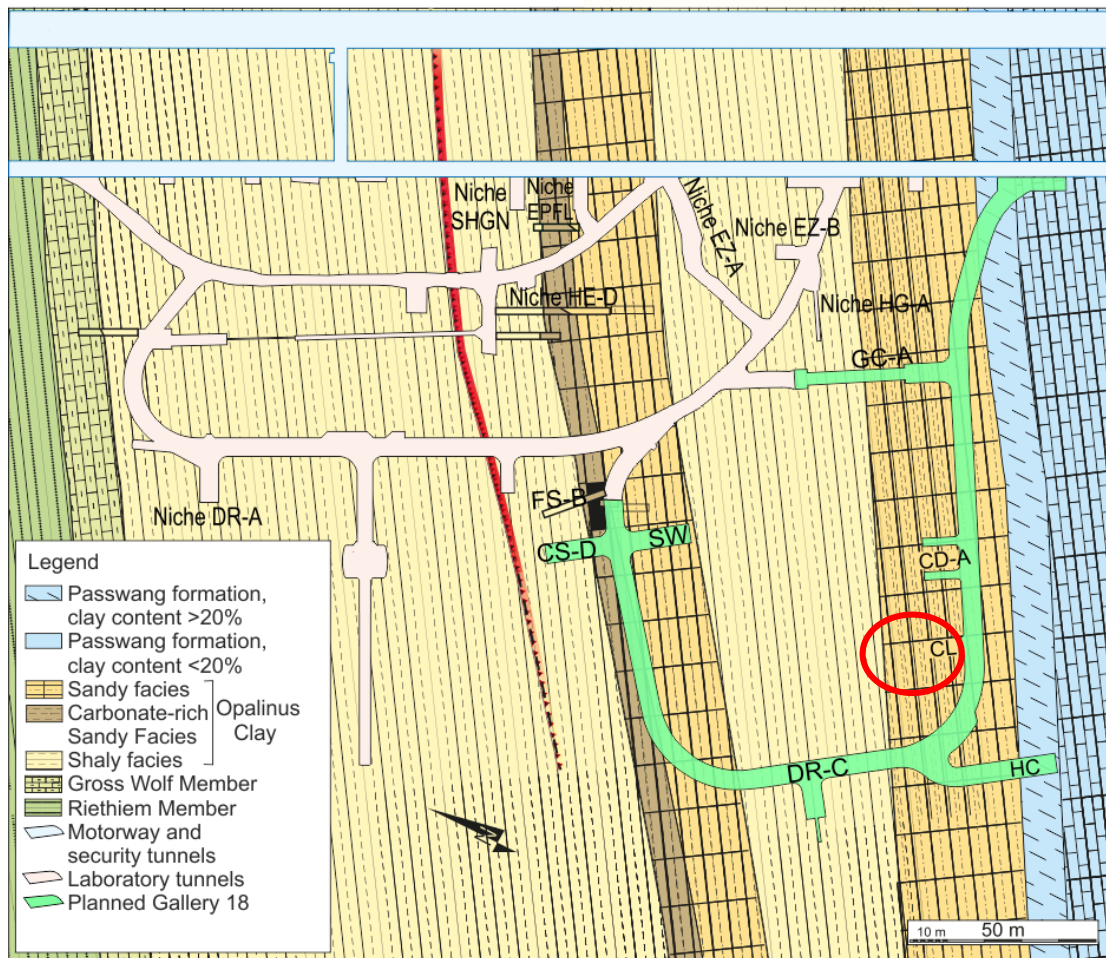


Figure 4.1. Schematic representation of the geological setting and location of the CO₂LPIE experiment (CL niche) at the Mont Terri rock laboratory. The new tunnels and niches are highlighted in green.

4.2. Overview of the Mont Terri rock laboratory and the CO₂LPIE experiment

The Mont Terri rock laboratory is located near St. Ursanne, in the North-West of Switzerland, and is operated by the Swiss Federal Office of Topography, swisstopo. The rock laboratory is nested at approximately 280 m below the Earth's surface and is accessible through the safety gallery of a nearby motorway tunnel, passing through the Jura Mountains (Figure 4.1). It has experienced a quarter-century period of development and constitutes an international and unified platform for cutting-edge research in the field of underground storage and waste disposal (see Bossart et al., 2018 for a review). The rock laboratory is excavated in the Aalenian-Toarcian age Opalinus Clay, deposited around 174 million years ago (Nussbaum et al., 2011). Owing to its ultralow permeability, Opalinus Clay has been primarily investigated as a potential repository host rock for nuclear waste and, more recently, as a representative caprock for geologic CO₂ storage. In this context, a variety of experiments were performed, concentrating, for example, on Thermo-Hydro-Mechanical (THM) behavior of Opalinus Clay (HE, Heating Experiment, Bossart et al., 2017), seasonally-induced HM processes (CD, Cyclic Deformation experiment, Ziefle et al., 2017), diffusion and sorption processes (DI, In Situ Diffusion, DR,

Diffusion and Retention, and FM-C, Flow Mechanism experiments, Leupin et al., 2018), the CO₂ sealing capacity of a clayey fault (CS-D, Carbon Storage experiment, Zappone et al., 2021) and fluid injection-induced earthquake rupture and fault reactivation (FS, Fault Slip experiments, Guglielmi et al., 2020a).

The CO₂LPIE experiment plans to inject CO₂ in pristine Opalinus Clay at the Mont Terri rock laboratory in a long-term (> 10 years) periodic fashion. CO₂LPIE is targeted at exploring the following:

1. the effective hydraulic and mechanical properties of the seal at the rock mass scale;
2. the effect of the cyclic injection scheme on the transient pore pressure evolution and rock deformation;
3. the extent to which CO₂ can penetrate into the intact caprock;
4. the Hydro-Mechanical-Chemical (HMC) processes governing CO₂ intrusion into and transport through caprock; and
5. potential alterations of the rock hydraulic and mechanical behavior in response to pressurization and chemical fluid-rock interactions.

CO₂LPIE will be carried out in the CL niche, oriented perpendicular to the minimum horizontal stress direction and the new Gallery 18. Here, the bedding planes dip 45° towards the SSE. CO₂LPIE will be performed through an inclined injection borehole, drilled from the sidewall of the niche with a diameter of 0.086 m and a length of about 10 m perpendicular to the local bedding planes (Figure 4.2). The plan is to inject CO₂ at a 0.2 m long segment at the lowermost portion of the borehole and far away from the excavation damage zone that extends to 1-2 m from the niche's wall (Bossart et al., 2002). As a consequence, we assume that the host rock is intact and fully saturated having negligible pore pressure and stress perturbations. The stress regime is estimated to be normal faulting, meaning that the maximum principal stress $\sigma_1 \approx 6.5$ MPa is close to vertical and roughly conformed to the overburden weight. The intermediate and minimum principal stresses are sub-horizontal with the values of $\sigma_2 \approx 4.0$ MPa and $\sigma_3 \approx 2.2$ MPa, respectively (Martin and Lanyon, 2003; Corkum, 2006).

Multiparameter monitoring will be performed using high-resolution sensors installed in both the injection borehole and adjacent observation boreholes. Injection pressure and flow rate will be recorded together with the induced rock deformation, perturbed pore pressure, and geochemical parameters of interest. Rock samples will be retrieved for complementary laboratory investigations. The laboratory tests will allow understanding possible fluid-rock chemical interactions and their impacts on the hydraulic and mechanical properties of the rock, to develop and calibrate constitutive models, and to assist in more efficient interpretation of the recorded data. Nevertheless, the design phase of CO₂LPIE also reaps the benefits of interpretative modeling for the best adjustment of the injection parameters and the monitoring setup. The model inception task is integrated with preliminary laboratory measurements of rock properties, which will be addressed in this paper with a primary focus on the governing HM processes. The main advantages of such a multidisciplinary elucidation of the recorded data are: (1) more realistic treatment of the caprock with CO₂ injection, advancing our knowledge of the underlying chemical and HM effects and (2) improved prediction capabilities of numerical models for field- and basin-scale CCS projects.

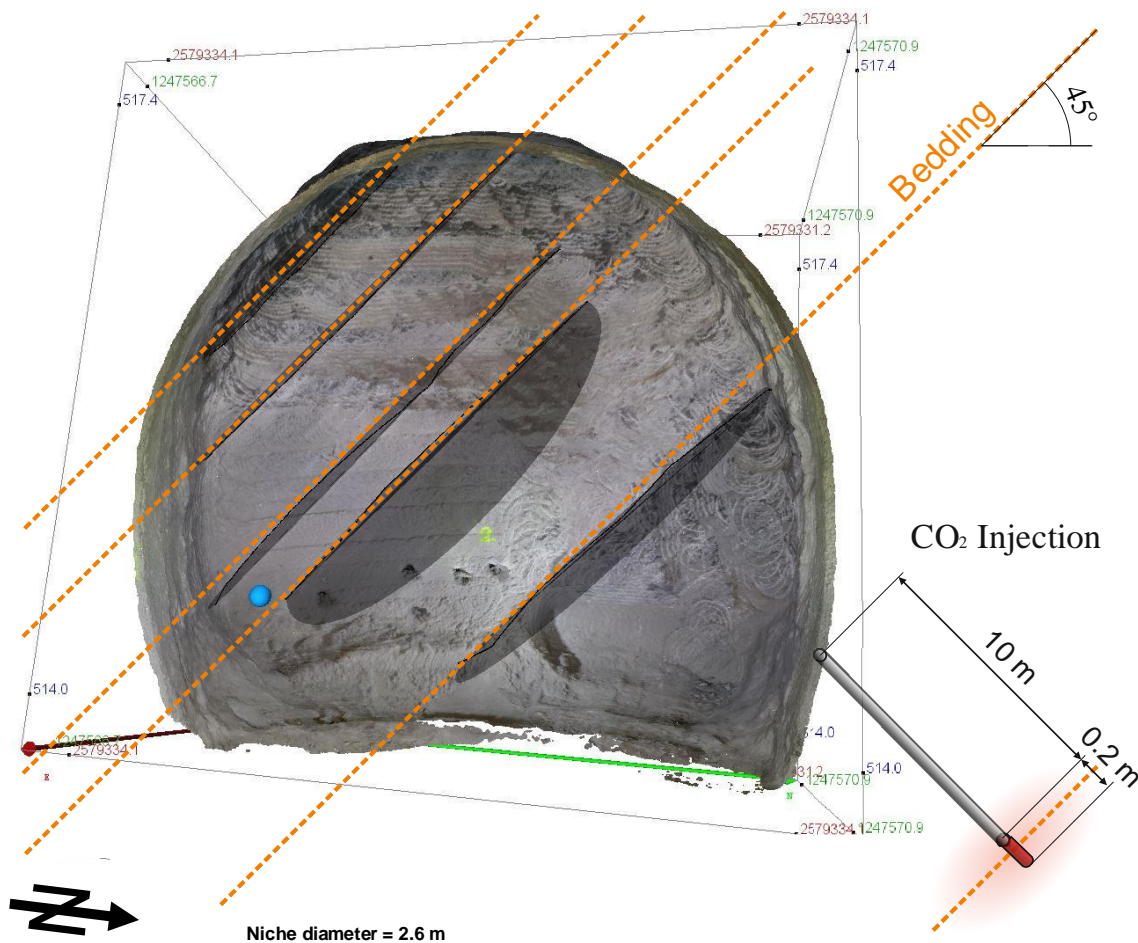


Figure 4.2. Photo of the excavation front with the inclination of the bedding planes (orange dashed lines) and a schematic drawing of the injection well proposed for the CO₂LPIE experiment (not to scale). The drilled well will be perpendicular to the bedding planes, with an injection interval of about 0.2 m at about 10 m depth (geology and stratigraphy modified from Jaeggi et al., 2020).

4.3. Methodology

4.3.1. Description of the Hydro-Mechanical model

We simulate the HM response of Opalinus Clay to CO₂ injection using the finite element code CODE_BRIGHT (Olivella et al., 1994; 1996), which allows for solving a wide range of THM problems in porous media, including CO₂ storage in deep geological formations (Villarrasa et al., 2010b). CO₂ injection into the brine-saturated rock induces a two-phase flow of brine and CO₂ as the wetting and non-wetting phases, respectively. Besides, CO₂ partially dissolves into water, initiating diffusive transport of dissolved CO₂ species in the brine phase. In order to simulate the coupled rock deformation and flow phenomena, the code simultaneously solves the mass conservation equation for the present components (here CO₂ and water) and the momentum balance. The mass balance equation for each component writes as

$$\frac{\partial}{\partial t} (\omega_l^i \rho_l^i S_l \phi + \omega_g^i \rho_g^i S_g \phi) + \nabla \cdot (\mathbf{i}_l^i + \mathbf{i}_g^i + \omega_l^i \rho_l^i \mathbf{q}_l + \omega_g^i \rho_g^i \mathbf{q}_g) = f^i, \quad i = c, w; \quad (4.1)$$

where the first term on the left-hand side renders the storage, which depends on the rock porosity ϕ [-], density ρ_ψ [ML^{-3}], the mass fraction ω_p^i [-] of component i (c for CO_2 and w for water) in each phase, and saturation S_ψ [-] of ψ phase. Here, ψ can be either l or g for the liquid and gas phases, respectively. The second term on the left-hand side denotes the conceivable flow mechanisms involving advective phase flux \mathbf{q} [LT^{-1}] and diffusive flux of individual components \mathbf{i} [$\text{ML}^{-2}\text{T}^{-1}$]. The right-hand side f^i accounts for an external source or sink of component i . The volumetric flow rate of the ψ phase is related to the existing pressure gradient and gravity, reading from Darcy's law as

$$\mathbf{q}_\psi = -\frac{\mathbf{k}k_{r\psi}}{\mu_\psi} (\nabla p_\psi + \rho_\psi g \nabla z), \quad \psi = l, g; \quad (4.2)$$

where \mathbf{k} [L^2] is the anisotropic intrinsic permeability tensor accounting for preferential flow paths along bedding planes, ρ_ψ [$\text{ML}^{-2}\text{T}^{-1}$] is the ψ -phase pressure, $k_{r\psi}$ [-] and μ_ψ [$\text{ML}^{-1}\text{T}^{-1}$] represent the relative permeability and dynamic viscosity of the fluid phase ψ , respectively, g [LT^{-2}] is the gravity acceleration, and z [L] is the elevation.

The molecular diffusion of the dissolved species is governed by Fick's law

$$\mathbf{i}_\psi^i = -\tau \phi \rho_\psi S_\psi D_\psi^i \nabla \omega_\psi^i; \quad (4.3)$$

where τ expresses the pore network tortuosity and D_ψ^i [L^2T^{-1}] the diffusion coefficient of component i in phase ψ . The product of tortuosity and diffusion coefficient represents the effective diffusion coefficient D of each component across the pore network. In our numerical simulations, we neglect diffusive transport of water vapor in the CO_2 phase, i.e., $\mathbf{i}_w^g = 0$.

The numerical model satisfies the linear momentum balance for the porous medium, which writes as

$$\nabla \cdot \boldsymbol{\sigma} + \mathbf{b} = 0; \quad (4.4)$$

where $\boldsymbol{\sigma}$ [$\text{ML}^{-1}\text{T}^{-2}$] is the total stress tensor and \mathbf{b} [$\text{ML}^{-2}\text{T}^{-2}$] the vector of the body forces. The constitutive behavior of the porous rock is established using linear poroelasticity (Cheng, 2016)

$$\boldsymbol{\sigma} = \mathbf{C}\boldsymbol{\varepsilon} + \boldsymbol{\alpha}p; \quad (4.5)$$

where $\boldsymbol{\varepsilon}$ [-] is the strain tensor, and p [$\text{ML}^{-1}\text{T}^{-2}$] is the pore pressure set as $p = \max(p_l, p_g)$. The elastic modulus tensor \mathbf{C} [$\text{ML}^{-1}\text{T}^{-2}$] defines the relation between effective stress $\boldsymbol{\sigma}' = \boldsymbol{\sigma} - \boldsymbol{\alpha}p$ and the strain tensor. $\boldsymbol{\alpha}$ [-] represents the Biot effective stress coefficient tensor, assumed to be isotropic ($\boldsymbol{\alpha} = \alpha \mathbf{I}$), with a value of scalar α , and \mathbf{I} the identity tensor. Following the transversely isotropic model defined by Cheng (1997), the elastic tensor is assumed to replicate the mechanical behavior of the host rock with bedding planes. Therefore, five elastic moduli are required to define the material model. Considering the generic plane $x'z'$ aligned parallel to the bedding planes and y' -direction perpendicular to them (see Figure 4.3), the elasticity tensor entries are expressed by the Young's moduli $E_{x'} = E_{z'} = E_p$, $E_{y'} = E_n$; the Poisson's ratios $\nu_{x'} = \nu_{z'} = \nu_p$, $\nu_{y'} = \nu_n$; and the shear modulus $G_{y'} = G_n$; where the subscripts "p" and "n" imply the directions parallel and normal to the bedding planes, respectively. Accordingly, the behavior of the rock mass is simulated as an anisotropic poroelastic continuum, without defining the precise geometry of the discontinuities, but using enriched constitutive models that consider the bedding plane dip angle.

We adopt the sign convention of geomechanics for stress and strain components throughout the paper, i.e., compression and compaction are positive. Finally, we present the stress evolution and stability analysis of the host rock in terms of total mean stress $\sigma_m = (\sigma_1 + \sigma_2 + \sigma_3)/3$; effective mean stress $\sigma_m' = \sigma_m - \alpha p$ and deviatoric stress $\mathbf{q} = [(\sigma_1 - \sigma_2)^2 + (\sigma_2 - \sigma_3)^2 + (\sigma_1 - \sigma_3)^2]^{1/2} / (2)^{1/2}$ where σ_1 , σ_2 , and σ_3 are principal stress components.

Given appropriate initial and boundary conditions, CODE_BRIGHT solves the formulation introduced in Equations (4.1) to (4.5) to determine primary unknowns: liquid and gas pressures and the displacement vector. The advective flow rate, diffusive flux and the stress tensor are then evaluated, respectively, from Equations (4.2), (4.3), and (4.5).

4.3.2. Geometry and model setup

We build a 2D plane strain model that reproduces a vertical cross-section of intact Opalinus Clay intersecting the injection borehole (Figure 4.3). The model geometry extends 10 m on each side of the injection borehole in horizontal and vertical directions, indicated as x and y , respectively, to avoid boundary effects. The bedding planes are inclined 45° from the x direction.

We hypothesize a horizontal injection well with a diameter of 0.086 m and a length of 0.2 m. Since the considered injection segment is substantially smaller than the model dimension, it resembles a point-like injection scheme. Thus, the borehole inclination plays a minor role from the perspective of simulation accuracy. To facilitate meshing, we adopt a horizontal borehole, which permits refinement around it while retaining the computational cost for a long-term simulation at an acceptable level. We discretize the model with a structured quadrilateral mesh consisting of 2560 elements. The mesh size progressively increases from 2 mm by 2 mm in the vicinity of the borehole up to 2.5 m by 2.5 m at the model boundaries. The refined mesh close to the injection segment allows accurate tracking of CO₂ intrusion into Opalinus Clay and the subsequent two-phase flow.

The vertical and minimum horizontal stresses coincide with the y and x directions, respectively (Figure 4.3). We impose $\sigma_1 = \sigma_y = 6.5$ MPa and $\sigma_3 = \sigma_x = 2.2$ MPa at the borehole level. The vertical stress varies with depth with a lithostatic stress gradient of 25 kPa/m, corresponding to the mean bulk density of the overlying layers of approximately 2500 kg/m³. The minimum horizontal stress distribution consistently follows the stress ratio $\sigma_x/\sigma_y = 0.34$ across the domain. We set a pore pressure gradient of 10 kPa/m, with an initial fluid pressure of 2 MPa at the depth of injection. We neglect thermal effects and consider a constant and uniform temperature of 14 °C.

We apply sinusoidal oscillations of the CO₂ pressure in the borehole at a mean pressure of 3 MPa, implying CO₂ injection occurs in a gas phase. The CO₂ pressure fluctuates in our reference model with an amplitude of $A_1 = 0.5$ MPa and a period of $T_0 = \pi/2$ d (~ 1.57 d). We perform a sensitivity analysis to examine the potential impact of the injection pressure amplitude on the HM response of the shale. To this end, we take into account two other injection scenarios: one with an amplitude lower by a factor of 2 and another one with an amplitude larger by a factor of 2 compared to the reference case, i.e., $A_2 = 0.25$ MPa and $A_3 = 1.0$ MPa. In all simulations, we impose a constant vertical stress of 6.25 MPa at the top boundary and restrict any deformation perpendicular to the bottom and lateral boundaries. The hydraulic boundary conditions account for constant pressures of 1.9 MPa at the top and 2.1 MPa at the bottom boundaries and no-flow constraints on the lateral ones. We begin the simulation with an equilibration phase after imposing the initial and boundary conditions for fluid pressure and stress fields in accordance with in-situ measurements at the Mont Terri rock laboratory (Martin and Lanyon, 2003; Corkum, 2006).

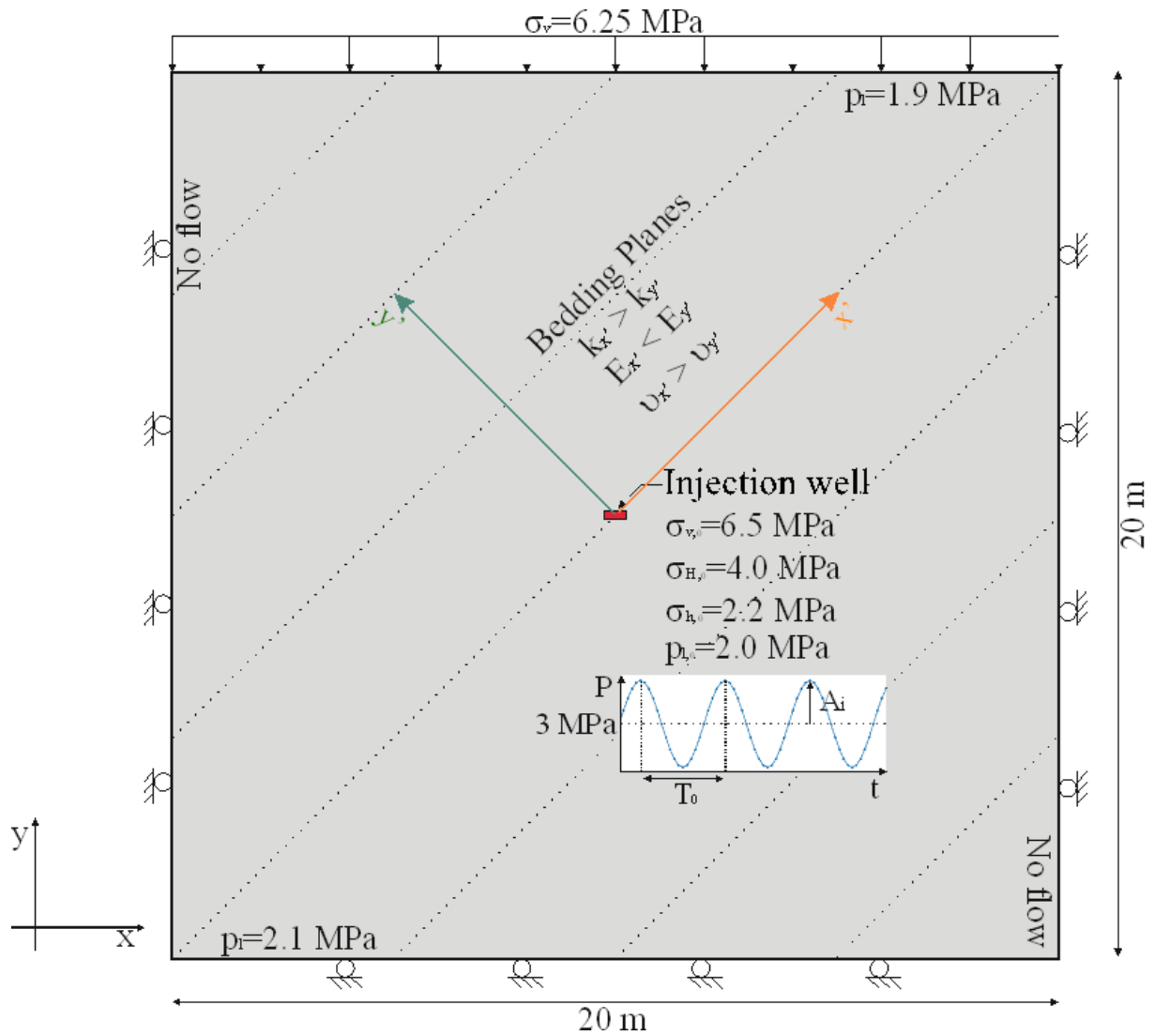


Figure 4.3. Schematic view of the numerical model setting for CO₂LPIE, including the model geometry and boundary conditions. The injection segment of the borehole is illustrated in red. The results are plotted along the x' and y' directions, representing the directions parallel and perpendicular to the bedding planes, respectively. Dotted lines schematically show the bedding plane directions.

4.3.3. Model parameters

The properties of Opalinus Clay used in our simulations are provided in Table 4.1. We define the orthotropic behavior of the shale using laboratory measurements performed by Makhnenko et al. (2017) and Makhnenko and Podladchikov (2018). An anisotropic intrinsic permeability tensor is used with $2.4 \cdot 10^{-20} \text{ m}^2$ and $0.8 \cdot 10^{-20} \text{ m}^2$ for the parallel- and normal-to-the-bedding directions, respectively (Marschall et al., 2004; Makhnenko et al., 2017). We assume that other hydraulic properties of the rock are isotropic. The relative permeability curves to both CO₂ and brine phases are assumed to follow power-law functions of the brine saturation with a high exponent of 6 (Bennion and Bachu, 2008; Kivi et al., 2022). The Biot coefficient anisotropy is estimated to be 5% and, therefore, is neglected, and the isotropic value of $\alpha = 0.76$ reported for the initial in-situ conditions for CO₂LPIE is adopted (Makhnenko and Podladchikov, 2018).

Stress dependence of hydraulic and poromechanical properties of Opalinus Clay is not considered in the simulation of the pressure oscillations during periodic injections.

Mercury intrusion porosimetry provides essential information on the rock pore structure (Kuila and Prasad, 2013). Application of this technique yields an interconnected rock porosity of 0.125 and a dominant pore throat size of 15 nm for Opalinus Clay. Based on estimates of the capillary pressure curve, we convert the measurements from the gaseous-liquid mercury to CO₂-brine capillary system using suitable interfacial properties. Given the average pressure and temperature of CO₂LPIE, a CO₂-brine interfacial tension of 50 mN/m is employed (Kvamme et al., 2007) and the contact angle on the mineral surface is set equal to 40° (Espinoza and Santamarina, 2017). We fit the capillary pressure curves with the van Genuchten model (van Genuchten, 1980)

$$S_{el} = \frac{S_l - S_{rl}}{S_{max,l} - S_{rl}} = \left[1 + \left(\frac{P_{cap}}{p_0} \right)^{1/(1-m)} \right]^{-m}; \quad (4.6)$$

where p_0 [ML⁻¹T⁻²] and m [-] are the gas entry pressure and shape parameter, respectively. S_{el} is the effective liquid saturation, normalizing the liquid phase saturation in its varying range from an irreducible saturation of S_{rl} to a maximum value of $S_{max,l}$. Assuming a high irreducible brine saturation of $S_{rl} = 0.5$ for the shale, we approximate the best-fit van Genuchten parameters to be $p_0 = 5$ MPa and $m = 0.7$. This model reproduces the capillary retention behavior of intact Opalinus Clay. Accounting for the effect of plausible rock heterogeneities at the URL scale, e.g., preferential entry pores for CO₂, we examine the sensitivity of the system response by assuming different hydraulic properties of the host rock. For this purpose, we perform additional simulations by enhancing the permeability by two orders of magnitude, while at the same time, reducing the capillary entry pressure by a factor of 10.

In accordance with Henry's law, the CO₂ solubility in water is linearly correlated with the CO₂ partial pressure. The Henry's law constant is picked at the temperature and pressure range of the in situ experiment (Spycher et al., 2003). We neglect the effect of pore network tortuosity on the diffusive flux of aqueous CO₂ and assume an effective diffusion coefficient of $1.6 \cdot 10^{-9}$ m²s⁻¹ that lies within the experimentally measured values for CO₂ diffusion in water (Tewes and Boury, 2005).

Table 4.1. Material properties used in the HM model.

Property	Unit	Value
Shear modulus along the bedding, G_p	GPa	0.63
Young's modulus along the bedding, E_p	GPa	1.7
Young's modulus perpendicular to bedding, E_n	GPa	2.1
Poisson's ratio along the bedding, ν_p	-	0.35
Poisson's ratio perpendicular to bedding, ν_n	-	0.32
Biot coefficient, α	-	0.76
Permeability along the bedding, k_p	m ²	$2.4 \cdot 10^{-20}$
Permeability perpendicular to bedding, k_n	m ²	$0.8 \cdot 10^{-20}$
Relative water permeability, k_{rw}	-	$(S_{el})^6$
Relative CO ₂ permeability, k_{rc}	-	$(1-S_{el})^6$
Porosity, ϕ	-	0.125
van Genuchten entry pressure, p_0	MPa	5
van Genuchten shape parameter, m	-	0.7

4.4. Results

4.4.1. Reference case with amplitude $A_I = 0.5$ MPa

The applied cyclic CO₂ injection generates a slight brine overpressure that propagates into the caprock formation (Figure 4.4a). The calculated liquid pressure distribution is distorted by the hydraulic anisotropy, advancing further along the bedding planes due to the fact that here the permeability is three times higher than the one normal to the bedding planes (Figure 4.4a). The imposed gas pressure, which changes between 2.5 MPa and 3.5 MPa, creates a brine overpressure that approaches 0.5 MPa around the borehole. Correspondingly, the capillary pressure (i.e., the difference between gas and brine pressures) does not build up to drive a meaningful desaturation and the free-phase CO₂ can only penetrate a few millimeters into Opalinus Clay. As a result, CO₂ flow appears to be controlled by molecular diffusion rather than advection. Additionally, although at negligible rates, the advecting brine promotes the spread of the dissolved CO₂ species (black dashed line in Figure 4.4a). The diffusion-dominated CO₂ front expands isotropically because it is not affected by the preferential flow path along the bedding planes (black dashed line in Figure 4.4a). It is noteworthy that gas transport has been the focus of various ongoing experiments conducted by the Mont Terri Consortium (see, e.g., Leupin et al., 2018; Heberling et al., 2022; Wüst et al., 2022)

The pore pressure buildup decreases the effective mean stress and, consequently, causes the rock to volumetrically expand (Figure 4.4c). The expanded region is correlated with the pressurized area and, thus, propagates further away along the bedding planes. The poroelastic coupling perturbs the initial state of stress and induces compressive stresses, with an increase in the total mean stress of 0.3 MPa close to the injector (Figure 4.4b). Similar to pore pressure propagation, the total mean stress and deviatoric stress are elongated along the bedding planes (Figure 4.4b and d).

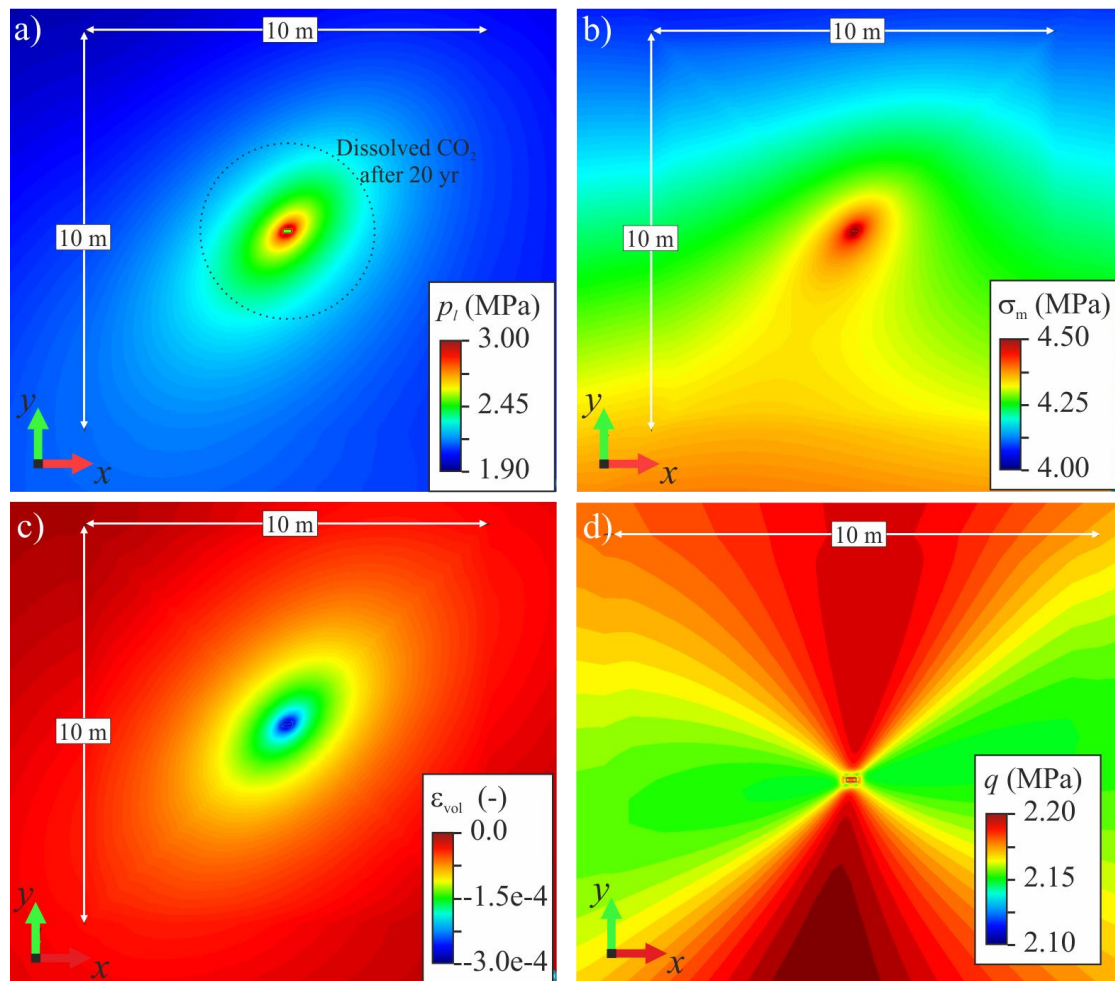


Figure 4.4. Spatial distribution after 20 years of cyclic CO₂ injection of (a) liquid pressure and advance of the front of dissolved CO₂, using as threshold concentration twice as large as the initial value after 20 years of CO₂ injection; (b) total mean stress (c) volumetric strain; and (d) deviatoric stress.

The applied periodic injection signal attenuates within a relatively short distance, i.e., tens of cm in the direction normal to the bedding, but advances significantly further along the bedding planes (Figure 4.5). The distance at which the signal completely fades barely increases with time. In order to illustrate the behavior, simulation results are plotted at four moments within a single periodic cycle (see the insets in Figure 4.5). Points P_2 and P_3 show two local maxima of the overpressure. The first one, marked with a dot, refers to the maximum gas pressure p_g , coinciding with the desaturated region around the well, while the second one refers to the maximum liquid pressure p_l . The region of desaturation is limited to a few cm around the well and does not propagate with time because of the high entry pressure of Opalinus Clay. In contrast, given the different permeability along and normal to the bedding planes, the pore pressure perturbation front advances with time in an anisotropic way, reaching 6 m and 3.5 m after 2 years of injection, and 14 m and 8 m after 20 years of injection along x' and y' directions, respectively.

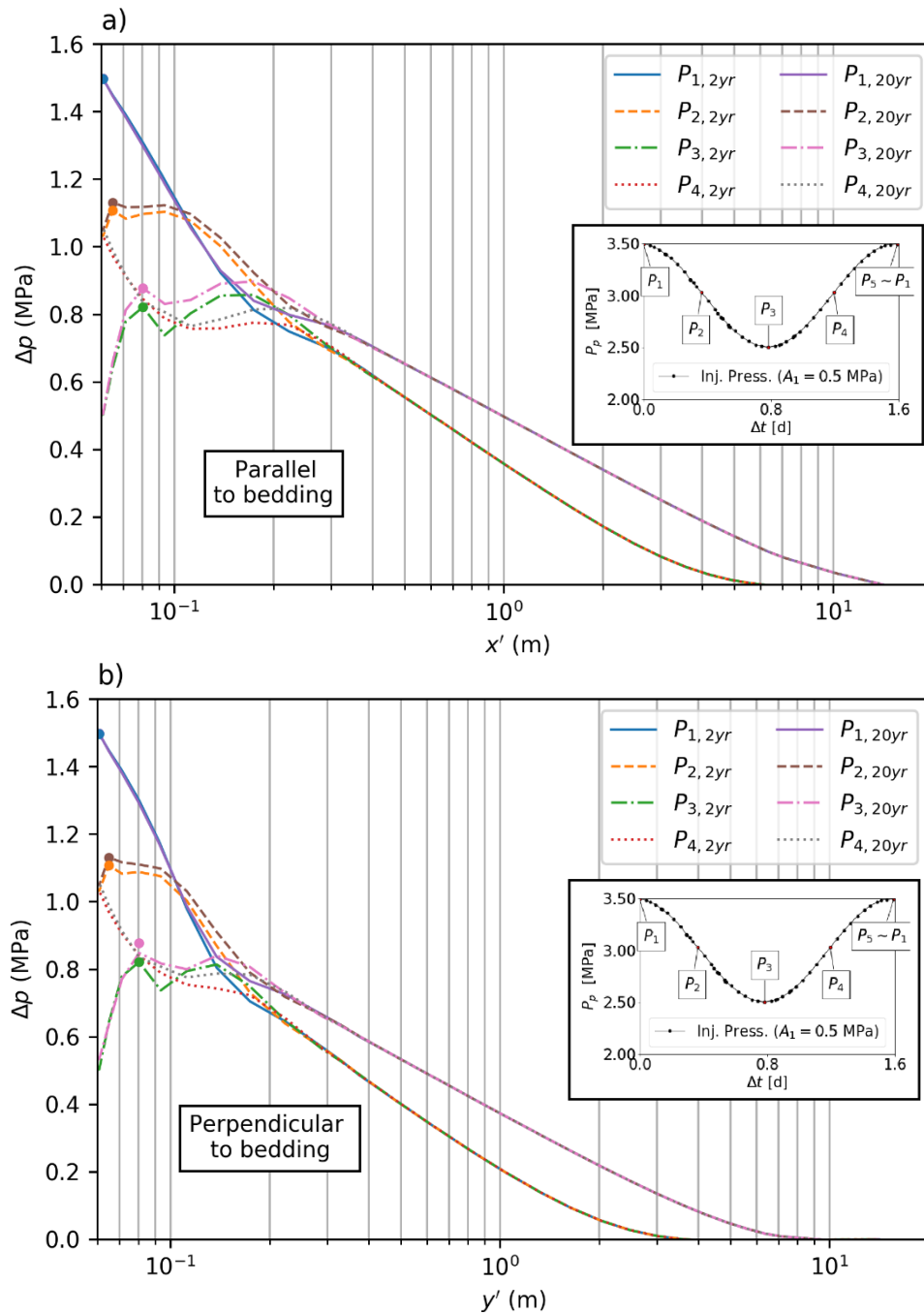


Figure 4.5. Pore pressure increase Δp due to CO₂ injection: (a) along x' , parallel to the bedding planes and (b) along y' , perpendicular to the bedding planes.

The plots follow one cycle of the injection pressure evolution after 2 years and 20 years of periodic injection. The dots represent the maximum capillary pressure ($p_c = p_g - p_l$), which corresponds to the minimum water saturation S_w for each curve. Given the van Genuchten parameters for Opalinus Clay in our reference model (see p_0 and m in Table), both the magnitude and extent of the rock desaturation are quite small. CO₂ cyclically desaturates a region of approximately 80 mm width around the borehole (Figure 4.6). Figure 4.6 represents the saturation degree evolution of the green and pink dots in Figure 4.5a (i.e., parallel to the bedding) after 2 years and 20 years of injection. The desaturation starts when the liquid pressure becomes lower than the gas pressure. After 20 years, the liquid pressure does not show an evident variation at the point of interest, while the gas pressure interestingly increases, resulting

in enhanced pore network desaturation (Figure 4.6b). However, final CO₂ saturation is yet negligible. The increased CO₂ pressure may be attributed to the fact that the pore-filling brine in the vicinity of the borehole has already become saturated with dissolved CO₂, preventing further dissolution. This reduced dissolution rate gives rise to higher CO₂ pressures. Additionally, it can be noted that the CO₂ pressure evolution lags behind the one of the water pressure, which is a result of the higher compressibility of CO₂ that leads to a delayed response to pressure changes (Vilarrasa et al., 2010b).

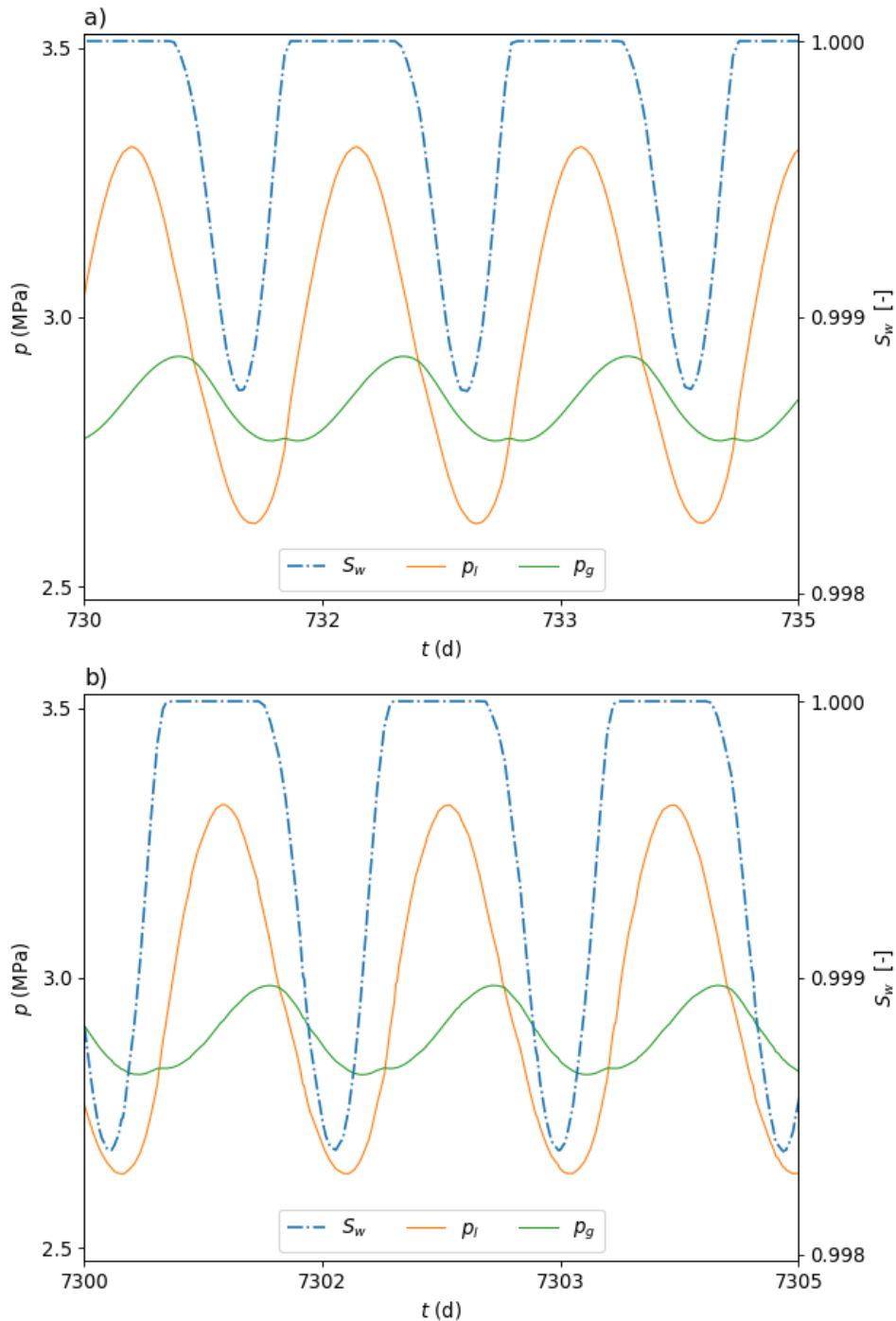


Figure 4.6. Evolution for three cycles of periodic injection of the pore pressure and water saturation at the point of maximum desaturation, which is ~ 80 mm along x' (green and pink points in Figure 4.5a). Results are reported after (a) 2 years and (b) 20 years of injection.

Pore pressure buildup induces an increase in the stress tensor components that results in a higher total mean stress (Figure 4.7). The total mean stress changes are smaller, by a factor of around two, than the pore pressure changes (compare Figures 4.7 and 4.5). This implies that the effective mean stress reduces in all directions and the rock expands. It is also worth mentioning that the perturbed pore pressure and stress zones develop to similar extents after two years of injection (compare Figures 4.7 and 4.5). Interestingly though, unlike the pore pressure changes, over time, the induced stress curves do not reach significantly deeper into the formation. Therefore, the stress perturbation stays behind the advancing pressure front after 20 years.

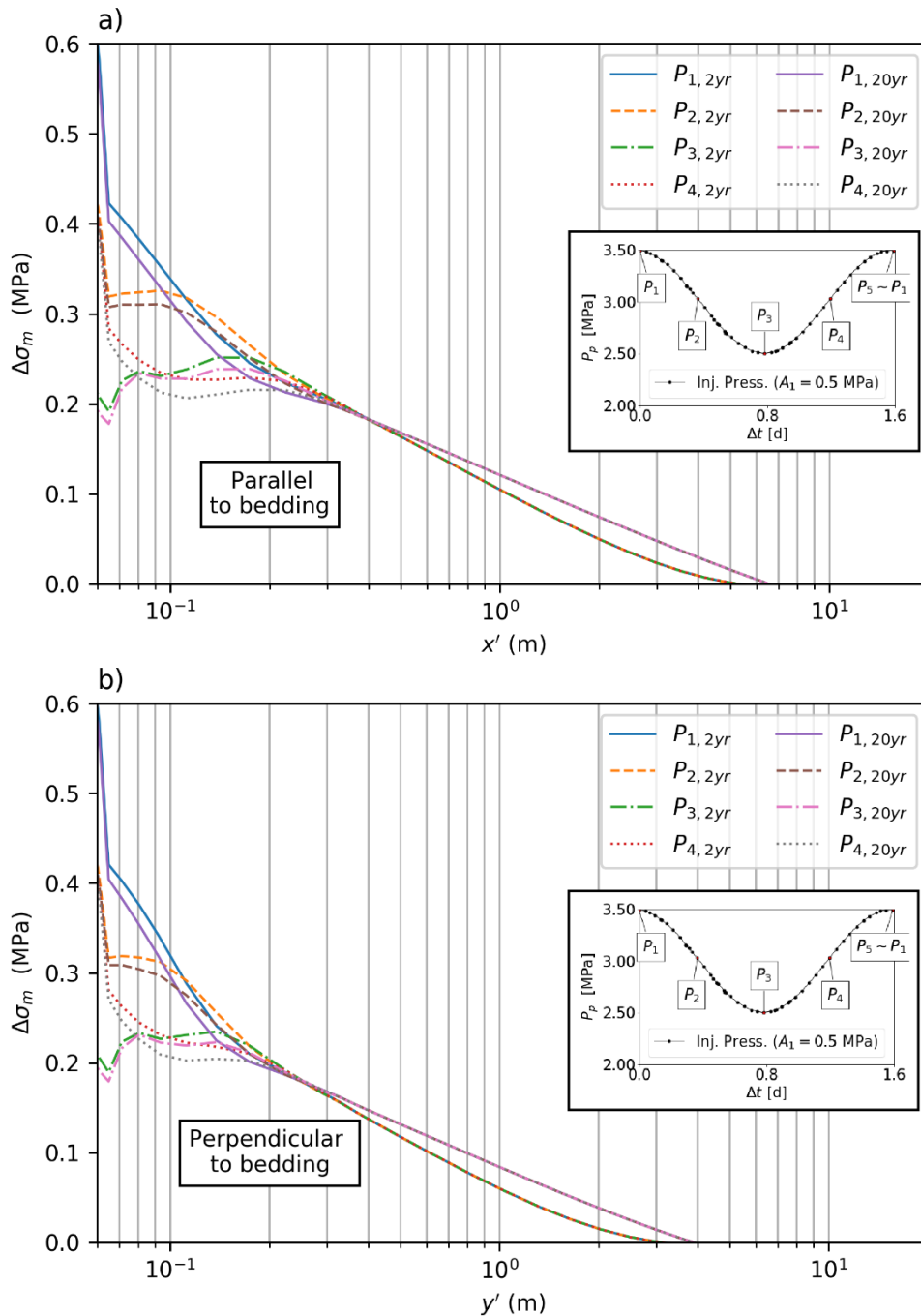


Figure 4.7. Total mean stress change $\Delta\sigma_m$ (a) along x' , parallel to bedding planes and (b) along y' , perpendicular to the bedding planes. Both plots represent one complete cycle after 2 and 20 years of periodic injection.

4.4.2. Long-term rock stability and deformation

In the context of fluid injection, the integrity of the caprock could be negatively affected, resulting in leakage. CO₂ could migrate into shallower formations or even escape to the atmosphere. A damage of the clayrock should also be adverted in the case of the in-situ experiment at Mont Terri. Here, the relatively low mean overpressure of 1 MPa, as proposed for CO₂LPIE, is not expected to induce sufficiently large changes in the effective stress to reach the failure conditions for Opalinus Clay (Figure 4.8). For the rock stability, we interpolated the laboratory measurements in undrained triaxial compression conditions on shaly facies of Opalinus Clay. The Mohr-Coulomb failure criterion in terms of the deviatoric and mean effective stresses is expressed as follow (Mayer and Labuz, 2013)

$$q = \frac{6 \sin(\phi)}{3 - \sin(\phi)} \sigma'_m + \frac{6c \cdot \sin(\phi)}{3 - \sin(\phi)}; \quad (4.7)$$

where c and ϕ are the rock cohesion and friction angle, respectively. Our laboratory measurements yield a cohesion of 4.9 MPa and a friction angle of 24.7 degrees for Opalinus Clay.

The initial stress state is far from failure conditions because of the high cohesion of Opalinus Clay, so stability is guaranteed during the experiment. Note that the reduction in the effective mean stress is lower (by a factor of 2) than the mean overpressure of 1 MPa because pore pressure buildup induces compressive stresses. As a result, Opalinus Clay at the Mont Terri rock laboratory can stand a large pressure buildup without reaching failure conditions.

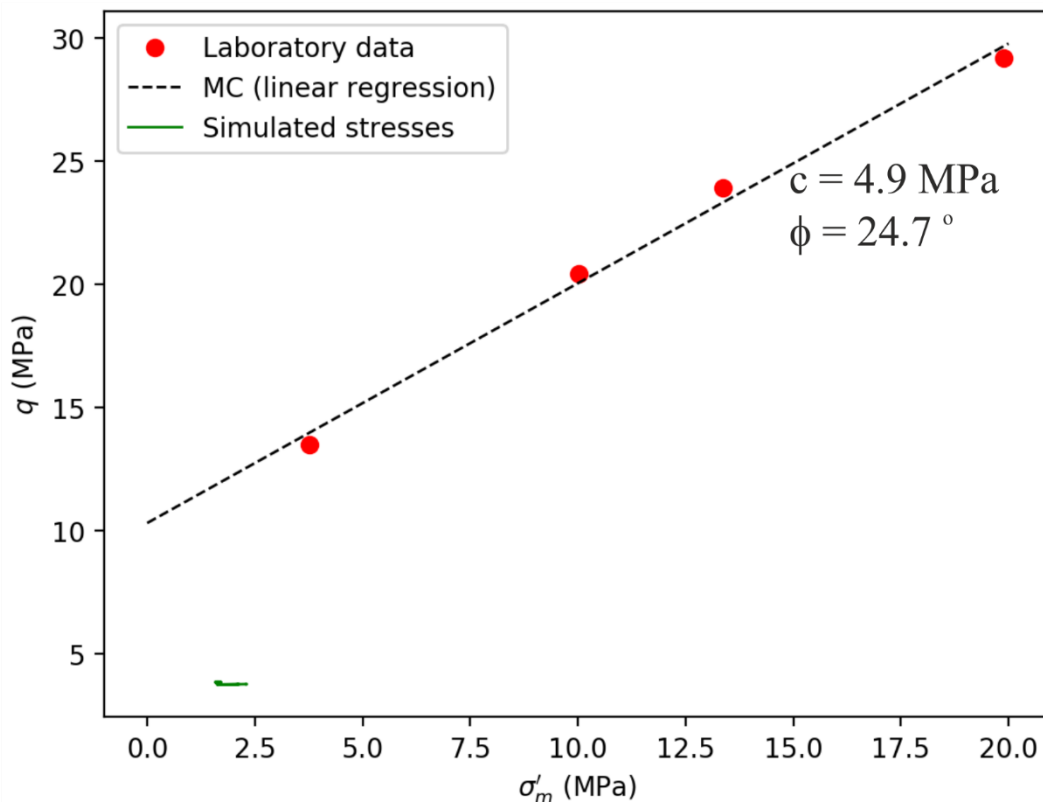


Figure 4.8. The stress trajectory for 20 years of cyclic injection of CO₂ in the q - σ'_m plane (green curve) and compared with the Mohr-Coulomb failure envelope of shaly facies of Opalinus Clay (dashed black line). The failure envelope is based on the linear interpolation of laboratory measurements (red dots), which gives a cohesion of 4.9 MPa and a friction angle of 24.7 degrees.

The displacements 1 m away from the injection well follow the trajectory that an observation well would follow, i.e., perpendicular to the bedding planes and parallel to the injection well (see inset in Figure 4.9). Displacements remain in the sub-mm scale, even after 20 years of injection. The maximum changes occur in the vicinity of the injection segment. The region is relatively small due to the low permeability of Opalinus Clay, which limits pore pressure changes and changes in the effective stresses that induce deformation.

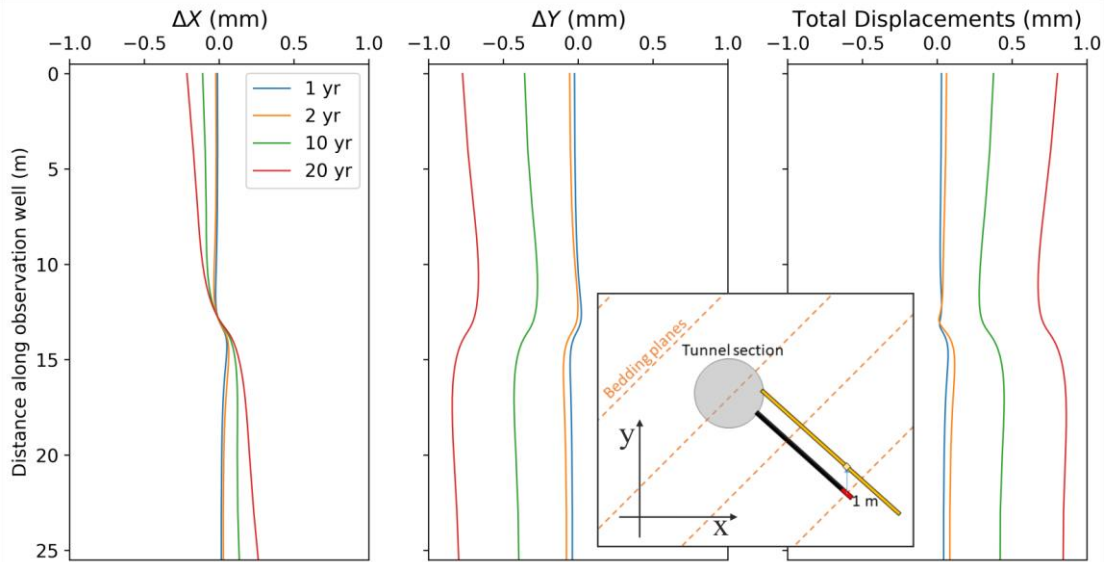


Figure 4.9. Displacements registered after 1, 2, 10, and 20 years of periodic injection along the direction of a potential observation well (shown in yellow in the inset, with zero set at the tunnel wall), i.e., perpendicular to the bedding planes and 1 m away from the injection well.

4.4.3. Sensitivity analysis of the amplitude of the periodic injection

We analyze the rock response to three source amplitudes of the periodic injection: 0.25 MPa, 0.5 MPa, and 1.0 MPa. In order to compare the results, the pore pressure changes are normalized with respect to each amplitude, which we denote as p^* .

Figure represents variations of the normalized pore pressure p^* after 20 years of injection at short distances from the injection well, both parallel and perpendicular to the bedding planes, for the three selected amplitudes. The signal amplitude along the bedding planes attenuates by 50% and 90% at distances of only 0.1 m and 0.2 m away from the injection well, respectively (Figure 4.10a). The attenuation is higher normal to the bedding planes (Figure 4.10b) compared to the direction parallel to the bedding. The shown curves correspond to a distance of 0.1 m and appear flattened in their minimum values because a slight desaturation takes place when brine pressure drops below CO_2 pressure (recall Figure 4.6). Note that injection at the lower amplitude of $A_2 = 0.25$ MPa does not desaturate the rock at a radius of 0.1 m. In contrast, injection at the highest amplitude $A_3 = 1$ MPa leads to a more pronounced desaturation lasting for a longer period of time. The desaturation yet remains limited to some centimeters next to the borehole as none of the injection scenarios drains the rock even to a 0.2 m distance.

To evaluate the possibility of measuring signal fluctuations in-situ, we draw the same plot but for distances that reach up to 1 m (Figure 4.11). Considering the amplitudes being on the order of 1 MPa, the periodic signal 0.5 m away from the injection well is calculated to be on the order of 1 kPa. As the distance from the well increases, the effect of shale anisotropy on the

attenuation of the periodic signal and the lag time increases as well. This effect is more pronounced for the lag time, which presents a delay of half a day.

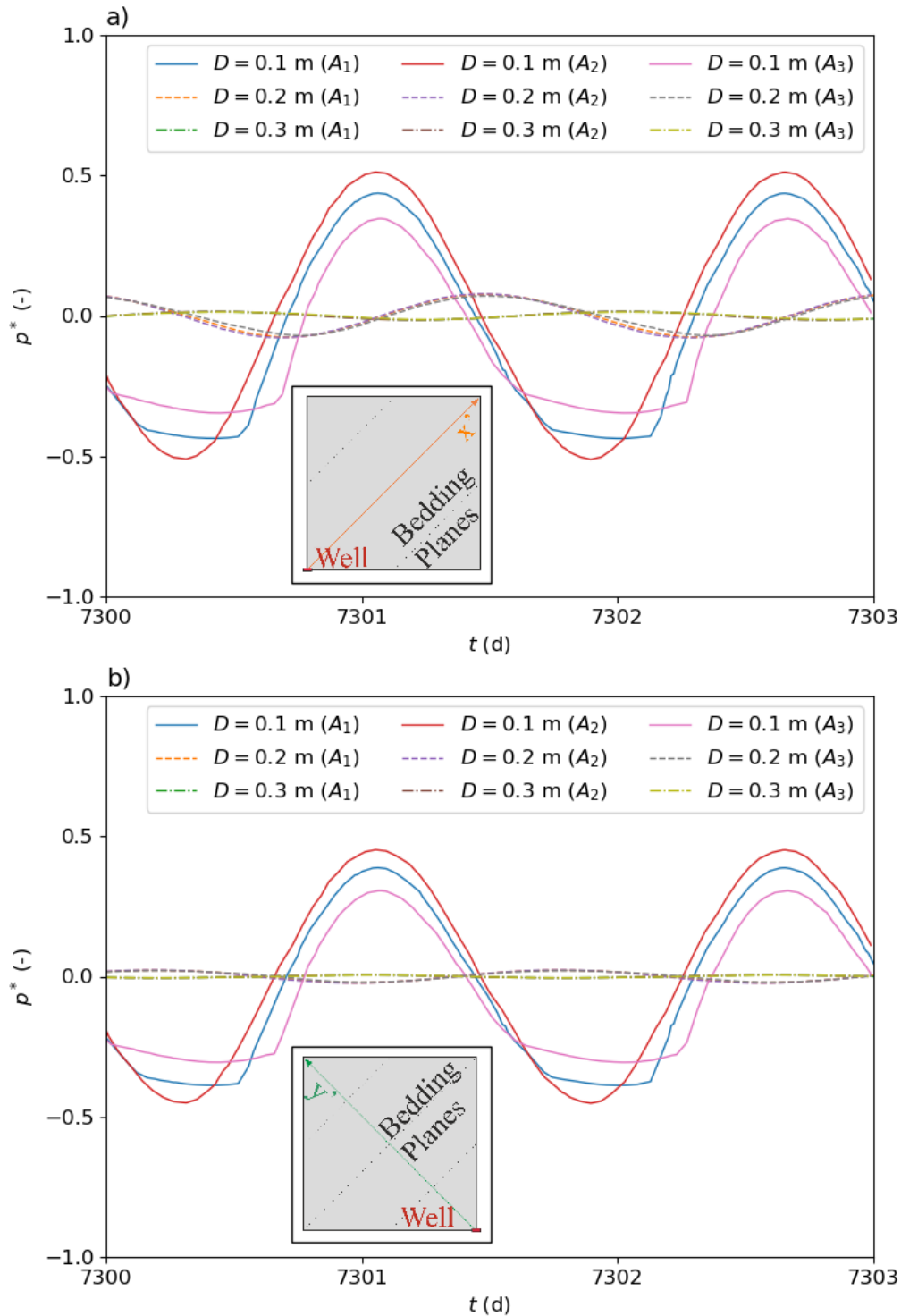


Figure 4.10. Temporal evolution of the normalized pressure $p^* = (p - \bar{p})/A_i$ in the vicinity of the injection well shown for distances, D , of 0.1 m, 0.2 m and 0.3 m away from the well.

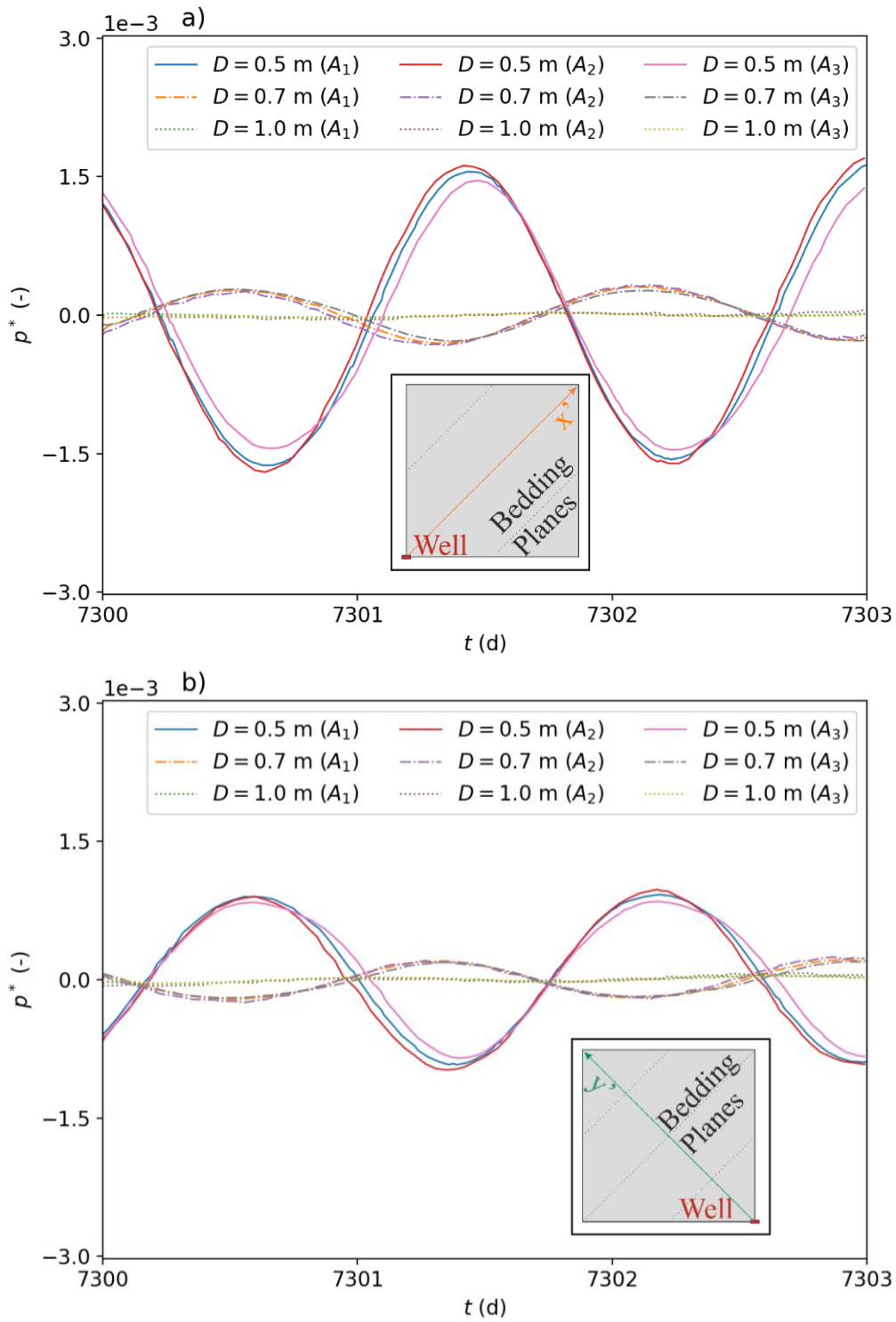


Figure 4.11. Temporal evolution of the normalized pressure $p^* = (p - \bar{p})/A_i$ around the injection well (shown for 0.5 m, 0.7 m, and 1.0 m away from the well); (a) parallel and (b) perpendicular to the bedding, for amplitudes $A_1 = 0.5$ MPa, $A_2 = 0.25$ MPa and $A_3 = 1.0$ MPa, after 20 years of periodic injection.

4.4.4. Sensitivity analysis of hydraulic properties at the site scale

The presented model parameterized with laboratory data on cm-scale intact specimens provides preliminary insights into the HM response of Opalinus Clay to CO₂ injection. However, uncertainties grow when dealing with the rock mass behavior on the m to km scale. Particularly, the presence of flow discontinuities like fractures leads to higher intrinsic permeability and lower capillary entry pressure of the rock mass. Site- and regional-scale permeability of clay-rich shales can be up to two to three orders of magnitude larger than those inferred from laboratory experiments (Neuzil, 2019). Furthermore, experimental measurements of relative permeability curves in low-permeability rocks are scarce, adding uncertainty to the model used in this study. In addition to our reference model, we simulate a scenario in which the intrinsic permeability is two orders of magnitude higher (i.e., $\sim 10^{-18}$ m²) and the capillary entry pressure is one order of magnitude lower than those in the reference model (i.e., 0.5 MPa). The relative permeability curves follow linear relationships with fluid saturations (i.e., exponents equal to one), which represents the least conservative case.

The high capillarity of the pore network and low permeability in the reference case hinder CO₂ intrusion into the caprock (Figure 4.12a), while the low entry pressure and relatively high effective permeability allow CO₂ to enter and flow through the rock mass (Figure 4.12b). In the former case, CO₂ dissolved into the brine spreads isotropically for almost 2 m away from the injector. For the latter case, the free-phase CO₂ spreads preferentially along the bedding, which promotes CO₂ dissolution along this direction. While the CO₂ front reaches a maximum distance of almost 2 m from the well along the bedding planes and 1 m normal to them, the extent of dissolved CO₂ ranges from almost 7 m along the bedding to 5 m normal to the bedding.

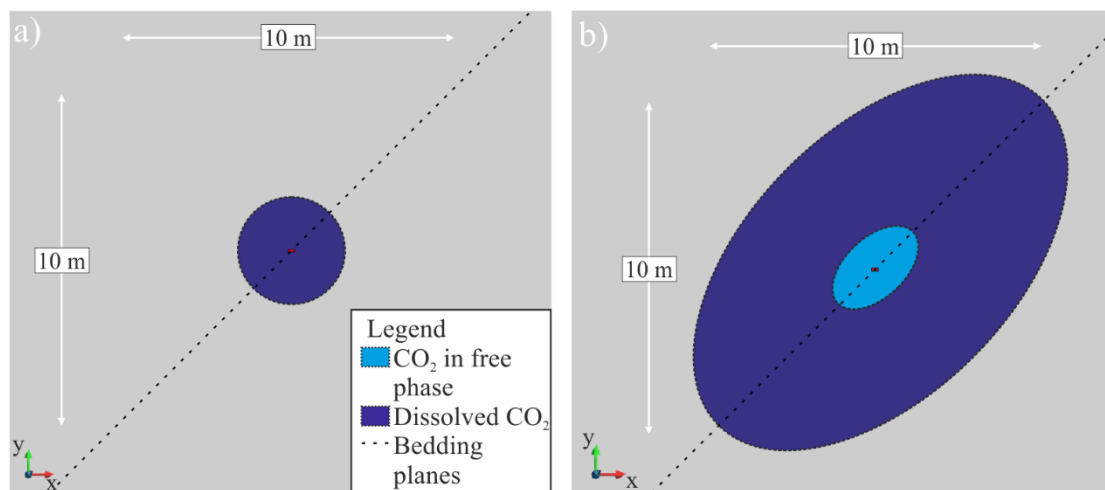


Figure 4.12. Simulation results for the advance of the CO₂ front in free phase (light blue) and dissolved into the brine (dark blue) after 10 years of cyclic CO₂ injection: (a) the reference model with the parameters listed in Table 1, (b) a scenario with a rock mass of potentially lower capillary entry pressure and higher permeability. The dotted line illustrates the bedding plane direction.

4.5. Discussion

Evaluation of the sealing capacity of anisotropic shaly caprocks, like Opalinus Clay, is complicated due to the presence of discontinuities that might provide preferential flow paths.

Our numerical simulations of long-term periodic CO₂ injection into Opalinus Clay at the Mont Terri rock laboratory manifest the anisotropic HM response caused by the presence of bedding planes. In particular, the injection-induced overpressure follows the direction of the bedding planes, also promoting stress changes in this direction. The rock expands volumetrically and discontinuities may locally open along weak bedding planes, as they are found to possess lower tensile and shear strengths than the intact rock (Amann et al., 2018). Such an effect, although unlikely to occur during the experiment, as shown by the stability analysis (Figure 4.8), could enhance intrinsic permeability and/or decrease the capillary entry pressure of the rock (Kim and Makhnenko, 2020; Kivi et al., 2022) and might compromise the caprock integrity. In addition to the bedding, pore-scale shale heterogeneities may pose preferential conduits through which the injected CO₂ could penetrate and flow with further ease (Damians et al., 2020). However, even with a capillary entry pressure of one order of magnitude smaller than the one measured in the laboratory ($p_0=0.5$ MPa) and enhanced permeability by two orders of magnitude, the free-phase CO₂ can hardly penetrate 2 m into Opalinus Clay after 10 years of periodic CO₂ injection (Figure 4.12b). If CO₂ does not advance in free phase, it dissolves in the pore fluid and spreads in the shale by the slower molecular diffusion process. The diffusive front advances uniformly and approaches a distance of about 2.5 m away from the borehole after 20 years of injection (black dashed line in Figure 4.4a).

The preliminary insights gained from our coupled HM simulations assist in designing the CO₂LPIE experiment. In particular, to facilitate using the attenuation at the monitoring point for in-situ characterization of rock properties, set as a primary goal of the CO₂LPIE, appropriately locating the monitoring borehole is of high importance. We find that the imposed periodic oscillation attenuates rapidly, raising the necessity to locate the observation wells as close as possible to the injection well but still away from the borehole disturbed zone, at a safe distance to inhibit a short-cut between the boreholes. The amplitude of the periodic signal should be proportional to the distance to the injection well at which the monitoring wells will be finally drilled. Measuring and characterizing the geomechanical response of Opalinus Clay is less problematic, since drilling the monitoring borehole parallel to the injection well at a distance of 1 m would permit to accurately address the components of the strain tensor (Figure 4.9).

The representability of our numerical simulations has been affected by some simplifying assumptions: (1) 2D plane-strain geometry, (2) high-exponent power-law model for the relative permeability curves, (3) constant poromechanical properties, permeability, capillary entry pressure, and irreducible water saturation with deformation, (4) linear elastic behavior of the rock matrix, and (5) neglecting chemical CO₂-brine-rock interactions. In more detail, the plane-strain model neglects fluid flow in the out-of-plane (parallel to the intermediate stress) direction. This simplification is thus anticipated to overestimate the generated overpressure and HM coupling along the bedding planes. Moreover, a true-triaxial evaluation of the stress alterations and rock deformation is of significance when dealing with strain-dependent mechanical and flow properties. Conducting multiscale laboratory experiments on a carbonate specimen, Haghgi et al. (2021) identified complex interactions between pore-scale deformations and two-phase flow mechanisms. They highlighted a systematically enhanced irreducible water saturation and decreased relative permeability with increasing the effective stress, as the pores become confined and flow paths get more tortuous. Nevertheless, similar coupling approaches in shales are underexplored, if considered at all, because of the challenging nature of such measurements in low-permeable rock. The considered power-law function in our study, although not calibrated, consistently reproduces the main relative permeability features of two shales obtained experimentally by Bennion and Bachu (2008), which is, to the best of our knowledge, the only (published) study of its kind. In that sense, CO₂ is found to remain immobile at saturations up to about 0.2 - much larger than the attained CO₂ saturations in our reference

model in the order of a few tenths of a percent (Figure 4.12) -. On the other hand, the capillary entry pressure can be expected to decrease with pore radius increments during rock expansion, according to the Young-Laplace equation. Additionally, given that CO₂ dissolves into the formation pore fluid, geochemical reactions are expected. CO₂ dissolution in water generates carbonic acid (H₂CO₃) and decreases the pH of the liquid, which may lead to mineral dissolution and precipitation, potentially causing changes in rock porosity, permeability, stiffness and strength (Rohmer et al., 2016; Dewhurst et al., 2020). Our sensitivity analysis on rock properties partially addresses these non-linear capillary and flow effects in an ideally static pore structure framework. Nevertheless, we believe that the employed model parameterization approach constrains the simulation uncertainties to reasonable limits and provides a rational first-order approximation of the system response. To better characterize the formation and to control the evolution of the properties of the material, it is necessary to implement a continuous characterization method, taking into account different scales in time (from days to years) and space (from mm to tens of m). This is a key point that will be achieved by real-time calibration of the model parameters against field measurements during the CO₂LPIE.

4.6. Conclusions

We have performed numerical analyses of the CO₂LPIE experiment that will be conducted at Mont Terri rock laboratory to assist with its design. Coupled HM simulations of periodic CO₂ injection in Opalinus Clay are performed using a 2D plane-strain geometry over a long period of a few decades. Given the high entry pressure and low permeability of the material, CO₂ cannot penetrate and flow through the rock in free phase, unless the site-scale properties of Opalinus Clay substantially differ from laboratory measurements or geochemical interactions cause significant deterioration of the HM characteristics of the rock around the injection well. The injected CO₂ rather advances by molecular diffusion, reaching 1 m after 2 years, and 2.5 m after 20 years of injection. The periodic signal of the injection pressure rapidly attenuates, which requires the pore pressure monitoring wells to be located very close to the injection well. The pore pressure increase causes rock deformation and stress changes, which preferentially advance along the bedding planes, allowing to explore the anisotropic properties of Opalinus Clay in-situ. Measurements should be done by placing observation wells in orthogonal directions and not farther than a few tens of centimeters from the injector. The presented simulation results serve as the first approximation of the system response to periodic CO₂ injection and will be updated as more data is available and eventually compared with field measurements to gain insight on the sealing capacity of Opalinus Clay at the field scale.

Chapter 5

Revealing hydro-mechanical properties of fractures in shale

5.1. Introduction

Characterization of low-permeability argillaceous lithologies, such as shales, is receiving increasing interest due to their potential applications in crucial geo-environmental and energy-related projects. These rocks have garnered attention as possible candidates for nuclear waste disposal (Neuzil 2013; Bossart et al., 2018; Sasaki and Rutqvist, 2022), caprocks for geologic carbon storage (IPCC, 2005; Makhnenko et al., 2017; Kivi et al., 2022), barriers against aquifer contamination (Bredehoeft et al., 1983; van der Kamp, 2001), and as unconventional oil and gas reservoirs (Jarvie et al., 2007; US Energy Inf. Admin, 2015). Characterization of shale behavior has proven to be a challenging task, especially concerning its ability to transmit fluids on a large scale, which is essential for all the mentioned applications.

Hydro-mechanical properties of shales are known to be dominantly anisotropic due to the layered structure of the clayey matrix (Thury and Bossart, 1999b; Gens et al., 2007; Neuzil, 2019). Experimental results confirm systematic differences in the sets of material properties depending on the direction with respect to the bedding, focusing on directions perpendicular and parallel to it (Makhnenko et al., 2017; Wu et al., 2017; van Noort and Yarushina, 2019; Voltorini and Ajo-Franklin, 2020; Braun et al., 2021; Wenning et al. 2021). Beyond the bedding, the presence of natural fractures further influences stress and pore pressure distribution, adding another form of anisotropy (Bredehoeft et al., 1983; Neuzil, 1986). Given the significant contrast in permeability and stiffness between intact material and fractures, proper characterization poses challenges when dealing with argillaceous materials (Bredehoeft et al., 1983; Neuzil et al., 2019).

Flow properties of fractured materials are strongly stress- and scale-dependent. Important factors include porosity and pore size distribution (Heap and Kennedy, 2016; Kim and Makhnenko, 2023b), testing conditions including the way to set up the fractured specimen (Bondarenko et al., 2022), thermal effect especially important for shales (Mohajerani et al., 2012; Makhnenko et al., 2023), and time-dependent deformation that is not only strongly pronounced for clay-rich rock, but also is enhanced for fractured materials (Makhnenko and Podladchikov, 2018; Zhu et al., 2023). At the field scale, fractured rock is reported to have a few orders of magnitude larger permeability compared to the intact material tested at the laboratory scale (Neuzil, 1986; Heap and Kennedy, 2016; Azizmohammadi and Matthai, 2017). Various experimental and modeling approaches have been proposed to link the hydro-mechanical properties of fractures (Witherspoon et al., 1980; Bandis et al., 1983; Barton et al., 1985; Cappa and Rutqvist, 2011; Rutqvist et al., 2013; Pyrak-Nolte and Nolte, 2016; Crawford et al., 2017; Bondarenko et al., 2022; Damians et al., 2022). However, few of these works focus on shales.

When it comes to modeling, bedding planes and natural fractures are typically treated differently, despite both being discontinuities. For the bedding planes, the flow can be represented using an orthotropic approach, coupled with the transversely isotropic mechanical model. In this case, the rock is described as a continuum material, with two sets of hydro-mechanical parameters assigned to the directions parallel and perpendicular to the bedding (Cheng, 1997; Gens et al., 2007; Olivella and Alonso, 2008; Ziefle et al., 2017; Damians et al.

2022). In contrast, explicitly including natural fractures in the model is generally more accurate to comprehensively represent their impact on the changes in pressure and stress distributions, which may affect fractures and faults stability (Zareidarmiyan et al., 2021).

The ability of a fracture to facilitate fluid flow primarily depends on its average opening. Despite their small apertures, fracture transmissivity is proportional to the cube of its aperture, i.e., the so-called cubic law (Snow, 1969; Witherspoon et al., 1980; Zimmerman and Bodvarsson, 1996), leading to a permeability that is orders of magnitude larger than the surrounding rock (Vialle et al., 2016; Wang et al., 2022). Fluid flow within fractures is also influenced by their contact areas (Barton et al., 1985; Pyrak-Nolte and Morris, 2000). The evolution of these geometrical parameters is ultimately contingent on the applied normal stress (Bandis et al., 1983). The experiments reveal that the relationship between stresses and aperture alteration is extremely nonlinear, implying that the normal stiffness of the fracture is dependent on the range of stresses under consideration (Witherspoon et al., 1980; Bandis et al., 1983; Barton et al., 1985). However, during modeling, it is common practice to assume a constant fracture normal stiffness.

This research is centered on the hydro-mechanical characterization of a naturally fractured shale specimen using both experimental and numerical approaches. Shaly facies of Opalinus Clay, a well-characterized shale located in Mont Terri, Switzerland (Thury and Bossart, 1999b; Bossart and Thury, 2011; Bossart et al., 2018), are selected in this study. The laboratory-scale experiments indicate that at a given effective mean stress the fractured specimen exhibits higher permeability compared to the intact material, primarily attributable to the presence of a fracture. We characterize the hydro-mechanical properties of the fracture numerically by employing the embedded model (Olivella and Alonso, 2008), which allows accounting for both spatial and temporal variations in fracture aperture and, consequently, permeability. Simulation results reveal inhomogeneous aperture changes along the fracture, highlighting the complex response of fractured rock to fluid injection.

5.2. Methodology

5.2.1. Governing equations

The coupled hydro-mechanical problem implies solving simultaneously the quasi-static momentum balance and fluid mass conservation. The former reads

$$\nabla \cdot \boldsymbol{\sigma} + \mathbf{b} = 0; \quad (5.1)$$

where $\boldsymbol{\sigma}$ [$\text{ML}^{-1}\text{T}^{-2}$] is the total stress tensor, taken positive for compression; and \mathbf{b} [$\text{ML}^{-2}\text{T}^{-2}$] is the body force. We consider a poroelastic response (Biot, 1941; Cheng, 2016), in which

$$\boldsymbol{\sigma} - \boldsymbol{\alpha}p = 2G\boldsymbol{\varepsilon} - \frac{2\nu G}{(1-2\nu)}\varepsilon_v \mathbf{I}, \quad (5.2)$$

where, on the right side of the equation, $G = E/2(1+\nu)$ [$\text{ML}^{-1}\text{T}^{-2}$] is the shear modulus, E [$\text{ML}^{-1}\text{T}^{-2}$] is Young's modulus, ν [-] is the Poisson ratio; $\boldsymbol{\varepsilon}$ [-] is the strain vector; ε_v [-] is the volumetric strain; and \mathbf{I} [-] is the identity vector. On the left-hand side, to govern the deformation of the rock, we adopt Biot effective stress $\boldsymbol{\sigma}' = \boldsymbol{\sigma} - \boldsymbol{\alpha}p$, where p [$\text{ML}^{-1}\text{T}^{-2}$] is pore pressure, and $\boldsymbol{\alpha}$ [-] is the Biot coefficient tensor, assumed isotropic ($\boldsymbol{\alpha} = \alpha \mathbf{I}$).

Assuming one-phase flow, fluid mass conservation is expressed as (Bear, 2013)

$$\frac{\partial(\phi\rho)}{\partial t} + \nabla \cdot (\mathbf{q}\rho) = f, \quad (5.3)$$

where ϕ [-] is the porosity of the material; t [T] is the time; $\nabla \cdot$ [L^{-1}] is the divergence operator; ρ [ML^{-3}] is the fluid density; f [$ML^{-3}T^{-1}$] is the external water supply (or withdrawal) term; and \mathbf{q} [$L^3 T^{-1} L^{-2}$] is the volumetric flux. The latter is calculated through Darcy's law

$$\mathbf{q} = -\frac{\mathbf{k}}{\mu} (\nabla p + \rho g \nabla z) \quad (5.4)$$

where \mathbf{k} [L^2] is the permeability tensor; μ [$ML^{-1}T^{-1}$] is the dynamic viscosity of water; ∇ [L^{-1}] is the gradient operator; g [LT^{-2}] is the gravity acceleration; z [L] is the vertical coordinate.

To simulate the hydro-mechanical behavior of the fractured Opalinus Clay specimen numerically, we use the fully-coupled finite element software CODE_BRIGHT (Olivella et al., 1994; 1996). The 3D model includes three materials: the Opalinus Clay matrix, the natural fracture, and two porous disks-one at the inflow and another at the outflow side (see Section 2.3).

The anisotropic permeability of the specimen is represented by the explicit definition of the fracture while, for each material, the parameter is isotropic, i.e., $\mathbf{k} = k\mathbf{I}$. However, permeability is defined differently for the three materials. While it is a constant and high value for the porous disk k_{pr} , it follows Kozeny-Carman's formulation for the intact material (Carman, 1937). Although shale materials are generally more susceptible to variation in porosity (Kim and Makhnenko, 2020), employing a cubic permeability-porosity law for the intact rock facilitates the identification of inhomogeneity associated with fracture. Finally, the natural fracture follows the embedded model that links the permeability evolution as a function of the volumetric deformations (Olivella and Alonso, 2008). We write the explicit fracture permeability as

$$k_{fr} = \begin{cases} k_0; & \text{if } \Delta \varepsilon_v < 0 \\ k_0 + \frac{(b_0 + a\Delta \varepsilon_v)^3}{12b_0}; & \text{if } \Delta \varepsilon_v \geq 0 \end{cases} \quad (5.5)$$

where k_{fr} [L^2] is the natural fracture permeability; k_0 [L^2] is the initial permeability; b_0 [L] is the initial hydraulic aperture of the fracture; $\Delta \varepsilon_v = \varepsilon_{v0} - \varepsilon_v$ [-] is the change in volumetric strain; ε_{v0} [-] is a reference volumetric strain; and a [L] is the fractures spacing, which corresponds to the characteristic size of the material, for a single fracture (Olivella and Alonso, 2008; Zareidarmiyan et al., 2020). In this way, our formulation can simulate the space- and time-dependent permeability alterations due to the changes in the pore pressure, deformation, and stress fields.

5.2.2. Specimen description

Opalinus Clay, a Jurassic shale from Mont Terri Underground Rock Laboratory, Switzerland, is considered as a potential host for radioactive waste and a representative caprock for geological carbon dioxide storage (Thury and Bossart, 1999b; Bossart and Thury, 2011; Bossart et al., 2018). It is divided into several sub-units (or facies) inconsistent across the region and varies with the investigation methods (Hostettler et al., 2017). The Opalinus Clay specimen tested in this study has been classified as shaly facies and contains 55-60 % clay minerals (including illite, chlorite, kaolinite, and illite/smectite mixed), quartz, carbonates, and others.

Three primary fault systems are present within the rock laboratory. These include moderately dipping SSE and SW fault systems, as well as an NNE striking fault system (Nussbaum et al., 2011). Of particular note, a significant Main Fault intersects gallery 98, characterized by an inclination of around 60°, which is steeper than the natural bedding of the rock. This unique

geological feature offered exceptional research opportunities and has been the subject of multiple studies (Zappone et al., 2018; Guglielmi et al., 2020a; 2021). Here, two specimens from shaly facies of Opalinus Clay specimens are tested – one intact and another one with a preexisting fracture that goes through the center of the cylindrical specimen with an inclination of the axis of 10° .

The difference in pore structure characteristics between intact and fractured Opalinus Clay is evaluated using mercury intrusion porosimetry (MIP). The MIP device (PoreMaster 60; Anton Paar, USA) can measure the amount of mercury intruded in relation to the injection pressure, allowing the calculation of effective porosity ϕ . Assuming cylindrical pores, the pore throat size (diameters from 3.6 nm to 1.0 mm) can be calculated (Kim and Makhnenko, 2023a). For the analysis, a chip of Opalinus Clay sample with a weight of around 1.0 g and a size of a few millimeters is brought to a dry state using a freeze dryer to minimize disturbance in the pore structure during the drying process. In the case of fractured Opalinus Clay, the tested samples are collected both near and far away from the natural fracture in the specimen after the permeability test. The sample representing intact Opalinus Clay is obtained from somewhere in the intact specimen.

Figure 5.1 illustrates the pore throat size distributions of intact and fractured Opalinus Clay. The terminology of pore size follows the recommendation suggested by the International Union of Pure and Applied Chemistry (Rouquerol et al., 1994). The sample collected far from the natural fracture in the fractured specimen exhibits the same unimodal pore size distribution and porosity as those from the intact specimen, meaning that the effect of fractures on the pore structure could be disregarded in this study. Consequently, the MIP results are reported only with representative intact and fractured Opalinus Clay samples. The pore structure analysis reveals that the existence of fractures may lead to the generation of the macropores ($d > 50$ nm) from mesopores ($2 \leq d \leq 50$ nm) with similar size of the dominant value, resulting in approximately the same ϕ (0.12 for intact and 0.13 for fractured Opalinus Clay). The main limitation of the pore structure analysis is related to the representation error, especially for fractured Opalinus Clay. A decimeter scale fracture in the cylindrical specimen utilized for the flow test cannot be fully detected by the MIP due to the sample size (\sim mm -scaled), but it could also be attributed to the assumption of pore shape in the MIP.

Moreover, the nitrogen (N_2) adsorption technique is utilized for the pore body size measurements and calculation of the specific surface area of intact and fractured Opalinus Clay based on the physisorption isotherm (Kim and Makhnenko, 2023b). Despite a phenomenological discrepancy in descriptions of pore size between MIP and N_2 adsorption (Kuila and Prasad, 2013) and different sample preparation methods, a higher population of macropores in the fractured sample is also observed by the N_2 adsorption technique. The specific surface area calculated based on the Brunauer-Emmett-Teller theory (Brunauer et al., 1938) is $26.6 \text{ m}^2/\text{g}$ for intact and $25.7 \text{ m}^2/\text{g}$ for fractured Opalinus Clay.

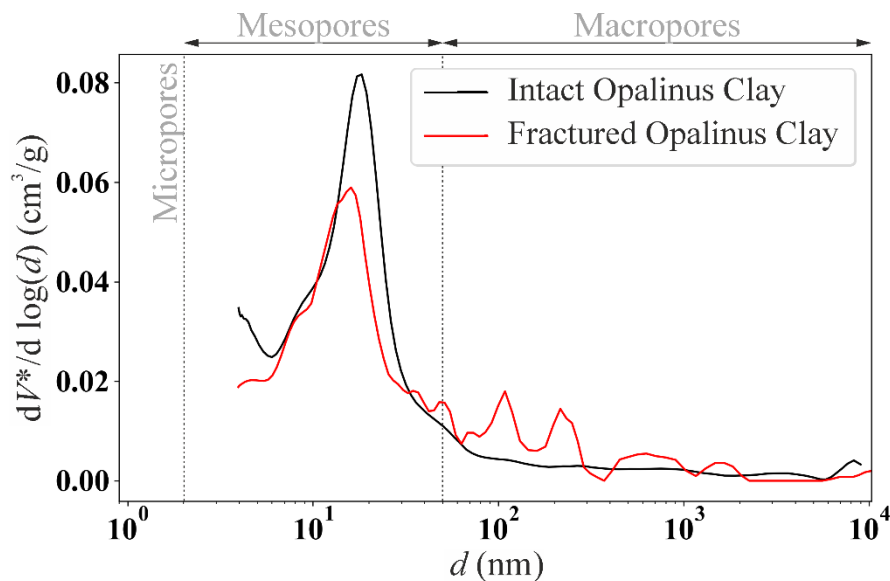


Figure 5.1. Distribution of pore throat size d obtained from the mercury intrusion porosimetry. The $dV^*/d \log(d)$ is used as the ordinate since the integral between two random points of pore size d can be considered as the partial pore volume in the given range, where V^* is the pore volume normalized by the sample weight.

5.2.3. Experimental procedure

The core flooding device is utilized for permeability measurements of intact (Kim and Makhnenko, 2020) and fractured Opalinus Clay. A cylindrical specimen with a diameter of 50 mm and length of 97 mm is placed inside a rubber Viton membrane and installed in the cell. In this configuration, lateral confining pressure is only applied to the specimen using an oil pressure controller (SANCHEZ, France). The axial deformation parallel to the direction of fluid flow is restricted by the end plug spacers on the upstream and downstream sides. The induced axial stress and, hence, total mean stress P can be calculated based on the poroelastic relationship

$$P = \frac{\sigma_{ax} + 2\sigma_{lat}}{3} = \frac{2(1+\nu)}{3} \sigma_{lat} + \frac{1-2\nu}{3} \alpha p \quad ; \quad (5.6)$$

where σ_{lat} and σ_{ax} [$ML^{-1}T^{-2}$] are the lateral and axial stress components applied on the specimen, respectively. The Poisson's ratio ν is determined for intact Opalinus Clay in triaxial compression tests performed on fluid-saturated specimens and is equal to 0.30 under the drained conditions and 0.42 for the undrained conditions (Kim and Makhnenko, 2020). Similarly, for fractured Opalinus Clay, Poisson's ratio is measured to be 0.38 under the drained conditions and 0.42 for the undrained conditions. During the triaxial test, the axial and lateral strains are measured using the linear variable differential transformers (LVDTs) attached to the specimen. The measurement is taken in the middle of the specimen (the distance of two fixing pads for LVDT is around 50 mm), less restrained than the end zone.

In the core flooding system, two syringe pumps (Teledyne ISCO, USA) are filled with deionized water and connected to the upstream and downstream sides respectively to control flow rates and fluid pressure gradient. Before the test, the specimen is fully saturated with water using the back pressure technique to allow air bubbles in the pores and system to collapse and

dissolve into water as the applied fluid pressure increases under undrained conditions (Black and Lee, 1973). Skempton's B coefficient (the ratio of induced pore fluid pressure to the change in total mean stress under undrained conditions) is measured at each saturation stage. Its value increases during the saturation process due to a decrease in pore fluid compressibility and eventually becomes constant when the specimen and system are fully saturated (Makhnenko and Labuz, 2016). The B values should be corrected due to the presence of dead volume in the pore pressure system (Bishop, 1976), but the correction factor appears to be comparable to the accuracy of the reported values (± 0.005) in the core flooding device (Kim and Makhnenko, 2020). The B value of the saturated specimens under effective mean stress of 2 MPa is 0.91 for intact and 0.96 for fractured Opalinus Clay.

The tests are conducted under different effective mean stresses P' to establish the k - P' relationship, and at each P' the permeability under the steady-state and laminar flow conditions is calculated using Darcy's law (Equation 5.4). Table 5.1 summarizes the experimental conditions for fractured Opalinus Clay. A constant pressure gradient Δp (the difference between upstream and downstream pressures) is applied to the specimen with cross-sectional area A and length L to promote fluid flow during the permeability measurements. The fluid volume change per unit time $Q = \Delta V / \Delta t$ and the volumetric flux $q = Q / A$ are measured during the permeability test. The dynamic viscosity of water at room temperature of 22°C is assumed to be 0.001 Pa·s (Linstrom and Mallard, 2023).

Table 5.1. Summary of experimental conditions in the core flooding device with fractured Opalinus Clay.

P' (MPa)	p_0 (MPa)	p_{in} (MPa)	p_{out} (MPa)	Δp (MPa)	σ_{lat} (MPa)	σ_{ax} (MPa)	q (m/s)
3	5.5	5.66	5.31	0.35	8.86	7.74	$1.8 \cdot 10^{-9}$
5	6.8	6.97	6.63	0.34	12.37	10.65	$9.2 \cdot 10^{-10}$
10	6.8	6.97	6.63	0.34	17.81	14.78	$3.5 \cdot 10^{-10}$
15	6.8	6.97	6.63	0.34	23.24	18.91	$2.4 \cdot 10^{-10}$
20	6.8	7.14	6.46	0.68	28.68	23.04	$3.2 \cdot 10^{-10}$

5.2.4. Numerical model geometry, initial and boundary conditions

To model the core flooding experiment performed on the fractured shale, we employ a dodecagon prism with the same diameter and length as the actual specimen. We include in the

model the porous disks at the two edges of the specimen, the Opalinus Clay rock matrix, and the fracture (Figure 5.2a and b). The material representing the natural fracture within the specimen is oriented at a 10° angle from the horizontal, consistent with the orientation in the actual fractured specimen. This fracture is surrounded by the low-permeable rock matrix, based on the results obtained for the intact Opalinus Clay specimen. Additionally, we include two porous disks on the specimen's ends, each with a thickness of 4 mm. Both the fracture and porous disks are crucial components for a realistic simulation of the advective flow of water during the test. The final 3D mesh used in the model consists of approximately 1200 nodes and 4700 tetrahedral elements, including 900 structured elements specifically representing the fractured zone (Figure 5.2c).

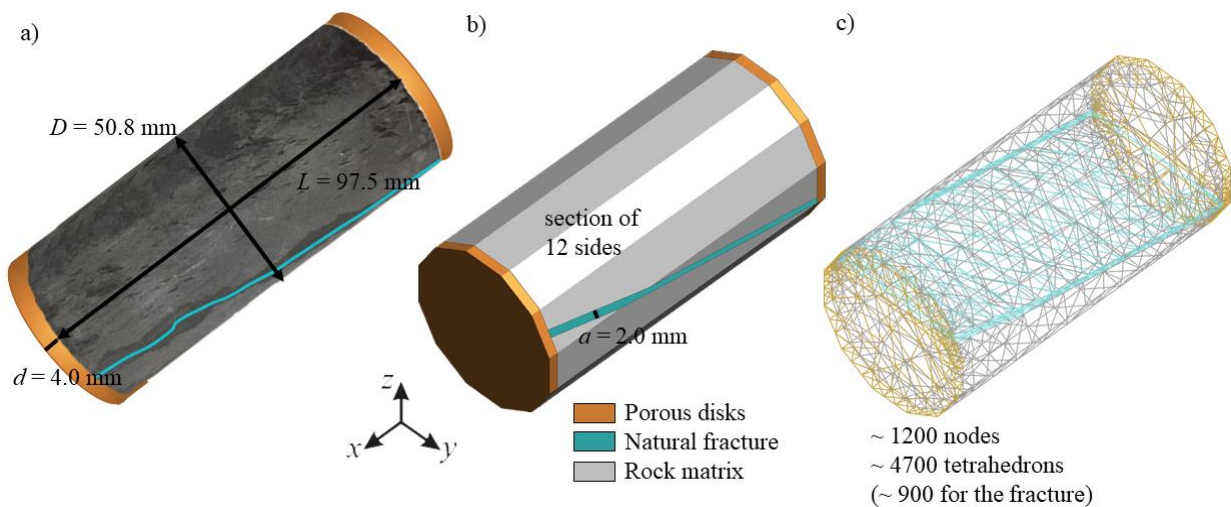


Figure 5.2. a) Image of the fractured specimen of Opalinus Clay; b) dodecagon prism used for the numerical modeling; and c) 3D finite element mesh. The different colors refer to different materials: bronze represents porous disks, cyan – the natural fracture material, and gray – the shale matrix.

We initiate the simulations by defining a constant pore pressure denoted as p_0 and the lateral and axial stresses σ_{lat} and σ_{ax} , respectively (Table 5.1). Figure 5.3 illustrates the hydro-mechanical boundary conditions to align with the experimental settings. We impose no-flow conditions and constant confining pressure on lateral boundaries. This is achieved by applying constant lateral stress, σ_{lat} , for each flat surface. The use of flat surfaces assures the accurate application of the confining pressure to the specimen. Additionally, we restrict axial displacements. Throughout the test, we maintain a constant room temperature of 22°C . For each loading stage, we run first an equilibrium phase, characterized by uniform pressures $p_{in} = p_{out} = p_0$. Once this equilibrium state is achieved, we induce fluid flow at the upstream and reduce the fluid pressure at the downstream according to the experimental data presented in Table 5.1.

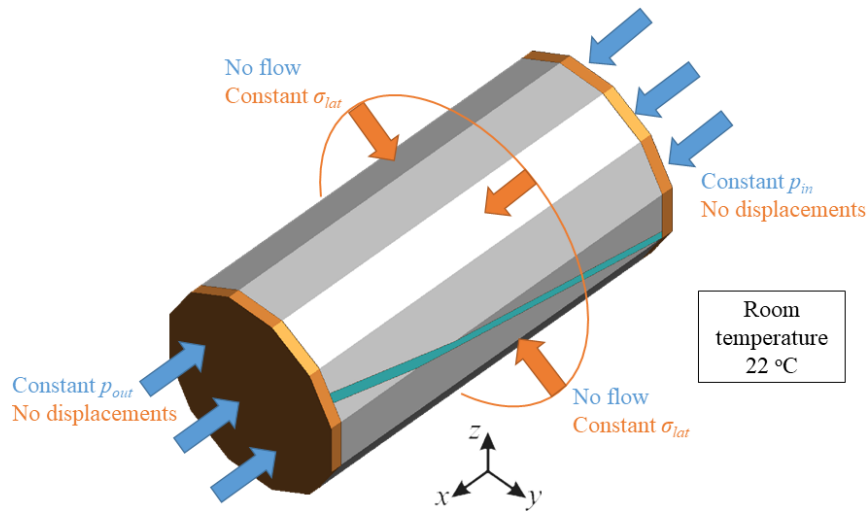


Figure 5.3. Hydro-mechanical boundary conditions applied during the simulations representing laboratory conditions.

The results are presented after reaching steady-flow conditions. Depending on the variable under consideration, outcomes for the natural fracture are represented on a 3D geometry when feasible, or, alternatively, along the axis labeled l , which follows the center of the fracture. To visualize both the fracture and the matrix results, we choose instead the xz representation plane (Figure 5.4).

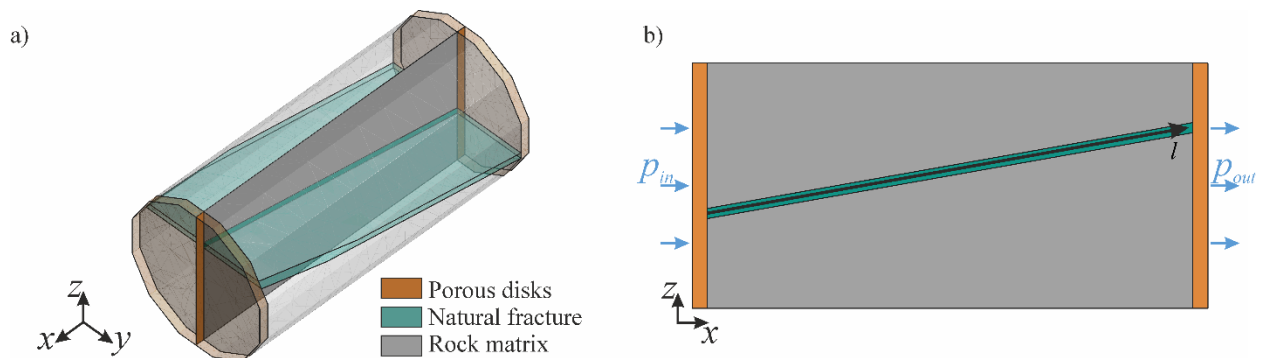


Figure 5.4. a) xz representation plane passing through the central axis of the specimen. b) The l coordinate is located within the xz plane along the center of the natural fracture.

5.3. Results

5.3.1. Hydro-mechanical properties

Table 5.2 presents the hydro-mechanical properties of a fractured Opalinus Clay specimen in comparison with a nearby intact specimen, as well as the properties of the natural fracture obtained from the calibration using numerical simulations. Additionally, the properties of porous disks utilized in steady-flow permeability tests in the laboratory are included.

Table 5.2. Hydro-mechanical properties for the fractured specimen, intact specimen, natural fracture, and porous disks. The values in the table include symbols that denote * measurements on the two specimens, ** inferred, and *** calibrated values for the natural fracture obtained through numerical simulations.

Hydro-mechanical properties	Fractured Opalinus Clay	Intact Opalinus Clay	Natural fracture	Porous disks
Young's modulus, E (GPa)	6.5*	2.9*	$(27.1-2.71)\times 10^{-6}$ ***	6.5*
Poisson ratio, ν (-)	0.38*	0.30*	0.38**	0.38*
Biot coefficient, α (-)	0.76*	0.73*	1.0**	0.7*
Porosity, ϕ (-)	0.13*	0.12*	1.0**	0.3*
Permeability, $k/10^{-20}$ (m ²)	49.1-4.5*	1.5-0.4*	$\sim 1\times 10^9$ -0.5**	5×10^7 *
Initial hydraulic aperture, b_0 (m)	-	-	2.7×10^{-7} **	-
Characteristic size, a (m)	-	-	2.0×10^{-3} **	-
Reference volumetric strain, ε_{v0} (-)	-	-	-5.0×10^{-4} ***	-

The mechanical properties, such as Young's modulus, Poisson's ratio, and Biot coefficient of the two specimens are reported under drained conditions, aligning with previous characterizations of shaly facies of Opalinus Clay (Bossart and Thury, 2011; Makhnenko and Podladchikov, 2018). Between the two specimens, there is approximately a two-fold difference in Young's moduli, suggesting a different orientation relative to the bedding (Bossart and Thury, 2011). Consequently, we assume the mechanical properties of the fractured specimen for the rock matrix during the numerical simulations (gray material in Figure 5.2b).

The permeability of the intact specimen, under a given effective mean stress, is at least one order of magnitude lower than that of the fractured specimen, and this difference is primarily attributed to the presence of the natural fracture. In the numerical simulations, the rock matrix permeability is assumed to be approximately 5×10^{-21} m², corresponding to the intact specimen. The natural fracture is initially considered sealed, i.e., its initial permeability matches that of the matrix. However, as the fracture expands (Equation 5.5), its permeability undergoes several orders of magnitude enhancement.

After establishing the hydraulic parameters of the fracture, we assume a constant Poisson's ratio identical to that of the matrix. Using an inferred value of the initial aperture b_0 of the fracture (Appendix C), we minimize the distance between numerical and experimental data changing the reference volumetric strain ε_{v0} and Young's modulus of the fracture E_{fr} . Finally, the normal stiffness of the natural fracture K_n is approximated as (Rutqvist and Stephansson, 2003; Zareidarmiyan et al., 2020)

$$K_n = \frac{1 - \nu_{fr}}{(1 + \nu_{fr})(1 - 2\nu_{fr})} \frac{E_{fr}}{b_0} \quad (5.7)$$

Here, the subscript *fr* denotes the values of Young's modulus and Poisson's ratio for the natural fracture, resulting in K_n values ranging from 18.7 to 187.2 MPa/mm.

5.3.2. Stress-dependent normal stiffness of the fracture

The intrinsic permeability of fractured Opalinus Clay ranges from 4.9×10^{-20} to $9.1 \times 10^{-19} \text{ m}^2$, approximately one to two orders of magnitude higher than the permeability of intact Opalinus Clay (Figure 5.5). This difference suggests that even under high P' values, the fractures within the Opalinus Clay do not close due to fracture roughness. Moreover, the presence of macropores in the fractured shale contributes to an increase in permeability at a given P' .

Our hydro-mechanical simulations are specifically built to reproduce the laboratory conditions (Section 5.2.4). Through these simulations, we determine that the normal stiffness of the fracture that provides the best match for our laboratory results is $K_n = 18.7 \text{ MPa/mm}$ (orange circles in Figure 5.5). However, for a mean effective stress of 20 MPa, the permeability of the specimen tended to be overestimated for this normal stiffness. To address this issue, we increase the stiffness value by an order of magnitude ($K_n = 187.2 \text{ MPa/mm}$). This adjustment allows us to achieve a good fitting of the experimental results (red circle in Figure 5.5). The alteration in mechanical behavior, which is also influenced by increased fluid flow, is primarily attributed to the distinct mechanical response of the fracture under higher confinement. Finally, we include the permeability values for the rock matrix (gray plus in Figure 5.5). These values remain within the same order of magnitude as the measured intrinsic permeability of intact shaly facies of Opalinus Clay, for the range of considered P' (blue crosses in Figure 5.5).

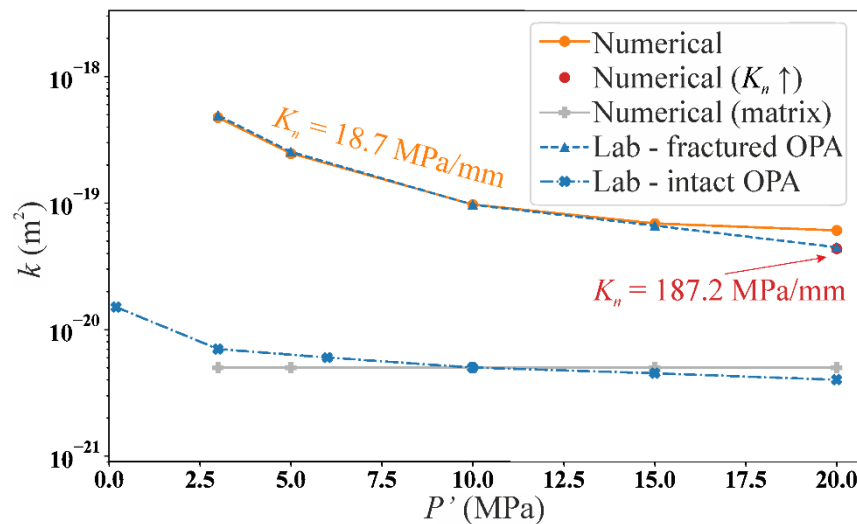


Figure 5.5. Intrinsic permeability of intact (blue crosses) and fractured (blue triangles) shaly facies of Opalinus Clay (OPA) presented as a function of the effective mean stress; compared with the results of the simulations for the whole specimen (circles in orange and red) and for the rock matrix (gray pluses).

5.3.3. Fracture deformation

After determining the natural fracture normal stiffness at each loading step, we proceed to provide a comprehensive analysis of the coupled hydro-mechanical behavior of fracture under steady-state flow conditions. To accomplish this, we define the l coordinate situated within the xz plane, which bisects the specimen into equal halves and aligns with the central axis of the fracture (Figure 5.4). The overpressure distribution Δp appears to be non-uniform along the fracture (Figure 5.6a). The difference between input and output pressures is approximately 0.34 MPa for effective mean stress P' ranging from 3 to 15 MPa. For $P' = 20$ MPa, the difference increases to approximately 0.68 MPa, as measured in the experiments (Table 5.1). Interestingly, higher pressure gradients concentrate at the edges of the fracture, close to the inflow and outflow boundaries, implying that a higher permeability is generated in the central part of the fracture (Figure 5.6a).

In response to the fluid pressure change, the fracture tends to expand. However, this expansion is partially restrained at the edges of the fracture by the boundary condition that assumes no axial displacement, resulting in a significant increase in the normal stress at the edges, especially at the inflow (Figure 5.6b). The normal stress changes are independent of the confinement, as the pressure variations are very similar in all cases and for the case of a stiffer fracture, the overpressure is also higher by a similar proportion. By subtracting the change in pore pressure Δp from the change in normal stress $\Delta\sigma_n$, we obtain the effective normal stress on the fracture $\Delta\sigma'_n$ (Figure 5.6c). Note that while in the central portion of the fracture the changes are negative, i.e., the effective normal stress becomes less compressive, the changes are positive at the edges, meaning that compression increases. Regarding the shear stress changes along the fracture $\Delta\tau$, given that the fracture is oriented sub-horizontally at 10° inclination and horizontal displacements are constrained by the boundaries, the values of $\Delta\tau$ are limited to tens of kilopascals - an order of magnitude lower than $\Delta\sigma'_n$ (Figure 5.6d).

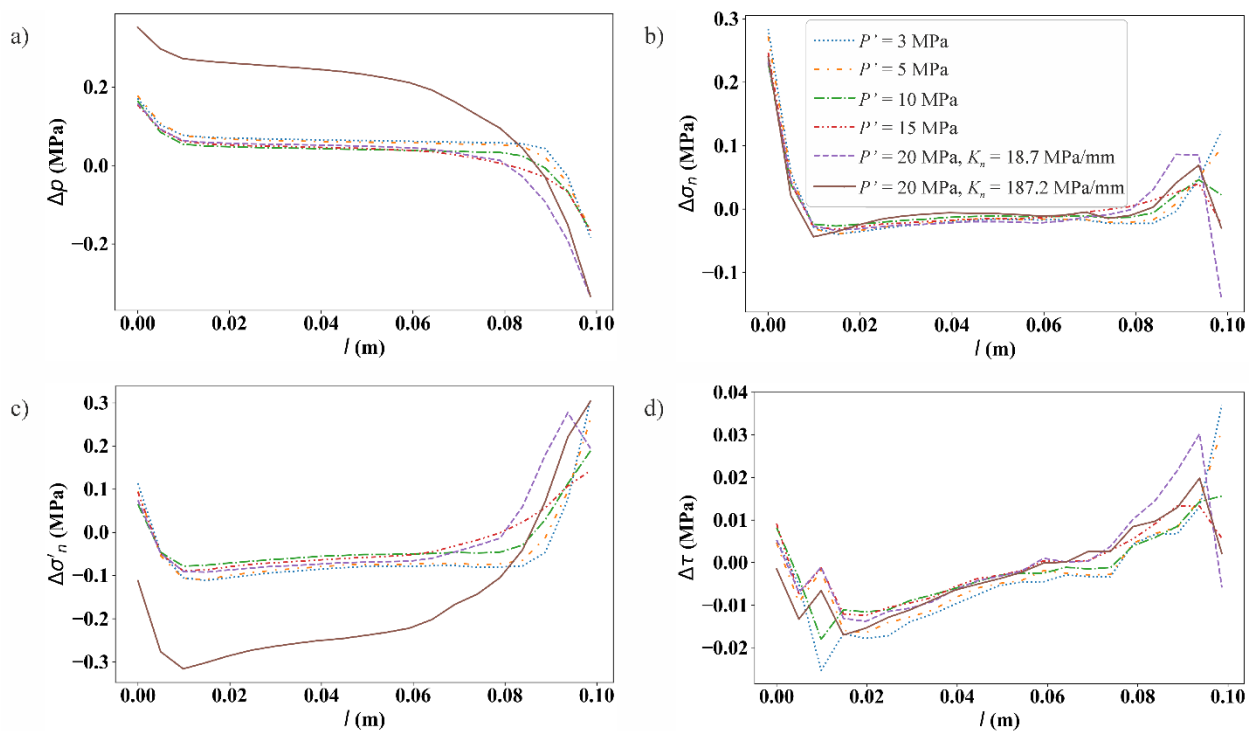


Figure 5.6. a) Fluid overpressure along the fracture Δp ; b) changes in stress normal to the fracture $\Delta\sigma_n$; c) changes in effective stress normal to the fracture $\Delta\sigma'_n$; and d) changes in shear

stress at the fracture $\Delta\tau$, within the coordinate l (see Figure 5.4), for the tested mean effective stresses P' .

The changes in effective normal stress and shear stress along the fracture result in changes in the deformation field (Figure 5.7). Figure 5.7 shows the volumetric deformation along with arrows representing the displacements of the fracture for section xz (Figure 5.4) for all the fitting points previously illustrated in Figure 5.5. The steady horizontal flow from left to right of the section results in a non-uniform opening of the fracture (Figure 5.7). In all cases, the edges of the fracture encounter constraints imposed by the boundary conditions that restrict expansion. In contrast, the central portion tends to expand, leading to a higher increase in permeability compared to the edges (see Section 5.3.4). The expansion of the fracture is only partially offset by the compression of the surrounding material such that an overall lateral deformation of the specimen is on the order of micrometers.

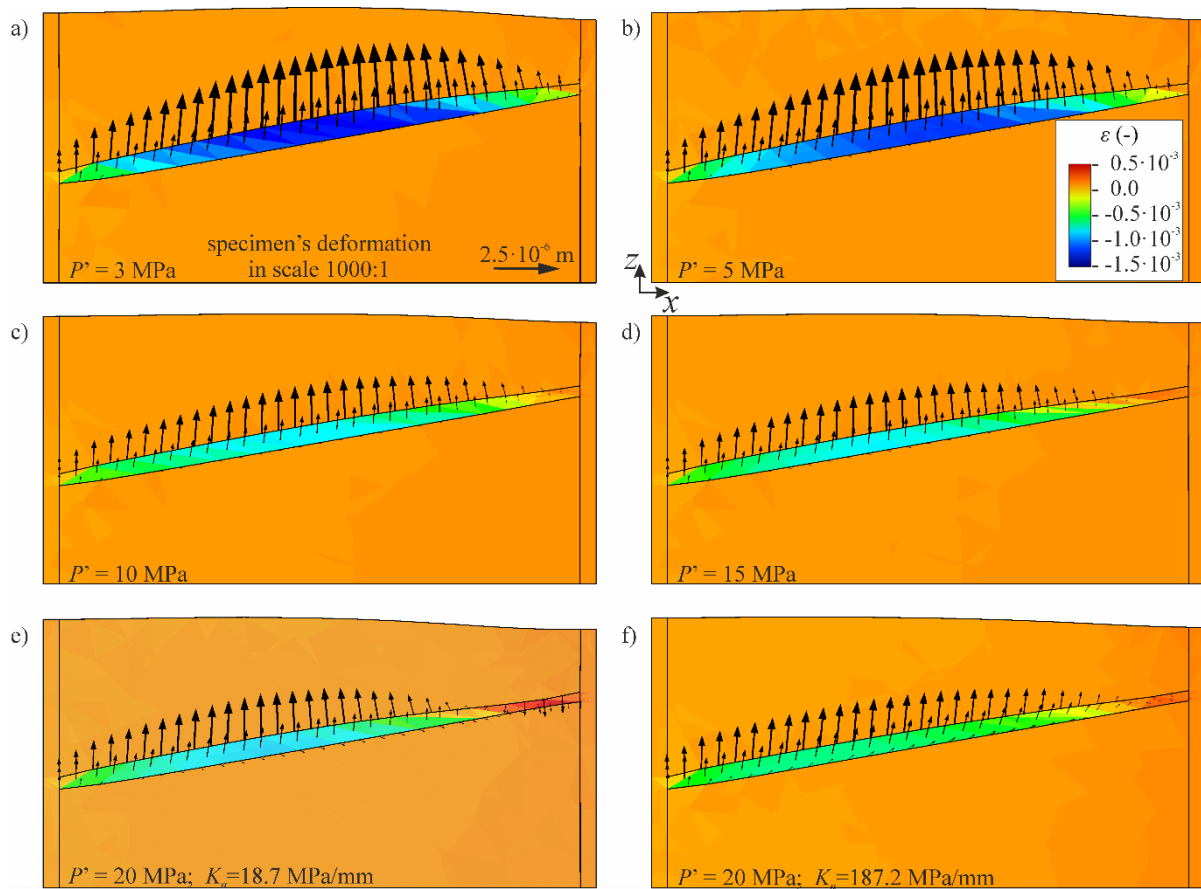


Figure 5.7. Contour plots of volumetric strain and arrows indicating fracture displacement in the xz section (Figure 5.4) for effective mean stress of a) $P' = 3$ MPa; b) $P' = 5$ MPa; c) $P' = 10$ MPa; d) $P' = 15$ MPa; e) $P' = 20$ MPa with a normal stiffness of $K_n = 18.7$ MPa/mm; and f) $P' = 20$ MPa with $K_n = 187.2$ MPa/mm. The normal stiffness in a) to d) is $K_n = 18.7$ MPa/mm.

Note that the specimen's deformation is scaled up by a factor of 1000 to clarify the final deformed state of the specimen and the fracture.

An examination of the arrows, i.e., fracture displacement, further reveals that the primary component of deformation is in the normal direction, resulting in an increase in opening due to tensile forces while the sliding component is secondary. This is caused by the boundary conditions and the geometry of the fracture (Zareidarmiyan et al., 2018) and aligns with the

results shown in Figure 5.6. The simulation indicates that the fracture tendency to expand is constrained under the relatively high effective mean stress P' (Figure 5.7). This constraint results in reduced permeability within the fracture, which subsequently leads to diminished permeability within the specimen as a whole (Figure 5.5).

Finally, Figures 5.7e and 5.7f distinguish the discrepancy in volumetric strain profile resulting from different fracture normal stiffness under the highest P' . In the case of lower normal stiffness (18.7 MPa/mm), the fracture opens more whereby permeability within the fracture increases significantly and ultimately causes a drop in upstream fluid pressure (dashed violet line in Figure 5.6a). Consequently, this scenario results in an overestimation of the permeability for the entire specimen (Figure 5.5). A stiffer fracture restricts fracture opening during fluid flow and provides a more accurate representation of permeability (Figure 5.5).

5.3.4. Permeability changes and flow along the fractured specimen

The non-uniform expansion along the fracture (Figure 5.7) causes a non-uniform spatial distribution of permeability within the natural fracture (Figure 5.8). Permeability changes are highly sensitive to deformation because they are proportional to the cube of the fracture aperture. The largest permeability is generated at the center of the specimen, while permeability remains low at the edges of the fracture due to different degrees of freedom. When considering the scenario with the lowest confinement (Figure 5.8a), the range of permeability values spans over nine orders of magnitude. It extends from the initial value k_0 of $5.0 \times 10^{-21} \text{ m}^2$ to a maximum value reaching approximately 10^{-11} m^2 , near the center. This range gradually narrows down to the maximum permeability of approximately 10^{-15} m^2 under the conditions of maximum confinement and stiff fracture (Figure 5.8f).

The tendency toward a reduction in the maximum permeability value within the fracture as the effective mean stress increases is altered between 15 and 20 MPa. The higher maximum permeability in Figure 5.8e ($P' = 20 \text{ MPa}$) than in Figure 8d ($P' = 15 \text{ MPa}$) is caused by the larger pressure change between the inflow and the outflow in the former case (recall Table 5.1). Yet, for a given overpressure, the higher the confinement, the lower the permeability enhancement. Similarly, the stiffer the fracture, the lower the permeability enhancement, as shown by a reduction in one order of magnitude in the maximum permeability (from 10^{-14} to 10^{-15} m^2) for the case in which the fracture is an order of magnitude stiffer (compare Figures 5.8e and 5.8f).

The permeability at the edges of the fracture remains similar to that of the rock matrix (Figure 5.8), making them barriers to the fluid flow. As a result, fluid exchange between the matrix and the fracture is enhanced at the edges of the fracture, resulting in non-uniform pressure contour lines (Figure 5.9). This deviation from vertical lines (see Appendix C for a comparison) indicates that the flow happens not exclusively in the horizontal direction, but instead creates distinct bulbous regions on both edges of the fracture. This result highlights the complexity of fluid flow in low-permeability fractured rock, in which accounting for the hydro-mechanical couplings is crucial to reproduce the observed response to fluid injection.

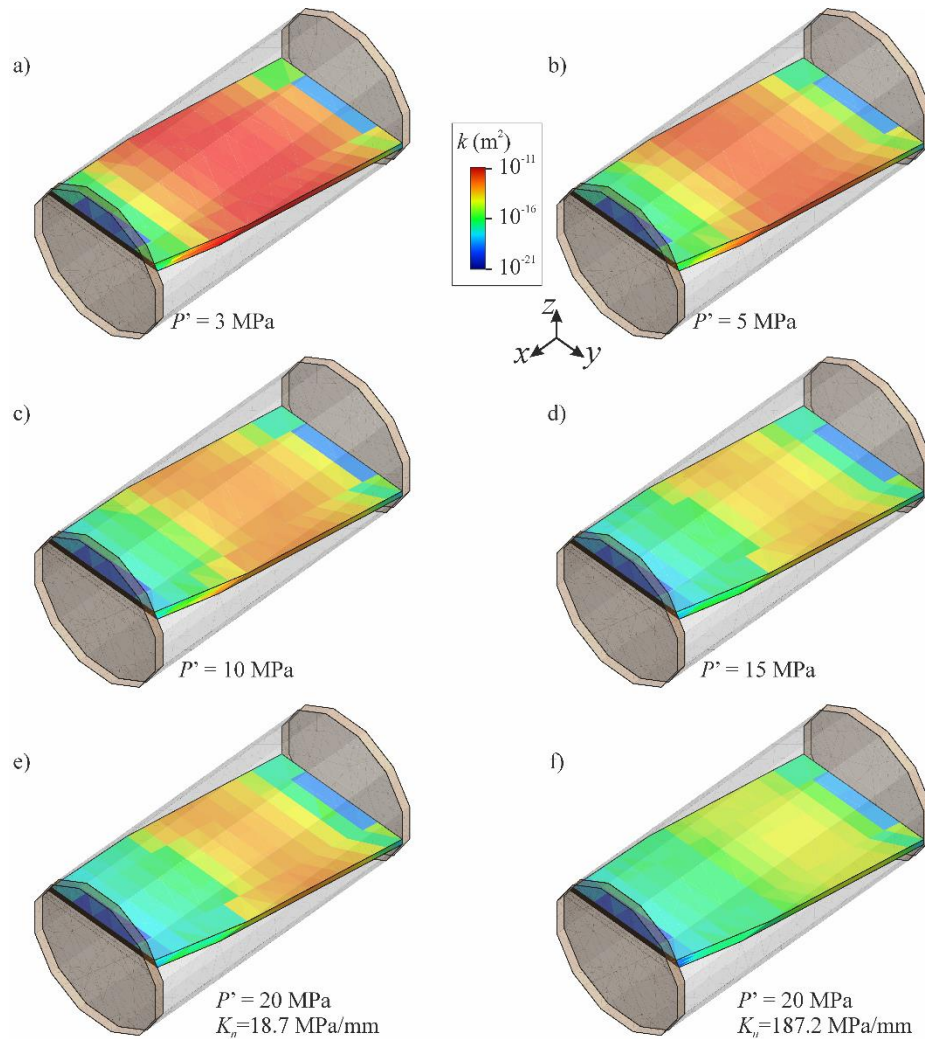


Figure 5.8. Distribution of fracture permeability for the effective mean stress of a) $P' = 3$ MPa; b) $P' = 5$ MPa; c) $P' = 10$ MPa; d) $P' = 15$ MPa; and e) $P' = 20$ MPa for two different normal stiffness of e) $K_n = 18.7$ MPa/mm; and f) $P' = 20$ MPa with $K_n = 187.2$ MPa/mm. The normal stiffness in a) to d) is $K_n = 18.7$ MPa/mm.

The bulb-shaped patterns around the fracture edges suggest that a vertical flow component is present in addition to horizontal flow within the specimen. Specifically, near the upstream side, the fluid is directed toward the fracture, while at the downstream, the fluid spreads away from the fracture. The flow lines in Figure 5.9 help to visualize how the fluid moves within the undisturbed material. However, it is important to note that we only depict directional arrows for the rock matrix because the flow rates within this region are relatively low with respect to the ones along the fracture, measuring less than 3×10^{-7} m³/s. In contrast, the flow rates within the natural fracture are over two orders of magnitude greater.

The described phenomenon tends to manifest consistently with minimal variations when the specimen is subject to low effective mean stresses, up to $P' = 15$ MPa. However, at $P' = 20$ MPa, it becomes evident that the higher pressure differences between the inflow and outflow boundaries result in increased fluid flow rates. Furthermore, the higher normal stiffness of the fracture alters the distribution of overpressures compared to the other cases (Figure 5.9f). In this case, fluid flow from the left to the right generates an overpressure front that extends across more than half of the specimen. This observation highlights the impact of the fracture's mechanical properties on the pressure distribution within the specimen.

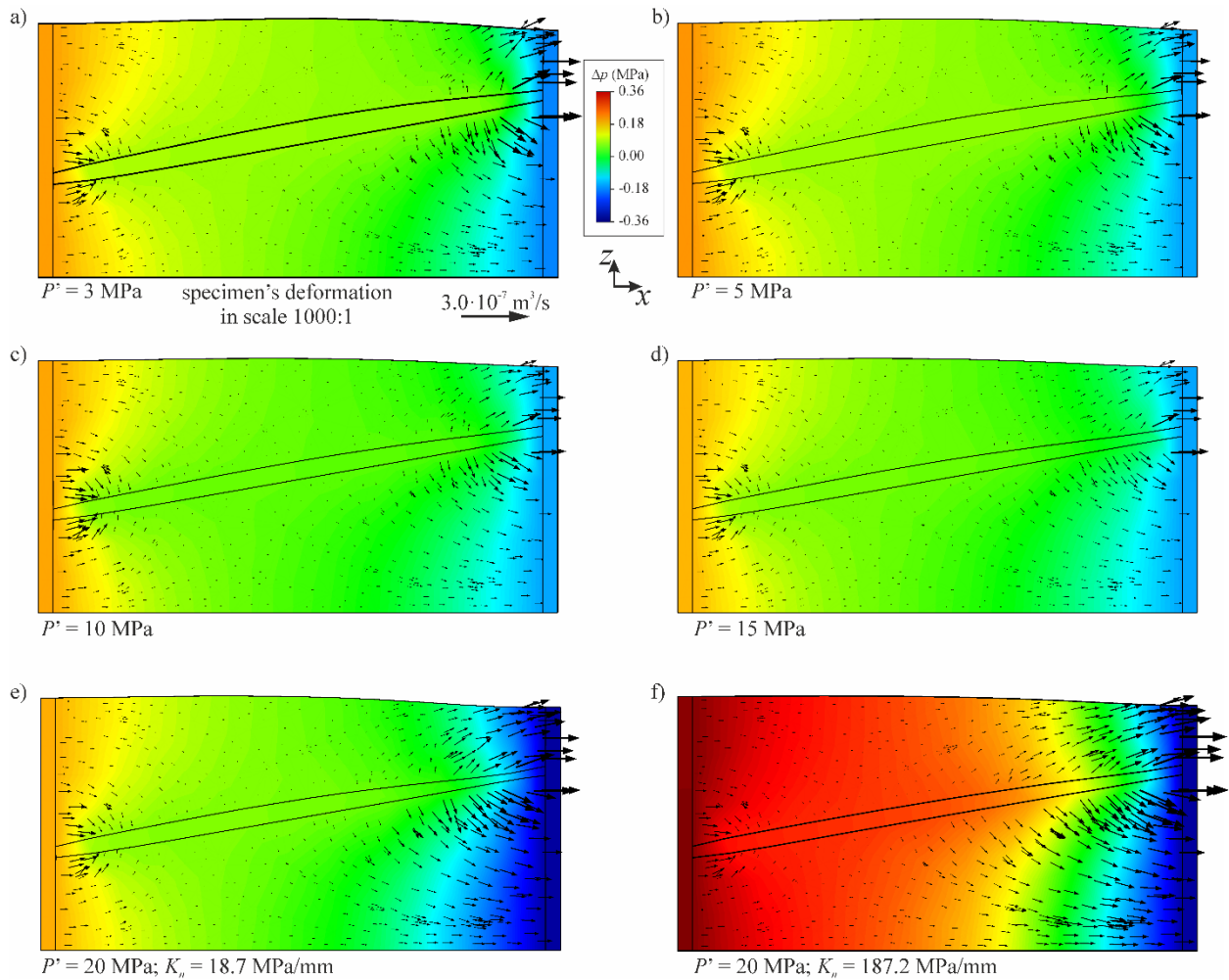


Figure 5.9. Contour plots of overpressure and arrows indicating fluid flow in the intact material. The specimens xz are deformed on a scale of 1:1000. The plots represent an effective mean stress of a) $P' = 3$ MPa; b) $P' = 5$ MPa; c) $P' = 10$ MPa; d) $P' = 15$ MPa; e) $K_n = 18.7$ MPa/mm; and f) $P' = 20$ MPa with $K_n = 187.2$ MPa/mm. The normal stiffness in a) to d) is $K_n = 18.7$ MPa/mm.

5.4. Discussion

The hydraulic tests carried out on the intact and fractured specimens allow the characterization of the hydro-mechanical response of a fracture, describing how it behaves in terms of opening and closing under different confinements. As normal stresses increase, fractures show a non-linear, stress-dependent closure due to the growing number of contact points (Bandis et al., 1983; Barton et al., 1985, Pyrak-Nolte and Morris, 2000). Contact areas within the fracture are not evenly distributed, and their evolution can vary significantly under different normal stresses. This non-uniform distribution makes it challenging to accurately describe how the fracture seals, especially at field scales (Rutqvist, 2015). Consequently, at high effective mean stresses, the fracture normal stiffness K_n undergoes a substantial enhancement. Our calibration reveals an enhancement in K_n by an order of magnitude, for effective mean stresses ranging from 3 to 20 MPa. However, under in-situ conditions P' up to 10 MPa at Mont Terri (Martin and Lanyon, 2003; Guglielmi et al., 2020a), we determine that the K_n remains relatively

constant compared to the lowest considered confining pressure, approximately at 20 MPa/mm. This stability in stiffness within the in-situ stress range suggests that the fracture behavior experiences minimal changes under these in-situ conditions. Our model also considers the initial sealing of the fracture as confinement increases, typical of in-situ conditions in shales (Guglielmi et al., 2021), by the numerical characterization of the threshold value for volumetric deformation ε_{v0} , above which the fracture permeability starts to increase.

Yet, the aperture of rough-walled natural fractures not only depends on normal effective stress but also on shear displacement (Barton et al., 1985). By separating aperture change Δb into these two contributions, it equals the sum of Δb_n (the change of aperture caused by the application of normal stress, characterized by the normal stiffness K_n) and Δb_s (the change of aperture due to shear displacements Δu_s), characterized by the shear stiffness $K_s = \Delta\tau/\Delta u_s$. Within the core flooding device steady-flow permeability test conducted on a poorly inclined fractured specimen, the axial displacements are inhibited. Consequently, shear displacement on the natural fracture is negligible under these conditions. Other experiments would be necessary to characterize the shear dilatant behavior of the natural fracture.

The hydraulic apertures of the natural fracture b range from one-tenth of a micrometer to a few micrometers. However, due to the rough surface of the fracture, the geometrical mean apertures (referred to as mechanical apertures, b_m) are larger. From the empirical relation of Barton et al. (1985), which links these two types of apertures based on a parameter called the Joint Roughness Coefficient (JRC), we represent the values of b_m (Figure 5.10). Depending on whether the fracture surface is relatively smooth or rough, the resulting mechanical mean apertures tend to be in the range of tens of micrometers. This observation is consistent with the direct observations of Voltolini and Ajo-Franklin (2020) for a single tensile artificial fracture induced in a shaly facies specimen of Opalinus Clay.

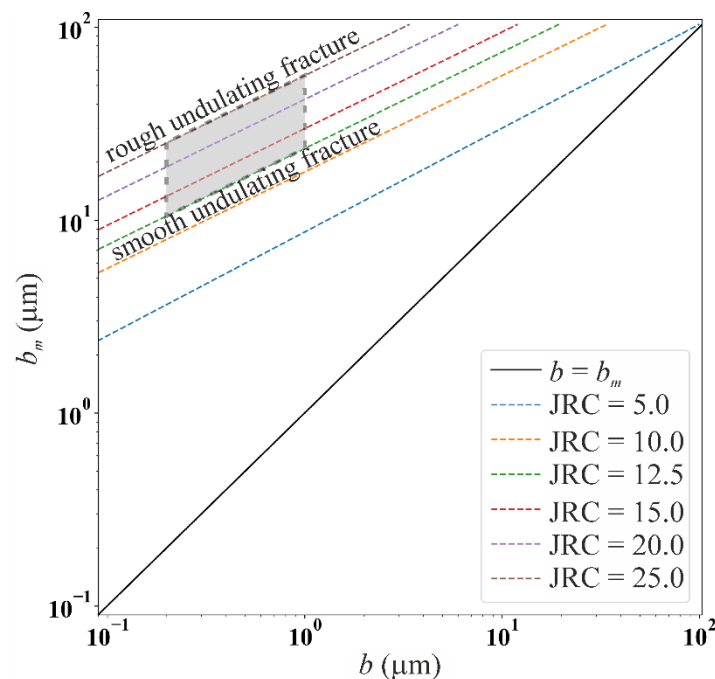


Figure 5.10. Empirical relation of hydraulic mean aperture b versus mechanical mean aperture b_m of a fracture, from Barton et al. (1985), for different Joint Roughness Coefficients (JRC) of the fracture.

Identifying the spatial permeability distribution of fractures in shale is important not only to assess their sealing potential but also to properly define the pore pressure distribution. Simulation results highlight the importance of considering aperture-dependent permeability

along the fracture to estimate pressure distribution in the rock matrix (Figure 5.9), compared with the constant fracture aperture conditions (Figure C1). Expansion is limited due to boundary conditions in the laboratory on both sides of the fracture. Near the downstream, this effect is more pronounced because pressure decreases compared to the initial conditions. In turn, these small aperture regions influence the distribution of pressure within the surrounding rock matrix. When certain parts of the fracture are sealed or partially sealed, it causes changes in the distribution of overpressure. The resulting non-uniform pressure field can lead to complex flow patterns where there are non-negligible exchanges of fluid between the fracture and the surrounding low-permeability matrix. This complex flow pattern challenges the common modeling assumption that the caprock material is impermeable, as there are instances where fluid can move between the fracture and the surrounding rock matrix.

Experimentally, the permeability of the fractured Opalinus Clay specimen decreases as the effective mean stress increases. The reduction in a fractured specimen is more pronounced than that in the intact specimen (Kim and Makhnenko, 2020). This difference is primarily because the fracture tends to close as the effective mean stress increases. Despite the fracture serving as a pathway for fluid flow within the rock, the fractured specimen exhibits hydraulic properties, i.e., permeability and porosity, within the same order of magnitude as those typically reported for shales (Neuzil, 2019). In particular, the permeability of fractured Opalinus Clay is in line with the acceptable range for potential caprock, ranging from about 10^{-18} to 10^{-21} m² (Dewhurst et al., 1999). Nonetheless, upscaling laboratory experiments to the field in underground rock laboratories is important to determine the potential permeability enhancement when pressurizing fractures contained in the caprock as our simulation results reveal that permeability enhancement not affected by the boundaries of the experiment can be of several orders of magnitude. The combination of laboratory experiments with the interpretation of results through coupled hydro-mechanical simulations permits gaining insight on the intricate processes that occur as a result of fluid injection into fractured rock.

5.5. Conclusions

Steady-state fluid flow experiments on a naturally fractured Opalinus Clay specimen have revealed a significant increase in permeability by up to two orders of magnitude with respect to the intact material. Through numerical analysis of the experimental results, we have successfully characterized the hydro-mechanical properties of the fracture and identified variations in hydraulic aperture across its spatial extent. Our numerical calibration suggests the value of normal stiffness for the fracture of 18.2 MPa/mm for effective mean stresses from 3 to 15 MPa, increasing by one order of magnitude for the highest confinement ($P' = 20$ MPa). These findings highlight the importance of considering stress-dependent parameters when characterizing fractures in shale. The fracture characterization approach enhances our understanding of its coupled hydro-mechanical behavior and contributes to more accurate predictions of stress and pore pressure along the fracture and within the surrounding rock matrix. Our approach enables a precise representation of stress and pore pressure distribution within fractured rock, which has crucial implications for subsurface geo-energy applications.

Chapter 6

Conclusions

The lack of a clearly defined methodological characterization protocol in geo-energy projects has led to undesirable consequences and failures. To prevent similar situations, a proper characterization should be performed not only prior to the start of operation, but also during the whole lifetime of the project. The impact of the total cost of an accurate subsurface characterization will in any case be minimal if compared to the advantages that may derive from it. Indeed, it is possible to reduce the uncertainties in design and adapt during operation with the right investigation, characterization and modelling.

We proposed diverse hydro-mechanical characterization over multiple scale and we focused on the application of clay-rich rocks as sealing formations for Geological Carbon Storage (GCS). The field-scale investigation focused on characterizing rocks using analytical and numerical methods to interpret periodic pressure signals in diverse scenarios, such as energy storage, CO₂ injection experiments, and geothermal stimulation. The study considered rock dimensions ranging from kilometers to half a meter and highlighted the importance of acknowledging potential errors when assuming the uncoupling of pore pressures and stress variations in rocks. Findings indicated that the relative error for simplified geometries was below 3% for one-dimensional diffusion and 1.4% for radial diffusion. However, complex in-situ scenarios, including geological heterogeneity and hydraulic barriers, could introduce more significant errors requiring careful examination.

Numerical analyses were conducted to assist in the design of the CO₂ Long-term Injection Experiment (CO₂LPIE) at the Mont Terri rock laboratory, focusing on Opalinus Clay. Due to the high entry pressure and low permeability of Opalinus Clay, free-phase CO₂ flow is limited, with injected fluid advancing primarily through molecular diffusion, reaching 1 m after 2 years and 2.5 m after 20 years. Rock deformation and stress changes occur along bedding planes, resembling the anisotropic properties of Opalinus Clay.

At laboratory scale, Steady-state fluid flow experiments conducted on naturally fractured Opalinus Clay revealed a substantial increase in permeability, reaching up to two orders of magnitude higher than that of the intact material. Through numerical analysis, the hydro-mechanical properties of the fracture were successfully characterized, including variations in hydraulic aperture across its spatial extent. The numerical calibration indicated stress-dependent behavior with an increase by one order of magnitude under higher confinement. These findings underscore the significance of considering stress-dependent parameters in shale fracture characterization.

Each of the proposed methodologies contributes to an enhanced comprehension of the coupled hydro-mechanical behavior within the matrix and fractures of shale formations. The multiscale analysis affords overall insights into the intricacies of the problem, having a robust initial approximation of the hydro-mechanical phenomena. Laboratory characterization serves to delineate the processes influencing the compromising of shales' sealing capacity. Underground rock laboratory experiments serve as a pivotal bridge between these scales, proving good capability in upscaling rock properties and exploring the conditions under which the defined laboratory processes predominate on a larger scale.

Appendix A

Validation of Adachi and Detournay (1997) solution at the core scale

To validate Adachi and Detournay's (1997) solution at the core scale, we run a coupled HM numerical simulation reproducing the same conditions. The geometry represents an axisymmetric domain composed of a slender specimen of radius $R = 0.03$ m and length $L = 0.1$ m with a symmetry axis of $y = 0$ and a downstream compartment of the same radius to the rock specimen and length $L_D = 0.106$ m, resulting in a dead volume $V_D = 3 \cdot 10^{-4}$ m³ (Figure A1).

We impose horizontal flow by applying a periodic pressure signal on the left-hand side of the specimen. The stress is constant on the lateral side of the specimen while displacement perpendicular to the downstream side is prevented (Figure A1). In this way, the downstream volume is constant, given also the stiffness assigned to the material (Table A1). We solve for pressure diffusion into the specimen both numerically and analytically (Equations 3.4 and 3.7) using material properties listed in Table A1. The comparison of the analytical and numerical solutions shows almost perfect fitting (Figure A2).

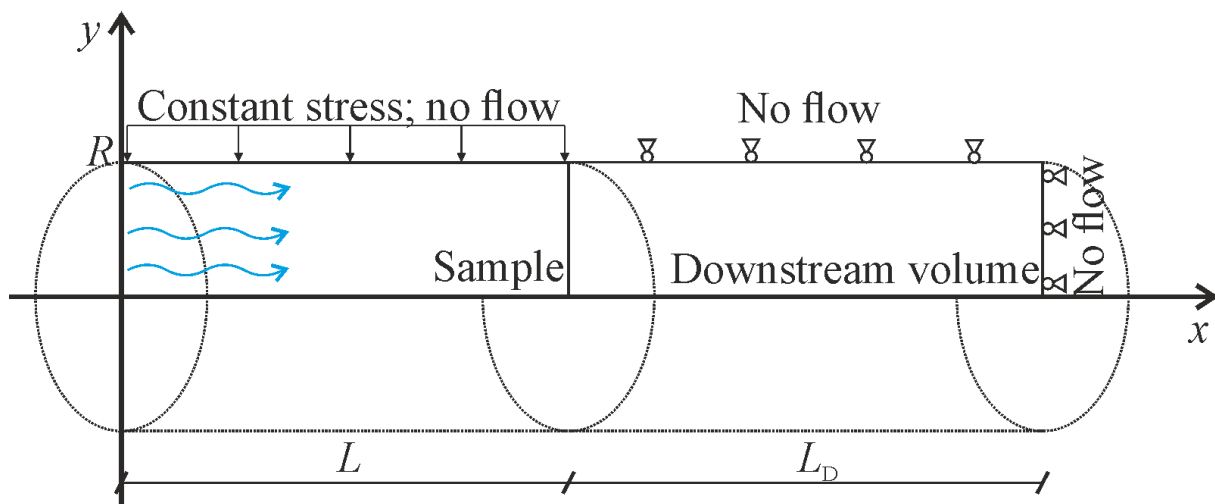


Figure A1. Axisymmetric numerical model (around x) with HM boundary conditions to reproduce Adachi and Detournay (1997) solution at the core scale.

Table A1. Parameters to replicate the case study of Adachi and Detournay (1997) in our HM numerical simulation.

Parameter	Sample	Downstream
K (GPa)	5.0	333.3
K_s (GPa)	33.0	222.2
K_f (GPa)	2.25	2.25
ϕ (-)	0.25	1.00
k (m ²)	$1.0 \cdot 10^{-14}$	$1.0 \cdot 10^{-9}$
B (-)	0.60	1.00
D (m ² /s)	$2.90 \cdot 10^{-2}$	$1.67 \cdot 10^3$

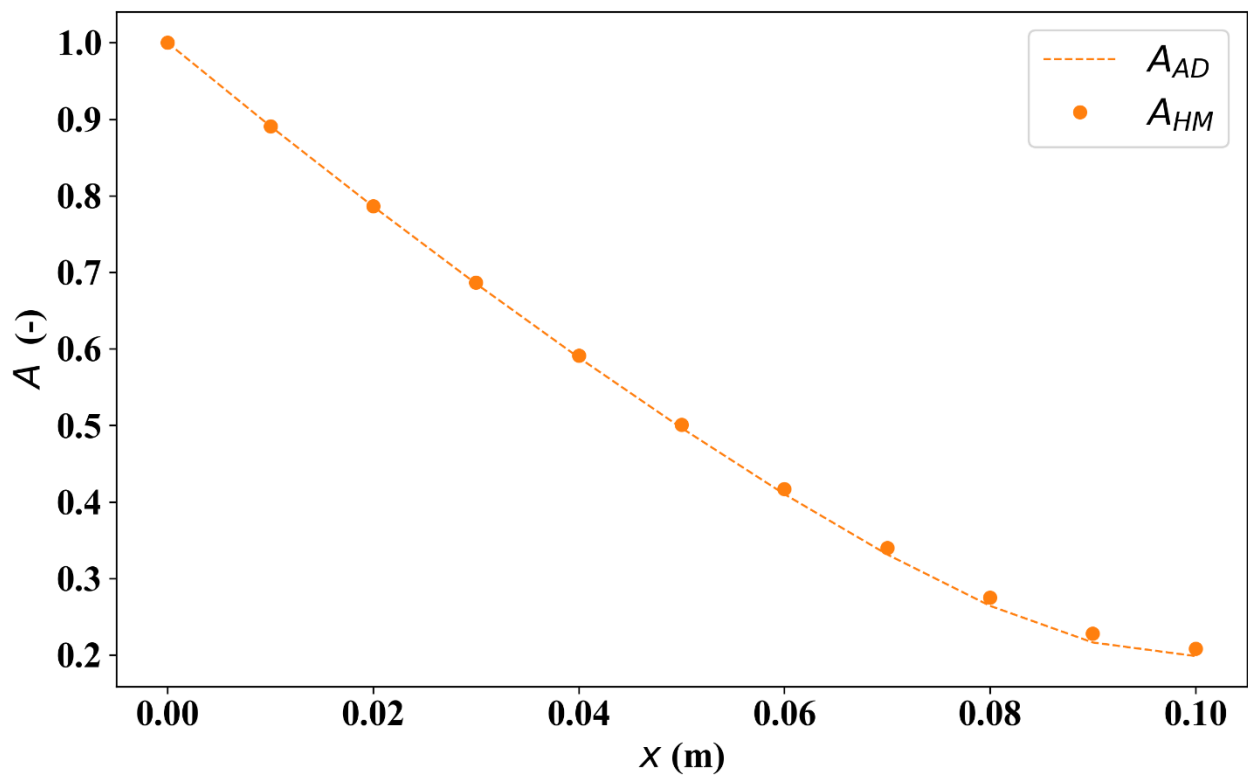


Figure A2. Amplitude ratio of Adachi and Detournay (1997) analytical solution A_{AD} and the numerical results A_{HM} .

Appendix B

3D hydro-mechanical modeling of shaly caprock response to CO₂ long-term periodic injection experiment (CO₂LPIE)

introduction

To limit global warming to 1.5 °C, net carbon removal after 2050 should be targeted (IPCC, 2014). To reach this goal, it is critical to develop novel technologies and a promising approach is Carbon Capture and Storage (CCS). CCS is generally understood as the set of CO₂ capture from a large stationary source, transport to an injection site, and permanent storage in the subsurface (Benson and Cook, 2005). CO₂ density at the pressure and temperature of typical underground storage formations in sedimentary basins is approximately 65 % of the in-situ brine density. As a result, the plume of the injected CO₂ will not only migrate outwards from the injection well, but also upwards until it finds a sealing layer called caprock (Tsang and Niemi, 2017). To assure long-term CO₂ trapping, it is of fundamental importance to properly characterize the caprock sealing capacity, commonly presented in terms of permeability, porosity, capillary entry pressure and relative permeability curves, and their evolution with time (Kaldi et al., 2011).

Several laboratory experiments analyzed the sealing capacity of intact caprock samples (Hildenbrand et al., 2002; Boulin et al., 2013; Makhnenko et al., 2017; Rezaee et al., 2017; Minardi et al., 2021; and Kivi et al., 2022a). However, upscaling these results to the reservoir scale and quantifying their evolution due to long CO₂ injection remain unclear. For example, at the Sleipner storage site, Cavanagh and Haszeldine (2014) inferred an entry pressure for the interbedding shale layers being 35 times lower than that measured in the laboratory. This discrepancy may arise from the coupled thermo-hydro-mechanical response of the intact material and the existence of discontinuities on a larger scale. The presence of fault zones and bedding planes may result in localized deformation and fluid flow (Rutqvist and Tsang, 2002; Rutqvist et al., 2016). In addition, the injection generates an overpressure, which favors CO₂ intrusion into the caprock. This may lead to the expansion of the formation that changes the caprock sealing capacity (Rutqvist, 2012; Vilarrasa et al., 2015).

In-situ monitoring during several demonstration and industrial-scale CO₂ injection projects have provided fundamental insights into the caprock sealing behavior. However, given the complexity of managing CCS, the associated costs, and the resolution of monitoring equipment, there is a lack of detailed comprehensive information concerning the hydro-mechanical (HM) response of the caprock to the injected CO₂. From this point of view, underground rock laboratories (URLs) represent a connection between laboratory experiments and in-situ observations. Particularly, the Mont Terri rock laboratory in Switzerland, with its tunnel and niches system mainly excavated in Opalinus Clay, provides a unique, undisturbed environment to drill and instrument wells for the conduction of different CO₂ injection experiments. In this context, the CO₂ Long-term Periodic Injection Experiment (CO₂LPIE) aims at assessing the caprock sealing capacity. The experiment plans to inject gaseous CO₂ into Opalinus Clay, with a mean overpressure of 1 MPa (above the initial 2 MPa pore pressure present in the rock laboratory) and a cyclic pressure variation. At the design stage, it is necessary to predict the values that measured properties may take and establish a starting point for the HM analysis. For this reason, we perform 3D-HM simulations of CO₂LPIE. The 3D model allows obtaining more

realistic predictions of the rock deformation and flow in the presence of bedding planes, and hence, is essential for the design of the experiment.

We present a synthetic description of the model and the representative parameters for Opalinus Clay. We evaluate the evolution of displacement and pressure fields inside the rock for a period of two years and inspect CO₂ flow mechanisms, as well as the stability of the rock mass and the bedding planes.

3D numerical model

We build a 3D model of the CO₂LPIE experiment using the fully coupled finite element code CODE_BRIGHT (Olivella et al., 1994; Olivella et al., 1996) extended and tested for CO₂ injection (Vilarrasa et al., 2010a; Vilarrasa et al., 2010b; Vilarrasa et al., 2017). The code solves simultaneously the momentum balance and the mass conservation of CO₂ and water. The advective fluxes of the two phases are calculated following Darcy's law, with different values of permeability parallel and normal to the bedding (Table B1). We stipulate no transport of vapor in the gas phase and estimate the diffusion of CO₂ inside the liquid phase with Fick's law. The strains are then evaluated using the poroelastic theory (Detournay and Cheng, 1993; Cheng, 2016)

$$\boldsymbol{\sigma} = \mathbf{C}\boldsymbol{\varepsilon} + \boldsymbol{\alpha}p; \quad (\text{B1})$$

where $\boldsymbol{\sigma}$ (Pa) is the stress tensor, $\boldsymbol{\varepsilon}$ (-) is the strain tensor, p (Pa) is the pore pressure, taken as $p = \max(p_g; p_l)$, in which p_g and p_l are the gas and liquid pressures, respectively, $\boldsymbol{\alpha}$ (-) is the Biot effective stress tensor, hypothesized here to be a scalar for the sake of simplicity and lack of laboratory measurements, and \mathbf{C} (Pa) is the elastic modulus tensor. We can also express the constitutive elastic behavior in terms of Biot effective stress ($\boldsymbol{\sigma}' = \boldsymbol{\sigma} - \boldsymbol{\alpha}p$)

$$\boldsymbol{\sigma}' = \mathbf{C}\boldsymbol{\varepsilon}; \quad (\text{B2})$$

Given the fact that Opalinus Clay shows a different behavior along and normal to the bedding planes (Thury and Bossart, 1999a; Bossart and Thury, 2008; Makhnenko et al., 2017; Makhnenko and Podladchikov, 2018; Kim and Makhnenko, 2020), we impose a rotational symmetry on the axis normal to the bedding, leading to a transverse isotropic elasticity tensor (Cheng, 1997). The model is defined by five linear independent moduli: the Young's moduli E_p and E_n , the Poisson's ratios ν_p and ν_n , and the shear modulus G_n , where the subscripts p and n refer to the directions parallel and normal to the bedding planes, respectively.

The model geometry comprises a 3D cube with an edge length $L = 30$ m (Figure B1), which is discretized with a total of 46,004 hexahedral finite elements variable in size: from 0.04-m sized elements around the injection well to 4.0-m sized elements near the model boundaries. In Figure B1, we draw the planes of transverse isotropy, with a dip $\beta = 45^\circ$ representing the bedding planes. Note that the spacing between the bedding is not a parameter in the simulation, since we are using the transverse isotropic model.

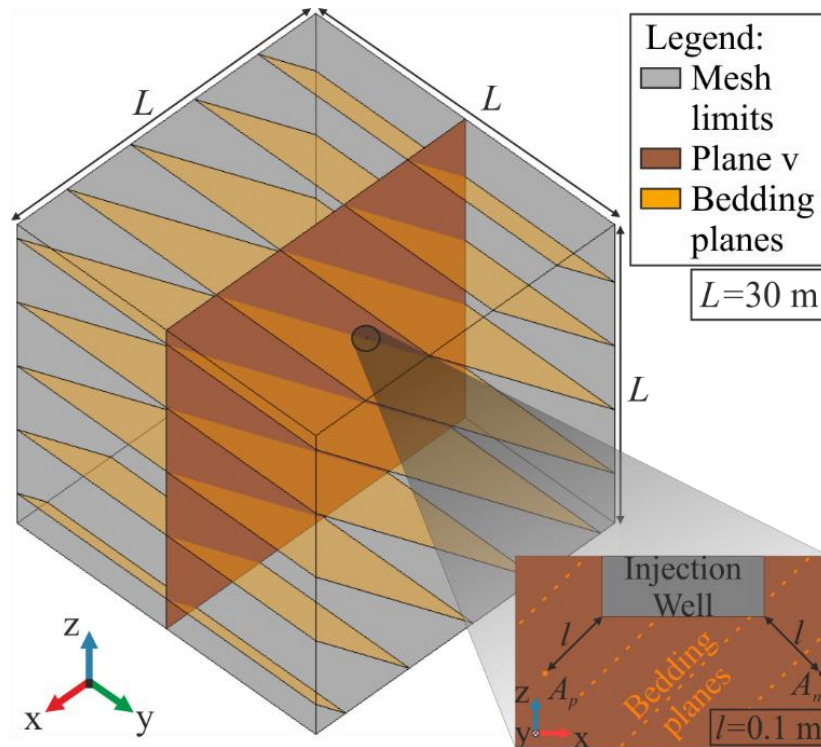


Figure B1. Schematic view of the numerical model setting for CO₂LPIE, including the model geometry (30×30×30 m³) and the injection well. The planes in orange represent the transverse isotropy directions (i.e., bedding planes) with a dip of $\beta = 45^\circ$. Plane v crosses the center of the injection well, it is vertical and forms an angle of 90° with the bedding planes. On the inset, we zoom around the injection well on Plane v. The dotted lines in orange show the inclination of the bedding planes along Plane v. The two representation points A_p and A_n , belong to Plane v and are located at a distance of 0.1 m from the injection well, in the directions parallel and normal to the bedding, respectively.

For the initialization of the simulation, we hypothesize undisturbed conditions. At the depth of the well, we impose an initial liquid pressure of 2.0 MPa, varying with depth using a linear gradient of 0.01 MPa/m. The gas pressure is uniform and equal to 0.1 MPa. Regarding initial stresses, we impose $\sigma_z = \sigma_v = 6.5$ MPa, $\sigma_y = \sigma_H = 4.0$ MPa, and $\sigma_x = \sigma_h = 2.2$ MPa at the injection depth, following Martin and Lanyon (2003) and Corkum (2006). The overburden stress corresponds to the maximum principal stress, which follows a linear distribution with a gradient of 0.025 MPa/m. This gradient results from an average density for Opalinus Clay of 2.45 g/cm³ (Bossart and Thury, 2008). Before simulating gas injection, we perform a steady-state calculation to bring the pressure and stress field to an initial equilibrium.

The boundary conditions include no-flow and zero-displacement perpendicular to lateral boundaries. At the top, we impose constant vertical stress and pressure. At the bottom, we prevent vertical displacement and impose constant hydrostatic pressure. We simulate the injection phase by applying a sinusoidal variation of the gaseous CO₂ in the borehole. The injection pressure varies between 2.5 MPa and 3.5 MPa, which implies a mean pressure of 3 MPa (1 MPa higher than the hydrostatic), with a period of $\pi/2 \approx 1.57$ d. The injection well is defined as a hexagonal prism of length 0.2 m (along the x-axis) and hexagon cross-section (on the plane yz) with sides of 0.043 m. It is worth mentioning that with the time scale considered and the permeability and stiffness of Opalinus Clay, the pressure and stress perturbations propagate no more than 2 m from the injection well. Thus, the simulation results are not affected by the model dimension.

In the insert of Figure B1, we zoom around the injection well in a vertical plane, called Plane v. This xz plane passes through the middle of the well. We display the simulation results at points A_p and A_n , located at a distance of 0.1 m from the wall of the well in directions parallel and normal to the bedding, respectively.

Finally, we plot the results after two years of periodic CO_2 injection in terms of:

- pore pressure p ;
- mean stress $P = (\sigma_x + \sigma_y + \sigma_z)/3$, where σ_i are the stresses along the axes of our reference system;
- effective mean stress $P' = P - \alpha p$;
- elastic volumetric strain ε_{vol} ;
- deviatoric stress $q = \{[(\sigma_x - \sigma_y)^2 + (\sigma_x - \sigma_z)^2 + (\sigma_y - \sigma_z)^2 + 6(\tau_{xy}^2 + \tau_{xz}^2 + \tau_{yz}^2)]/2\}^{1/2}$, where the τ_{ij} are the tangential stresses in the reference system; and
- the Coulomb Failure Stress evolution $\Delta\text{CFS} = \Delta\tau + \Delta\sigma'_n \cdot \tan(\phi)$, following Harris (1998). $\Delta\tau$ and $\Delta\sigma'_n$ denote changes in shear and normal effective stresses compared to the initial conditions, respectively; and ϕ is the friction angle.

Here, the sign convention of geomechanics is adopted, i.e., positive for compressive stresses and strains.

Opalinus Clay parameters

We implement the 3D-HM modeling of the experiment using rock parameters derived from laboratory tests performed on Opalinus Clay specimens under representative in-situ conditions (Makhnenko et al., 2017; Makhnenko and Podladchikov, 2018; see Table B1 for a summary). The elastic parameters have been measured both parallel and normal to the bedding planes. Opalinus Clay has a porosity of 0.125. The intrinsic permeability equals $2.4 \cdot 10^{-20} \text{ m}^2$ and $0.8 \cdot 10^{-20} \text{ m}^2$ parallel and perpendicular to the bedding planes, respectively. We assume the Biot coefficient to be isotropic and equal to 0.76, neglecting the 5 % anisotropy estimated by Makhnenko and Podladchikov (2018). The adopted values represent our first approximation of the rock mass behavior and agree well with those inferred from the twenty-years characterization of Opalinus Clay (e.g., Bossart and Thury, 2008).

The retention curve, which correlates the capillary pressure p_c with the wetting phase saturation, is fitted with the van Genuchten power law (van Genuchten, 1980)

$$S_{el} = \frac{S_l - S_{rl}}{S_{\max,l} - S_{rl}} = \left[1 + \left(\frac{P_{cap}}{p_0} \right)^{1/(1-m)} \right]^{-m}; \quad (\text{B3})$$

where S_{el} (-) is the effective liquid saturation, S_l (-) is the liquid saturation, S_{rl} (-) is the residual liquid saturation and S_{ml} (-) is the maximum liquid saturation. The parameters m and p_0 represent the shape function and the gas entry pressure, respectively. We presume an irreducible brine saturation of $S_{rl} = 0.5$ for Opalinus Clay and approximate the van Genuchten parameters to be $m = 0.7$ and $p_0 = 5 \text{ MPa}$. Finally, the relative permeability curves of CO_2 and brine phases are assumed to be represented by power law functions of the corresponding phase saturations with an exponent of 6 (Bennion and Bachu, 2008; Kivi et al., 2022).

Table B1. Material properties used to describe the HM behavior of Opalinus Clay under CO_2 injection.

Property	Unit	OPA
Young's modulus parallel to bedding, E_p	(GPa)	1.7
Young's modulus normal to bedding, E_n	(GPa)	2.1
Poisson's ratio parallel to bedding, ν_p	(-)	0.35
Poisson's ratio normal to bedding, ν_n	(-)	0.32
Permeability parallel to bedding, k_p	(m ²)	$2.4 \cdot 10^{-20}$
Permeability normal to bedding, k_n	(m ²)	$0.8 \cdot 10^{-20}$
Porosity, ϕ	(-)	0.125
Gas entry pressure, p_0	(MPa)	5
Relative water permeability, k_{rw}	(-)	$(S_w)^6$
Relative CO ₂ permeability, k_{rc}	(-)	$(S_c)^6$
Van Genuchten shape parameter, m	(-)	0.7

We assess the rock stability evolution during the experiment using the Mohr-Coulomb failure criterion, which is expressed in terms of the deviatoric and effective mean stresses as (Meyer and Labuz, 2013)

$$q = \frac{6 \cdot \sin(\phi)}{3 - \sin(\phi)} P' + \frac{6c \cdot \sin(\phi)}{3 - \sin(\phi)} ; \quad (\text{B4})$$

where c (Pa) denotes the rock cohesion, with values for Opalinus Clay extracted from the literature (Table B2).

Table B2. Reference Mohr-Coulomb cohesion and friction angle values used for Opalinus Clay.

Reference	c (MPa)	ϕ (°)
Parallel to bedding (Gräsle, 2011)	4.9	24.9
Rock mass (Bossart and Thury, 2008)	2.2-5.0	23-25

Results: pore pressure diffusion

The continuous cyclic CO₂ injection generates two pore pressure effects on the surrounded rock: a general increase of the mean value and a wave diffusion (Figure B2). After two years of injection, pore pressure variations at points A_n and A_p are found to attenuate by two orders of magnitude compared to that prescribed at the injection well. This is a consequence of the low hydraulic diffusivity of the rock, which significantly reduces the wave amplitude, even at a short distance from the well. If we consider the direction normal to the bedding planes, the amplitude is reduced to tens of kPa. Also the lag in time (or phase shift) is different in the two directions, with a delay from 11 h to 19 h for A_n and A_p , respectively.

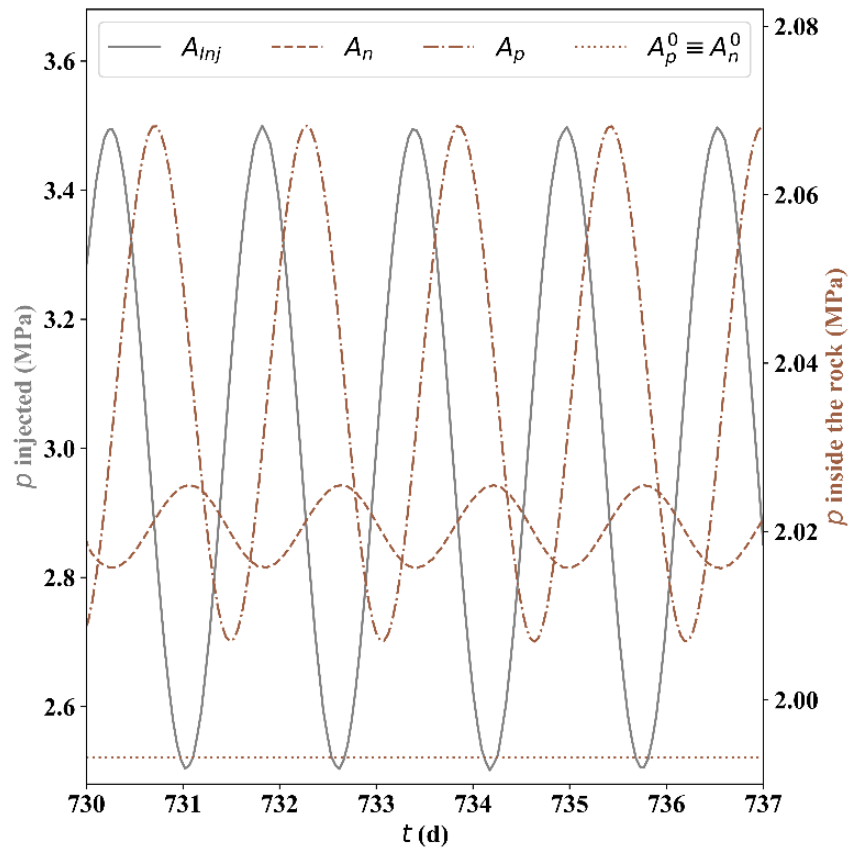


Figure B2. Pore pressure imposed at the injection well (in grey) and pore pressure at 0.1 m from the injection well boundary (in brown) for a representative time period of seven days after two years of periodic injection. A_n and A_p refer to the directions of the pressure variations normal and parallel to bedding, respectively (inset in Figure B2) and $A_p^0 \equiv A_n^0$ refers to the hydrostatic value of the pore pressure at the same points; here, they coincide since we choose points at the same depth.

Apart from the wave diffusion, the injection also imposes a brine overpressure around the borehole of approximately 0.044 MPa for A_p and 0.027 MPa for A_n after two years of injection. The high entry pressure of Opalinus Clay prevents the rock from desaturating, and the free-phase CO_2 penetrates into the rock only by a few millimeters. Therefore, the flow of CO_2 in our simulation is due to molecular diffusion inside the resident brine, with no significant gas advection.

Results: coupled hydro-mechanical effects

The pore pressure perturbation changes the stress field around the well (Figure B3a). We notice simultaneous growth of the mean value and a wave-form diffusion of the mean stress, similar to that observed for the pore pressure (Figure B2). The anisotropic behavior is still evident with higher variations parallel to the bedding planes, but this time on the order of a few kPa (0.0076 MPa and 0.0050 MPa for points A_n and A_p , respectively). As for the phase of the waves, comparing pore pressure diffusion and mean stress (Figure B2 and B3a), the curves for A_p have the same phase while the curves for A_n have an opposed phase. Finally, the injection of CO_2 causes an increase of the total stresses by 0.010 MPa for both A_n and A_p .

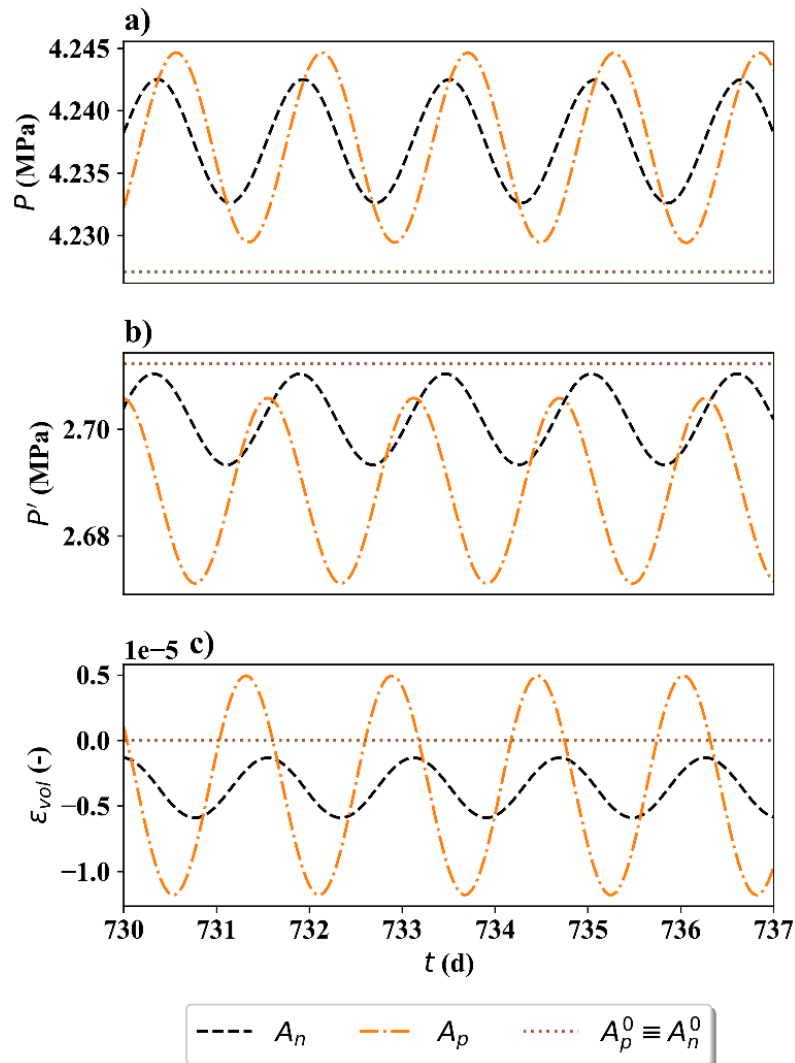


Figure B3. a) Mean stress P , b) mean effective stress P' , and c) volumetric deformation ε_{vol} over time at 0.1m from the injection well boundary for seven days after two years of periodic injection. The results for A_n (in black) and A_p (in orange) refer to the directions normal and parallel to bedding, respectively (inset in Figure B1). $A_p^0 \equiv A_n^0$ (in brown) refers to the initial values in the same points; they coincide since we choose points at the same depth.

The pore pressure buildup is higher than the induced poromechanical stress, as a result, the effective mean stress decreases (Figure B3b) and causes the rock to expand (Figure B3c). The larger changes in pore pressure and, thus, the effective mean stress in the direction parallel to bedding give rise to larger expansion in this direction.

Results: long-term stability of the rock mass

Having described the HM effect on the rock mass during the injection, we focus on assessing whether it contributes to a destabilization of the rock. After two years of injection, we find only minor changes in stresses on the q - P' plane, which form a closed loop in response to each cycle of pressure variation (Figure B4). We notice a gradual decrease of the effective mean stress and an increase of the deviatoric stress. The stress loop dimension is larger in the direction parallel to the bedding, pointing to preferential perturbations of stress and pressure in this direction. However, the stress values are still far from the failure range provided by Bossart and Thury

(2008) and shear failure along the bedding provided by Gräsle (2011), meaning that the rock failure is quite unlikely to take place during the experiment.

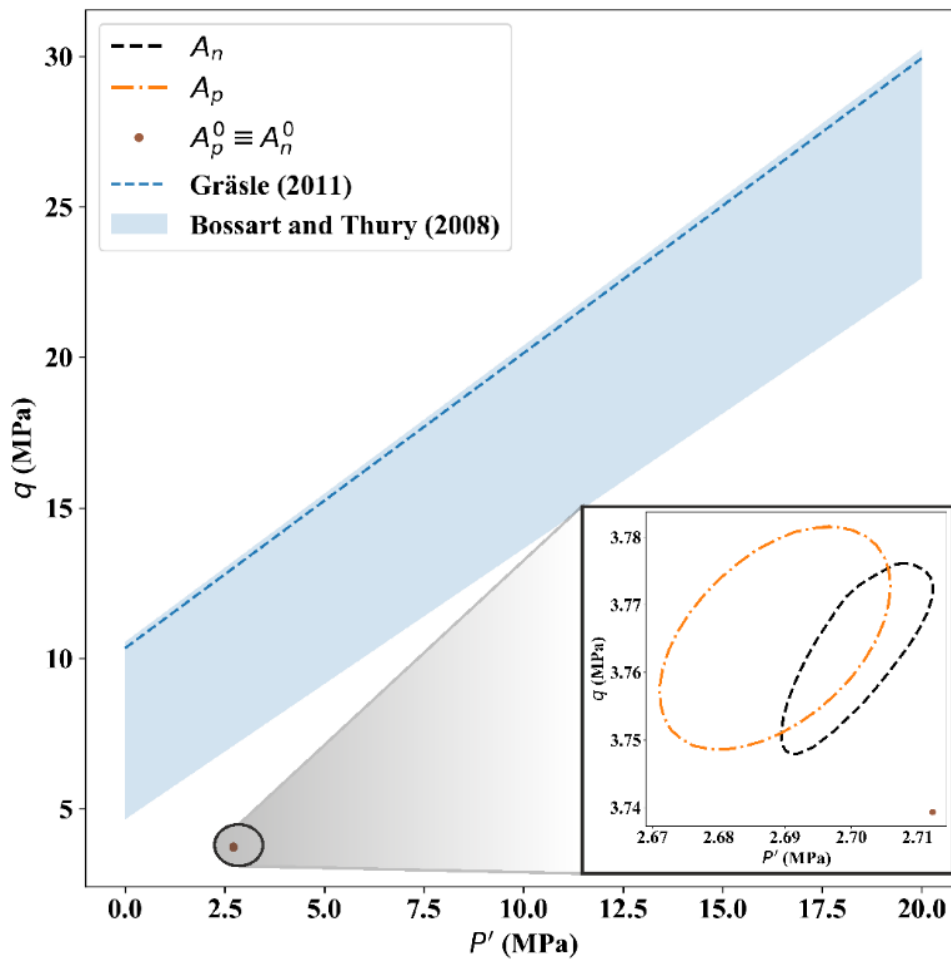


Figure B4. Deviatoric stress vs. mean effective stress plot for A_n and A_p after two years of periodic injection (inset in Figure B1). The trajectories remain far from the Mohr-Coulomb shear failure values for Opalinus Clay (Table B2). $A_p^0 \equiv A_n^0$ refer to the initial values in the same points; they coincide since we choose points at the same depth. On the inset, deviatoric and mean effective stresses for A_n (in black) and A_p (in orange) are presented for the directions normal and parallel to bedding, respectively, for an entire cycle and after two years of periodic injection (from 731.82 d to 733.40 d).

Results: long-term stability of the discontinuity

We calculate the variations of the Coulomb Failure Stress (ΔCFS) with respect to its initial magnitude to assess the rock's tendency to fail along the bedding planes. The shear stress τ and normal effective stress σ'_n acting on the bedding planes dipping at $\beta = 45^\circ$ are determined by transforming the stress components from the Cartesian system (shown graphically on the Mohr circle, Figure B5).

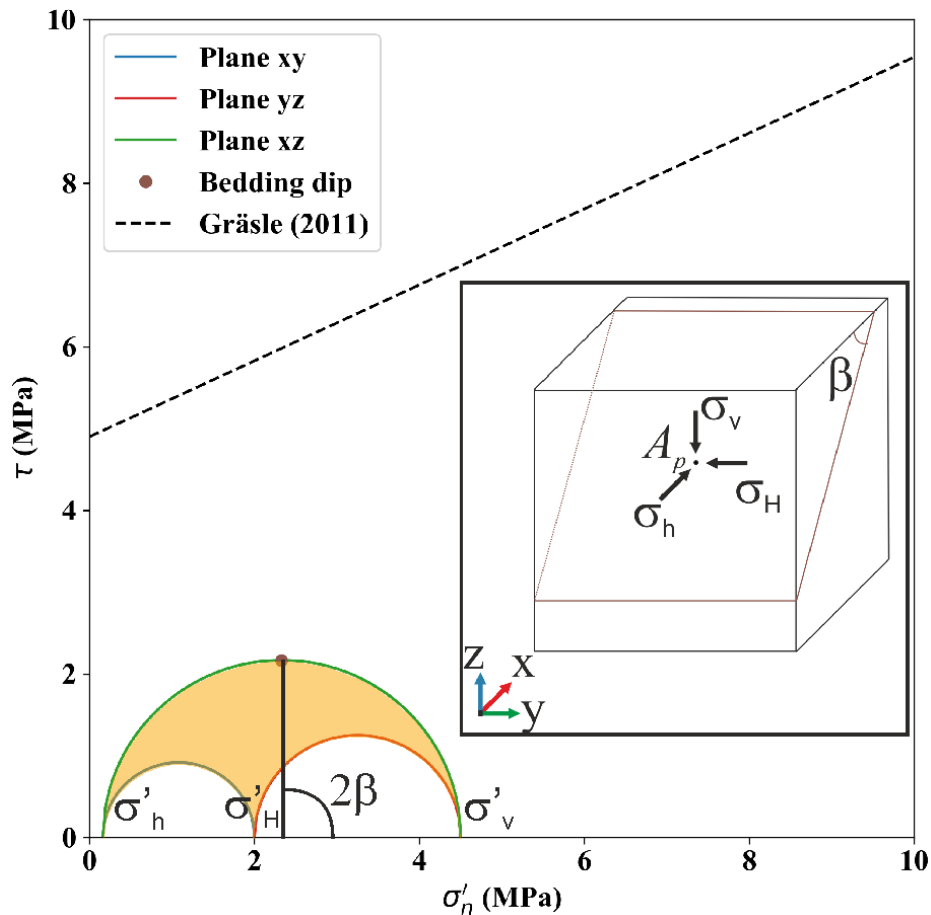


Figure B5. Representation of the 3D Mohr circles for the point A_p (inset in Figure B1) compared with the failure surface of the bedding planes of Opalinus Clay (Gräsle, 2011). In particular, the blue, red, and green Mohr circles refer to planes xy, yz, and xz, respectively. Finally, with the dip of $\beta = 45^\circ$, we extract the couple $\{\tau; \sigma'_n\}$ along the bedding (brown dot).

The ΔCFS fluctuates with time at points A_n and A_p , consistent with cyclic evolutions of the pressure and stresses (Figure B6). The ΔCFS returns positive values that follow the evolution of the effective stresses (Figure B3b). In particular, the effective stress state undergoes greater variations in A_p rather than in A_n , and this leads to higher ΔCFS in A_p , both for the mean value and the amplitude. The ΔCFS enhancements of a few hundreds of kPa after two years of injection reveal decreased stability. Since the bedding planes are not critically stressed, failure conditions are not reached.

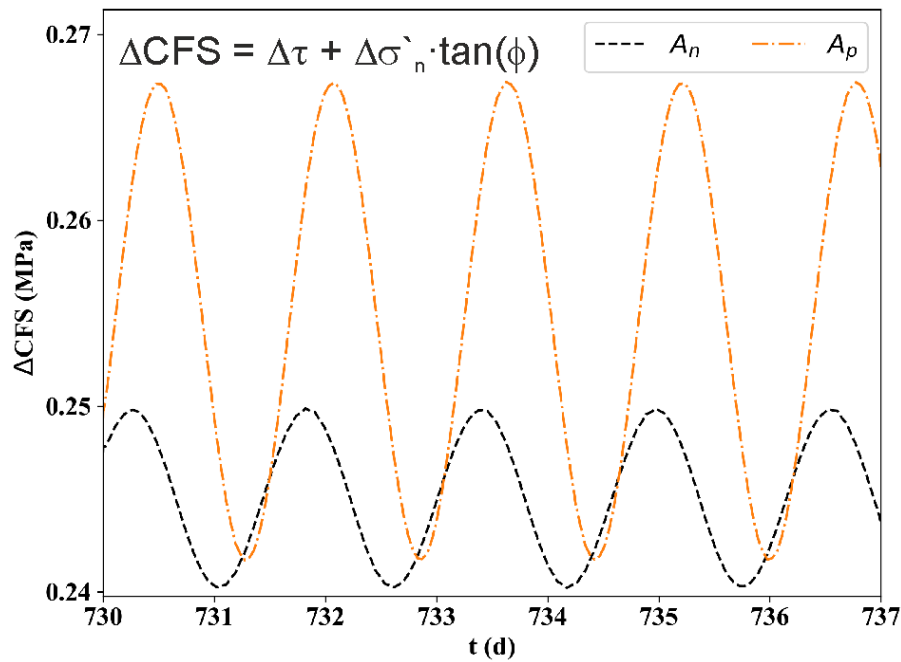


Figure B6. We use the transformed stresses at A_n and A_p (inset in Figure B1) to evaluate the change in Coulomb Failure Stress evolution (ΔCFS) along the bedding planes for seven days, after two years of periodic injection.

discussion and conclusions

Simulation results show that both the intact rock mass and bedding planes of Opalinus Clay are far from failure conditions during the periodic injection in the CO₂LPIE experiment. Thus, it is reasonable to assume an elastic behavior of the rock mass during CO₂LPIE. However, there is a number of uncertainties that are associated with the experiment. First of all, the injection causes a cyclic evolution of stresses (Figure B4), which may degrade the rock surrounding the well if approaching the rock damage (microcracking) thresholds. During CO₂LPIE, among other parameters, strains and pressures will be monitored, allowing for a continuous characterization of the material response and improved modeling capabilities and process understanding.

The coupled HM simulations show that bedding planes control pore pressure diffusion and stress changes. The caprock expands (Figure B3c), which may cause the porosity to increase and trigger indirect poroelastic effects (Figure B7), although not considered in our simulation. Another factor that may alter the porosity around the well is caused by the geochemical interactions with CO₂ potentially promoting mineral dissolution and precipitation, which is evaluated in another study performed by CO₂LPIE partners (Rebscher et al., 2020). Importantly, small porosity changes in caprock-like materials may result in significant permeability variations, governed by a power-law with exponents as high as 17 (Kim and Makhnenko, 2020). Geochemical interactions between CO₂ and brine-saturated shales can also impose notable impacts on the capillary entry pressure of the rock (Rezaee et al., 2017). Dissolution-induced reduction of the capillary entry pressure may promote CO₂ intrusion into Opalinus Clay. Consequently, the porosity alterations and the ensuing impacts on the HM behavior of the rock during the CO₂LPIE experiment have yet to be addressed in more detail.

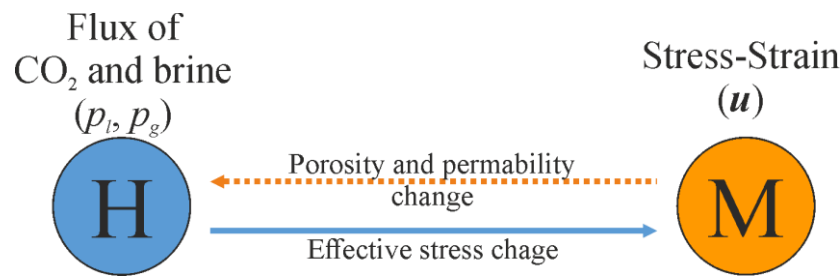


Figure B7. Coupled Hydro-Mechanical (HM) effects in porous geological media during CO₂ injection. The hydraulic to mechanical direct effect consists of a change in the effective stress state which leads to the deformation of the media. Inversely, the mechanical to indirect hydraulic effect results in changing the hydraulic properties of the medium (i.e., porosity and permeability). Permeability changes are omitted in our simulation.

Given the unknowns still present in this phase of the experiment, it has not seemed pertinent to further complicate the selected model. Indeed, the characteristics of the rock mass are taken from a different part of the URL, since the niche for CO₂LPIE is located in the more recently excavated gallery. For the initial stress state, we also used values prior to the construction of the last section of the tunnel (Martin and Lanyon 2003; Corkum 2006). It is of fundamental importance to accurately evaluate the stress field at the niche, in order to properly predict the behavior of the caprock during the injection of CO₂ (Rutqvist et al. 2008). We consider this work as a first approximation that will be updated with the data from CO₂LPIE.

The main concern of the simulation is to evaluate the radial extent of the injected CO₂ at different times. In the long term, the CO₂ does not flow in free phase due to the high entry pressure, but it dissolves and diffuses uniformly into the pore water. Dominated by molecular diffusion, the rate of CO₂ transport is controlled by its solubility in the resident brine and the diffusion coefficient. We use the effective diffusion coefficient of dissolved CO₂ in brine, equal to $1.6 \cdot 10^{-9}$ m²/s (Tewes and Boury 2005), drawing an upper bound limit for CO₂ diffusion through the tortuous pore network of tight shales. CO₂ solubility in water is linearly correlated with the CO₂ partial pressure in accordance with Henry's law. We picked a Henry's constant at the temperature and pressure range of Mont Terri URL, following Spycher et al. (2003). The diffusion in our simulation is uniform, driven by the dissolution of CO₂ inside the resident brine. Therefore, there is no flow of the gaseous CO₂ in free phase inside the rock. With these hypotheses, we took a threshold of the dissolved CO₂ inside the brine as the double of the initial one and estimated that CO₂ penetrates Opalinus Clay for 0.42 m and 0.52 m after one and two years, respectively. These values confirm that the behavior of Opalinus Clay is compatible with that of a caprock. On the other hand, this means that the monitoring wells must be positioned as close as possible to the injection well to be able to capture the mechanical and hydraulic perturbations.

Appendix C

Solution of the hydraulic problem and calibration of natural fracture initial aperture

To determine a rational initial hydraulic mean aperture b_0 for the hydro-mechanical modeling, an uncoupled hydraulic problem is solved. This simplified scenario exclusively addresses fluid mass conservation and Darcy's law (Equations (5.3) and (5.4), respectively). The hydraulic boundary conditions follow the experimental test and, therefore, correspond to those defined for the hydro-mechanical models and described in Section 5.2.4. Employing the cubic law, the permeability k_{fr} of the natural fracture is derived from its aperture b , i.e., $k_{fr} = b^2/12$ (Snow, 1969; Witherspoon et al., 1980; Zimmerman and Bodvarsson, 1996).

Figure C1 represents the characteristic overpressure distribution resulting from the uncoupled numerical simulation upon reaching steady-state conditions. Iso-pressure lines exhibit a horizontal orientation within the matrix, while closer inspection reveals a slight tilt on the fracture material, aligning perpendicularly with the fracture walls. Thus, the flow within the fracture material remains uninfluenced by the matrix flow. Given the substantial disparity in permeability between the fracture and matrix, spanning approximately 6 to 7 orders of magnitude, flow preferentially occurs through the fracture. Ultimately, the overall permeability k_{sp} of the simulated specimen is computed through Darcy's law (Equation (5.4)).

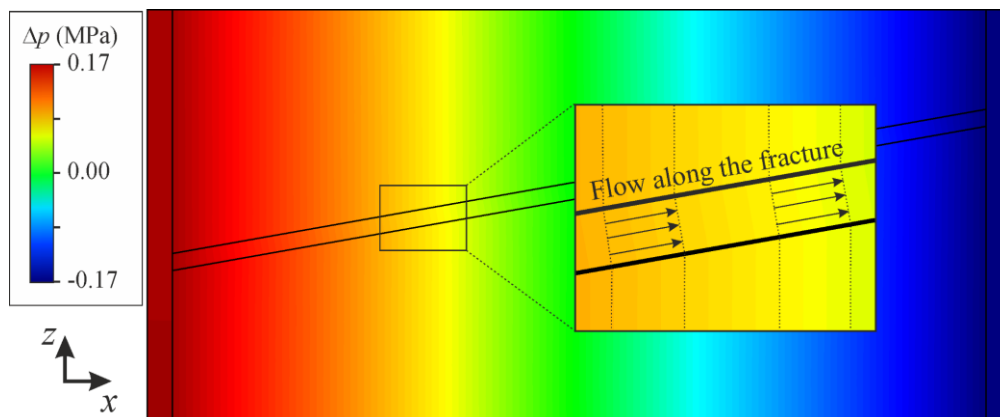


Figure C1. Contour plots of overpressure distribution during a hydraulic simulation on plane xz (Figure 5.4b) with zoom on the natural fracture showing the direction of the flow.

By systematically varying the aperture (and permeability) of the natural fracture, a spectrum of k_{sp} values is acquired. Within this framework, for the range of experimental values of the fractured specimen (blue triangles in Figure 5.5), we observe a linear relationship between the natural fracture permeability and the permeability of the fractured specimen (Figure C2).

To deduce the initial hydraulic mean aperture, we consider the permeability of the whole specimen to be $4.46 \times 10^{-20} \text{ m}^2$ – corresponding to the experimentally measured value of the fractured specimen at the highest confinement ($P' = 20 \text{ MPa}$). Using the linear relationship in Figure C2, this corresponds to a uniform value for $k_{fr} = 6.24 \times 10^{-15} \text{ m}^2$. Finally, from cubic law, we infer an initial hydraulic aperture $b_0 = 2.7 \times 10^{-7} \text{ m}$ (Table 5.2).

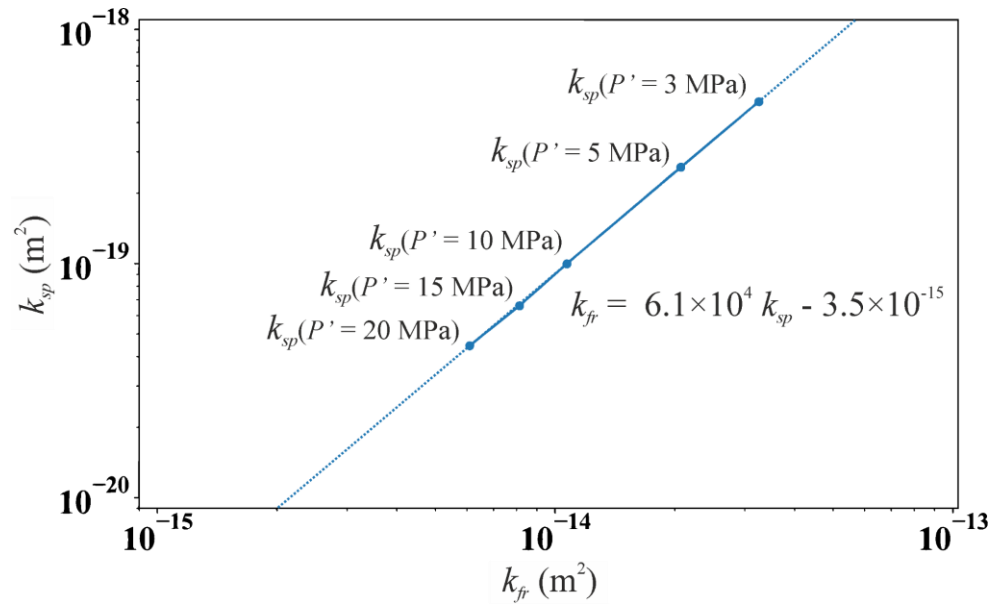


Figure C2. Linear relation between permeability of the whole simulated specimen k_{sp} and permeability of the natural fracture k_{fr} , solving only the hydraulic problem. The dots correspond to the experimental fracture permeability under different confinement pressures.

References

- Adachi, J., & Detournay, E., (1997). A poroelastic solution of the oscillating pore pressure method to measure permeabilities of ‘tight’ rocks. *International Journal of Rock Mechanics & Mining Sciences* 34(3–4), Paper No. 062.
- Ajayi, T., Gomes, J. S., & Bera, A. (2019). A review of CO₂ storage in geological formations emphasizing modeling, monitoring and capacity estimation approaches. *Petroleum Science*, 16, 1028-1063.
- Al-Bazali, T. M., Zhang, J., Chenevert, M. X. E., & Sharma, M. M. (2005). Measurement of the sealing capacity of shale caprocks. In *SPE Annual Technical Conference and Exhibition* (pp. SPE-96100)
- Alcalde, J., Flude, S., Wilkinson, M., Johnson, G., Edlmann, K., Bond, C. E., ... & Haszeldine, R. S. (2018). Estimating geological CO₂ storage security to deliver on climate mitigation. *Nature communications*, 9(1), 2201.
- Alcaraz, M., Carrera, J., Cuello, J., Guarracino, L., & Vives, I. (2021). Determining hydraulic connectivity of the coastal aquifer system of La Plata river estuary (Argentina) to the ocean by analysis of aquifer response to low-frequency tidal components. *Hydrogeol J* 29, 1587–1599. <https://doi.org/10.1007/s10040-021-02332-0>
- Amann, F., Le Gonidec, Y., Senis, M., Gschwind, S., Wassermann, J., Nussbaum, C., & Sarout, J. (2018). Analysis of acoustic emissions recorded during a mine-by experiment in an underground research laboratory in clay shales. *International Journal of Rock Mechanics and Mining Sciences*, 106, 51-59. <https://doi.org/10.1016/j.ijrmms.2018.04.021>
- Amann-Hildenbrand, A., Bertier, P., Busch, A., & Krooss, B. M. (2013). Experimental investigation of the sealing capacity of generic clay-rich caprocks. *International Journal of Greenhouse Gas Control*, 19, 620-641.
- Amann-Hildenbrand, A., Ghanizadeh, A., & Krooss, B. M. (2012). Transport properties of unconventional gas systems. *Marine and Petroleum Geology*, 31(1), 90-99.
- Angeli, M., Soldal, M., Skurtveit, E., & Aker, E. (2009). Experimental percolation of supercritical CO₂ through a caprock. *Energy Procedia*, 1(1), 3351-3358.
- Anovitz, L. M., & Cole, D. R. (2015). Characterization and analysis of porosity and pore structures. *Reviews in Mineralogy and geochemistry*, 80(1), 61-164. Bennaceur, K.; Gielen, D.; Kerr, T.; Tam, C. CO₂ Capture and Storage: A Key Carbon Abatement Option; IEA/OECD: Paris, 2008.
- Arts, R., Eiken, O., Chadwick, A., Zweigel, P., Van der Meer, L., & Zinszner, B. (2004). Monitoring of CO₂ injected at Sleipner using time-lapse seismic data. *Energy*, 29(9-10), 1383-1392. <https://doi.org/10.1016/j.energy.2004.03.072>

- Arts, R. J., Chadwick, A., Eiken, O., Thibeau, S., & Nooner, S. (2008). Ten years' experience of monitoring CO₂ injection in the Utsira Sand at Sleipner, offshore Norway. *First break*, 26(1).
- Azizmohammadi, S., & Matthäi, S. K. (2017). Is the permeability of naturally fractured rocks scale dependent?. *Water Resources Research*, 53(9), 8041-8063. <https://doi.org/10.1002/2016WR019764>
- Bachu, S. (2003). Screening and ranking of sedimentary basins for sequestration of CO₂ in geological media in response to climate change. *Environmental Geology*, 44(3), 277-289. <https://doi.org/10.1007/s00254-003-0762-9>
- Bachu, S., & Bennion, B. (2008). Effects of in-situ conditions on relative permeability characteristics of CO₂-brine systems. *Environmental Geology*, 54, 1707-1722.
- Bandis, S. C., Lumsden, A. C., & Barton, N. R. (1983). Fundamentals of rock joint deformation. *International Journal of Rock Mechanics and Mining Sciences & Geomechanics Abstracts*, 20(6), 249-268. [https://doi.org/10.1016/0148-9062\(83\)90595-8](https://doi.org/10.1016/0148-9062(83)90595-8)
- Barton, N., Bandis, S., & Bakhtar, K. (1985). Strength, deformation and conductivity coupling of rock joints. *International journal of rock mechanics and mining sciences & geomechanics abstracts*, 22(3), 121-140. [https://doi.org/10.1016/0148-9062\(85\)93227-9](https://doi.org/10.1016/0148-9062(85)93227-9)
- Bear, J. (2013). *Dynamics of fluids in porous media*. Courier Corporation.
- Bennaceur, K. (2008). *CO₂ capture and storage: a key carbon abatement option*. OECD/Iea, Paris.
- Bennion, D. B., & Bachu, S. (2008). Drainage and imbibition relative permeability relationships for supercritical CO₂/brine and H₂S/brine systems in intergranular sandstone, carbonate, shale, and anhydrite rocks. *SPE Reservoir Evaluation & Engineering*, 11(03), 487-496. <https://doi.org/10.2118/99326-PA>
- Benson, S., & Myer, L. (2002). Monitoring to ensure safe and effective geologic sequestration of carbon dioxide. *See Ref*, 105, 137-51.
- Benson, S., Cook, P., Anderson, J., Bachu, S., Nimir, H., Basu, B., ... & von Goerne, G. (2005). Underground geological storage, IPCC Special Report on Carbon Dioxide Capture and Storage. *Intergovernmental Panel on Climate Change*.
- Bernabé, Y., Mok, U., Evans, B., & Herrmann, F. J. (2004). Permeability and storativity of binary mixtures of high- And low-permeability materials. *Journal of Geophysical Research: Solid Earth* 109. <https://doi.org/10.1029/2004JB003111>
- Biot, M. A. (1941). General theory of three-dimensional consolidation. *Journal of applied physics*, 12(2), 155-164. <https://doi.org/10.1063/1.1712886>
- Biot, M. A. (1956). Thermoelasticity and irreversible thermodynamics. *Journal of applied physics*, 27(3), 240-253. <https://doi.org/10.1063/1.1722351>

- Bishop, A. W. (1976). The influence of system compressibility on the observed pore-pressure response to an undrained change in stress in saturated rock. *Géotechnique*, 26(2), 371-375. <https://doi.org/10.1680/geot.1976.26.2.371>
- Black, D. K., & Lee, K. L. (1973). Saturating laboratory samples by back pressure. *Journal of the soil mechanics and foundations division*, 99(1), 75-93. <https://doi.org/10.1061/JSFEAQ.0001847>
- Blöcher, G., Moeck, I., Milsch, H., & Zimmermann, G. (2008). Modelling of pore pressure response due to hydraulic stimulation treatments at the geothermal research doublet EGRSK3/90 and GTGRSK4/05 in summer 2007. *IIB*, 4026(4086), 60.
- Blunt, M., King, M. J., & Scher, H. (1992). Simulation and theory of two-phase flow in porous media. *Physical review A*, 46(12), 7680. <https://doi.org/10.1103/PhysRevA.46.7680>
- Bondarenko, N., Podladchikov, Y., & Makhnenko, R. (2022). Hydromechanical impact of basement rock on injection-induced seismicity in Illinois Basin. *Scientific reports*, 12(1), 15639. <https://doi.org/10.1038/s41598-022-19775-4>
- Bossart, P. & Thury, M. (2008). Mont Terri Rock Laboratory. Project, programme 1996 to 2007 and results. *Wabern: Reports of the Swiss Geological Survey no. 3*.
- Bossart, P., & Thury, M. (2011). Characteristics of the Opalinus clay at Mont Terri. *Reports of the Swiss Geological Survey*, 3.
- Bossart, P., Meier, P. M., Moeri, A., Trick, T., & Mayor, J. C. (2002). Geological and hydraulic characterisation of the excavation disturbed zone in the Opalinus Clay of the Mont Terri Rock Laboratory. *Engineering Geology*, 66(1-2), 19-38. [https://doi.org/10.1016/S0013-7952\(01\)00140-5](https://doi.org/10.1016/S0013-7952(01)00140-5)
- Bossart, P., Jaeggi, D., & Nussbaum, C. (2017). Experiments on thermo-hydro-mechanical behaviour of Opalinus Clay at Mont Terri rock laboratory, Switzerland. *Journal of Rock Mechanics and Geotechnical Engineering*, 9(3), 502-510. <https://doi.org/10.1016/j.jrmge.2016.11>
- Bossart, P., Bernier, F., Birkholzer, J., Bruggeman, C., Connolly, P., Dewonck, S., ... & Wieczorek, K. (2018). Mont Terri rock laboratory, 20 years of research: introduction, site characteristics and overview of experiments. *Mont Terri Rock Laboratory, 20 Years: Two Decades of Research and Experimentation on Claystones for Geological Disposal of Radioactive Waste*, 3-22.
- Boulin, P. F., Bretonnier, P., Vassil, V., Samouillet, A., Fleury, M., & Lombard, J. M. (2013). Sealing efficiency of caprocks: Experimental investigation of entry pressure measurement methods. *Marine and Petroleum Geology*, 48, 20-30. <https://doi.org/10.1016/j.marpetgeo.2013.07.010>
- Brace, W. F. (1980). Permeability of crystalline and argillaceous rocks. *International Journal of Rock Mechanics and Mining Sciences and Geomechanics* 17(5): 241-51. [https://doi.org/10.1016/0148-9062\(80\)90807-4](https://doi.org/10.1016/0148-9062(80)90807-4)

- Brace, W., Walsh, J. B., & Frangos, W. T. (1968). Permeability of granite under high pressure. *Journal of Geophysical research*, 73(6), 2225-2236.
- Braun, P., Ghabezloo, S., Delage, P., Sulem, J., & Conil, N. (2021). Transversely isotropic poroelastic behaviour of the Callovo-Oxfordian claystone: A set of stress-dependent parameters. *Rock Mechanics and Rock Engineering*, 54, 377-396. <https://doi.org/10.1007/s00603-020-02268-z>
- Bredehoeft, J. D. (1967). Response of well-aquifer systems to Earth tides. *Journal of Geophysical Research* 72(12): 3075–87. <https://doi.org/10.1029/JZ072i012p03075>
- Bredehoeft, J. D., Neuzil, C. E., & Milly, P. C. D. (1983). *Regional flow in the Dakota aquifer: a study of the role of confining layers* (Vol. 2237). US Government Printing Office.
- Brooks, R. H. (1965). *Hydraulic properties of porous media*. Colorado State University.
- Brunauer, S., Emmett, P. H., & Teller, E. (1938). Adsorption of gases in multimolecular layers. *Journal of the American chemical society*, 60(2), 309-319. <https://doi.org/10.1021/ja01269a023>
- Bui, M., Adjiman, C. S., Bardow, A., Anthony, E. J., Boston, A., Brown, S., ... & Mac Dowell, N. (2018). Carbon capture and storage (CCS): the way forward. *Energy & Environmental Science*, 11(5), 1062-1176. <https://doi.org/10.1039/C7EE02342A>
- Busch, A., Alles, S., Gensterblum, Y., Prinz, D., Dewhurst, D. N., Raven, M. D., ... & Krooss, B. M. (2008). Carbon dioxide storage potential of shales. *International journal of greenhouse gas control*, 2(3), 297-308.
- Busch, A., Amann, A., Bertier, P., Waschbusch, M., & Krooss, B. M. (2010). The significance of caprock sealing integrity for CO₂ storage. In *SPE International Conference on CO₂ Capture, Storage, and Utilization* (pp. SPE-139588). SPE.
- Bustin, R. M., Bustin, A. M., Cui, X., Ross, D. J. K., & Pathi, V. M. (2008). Impact of shale properties on pore structure and storage characteristics. In *SPE shale gas production conference* (pp. SPE-119892). SPE.
- Candela, T., Brodsky, E. E., Marone, C., & Elsworth, D. (2015). Flow rate dictates permeability enhancement during fluid pressure oscillations in laboratory experiments. *Journal of Geophysical Research: Solid Earth* 120: 2037–55. <https://doi.org/10.1002/2014JB011511>
- Cappa, F., & Rutqvist, J. (2011). Modeling of coupled deformation and permeability evolution during fault reactivation induced by deep underground injection of CO₂. *International Journal of Greenhouse Gas Control*, 5(2), 336-346. <https://doi.org/10.1016/j.ijggc.2010.08.005>
- Capuano, R. M. (1993). Evidence of fluid flow in microfractures in geopressured shales. *AAPG bulletin*, 77(8), 1303-1314.
- Carman, P. C. (1937). Fluid flow through a granular bed. *Trans. Inst. Chem. Eng. London*, 15, 150-156.

- Carman, P. C. (1956). *Flow of gases through porous media*. Butterworths Scientific Publications, London
- Carslaw, H. S., & Jaeger, J. C. (1959). The flow of heat in an infinite circular cylinder. In: Carslaw, H. S., Jaeger, J. C. (2nd ed.) *Conduction of heat in solids*. Oxford, UK: Clarendon Press, 188-213.
- Chalbaud, C., Robin, M., Lombard, J. M., Martin, F., Egermann, P., & Bertin, H. (2009). Interfacial tension measurements and wettability evaluation for geological CO₂ storage. *Advances in water resources*, 32(1), 98-109.
- Cavanagh, A. J., & Haszeldine, R. S. (2014). The Sleipner storage site: Capillary flow modeling of a layered CO₂ plume requires fractured shale barriers within the Utsira Formation. *International Journal of Greenhouse Gas Control*, 21, 101-112. <https://doi.org/10.1016/j.ijggc.2013.11.017>
- Cesca, S., Grigoli, F., Heimann, S., Gonzalez, A., Buforn, E., Maghsoudi, S., ... & Dahm, T. (2014, May). The 2013 seismic sequence close to gas injection platform of the Castor project, offshore Spain. In *EGU General Assembly Conference Abstracts* (p. 7171).
- Cheng, A. D. (1997). Material coefficients of anisotropic poroelasticity. *International journal of rock mechanics and mining sciences*, 34(2), 199-205. [https://doi.org/10.1016/S0148-9062\(96\)00055-1](https://doi.org/10.1016/S0148-9062(96)00055-1)
- Cheng, A. D. (2016). *Poroelasticity*. Book series: Theory and Applications of Transport in Porous Media, Vol.27 Springer, US
- Clennell, M. B., Dewhurst, D. N., Brown, K. M., & Westbrook, G. K. (1999). Permeability anisotropy of consolidated clays. *Geological Society, London, Special Publications*, 158(1), 79-96.
- Cooper, Jr. H. H., & Jacob, C. E. (1946). A generalized graphical method for evaluating formation constants and summarizing well-field history. *Eos, Transactions American Geophysical Union*, 27(4), 526-534.
- Corkum, A. G. (2006). PhD thesis: Department of Civil and Environmental Engineering, University of Alberta, Canada.
- Crawford, B. R., Tsenn, M. C., Homburg, J. M., Stehle, R. C., Freyesteinson, J. A., & Reese, W. C. (2017). Incorporating scale-dependent fracture stiffness for improved reservoir performance prediction. *Rock Mechanics and Rock Engineering*, 50(12), 3349-3359. <https://doi.org/10.1007/s00603-017-1314-z>
- Cryer, C. W. (1963). A comparison of the three-dimensional consolidation theories of Biot and Terzaghi. *Q J Mech Appl Math* 16(4):401-412.
- Damians, I. P., Olivella, S., & Gens, A. (2020). Modelling gas flow in clay materials incorporating material heterogeneity and embedded fractures. *International Journal of*

- Rock Mechanics and Mining Sciences*, 136, 104524.
<https://doi.org/10.1016/j.ijrmms.2020.104524>
- Damians, I. P., Olivella, S., & Gens, A. (2022). 3D Simulations of gas injection on callovo-oxfordian claystone assuming spatial heterogeneity and anisotropy. *International Journal of Rock Mechanics and Mining Sciences*, 159, 105232.
<https://doi.org/10.1016/j.ijrmms.2022.105232>
- De Simone, S., & Carrera, J. (2017). Analytical solutions to coupled HM problems to highlight the nonlocal nature of aquifer storage. *Water Resources Research*, 53(11), 9580-9599.
- De Simone, S., Carrera, J., & Vilarrasa, V. (2017). Superposition approach to understand triggering mechanisms of post-injection induced seismicity. *Geothermics*, 70, 85-97.
- Deng, Y. F., Tang, A. M., Cui, Y. J., Nguyen, X. P., Li, X. L., & Wouters, L. (2011). Laboratory hydro-mechanical characterisation of Boom Clay at Essen and Mol. *Physics and Chemistry of the Earth, Parts A/B/C*, 36(17-18), 1878-1890.
- Detournay, E. and Cheng, A.H.-D. (1993). *Fundamentals of Poroelasticity*. In: Fairhurst C (ed) *Comprehensive rock engineering: principles, practice and projects, vol. II, Analysis and design method*. Pergamon Press, Oxford/New York. <https://doi.org/10.1016/B978-0-08-040615-2.50011-3>
- Dewhurst, D. N., Aplin, A. C., Sarda, J. P., & Yang, Y. (1998). Compaction-driven evolution of porosity and permeability in natural mudstones: An experimental study. *Journal of Geophysical Research: Solid Earth*, 103(B1), 651-661.
- Dewhurst, D. N., Yang, Y., & Aplin, A. C. (1999). Permeability and fluid flow in natural mudstones. *Geological Society, London, Special Publications*, 158(1), 23-43.
<https://doi.org/10.1144/GSL.SP.1999.158.01.03>
- Dewhurst, D. N., Raven, M. D., Shah, S. S. B. M., Ali, S. S. B. M., Giwelli, A., Firms, S., ... & White, C. (2020). Interaction of super-critical CO₂ with mudrocks: Impact on composition and mechanical properties. *International Journal of Greenhouse Gas Control*, 102, 103163.
- Duxbury, A., White, D., Samson, C., Hall, S. A., Wookey, J., & Kendall, J. M. (2012). Fracture mapping using seismic amplitude variation with offset and azimuth analysis at the Weyburn CO₂ storage site. *Geophysics*, 77(6), B295-B306.
- Edlmann, K., Haszeldine, S., & McDermott, C. I. (2013). Experimental investigation into the sealing capability of naturally fractured shale caprocks to supercritical carbon dioxide flow. *Environmental Earth Sciences*, 70, 3393-3409.
- Egermann, P. (2006). A fast and accurate method to measure threshold capillary pressures under representative conditions. In *SCA International Symposium, 2006*.
- Einstein, H. H. (1989). Suggested methods for laboratory testing of argillaceous swelling rocks. *Intl J of Rock Mech & Mining Sci & Geomechanic Abs*, 26(5).

- Ellsworth, W. L. (2013). Injection-induced earthquakes. *Science*, *341*(6142), 1225942. <https://doi.org/10.1126/science.1225942>
- Ellsworth, W. L., Giardini, D., Townend, J., Ge, S., & Shimamoto, T. (2019). Triggering of the Pohang, Korea, earthquake (M w 5.5) by enhanced geothermal system stimulation. *Seismological Research Letters*, *90*(5), 1844-1858.
- Ennis-King, J., LaForce, T., Paterson, L., Dance, T., Jenkins, C., & Cinar, Y. (2017). Interpretation of above zone and storage zone pressure responses to carbon dioxide injection in the 2016 CO₂CRC field test. *Energy Procedia*, *114*, 5671-5679. <https://doi.org/10.1016/j.egypro.2017.03.1706>
- Espinoza, D. N., & Santamarina, J. C. (2010). Water-CO₂-mineral systems: Interfacial tension, contact angle, and diffusion—Implications to CO₂ geological storage. *Water resources research*, *46*(7).
- Espinoza, D. N., & Santamarina, J. C. (2017). CO₂ breakthrough—Caprock sealing efficiency and integrity for carbon geological storage. *International Journal of Greenhouse Gas Control*, *66*, 218-229. <http://dx.doi.org/10.1016/j.ijggc.2017.09.019>
- Faulkner, D. R., & Rutter, E. H. (2000). Comparisons of water and argon permeability in natural clay-bearing fault gouge under high pressure at 20°C. *Journal of Geophysical Research: Solid Earth* *105*(B7): 16415–26. <https://doi.org/10.1029/2000JB900134>
- Ferris, J. G. (1952). Cyclic fluctuation of water level as a basis for determining aquifer transmissibility. *U.S. Geological Survey*. <https://doi.org/10.3133/70133368>
- Ferris, J. G., Knowles, D. B., Brown, R. H., & Stallman, R. W. (1962). *Theory of aquifer tests*. US Government Print Office, Washington.
- Ferronato, M., Gambolati, G., Janna, C., & Teatini, P. (2010). Geomechanical issues of anthropogenic CO₂ sequestration in exploited gas fields. *Energy Conversion and Management*, *51*(10), 1918-1928.
- Fleury, M., Berne, P., & Bachaud, P. (2009). Diffusion of dissolved CO₂ in caprock. *Energy Procedia*, *1*(1), 3461-3468.
- Foulger, G. R., Wilson, M. P., Gluyas, J. G., Julian, B. R., & Davies, R. J. (2018). Global review of human-induced earthquakes. *Earth-Science Reviews*, *178*, 438-514.
- Gautschi, A. (2001). *Self-sealing faults in the Opalinus Clay-evidence from field observations, hydraulic testing and pore water chemistry* (No. NEA-RWM-CLAYCLUB--2001-5).
- Ge, S., & Saar, M. O. (2022). Review: induced seismicity during geoenergy development—A hydromechanical perspective. *Journal of Geophysical Research: Solid Earth* *127*(3). <https://doi.org/10.1029/2021JB023141>
- Gens, A., Vaunat, J., Garitte, B., & Wileveau, Y. (2007). In situ behaviour of a stiff layered clay subject to thermal loading: Observations and interpretation. *Géotechnique*, *57*(2), 207-228. <https://doi.org/10.1680/ssc.41080.0011>

- Gertz, K. H., & Loeschke, H. H. (1956). Bestimmung des Diffusionskoeffizienten von CO₂ in Wasser. *Zeitschrift für Naturforschung B*, 11(2), 61-64.
- Gräsele, W. (2011). Multistep Triaxial Strength Tests: Investigating Strength Parameters and Pore Pressure Effects on Opalinus Clay. *Physics and Chemistry of the Earth*, 36(17–18), 1898–1904. <https://doi.org/10.1016/j.pce.2011.07.024>
- Guglielmi, Y., Cappa, F., & Amitrano, D. (2008). High-definition analysis of fluid-induced seismicity related to the mesoscale hydromechanical properties of a fault zone. *Geophysical Research Letters*, 35(6).
- Guglielmi, Y., Nussbaum, C., Jeanne, P., Rutqvist, J., Cappa, F., & Birkholzer, J. (2020a). Complexity of fault rupture and fluid leakage in shale: insights from a controlled fault activation experiment. *Journal of Geophysical Research: Solid Earth* 125(2), 1–19. <https://doi.org/10.1029/2019JB017781>
- Guglielmi, Y., Nussbaum, C., Rutqvist, J., Cappa, F., Jeanne, P., & Birkholzer, J. (2020b). Estimating perturbed stress from 3-D borehole displacements induced by fluid injection in fractured or faulted shales. *Geophysical Journal International*, 221(3), 1684-1695.
- Guglielmi, Y., Nussbaum, C., Cappa, F., De Barros, L., Rutqvist, J., & Birkholzer, J. (2021). Field-scale fault reactivation experiments by fluid injection highlight aseismic leakage in caprock analogs: Implications for CO₂ sequestration. *International Journal of Greenhouse Gas Control*, 111, 103471. <https://doi.org/10.1016/j.ijggc.2021.103471>
- Haghi, A. H., Chalaturnyk, R., Blunt, M. J., Hodder, K., & Geiger, S. (2021). Poromechanical Controls on Spontaneous Imbibition in Earth Materials. *Scientific Reports* 11(1): 1–11. <https://doi.org/10.1038/s41598-021-82236-x>
- Hansen, O., Gilding, D., Nazarian, B., Osdal, B., Ringrose, P., Kristoffersen, J. B., ... & Hansen, H. (2013). Snøhvit: The history of injecting and storing 1 Mt CO₂ in the fluvial Tubåen Fm. *Energy Procedia*, 37, 3565-3573.
- Hantush, M. S. (1964). *Hydraulics of wells*. In: Chow VT (ed) *Advances in hydroscience*, vol 1. Academic, New York/London, pp 281–432.
- Häring, M. O., Schanz, U., Ladner, F., & Dyer, B. C. (2008). Characterisation of the Basel 1 enhanced geothermal system. *Geothermics*, 37(5), 469-495. <https://doi.org/10.1016/j.geothermics.2008.06.002>
- Harrington, J. F., de La Vaissière, R., Noy, D. J., Cuss, R. J., & Talandier, J. (2012). Gas flow in Callovo-Oxfordian claystone (COx): results from laboratory and field-scale measurements. *Mineralogical Magazine*, 76(8), 3303-3318.
- Harris, R.A. (1998). Introduction to Special Section: Stress Triggers, Stress Shadows, and Implications for Seismic Hazard. *Journal of Geophysical Research: Solid Earth*, 103(10), 24347–58. <https://doi.org/10.1029/98JB01576>

- Hasanov, A. K., Dugan, B., Batzle, M. L., & Prasad, M. (2019). Hydraulic and poroelastic rock properties from oscillating pore pressure experiments. *Journal of Geophysical Research: Solid Earth* 124(5): 4473–91. <https://doi.org/10.1029/2018JB017276>
- Hasanov, A. K., Dugan, B., & Batzle, M. L. (2020). Numerical simulation of oscillating pore pressure experiments and inversion for permeability. *Water Resources Research* 56(6): 1–16. <https://doi.org/10.1029/2019WR025681>
- Heap, M. J., & Kennedy, B. M. (2016). Exploring the scale-dependent permeability of fractured andesite. *Earth and Planetary Science Letters*, 447, 139-150. <https://doi.org/10.1016/j.epsl.2016.05.004>
- Heberling, F., Albers, H., Beilecke, T., Deissmann, G., Furche, M., Geckeis, H., Hoyer, E. M., Joseph, C., Liebscher, A., Lüth, S., Metz, V., Müller, K., Nowak, U., Rebscher, D., Schulte, F., Steegborn, F., & Tietz, T. (2022). DR-D: The Heterogeneity of the sandy facies of Opalinus Clay, geophysical characterization and diffusion study, Technical Meeting TM-39, 26. January 2022, virtual, Switzerland
- Hildenbrand, A., Schlömer, S., & Krooss, B. M. (2002). Gas breakthrough experiments on fine-grained sedimentary rocks. *Geofluids*, 2(1), 3–23. <https://doi.org/10.1046/j.1468-8123.2002.00031.x>
- Hildenbrand, A., & Krooss, B. M. (2003). CO₂ migration processes in argillaceous rocks: pressure-driven volume flow and diffusion. *Journal of geochemical exploration*, 78, 169-172.
- Hofmann, H., Zimmermann, G., Zang, A., & Min, K. (2018). Cyclic soft stimulation (CSS): A new fluid injection protocol and traffic light system to mitigate seismic risks of hydraulic stimulation treatments. *Geothermal Energy*, 6(1), 1-33. <https://doi.org/10.1186/s40517-018-0114-3>
- Hofmann, H., Zimmermann, G., Farkas, M., Huenges, E., Zang, A., Leonhardt, M., ... & Kim, K. Y. (2019). First field application of cyclic soft stimulation at the Pohang Enhanced Geothermal System site in Korea. *Geophysical Journal International*, 217(2), 926-949.
- Hopp, C., Guglielmi, Y., Rinaldi, A. P., Soom, F., Wenning, Q., Cook, P., ... & Zappone, A. (2022). The effect of fault architecture on slip behavior in shale revealed by distributed fiber optic strain sensing. *Journal of Geophysical Research: Solid Earth*, 127(1), e2021JB022432.
- Hostettler, B., Reisdorf, A. G., Jaeggi, D., Deplazes, G., Bläsi, H.-R., Morard, A., Feist-Burkhardt, S., Waltschew, A., Dietze, V., & Menkveld-Gfeller, U. (2017). Litho- and biostratigraphy of the Opalinus Clay and bounding formations in the Mont Terri rock laboratory (Switzerland). *Swiss Journal of Geosciences*, 110, 23-37. <https://doi.org/10.1007/s00015-016-0250-3>
- Hsieh, P. A. (1996). Deformation-induced changes in hydraulic head during ground-water withdrawal. *Groundwater*, 34(6), 1082-1089.

- Hsieh, P. A., Tracy, J. V., Neuzil, C. E., Bredehoeft, J. D., & Silliman, S. E. (1981). A transient laboratory method for determining the hydraulic properties of ‘tight’ rocks—I. Theory. *International Journal of Rock Mechanics and Mining Sciences & Geomechanics Abstracts* 18(3), 245-252. Pergamon. [https://doi.org/10.1016/0148-9062\(81\)90979-7](https://doi.org/10.1016/0148-9062(81)90979-7)
- Hsieh, P. A., Bredehoeft, J. D., & Farr, J. M. (1987). Determination of aquifer transmissivity from Earth tide analysis. *Water Resources Research* 23(10): 1824–32. <https://doi.org/10.1029/WR023i010p01824>
- Hsieh, P. A., Bredehoeft J. D., & Rojstaczer, S. A. (1988). Response of well aquifer systems to Earth tides: problem revisited. *Water Resources Research* 24(3): 468–72. <https://doi.org/10.1029/WR024i003p00468>
- Iding, M., & Ringrose, P. (2009). Evaluating the impact of fractures on the long-term performance of the In Salah CO₂ storage site. *Energy Procedia*, 1(1), 2021-2028.
- IEA GHG (2009). CCS site characterisation criteri. IEA Greenhouse Gas R&D Programme
- IPCC (2005). *IPCC Special Report on Carbon Dioxide Capture and Storage*. Prepared by Working Group III of the Intergovernmental Panel on Climate Change [Metz, B., O. Davidson, H. C. de Coninck, M. Loos, and L. A. Meyer (Eds.)]. Cambridge University Press, Cambridge, United Kingdom and New York, NY, USA.
- IPCC (2014). *Climate Change 2014: Synthesis Report*. Contribution of Working Groups I, II and III to the Fifth Assessment Report of the Intergovernmental Panel on Climate Change. IPCC, Geneva, Switzerland, 151 pp
- IPCC (2022). *Climate Change 2022: Mitigation of Climate Change*. Contribution of working group III to the Sixth Assessment Report of the Intergovernmental Panel on Climate Change [P.R. Shukla, J. Skea, R. Slade, A. Al Khourdajie, R. van Diemen, D. McCollum, M. Pathak, S. Some, P. Vyas, R. Fradera, M. Belkacemi, A. Hasija, G. Lisboa, S. Luz, J. Malley, (eds.)]. Cambridge University Press, Cambridge, UK and New York, NY, USA.
- Jacob, C. E. (1950). *Flow of Groundwater in Engineering Hydraulic*. John Wiley & Sons, New York.
- Jaeggi, D., Laurich, B., Nussbaum, C., Schuster, K., & Connolly, P. (2018). Tectonic structure of the “main fault” in the Opalinus Clay, Mont Terri rock laboratory (Switzerland). *Mont Terri Rock Laboratory, 20 Years: Two Decades of Research and Experimentation on Claystones for Geological Disposal of Radioactive Waste*, 69-86.
- Jaeggi, D., Galletti, M., Amacher, F., Dunst, R., Nussbaum, C., Raselli, R., Ringeisen, M., Schefer, S., & Bossart, P. (2020). Gallery 2018: Excavation and geological documentation. Mont Terri Technical Report, TR2018-04
- Jarvie, D. M., Hill, R. J., Ruble, T. E., & Pollastro, R. M. (2007). Unconventional shale-gas systems: The Mississippian Barnett Shale of north-central Texas as one model for thermogenic shale-gas assessment. *AAPG bulletin*, 91(4), 475-499. <https://doi.org/10.1306/12190606068>

- Jenkins, C. (2020). The State of the Art in Monitoring and Verification: an update five years on. *International Journal of Greenhouse Gas Control*, *100*, 103118.
- Jenkins, C., Chadwick, A., & Hovorka, S. D. (2015). The state of the art in monitoring and verification—ten years on. *International Journal of Greenhouse Gas Control*, *40*, 312–349.
- Jiao, J. J., & Tang, Z. (1999). An analytical solution of groundwater response to tidal fluctuation in a leaky confined aquifer. *Water Resources Research* *35*(3): 747–51. <https://doi.org/10.1029/1998WR900075>
- Kalam, S., Olayiwola, T., Al-Rubaii, M. M., Amaechi, B. I., Jamal, M. S., & Awotunde, A. A. (2021). Carbon dioxide sequestration in underground formations: review of experimental, modeling, and field studies. *Journal of Petroleum Exploration and Production*, *11*, 303–325.
- Kaldi, J., Daniel, R., Tenthorey, E., Michael, K., Schacht, U., Nicol, A., Underschultz, J., & Backe, G. (2011). Caprock systems for CO₂ geological storage. *IAEGHG Rep*, *1*, 149.
- Kim, H., & Makhnenko, R. Y. (2023a). Evaluation of CO₂ sealing potential of heterogeneous Eau Claire shale. *Geological Society, London, Special Publications*, *528*(1), SP528–2022. <https://doi.org/10.1144/SP528-2022-134>
- Kim, H., & Makhnenko, R. Y. (2023b). Characterization of multiphase flow in shaly caprock for geologic CO₂ storage. *Advances in Water Resources*, 104570. <https://doi.org/10.1016/j.advwatres.2023.104570>
- Kim, K., & Makhnenko, R. Y. (2020). Coupling between poromechanical behavior and fluid flow in Tight Rock. *Transport in Porous Media* *135*(2), 487–512. <https://doi.org/10.1007/s11242-020-01484-z>
- Kim, K. H., Ree, J. H., Kim, Y., Kim, S., Kang, S. Y., & Seo, W. (2018). Assessing whether the 2017 M w 5.4 Pohang earthquake in South Korea was an induced event. *Science*, *360*(6392), 1007–1009.
- Kim, S., & Hosseini, S. A. (2014). Above-zone pressure monitoring and geomechanical analyses for a field-scale CO₂ injection project in Cranfield, MS. *Greenhouse Gases: Science and Technology* *4*(1), 81–98. <https://doi.org/10.1002/ghg.1388>
- Kivi, I. R., Makhnenko, R. Y., Oldenburg, C. M., Rutqvist, J., & Vilarrasa, V. (2022a). Multi-layered systems for permanent geologic storage of CO₂ at the gigatonne scale. *Geophysical Research Letters*, *49*, e2022GL100443. <https://doi.org/10.1029/2022GL100443>
- Kivi, I. R., Makhnenko, R. Y., & Vilarrasa, V. (2022b). Two-Phase flow mechanisms controlling CO₂ intrusion into shaly Caprock. *Transport in Porous Media*, *141*, 771–798. <https://doi.org/10.1007/s11242-022-01748-w>
- Klewiah, I., Berawala, D. S., Walker, H. C. A., Andersen, P. Ø., & Nadeau, P. H. (2020). Review of experimental sorption studies of CO₂ and CH₄ in shales. *Journal of Natural Gas Science and Engineering*, *73*, 103045.

- Kozeny, J. (1927). Ueber kapillare leitung des wassers im boden. *Sitzungsberichte der Akademie der Wissenschaften in Wien*, 136, 271.
- Kranz, R. L., Saltzman, J. S., & Blacic, J. D. (1990). Hydraulic diffusivity measurements on laboratory rock samples using an oscillating pore pressure method. *International Journal of Rock Mechanics and Mining Sciences and* 27(5): 345–52. [https://doi.org/10.1016/0148-9062\(90\)92709-N](https://doi.org/10.1016/0148-9062(90)92709-N)
- Krooss, B. M., & Leythaeuser, D. (1988). Experimental measurements of the diffusion parameters of light hydrocarbons in water-saturated sedimentary rocks—II. Results and geochemical significance. *Organic Geochemistry*, 12(2), 91-108.
- Krooss, B. M., Leythaeuser, D., & Schaefer, R. G. (1992). The quantification of diffusive hydrocarbon losses through caprocks of natural gas reservoirs—a reevaluation: reply. *Aapg Bulletin*, 76(11), 1842-1846.
- Kruseman, G. P., De Ridder, N. A., & Verweij, J. M. (1970). *Analysis and evaluation of pumping test data* (Vol. 11, p. 200). The Netherlands: International institute for land reclamation and improvement.
- Kuila, U., & Prasad, M. (2013). Specific surface area and pore-size distribution in clays and shales. *Geophysical Prospecting*, 61 (2-Rock Physics for Reservoir Exploration, Characterisation and Monitoring), 341-362.
- Kvamme, B., Kuznetsova, T., Hebach, A., Oberhof, A., & Lunde, E. (2007). Measurements and modelling of interfacial tension for water + carbon dioxide systems at elevated pressures. *Computational Materials Science* 38(3), 506–13. <https://doi.org/10.1016/j.commatsci.2006.01.020>
- Leupin, O. X., Van Loon, L. R., Gimmi, T., Wersin, P., & Soler, J. M. (2018). Exploring diffusion and sorption processes at the Mont Terri rock laboratory (Switzerland): Lessons Learned from 20 Years of Field Research. *Swiss Journal of Geosciences* 110(1), 393–405.
- Li, Z., Dong, M., Li, S., & Huang, S. (2006). CO₂ sequestration in depleted oil and gas reservoirs—caprock characterization and storage capacity. *Energy Conversion and Management*, 47(11-12), 1372-1382.
- Lee, K., Yeo, I., Lee, J., Kang, T., Rhie, J., Sheen, D., ... & Oh, S. (2019). Summary report of the Korean Government Commission on relations between the 2017 Pohang earthquake and the EGS project, Geological Society of Korea and Korean Government Commission on the Cause of the Pohang Earthquake, S. 205.
- Lohman, S. W. (1972). *Ground-Water Hydraulics*. US Government Printing Office, Washington. <https://pubs.usgs.gov/pp/0708/report.pdf>
- Lu, P., Lalam, N., Badar, M., Liu, B., Chorpening, B. T., Buric, M. P., & Ohodnicki, P. R. (2019). Distributed optical fiber sensing: Review and perspective. *Applied Physics Reviews*, 6(4).

- Lysy, M., Fernø, M., & Ersland, G. (2021). Seasonal hydrogen storage in a depleted oil and gas field. *International Journal of Hydrogen Energy*, 46(49), 25160-25174. <https://doi.org/10.1016/j.ijhydene.2021.05.030>
- Makhnenko, R. Y., & Labuz, J. F. (2016). Elastic and inelastic deformation of fluid-saturated rock. *Philosophical Transactions of the Royal Society A: Mathematical, Physical and Engineering Sciences*, 374(2078), 20150422. <https://doi.org/10.1098/rsta.2015.0422>
- Makhnenko, R. Y., & Podladchikov, Y. Y. (2018). Experimental poroviscoelasticity of common sedimentary rocks. *Journal of Geophysical Research: Solid Earth* 123(9), 7586–7603. <https://doi.org/10.1029/2018JB015685>
- Makhnenko, R. Y., Vilarrasa, V., Mylnikov, D., & Laloui, L. (2017). Hydromechanical aspects of CO₂ breakthrough into clay-rich caprock. *Energy Procedia* 114, 3219–28. <http://dx.doi.org/10.1016/j.egypro.2017.03.1453>
- Makhnenko, R. Y., Kim, H., & Kim, K. (2023). Thermal effect on long-term shale behavior in nuclear waste storage. In *ARMA US Rock Mechanics/Geomechanics Symposium* (pp. ARMA-2023). ARMA. <https://doi.org/10.56952/ARMA-2023-0908>
- Maldal, T., & Tappel, I. M. (2004). CO₂ underground storage for Snøhvit gas field development. *Energy*, 29(9-10), 1403-1411.
- Maliva, R. G. (2016). *Schlumberger Methods in Water Resources Evaluation Series No.4 Aquifer Characterization Techniques*. Springer Hydrogeology.
- Marschall, P., Croisé, J., Schlickenrieder, L., Boisson, J. Y., Vogel, P., & Yamamoto, S. (2004). Synthesis of hydrogeological investigations at the Mont Terri site (phases 1 to 5). *Mont Terri Project—Hydrogeological Synthesis, Osmotic Flow*, edited by: Heitzmann, P., *Reports of the Federal Office for Water and Geology, Geology Series*, 6, 7-92.
- Martin, C. D., & Lanyon, G. W. (2003). Measurement of in-situ stress in weak rocks at Mont Terri rock laboratory, Switzerland. *International Journal of Rock Mechanics and Mining Sciences*, 40(7–8), 1077–88.
- Mazurek, M., Alt-Epping, P., Bath, A., Gimmi, T., Waber, H. N., Buschaert, S., ... & Wouters, L. (2011). Natural tracer profiles across argillaceous formations. *Applied Geochemistry*, 26(7), 1035-1064.
- Merritt, M. L. (2004). Estimating hydraulic properties of the Floridan Aquifer System by analysis of Earth-tide, ocean-tide, and barometric effects, Collier and Hendry Counties, Florida. *U.S. Geological Survey*. https://pubs.usgs.gov/wri/wri034267/wri03_4267.pdf
- Meyer, J. P., & Labuz, J. F. (2013). Linear failure criteria with three principal stresses. *International Journal of Rock Mechanics and Mining Sciences*, 60, 180–87. <http://dx.doi.org/10.1016/j.ijrmms.2012.12.040>
- Min, K. B., Lee, J., & Stephansson, O. (2013). Implications of thermally-induced fracture slip and permeability change on the long-term performance of a deep geological repository. *International Journal of Rock Mechanics and Mining Sciences*, 61, 275-288.

- Minardi, A., Stavropoulou, E., Kim, T., Ferrari, A., & Laloui, L. (2021). Experimental Assessment of the Hydro-Mechanical Behaviour of a Shale Caprock during CO₂ Injection. *International Journal of Greenhouse Gas Control*, 106, 103225. <https://doi.org/10.1016/j.ijggc.2020.103225>
- Miocic, J. M., Gilfillan, S. M., Roberts, J. J., Edlmann, K., McDermott, C. I., & Haszeldine, R. S. (2016). Controls on CO₂ storage security in natural reservoirs and implications for CO₂ storage site selection. *International Journal of Greenhouse Gas Control*, 51, 118-125. <http://dx.doi.org/10.1016/j.ijggc.2016.05.019>
- Mohajerani, M., Delage, P., Sulem, J., Monfared, M., Tang, A. M., & Gatmiri, B. (2012). A laboratory investigation of thermally induced pore pressures in the Callovo-Oxfordian claystone. *International Journal of Rock Mechanics and Mining Sciences*, 52, 112-121.
- Neuzil, C. E. (1986). Groundwater flow in low-permeability environments. *Water Resources Research*, 22(8), 1163-1195.
- Neuzil, C. E. (1993). Low fluid pressure within the Pierre Shale: a transient response to erosion. *Water Resources Research*, 29(7), 2007-2020.
- Neuzil, C. E. (1994). How permeable are clays and shales?. *Water resources research*, 30(2), 145-150.
- Neuzil, C. E. (2013). Can shale safely host US nuclear waste?. *Eos, Transactions American Geophysical Union*, 94(30), 261-262. <https://doi.org/10.1002/2013EO300001>
- Neuzil, C. E. (2019). Permeability of Clays and Shales. *Annual Review of Earth and Planetary Sciences*, 47, 247-73. <https://doi.org/10.1146/annurev-earth-053018-060437>
- Neuzil, C. E., & Tracy, J. V. (1981). Flow through fractures. *Water Resources Research*, 17(1), 191-199. <https://doi.org/10.1029/WR017i001p00191>
- Niemi, A., Bear, J., & Bensabat, J. (2017). *Geological storage of CO₂ in deep saline formations* (Vol. 29). Dordrecht, Netherlands: Springer.
- Nur, A., & Byerlee, J. (1971). An exact effective stress law for elastic deformation of rock with fluids. *Journal of geophysical research*, 76(26), 6414-6419. <https://doi.org/10.1029/JB076i026p06414>
- Nussbaum, C., Bossart, P., Amann, F., & Aubourg, C. (2011). Analysis of tectonic structures and excavation induced fractures in the Opalinus Clay, Mont Terri Underground rock laboratory (Switzerland). *Swiss Journal of Geosciences*, 104(2), 187-210. <https://doi.org/10.1007/s00015-011-0070-4>
- Oldenburg, C. M., Bryant, S. L., & Nicot, J. P. (2009). Certification framework based on effective trapping for geologic carbon sequestration. *International Journal of Greenhouse Gas Control*, 3(4), 444-457.
- Olivella, S., & Alonso, E. E. (2008). Gas flow through clay barriers. *Géotechnique*, 58(3), 157-176. <https://doi.org/10.1680/geot.2008.58.3.157>

- Olivella, S., Carrera, J., Gens, A., & Alonso, E. E. (1994). Nonisothermal multiphase flow of brine and gas through saline media. *Transport in Porous Media* 15, 271–93. <https://doi.org/10.1007/BF00613282>
- Olivella, S., Gens, A., Carrera, J., & Alonso, E. E. (1996). Numerical formulation for a Simulator (CODE_BRIGHT) for the coupled analysis of saline media. *Engineering Computations*, 13(7), 87–112.
- Olver, F. W., & Maximon, L.C. (2010). Bessel Functions. In: Olver, F. W., Lozier, D. W., Boisvert, R. F., & Clark, C. W. (1st ed.). *NIST handbook of mathematical functions hardback*. Cambridge university press, pp 215-286.
- Onuma, T., & Ohkawa, S. (2009). Detection of surface deformation related with CO₂ injection by DInSAR at In Salah, Algeria. *Energy Procedia*, 1(1), 2177-2184.
- Orr, F. M. (2009). Onshore geologic storage of CO₂. *Science*, 325(5948), 1656-1658.
- Osif, T. L. (1988). The effects of salt, gas, temperature, and pressure on the compressibility of Water. *SPE Res Eng* 3 (1988): 175–181. <https://doi.org/10.2118/13174-PA>
- Oudinot, A. Y., Koperna, G. J., Philip, Z. G., Liu, N., Heath, J. E., Wells, A., ... & Wilson, T. (2011). CO₂ injection performance in the Fruitland coal fairway, San Juan Basin: results of a field pilot. *SPE Journal*, 16(04), 864-879.
- Preston, C., Monea, M., Jazrawi, W., Brown, K., Whittaker, S., White, D., ... & Rostron, B. (2005). IEA GHG Weyburn CO₂ monitoring and storage project. *Fuel Processing Technology*, 86(14-15), 1547-1568.
- Pruess, K (2008). On CO₂ fluid flow and heat transfer behavior in the subsurface, following leakage from a geologic storage reservoir. *Environ. Geol.* 54, 1677–1686. <https://doi.org/10.1007/s00254-007-0945-x>.
- Pyrak-Nolte, L. J., & Morris, J. P. (2000). Single fractures under normal stress: The relation between fracture specific stiffness and fluid flow. *International Journal of Rock Mechanics and Mining Sciences*, 37(1-2), 245-262. [https://doi.org/10.1016/S1365-1609\(99\)00104-5](https://doi.org/10.1016/S1365-1609(99)00104-5)
- Pyrak-Nolte, L. J., & Nolte, D. D. (2016). Approaching a universal scaling relationship between fracture stiffness and fluid flow. *Nature communications*, 7(1), 10663. <https://doi.org/10.1038/ncomms10663>
- Rebscher, D., Vilarrasa, V., Makhnenko, R. Y., Nussbaum, C., Kipfer, C., & Wersin, P. (2020). CO₂LPIE Project—Combining in-situ, laboratory, and modelling work to investigate periodic CO₂ injection into an argillaceous claystone. [https://digital.csic.es/bitstream/10261/224405/1/Rebscher_et_al_2020_CouFrac_ext_Abs tract_CO2LPIE.pdf](https://digital.csic.es/bitstream/10261/224405/1/Rebscher_et_al_2020_CouFrac_ext_Abstract_CO2LPIE.pdf)
- Reeves, S. R. (2001). Geological sequestration of CO₂ in deep, unmineable coalbeds: an integrated research and commercial-scale field demonstration project. *SPE Annual Technical Conference and Exhibition* (pp. SPE-71749). SPE.

- Reinsch, T., Hennings, J., & Ásmundsson, R. (2013). Thermal, mechanical and chemical influences on the performance of optical fibres for distributed temperature sensing in a hot geothermal well. *Environmental earth sciences*, *70*, 3465-3480.
- Revil, A., & Cathles III, L. M. (1999). Permeability of shaly sands. *Water Resources Research*, *35*(3), 651-662.
- Rezaee, R., Saeedi, A., Iglauer, S., & Evans, B. (2017). Shale Alteration after Exposure to Supercritical CO₂. *International Journal of Greenhouse Gas Control*, *62*, 91–99. <http://dx.doi.org/10.1016/j.ijggc.2017.04.004>.
- Rezaeyan, A., Tabatabaei-Nejad, S. A., Khodapanah, E., & Kamari, M. (2015). Parametric analysis of caprock integrity in relation with CO₂ geosequestration: capillary breakthrough pressure of caprock and gas effective permeability. *Greenhouse Gases: Science and Technology*, *5*(6), 714-731.
- Ringrose, P. S., Mathieson, A. S., Wright, I.W., Selama, F., Hansen, O., Bissell, R., Saoula, N., & Midgley, J. (2013). The In Salah CO₂ storage project: lessons learned and knowledge transfer. *Energy Procedia*, *37*, 6226–36. <https://doi.org/10.1016/j.egypro.2013.06.551>
- Ringrose, P. R., Furre, A. K., Gilfillan, S. M. V., Krevor, S., Landrø, M., Leslie, R., Meckel, T., Nazarian, B., & Zahid, A. (2021). Storage of carbon dioxide in saline aquifers: physicochemical processes, key constraints, and scale-up potential. *Annual Review of Chemical and Biomolecular Engineering*, *12*, 471–94. <https://doi.org/10.1146/annurev-chembioeng-093020-091447>
- Rohmer, J., Pluymakers, A., & Renard, F. (2016). Mechano-chemical interactions in sedimentary rocks in the context of CO₂ storage: Weak acid, weak effects?. *Earth-Science Reviews*, *157*, 86-110.
- Ross, D. J., & Bustin, R. M. (2009). The importance of shale composition and pore structure upon gas storage potential of shale gas reservoirs. *Marine and petroleum Geology*, *26*(6), 916-927.
- Rouquerol, J., Avnir, D., Fairbridge, C. W., Everett, D. H., Haynes, J. M., Pernicone, N., ... & Unger, K. K. (1994). Recommendations for the characterization of porous solids (Technical Report). *Pure and applied chemistry*, *66*(8), 1739-1758. <https://doi.org/10.1351/pac199466081739>
- Rutqvist, J. (2012). The geomechanics of CO₂ storage in deep sedimentary formations. *Geotechnical and Geological Engineering*, *30*(3), 525–51. <https://doi.org/10.1007/s10706-011-9491-0>
- Rutqvist, J. (2015). Fractured rock stress-permeability relationships from in situ data and effects of temperature and chemical-mechanical couplings. *Geofluids*, *15*(1-2), 48-66.
- Rutqvist, J., & Tsang, C. F. (2002). A study of caprock hydromechanical changes associated with CO₂-Injection into a brine formation. *Environmental Geology*, *42*, 296–305. <https://doi.org/10.1007/s00254-001-0499-2>

- Rutqvist, J., & Stephansson, O. (2003). The role of hydromechanical coupling in fractured rock engineering. *Hydrogeology Journal*, *11*, 7-40. <https://doi.org/10.1007/s10040-002-0241-5>
- Rutqvist, J., Birkholzer, J. T., & Tsang, C. F. (2008). Coupled reservoir-geomechanical analysis of the potential for tensile and shear failure associated with CO₂ injection in multilayered reservoir-caprock systems. *International Journal of Rock Mechanics and Mining Sciences* *45*(2), 132–43. <https://doi.org/10.1016/j.ijrmms.2007.04.006>
- Rutqvist, J., Vasco, D. W., & Myer, L. (2010). Coupled reservoir-geomechanical analysis of CO₂ injection and ground deformations at In Salah, Algeria. *International Journal of Greenhouse Gas Control*, *4*(2), 225–30. <https://doi.org/10.1016/j.ijggc.2009.10.017>
- Rutqvist, J., Rinaldi, A. P., Cappa, F., & Moridis, G. J. (2013). Modeling of fault reactivation and induced seismicity during hydraulic fracturing of shale-gas reservoirs. *Journal of Petroleum Science and Engineering*, *107*, 31-44. <https://doi.org/10.1016/j.petrol.2013.04.023>
- Rutqvist, J., Rinaldi, A. P., Cappa, F., Jeanne, P., Mazzoldi, A., Urpi, L., Guglielmi, Y., & Vilarrasa, V. (2016). Fault activation and induced seismicity in geological carbon storage – lessons learned from recent modeling studies. *Journal of Rock Mechanics and Geotechnical Engineering*, *8*(6), 789–804. <https://doi.org/10.1016/j.jrmge.2016.09.001>
- Samara, H., Ostrowski, T. V., & Jaeger, P. (2024). Interfacial and transport properties of supercritical hydrogen and carbon dioxide in unconventional formations. *The Journal of Supercritical Fluids*, *205*, 106-124.
- Sasaki, T., & Rutqvist, J. (2022). Effects of time-dependent deformation of shale on the integrity of a geological nuclear waste repository. *International Journal of Rock Mechanics and Mining Sciences*, *158*, 105206. <https://doi.org/10.1016/j.ijrmms.2022.105206>
- Schlömer, S., & Krooss, B. M. (1997). Experimental characterisation of the hydrocarbon sealing efficiency of cap rocks. *Marine and Petroleum Geology*, *14*(5), 565-580.
- Schmitt, L., Forsans, T., & Santarelli, F. J. (1994). Shale testing and capillary phenomena. *International Journal of Rock Mechanics and Mining Sciences & Geomechanics Abstracts*, *31*(5), 411-427.
- Schneider, J., Flemings, P. B., Day-Stirrat, R. J., & Germaine, J. T. (2011). Insights into pore-scale controls on mudstone permeability through resedimentation experiments. *Geology*, *39*(11), 1011-1014.
- Sciandra, D., Vilarrasa, V., Rahimzadeh Kivi, I., Makhnenko, R., Nussbaum, C., & Rebscher, D. (2021). Coupled HM modeling assists in designing CO₂ long-term periodic injection experiment (CO₂LPIE) in Mont Terri rock laboratory. In *EGU General Assembly Conference Abstracts* (pp. EGU21-8982).
- Sciandra, D., Rahimzadeh Kivi, I., Vilarrasa, V., Makhnenko, R., Jaeggi, D., & Rebscher, D. (2022a). 3D hydro-mechanical modeling of shaly caprock response to CO₂ long-term periodic injection experiment (CO₂LPIE). In *ARMA US Rock Mechanics/Geomechanics Symposium* (pp. ARMA-2022). ARMA.

- Sciandra, D., Kivi, I. R., Vilarrasa, V., Makhnenko, R. Y., & Rebscher, D. (2022b). Hydro-mechanical response of Opalinus Clay in the CO₂ long-term periodic injection experiment (CO₂LPIE) at the Mont Terri rock laboratory. *Geomechanics and Geophysics for Geo-Energy and Geo-Resources*, 8(5), 166.
- Sciandra, D.; Kivi, I. R.; Makhnenko, R. Y.; Rebscher, D.; & Vilarrasa, V. (2023). Dataset for analytical and numerical solutions of cyclic pore pressure diffusion equation [Dataset]; DIGITAL.CSIC. <https://doi.org/10.20350/digitalCSIC/15676>
- Seto, C. J., & McRae, G. J. (2011). Reducing risk in basin scale CO₂ sequestration: a framework for integrated monitoring design. *Environmental science & technology*, 45(3), 845-859.
- Shih, D. C. F. (2018). Hydraulic diffusivity in a coastal aquifer: spectral analysis of groundwater level in responses to marine system. *Stochastic Environmental Research and Risk Assessment* 32(2): 311–20.
- Shukla, R., Ranjith, P., Haque, A., & Choi, X. (2010). A review of studies on CO₂ sequestration and caprock integrity. *Fuel*, 89(10), 2651-2664.
- Slack, T. Z., Murdoch, L. C., Germanovich, L. N., & Hisz, D. B. (2013). Reverse water-level change during interference slug tests in fractured rock. *Water Resources Research*, 49, 1552–1567.
- Snow, D. T. (1969). Anisotropic permeability of fractured media. *Water Resources Research*, 5(6), 1273-1289. <https://doi.org/10.1029/WR005i006p01273>
- Song, J., & Zhang, D. (2013). Comprehensive review of caprock-sealing mechanisms for geologic carbon sequestration. *Environmental science & technology*, 47(1), 9-22.
- Span, R., & Wagner, W. (1996). A new equation of state for carbon dioxide covering the fluid region from the triple-point temperature to 1100 K at pressures up to 800 MPa. *Journal of physical and chemical reference data*, 25(6), 1509-1596.
- Spycher, N., Pruess, K., & Ennis-King, J. (2003). CO₂-H₂O Mixtures in the geological sequestration of CO₂. I. Assessment and calculation of mutual solubilities from 12 to 100°C and up to 600 Bar. *Geochimica et Cosmochimica Acta*, 67(16), 3015–31. [https://doi.org/10.1016/S0016-7037\(03\)00273-4](https://doi.org/10.1016/S0016-7037(03)00273-4)
- Streit, J. E., & Hillis, R. R. (2004). Estimating fault stability and sustainable fluid pressures for underground storage of CO₂ in porous rock. *Energy*, 29(9-10), 1445-1456.
- Sun, Y., Xue, Z., & Hashimoto, T. (2018). Fiber optic distributed sensing technology for real-time monitoring water jet tests: Implications for wellbore integrity diagnostics. *Journal of Natural Gas Science and Engineering*, 58, 241-250.
- Sun, Y., Liu, J., Xue, Z., Li, Q., Fan, C., & Zhang, X. (2021). A critical review of distributed fiber optic sensing for real-time monitoring geologic CO₂ sequestration. *Journal of Natural Gas Science and Engineering*, 88, 103751.

- Takahashi, M. (2003). Permeability change during experimental fault smearing. *Journal of Geophysical Research: Solid Earth* 108(B5). <https://doi.org/10.1029/2002JB001984>
- Tamburini, A., Bianchi, M., Giannico, C., & Novali, F. (2010). Retrieving surface deformation by PSInSAR™ technology: A powerful tool in reservoir monitoring. *International Journal of Greenhouse Gas Control*, 4(6), 928-937.
- Tewes, F., & Boury, F. (2005). Formation and rheological properties of the supercritical CO₂–water pure interface. *The Journal of Physical Chemistry B*, 109(9), 3990-3997. <https://doi.org/10.1021/jp046019w>
- Theis, C. V. (1935). The relation between the lowering of the piezometric surface and the rate and duration of discharge of a well using ground-water storage. *Eos, Transactions American Geophysical Union*, 16(2), 519-524. <https://doi.org/10.1029/TR016i002p00519>
- Thiem, G. (1906). *Hydrologic methods*. Gebhardt, Leipzig, Germany.
- Thomas, L. K., Katz, D. L., & Tek, M. R. (1968). Threshold pressure phenomena in porous media. *Society of Petroleum Engineers Journal*, 8(02), 174-184.
- Thury, M., & Bossart, P. (1999a). Mont Terri Rock Laboratory. Results of the hydrogeological, geochemical and geotechnical experiments performed in 1996 and 1997. Geological Reports No.23, *Federal Office of Topography (swisstopo)*, Wabern, Switzerland.
- Thury, M., & Bossart, P. (1999b). The Mont Terri rock laboratory, a new international research project in a Mesozoic shale formation, in Switzerland. *Engineering Geology*, 52(3-4), 347-359. [https://doi.org/10.1016/S0013-7952\(99\)00015-0](https://doi.org/10.1016/S0013-7952(99)00015-0)
- US Energy Inf. Admin (2015). World shale resource assessments. Rep., *US Energy Inf. Admin.*, Washington, DC. <https://www.eia.gov/analysis/studies/worldshalegas/>
- van Genuchten, M. T. (1980). A closed-form equation for predicting the hydraulic conductivity of unsaturated soils. *Soil Science Society of America Journal*, 44(5), 892–98. <https://doi.org/10.2136/sssaj1980.03615995004400050002x>
- van der Kamp, G. (2001). Methods for determining the in situ hydraulic conductivity of shallow aquitards—an overview. *Hydrogeology Journal*, 9, 5-16. <https://doi.org/10.1007/s100400000118>
- van der Kamp, G., & Gale, J. E. (1983). Theory of Earth tide and barometric effects in porous formations with compressible grains. *Water Resources Research* 19(2): 538–44. <https://doi.org/10.1029/WR019i002p00538>
- van Noort, R., & Yarushina, V. (2019). Water, CO₂ and argon permeabilities of intact and fractured shale cores under stress. *Rock Mechanics and Rock Engineering*, 52(2), 299-319. <https://doi.org/10.1007/s00603-018-1609-8>
- Vasco, D. W., Ferretti, A., & Novali, F. (2008). Reservoir monitoring and characterization using satellite geodetic data: Interferometric synthetic aperture radar observations from the Krechba field, Algeria. *Geophysics*, 73(6), WA113-WA122.

- Vasco, D. W., Rucci, A., Ferretti, A., Novali, F., Bissell, R. C., Ringrose, P. S., ... & Wright, I. W. (2010). Satellite-based measurements of surface deformation reveal fluid flow associated with the geological storage of carbon dioxide. *Geophysical Research Letters*, *37*(3).
- Vavra, C. L., Kaldi, J. G., & Sneider, R. M. (1992). Geological applications of capillary pressure: a review. *AAPG bulletin*, *76*(6), 840-850.
- Verdon, J. P. (2014). Significance for secure CO₂ storage of earthquakes induced by fluid injection. *Environmental Research Letters*, *9*(6), 064022. <https://doi.org/10.1088/1748-9326/9/6/064022>
- Verdon, J. P., Kendall, J. M., White, D. J., Angus, D. A., Fisher, Q. J., & Urbancic, T. (2010). Passive seismic monitoring of carbon dioxide storage at Weyburn. *The Leading Edge*, *29*(2), 200-206.
- Verdon, J. P., Kendall, J. M., White, D. J., & Angus, D. A. (2011). Linking microseismic event observations with geomechanical models to minimise the risks of storing CO₂ in geological formations. *Earth and Planetary Science Letters*, *305*(1–2), 143–52. <https://doi.org/10.1016/j.epsl.2011.02.048>
- Vilarrasa, V. (2014). Impact of CO₂ injection through horizontal and vertical wells on the caprock mechanical stability. *International Journal of Rock Mechanics and Mining Sciences*, *66*, 151-159. <https://doi.org/10.1016/j.ijrmms.2014.01.001>
- Vilarrasa, V., & Makhnenko, R. Y. (2017). Caprock integrity and induced seismicity from laboratory and numerical experiments. *Energy Procedia*, *125*, 494–503. <https://doi.org/10.1016/j.egypro.2017.08.172>
- Vilarrasa, V., & Rutqvist, J. (2017). Thermal effects on geologic carbon storage. *Earth-science reviews*, *165*, 245-256.
- Vilarrasa, V., Bolster, D., Olivella, S., & Carrera, J. (2010a) Coupled hydromechanical modeling of CO₂ sequestration in deep saline aquifers. *International Journal of Greenhouse Gas Control*, *4*(6), 910–19. <https://doi.org/10.1016/j.ijggc.2010.06.006>
- Vilarrasa, V., Bolster, D., Dentz, M., Olivella, S., & Carrera, J. (2010b). Effects of CO₂ compressibility on CO₂ storage in deep saline aquifers. *Transport in Porous Media*, *85*(2), 619–39. <https://doi.org/10.1007/s11242-010-9582-z>
- Vilarrasa, V., Olivella, S., & Carrera, J. (2011). Geomechanical stability of the caprock during CO₂ sequestration in deep saline aquifers. *Energy Procedia*, *4*, 5306-5313.
- Vilarrasa, V., Carrera, J., & Olivella, S. (2013). Hydromechanical characterization of CO₂ injection sites. *International Journal of Greenhouse Gas Control*, *19*, 665-677. <https://doi.org/10.1016/j.ijggc.2012.11.014>

- Vilarrasa, V., Olivella, S., Carrera, J., & Rutqvist, J. (2014). Long term impacts of cold CO₂ injection on the caprock integrity. *International Journal of Greenhouse Gas Control*, 24, 1-13.
- Vilarrasa, V., Rutqvist, J., & Rinaldi, A. P. (2015). Thermal and capillary effects on the caprock mechanical stability at In Salah, Algeria. *Greenhouse Gases: Science and Technology*, 5(4), 449–61. <https://doi.org/10.1002/ghg.1486>
- Vilarrasa, V., Makhnenko, R. Y., & Laloui, L. (2017). Potential for fault reactivation due to CO₂ injection in a semi-closed saline aquifer. *Energy Procedia*, 114, 3282–90. <https://doi.org/10.1016/j.egypro.2017.03.1460>
- Vilarrasa, V., Carrera, J., Olivella, S., Rutqvist, J., & Laloui, L. (2019). Induced seismicity in geologic carbon storage. *Solid Earth*, 10(3), 871-892.
- Vilarrasa, V., De Simone, S., Carrera, J., & Villaseñor, A. (2021). Unraveling the causes of the seismicity induced by underground gas storage at Castor, Spain. *Geophysical Research Letters*, 48(7), e2020GL092038.
- Vinsot, A., Delay, J., de La Vaissière, R., & Cruchaudet, M. (2011). Pumping tests in a low permeability rock: Results and interpretation of a four-year long monitoring of water production flow rates in the Callovo-Oxfordian argillaceous rock. *Physics and Chemistry of the Earth, Parts A/B/C*, 36(17-18), 1679-1687.
- Voltolini, M., & Ajo-Franklin, J. B. (2020). The sealing mechanisms of a fracture in opalinus clay as revealed by in situ synchrotron x-ray micro-tomography. *Frontiers in Earth Science*, 8, 207. <https://doi.org/10.3389/feart.2020.00207>
- Walton, W. C. (2020). *Principles of Groundwater Engineering*. CRC Press.
- Wang, H. (2000). *Theory of linear poroelasticity with applications to geomechanics and hydrogeology* (Vol. 2). Princeton university press.
- Warszawski, L., Kriegler, E., Lenton, T. M., Gaffney, O., Jacob, D., Klingensfeld, D., ... & Rockström, J. (2021). All options, not silver bullets, needed to limit global warming to 1.5° C: a scenario appraisal. *Environmental Research Letters*, 16(6), 064037. <https://doi.org/10.1088/1748-9326/abfeec>
- Washburn, E. W. (1921). The dynamics of capillary flow. *Physical review*, 17(3), 273.
- Wemaere, I., Marivoet, J., & Labat, S. (2008). Hydraulic conductivity variability of the Boom Clay in north-east Belgium based on four core drilled boreholes. *Physics and Chemistry of the Earth, Parts A/B/C*, 33, S24-S36.
- Wenning, Q. C., Madonna, C., Zappone, A., Grab, M., Rinaldi, A. P., Plötze, M., ... & Wiemer, S. (2021). Shale fault zone structure and stress dependent anisotropic permeability and seismic velocity properties (Opalinus Clay, Switzerland). *Journal of Structural Geology*, 144, 104273. <https://doi.org/10.1016/j.jsg.2020.104273>

- White, D. (2013). Seismic characterization and time-lapse imaging during seven years of CO₂ flood in the Weyburn field, Saskatchewan, Canada. *International Journal of Greenhouse Gas Control*, 16, S78-S94.
- Whittaker, S., Rostron, B., Hawkes, C., Gardner, C., White, D., Johnson, J., ... & Seeburger, D. (2011). A decade of CO₂ injection into depleting oil fields: monitoring and research activities of the IEA GHG Weyburn-Midale CO₂ Monitoring and Storage Project. *Energy Procedia*, 4, 6069-6076.
- Witherspoon, P. A., Wang, J. S., Iwai, K., & Gale, J. E. (1980). Validity of cubic law for fluid flow in a deformable rock fracture. *Water Resources Research*, 16(6), 1016-1024. <https://doi.org/10.1029/WR016i006p01016>
- Wollenweber, J., a Alles, S., Kronimus, A., Busch, A., Stanjek, H., & Krooss, B. M. (2009). Caprock and overburden processes in geological CO₂ storage: An experimental study on sealing efficiency and mineral alterations. *Energy Procedia*, 1(1), 3469-3476.
- Wollenweber, J., Alles, S., Busch, A., Krooss, B. M., Stanjek, H., & Littke, R. (2010). Experimental investigation of the CO₂ sealing efficiency of caprocks. *International Journal of Greenhouse Gas Control*, 4(2), 231-241.
- Wu, W., Zoback, M. D., & Kohli, A. H. (2017). The impacts of effective stress and CO₂ sorption on the matrix permeability of shale reservoir rocks. *Fuel*, 203, 179-186. <https://doi.org/10.1016/j.fuel.2017.04.103>
- Wüst, R., Bauer, W., Surkova, M., De Cannière, P., Yang, T., Fink, R., Elam, W. T., Grundl, T., Gimmi, T., van Loon, T., Glaus, M., Schefer, S., & Leupin, O. X. (2022). DR-B & DR-E Experiment: Long-term diffusion experiments in FMT – past and future with comparison to TBO experimental data, Technical Meeting TM-39, 26. January 2022, virtual, Switzerland.
- Yang, H., Zhou, P., Fang, N., Zhu, G., Xu, W., Su, J., ... & Chu, R. (2020). A shallow shock: the 25 February 2019 ML 4.9 earthquake in the Weiyuan shale gas field in Sichuan, China. *Seismological Society of America*, 91(6), 3182-3194.
- Yang, Y., & Aplin, A. C. (2010). A permeability–porosity relationship for mudstones. *Marine and Petroleum Geology*, 27(8), 1692-1697.
- Ye, Z., & Ghassemi, A. (2018). Injection-induced shear slip and permeability enhancement in granite fractures. *Journal of Geophysical Research: Solid Earth*, 123(10), 9009-9032.
- Yu, C., Matray, J. M., Gonçalves, J., Jaeggi, D., Gräsle, W., Wieczorek, K., ... & Sykes, E. (2018). Comparative study of methods to estimate hydraulic parameters in the hydraulically undisturbed Opalinus Clay (Switzerland). *Mont Terri Rock Laboratory, 20 Years: Two Decades of Research and Experimentation on Claystones for Geological Disposal of Radioactive Waste*, 87-106.
- Yu, L., Rogiers, B., Gedeon, M., Marivoet, J., De Craen, M., & Mallants, D. (2013). A critical review of laboratory and in-situ hydraulic conductivity measurements for the Boom Clay in Belgium. *Applied Clay Science*, 75, 1-12.

- Yuan, H., Agostini, F., Skoczylas, F., & Talandier, J. (2017). Investigation on gas-adsorption-induced swelling and permeability evolutions of CO_x argillite. In *CFM 2017-23ème Congrès Français de Mécanique*. AFM, Maison de la Mécanique, 39/41 rue Louis Blanc-92400 Courbevoie.
- Zang, A., Yoon, J. S., Stephansson, O., & Heidbach, O. (2013). Fatigue hydraulic fracturing by cyclic reservoir treatment enhances permeability and reduces induced seismicity. *Geophysical journal international*, 195(2), 1282-1287. <https://doi.org/10.1093/gji/ggt301>
- Zang, A., Zimmermann, G., Hofmann, H. *et al.* (2019). How to reduce fluid-injection-induced seismicity. *Rock Mech. Rock Eng.* 52, 475–493. <https://doi.org/10.1007/s00603-018-1467-4>
- Zappone, A., Rinaldi, A. P., Grab, M., Obermann, A., Claudio, M., Nussbaum, C., & Wiemer, S. (2018). CO₂ Sequestration: studying caprock and fault sealing integrity, The CS-D Experiment In Mont Terri. *Fifth CO₂ Geological Storage Workshop*, 2018(1), 1-5. European Association of Geoscientists & Engineers. <https://doi.org/10.3997/2214-4609.201803002>
- Zappone, A., Rinaldi, A. P., Grab, M., Wenning, Q., Roques, C., Madonna, C., ... & Wiemer, S. (2020). Fault sealing and caprock integrity for CO₂ storage: an in-situ injection experiment. *Solid Earth Discussions*, 2020, 1-51. <https://doi.org/10.5194/se-12-319-2021>
- Zareidarmiyani, A., Salarirad, H., Vilarrasa, V., De Simone, S., & Olivella, S. (2018). Geomechanical response of fractured reservoirs. *Fluids*, 3(4), 70.
- Zareidarmiyani, A., Salarirad, H., Vilarrasa, V., Kim, K. I., Lee, J., & Min, K. B. (2020). Comparison of numerical codes for coupled thermo-hydro-mechanical simulations of fractured media. *Journal of Rock Mechanics and Geotechnical Engineering*, 12(4), 850-865. <https://doi.org/10.1016/j.jrmge.2019.12.016>
- Zareidarmiyani, A., Parisio, F., Makhnenko, R. Y., Salarirad, H., & Vilarrasa, V. (2021). How equivalent are equivalent porous media?. *Geophysical Research Letters*, 48(9), e2020GL089163. <https://doi.org/10.1029/2020GL089163>
- Zeelmaekers, E. (2011). Computerized Qualitative and Quantitative Clay Mineralogy: Introduction and Application to Known Geological Cases.
- Zhang, C., & Rothfuchs, T. (2004). Experimental study of the hydro-mechanical behaviour of the Callovo-Oxfordian argillite. *Applied Clay Science*, 26(1-4), 325-336.
- Zhang, R., Ning, Z., Yang, F., Wang, X., Zhao, H., & Wang, Q. (2015). Impacts of nanopore structure and elastic properties on stress-dependent permeability of gas shales. *Journal of Natural Gas Science and Engineering*, 26, 1663-1672.
- Zhu, N., Cheng, P., & Yu, Q. (2023). Experimental study on the time-dependent gas permeability of fractures in shales. *Rock Mechanics and Rock Engineering*, 1-24. <https://doi.org/10.1007/s00603-023-03578-8>

- Ziefle, G., Matray, J. M., Maßmann, J., & Möri, A. (2017). Coupled hydraulic-mechanical simulation of seasonally induced processes in the Mont Terri rock laboratory (Switzerland). *Swiss Journal of Geosciences*, *110*(1), 195–212. <https://doi.org/10.1007/s00015-016-0252-1>
- Zimmerman, R. W., & Bodvarsson, G. S. (1996). Hydraulic conductivity of rock fractures. *Transport in porous media*, *23*, 1-30. <https://doi.org/10.1007/BF00145263>
- Zivar, D., Kumar, S., & Foroozesh, J. (2021). Underground hydrogen storage: A comprehensive review. *International journal of hydrogen energy*, *46*(45), 23436-23462.